Seismic travel time forward modelling and inversion of fluid flow conduits in marine sediments using ocean bottom seismometers

Dissertation

zur Erlangung des Doktorgrades

der Mathematisch-Naturwissenschaftlichen Fakultät

der Christian-Albrechts-Universität zu Kiel

vorgelegt von

Bettina Schramm

Kiel, 2023

Erster Gutachter:	Prof. Dr. Christian Berndt
Zweiter Gutachter:	Prof. Dr. Sebastian Krastel
Tag der mündlichen Prüfung:	26.10.2023
Zum Druck genehmigt am:	22.09.2023

…….

Der Dekan

Erklärung

Hiermit erkläre ich, dass die vorliegende Doktorarbeit selbständig, abgesehen von der Beratung durch die Betreuer, und ohne Zuhilfenahme unerlaubter Hilfsmittel erstellt habe. Weder diese Arbeit noch eine ähnliche Arbeit wurde im Rahmen eines Prüfungsverfahrens veröffentlicht und oder zur Veröffentlichung vorgelegt. Ferner versichere ich, dass die Arbeit unter Einhaltung der Regeln guter wissenschaftlicher Praxis der Deutschen Forschungsgemeinschaft angefertigt wurde. Des Weiteren wurde mir kein akademischer Grad entzogen.

Kiel, den

Bettina Schramm

Summary

The increasing concentration of greenhouse gases in the atmosphere and hydrosphere is causing changes to global climate. Geological carbon sequestration is a proven technology for reducing anthropogenic emissions in the atmosphere. However, leakage of CO_2 along natural fluid pathways, which are imaged as seismic pipes and chimneys, may affect storage formation integrity. These fluid flow conduits are observed in marine basins globally and can extend over 500 m in diameter, passing vertically through kilometres of sedimentary overburden. However, the nature and physical properties of fluid flow conduits are currently poorly understood. In this thesis, I characterise active fluid conduits in the Central North Sea and at the Svalbard Margin, as well as analogous onshore in Varna, Bulgaria. I present three-dimensional seismic P-wave travel time tomographies using ocean bottom seismometers to constrain the geometry, the geophysical properties and the material inside of fluid flow conduits. Furthermore, I discuss the constraints from 2D and 3D multi-channel seismic, bathymetric, and geochemical data for the characterization of fluid flow conduit. A discussion of stress constrains from shear-splitting aims at anisotropic behaviour of fluid migration in shallow sediments. A key aim is to compare fluid flow conduits in marine basins based on the studies of a pipe structure beneath the Scanner Pockmark, Central North Sea, and a chimney below the Lunde Pockmark, Svalbard Margin. The imaging of the active pipe structure below the Scanner Pockmark shows a separation in an upper part that represents a network of open, gas filled fractures with seismic velocities up to 100 m/s slower than the surrounding strata and a lower part, which is characterised by 50 m/s seismic velocity increase compared to background velocity. The three-dimensional distribution of P-wave velocities below the Lunde Pockmark shows high seismic velocity anomalies up to 14% in the chimney interior compared to the surrounding sediments. This analysis, combined with earlier datasets and a priori information, provides evidence for redirection of vertically migrating fluids controlled by buried authigenic carbonate concretions and gas hydrates at specific depths. This fluid migration diversion presumably corresponds to major past seafloor seepage events. Additionally, the ocean bottom seismometer data shows differences in symmetry plane directions in anisotropic media. My results imply a diverse range of the internal structures of fluid flow conduits. The analysis of the 3D P-wave velocity demonstrates that fluid flow conduits are fundamentally different in their geophysical and hydraulic characteristics depending on depth and the geological setting.

The results of my thesis highlight the complexity in evaluating fluid flow conduits, the necessity of their detailed assessment for any offshore carbon storage site selection, and the necessity to

investigate their potential to function as pathways for CO_2 and to ensure the integrity of the reservoir for CO_2 sequestration. These findings improve our understanding of the evolution of vertical fluid migration features globally.

Zusammenfassung

Der zunehmende Anstieg von Treibhausgasen in der Atmosphäre und der Hydrosphäre führt zu Veränderungen des globalen Klimas. Die geologische Kohlenstoffsequestrierung ist eine erprobte Technologie zur Verringerung der anthropogenen Emissionen in die Atmosphäre. Die Migration von CO_2 entlang natürlicher Fluidmigrationsstrukturen im Untergrund, die als seismische Pipes und Chimneys abgebildet werden, kann die Integrität der Speicherformation beeinträchtigen. Diese Fluidmigrationsstrukturen werden weltweit im Meeresboden beobachtet und können einen Durchmesser von über 500 m haben und sich vertikal kilometerlang durch Sedimentschichten erstrecken. Die Beschaffenheit und die physikalischen Eigenschaften dieser Fluidmigrationsstrukturen sind jedoch bisher nur unzureichend erforscht. In dieser Arbeit untersuche ich aktive Fluidmigrationsstrukturen in der zentralen Nordsee und am Svalbard Margin sowie Pipestrukturen in Varna, Bulgarien, als Analogie an Land. Dafür berechne ich dreidimensionale seismische P-Wellen-Laufzeit-Tomographien auf Grundlage von Ozeanboden-Seismometer-Daten, um die Geometrie, die geophysikalischen Eigenschaften und das Material im Innern der Strukturen zu bestimmen. Zusätzlich beziehe ich in meiner Dissertation 2D und 3D Mehrkanalseismik, bathymetrische Daten und geochemische Daten zur Charakterisierung der Fluidmigrationsstrukturen mit ein. Ein Hauptziel ist dabei der Vergleich jener Strukturen im Meeresboden auf der Grundlage der Untersuchungen einer Pipestruktur unter dem Scanner Pockmark in der zentralen Nordsee und eines Chimneys unter dem Lunde Pockmark im Svalbard Margin. Die Tomographie der aktiven Pipestruktur unter dem Scanner Pockmark zeigt eine Differenzierung der internen Architektur der Struktur in zwei Bereiche: einen oberen Teil, der aus einem Netzwerk offener, gasgefüllter Klüfte besteht, deren seismische Geschwindigkeiten bis zu 100 m/s langsamer als die umgebenden Schichten sind, und einen unteren Teil, der durch einen Anstieg der seismischen Geschwindigkeit um 50 m/s im Vergleich zur Hintergrundgeschwindigkeit charakterisiert ist. Die dreidimensionale Verteilung der P-Wellen-Geschwindigkeiten unterhalb des Lunde-Pockmarks zeigt eine Anomalie von bis zu 14 % höheren seismischen Geschwindigkeiten im Inneren des Chimneys im Vergleich zu den umgebenden Sedimenten. Diese Analyse liefert in Verbindung mit früheren Datensätzen und A-priori-Informationen Beweise für die Umlenkung vertikal aufsteigender Fluide, die durch vergrabene authigene Karbonate und Gashydrate in bestimmten Tiefen herbeigeführt wurde. Diese Umlenkung der Fluide wurde vermutlich durch frühere Versickerungsereignisse am Meeresboden verursacht. Außerdem zeigen die Ozeanboden-

Seismometer-Daten Unterschiede in den Richtungen der Symmetrieebenen in anisotropen Medien.

Die Ergebnisse meiner Arbeit deuten auf ein breites Spektrum der internen Architektur von Fluidmigrationsstrukturen hin. Die Analyse der 3D-P-Wellengeschwindigkeit zeigt, dass sich die geophysikalischen und hydraulischen Eigenschaften von Fluidmigrationsstrukturen je nach Tiefe und geologischem Umfeld grundlegend unterscheiden. Die Erkenntnisse meiner Dissertation verdeutlichen die Komplexität der Bewertung von Fluidmigrationsstrukturen, die notwendige detaillierte Bewertung bei der Auswahl von Offshore-Kohlenstoffspeicherstätten und die Notwendigkeit, ihr Potenzial als CO_2-Migrationsweg zu untersuchen, um die Integrität des Reservoirs für die CO_2-Sequestrierung zu gewährleisten. Diese Ergebnisse verbessern unser Verständnis der Entwicklung vertikaler Fluidmigrationswege weltweit.

Table of Content

Abbreviations

BSR	Bottom-simulating reflection
BGHSZ	Base of gas hydrate stability zone
CCS	Carbon Capture and Storage
CORK	Circulation Obviation Retrofit Kit
CO_2	Carbon dioxide
CSEM	Controlled Source Electromagnetic
DHI	Direct hydrocarbons indicators
FAST	First Arrival Seismic Tomography
IPPC	Intergovernmental Panel on Climate Change
Jive3D	Joint Interface and Velocity Estimation in Three Dimensions
LSQR	Least Squares
mbsf	Meter below seafloor
MCS	Multichannel Seismic
OBS	Ocean Bottom Seismometer
STEMM-CCS	Strategies for Environmental Monitoring of Marine Carbon Capture and Storage
UNEP	United Nations Environment Programme
UNFCCC	United Nations Framework Convention on Climate Change WMO World Meteorological Organisation
Vp	P (primary, compressional) wave velocity
Vs	S (secondary, shear) wave velocity
WMO	World Meteorological Organisation

1. Introduction

1.1. Motivation

The migration of fluids through the subsurface is an important geological process in the Earth system. Fluids have an influence, for example, on the Earth's climate, ecosystems, hydrocarbon resources, natural and exploration-related geohazards including earthquakes and landslides, the carbon cycle or the integrity of storage sites. Spatial and temporal variations in flow activity alter the dynamic between the atmosphere, hydrosphere, cryosphere and geosphere with far-reaching implications for the global carbon cycle and climate system. The increasing concentration of greenhouse gases is one of the major challenges in the 21st century and is directly influenced by fluid migration from marine sediments through the water column into the atmosphere (Ciais et al., 2013; Saunois et al., 2016; IPCC, 2022). For one, greenhouse gases such as carbon dioxide and methane are emitted from offshore reservoirs, and for another the Intergovernmental Panel on Climate Change (IPCC) identified carbon dioxide capture and storage (CCS) as a key component of mitigation strategies to reduce the carbon dioxide (CO_2) concentration in the atmosphere in order to limit global warming to 1.5° C by the end of this century (IPCC, 2022). Many of the potential storage sites like saline aquifers or deleted hydrocarbon reservoirs are offshore (Haszeldine, 2009). Therefore, the safety of CO_2 storage sites requires accurate knowledge of the subsurface fluid flow system. However, a qualitative and quantitative understanding of marine fluid flow and the release into the ocean and atmosphere is challenging, particularly in the marine environment, by its inaccessibility of nearshore regions and the associated difficulties in monitoring at sufficient spatial and temporal scales. This leads to large uncertainties in quantifying and attributing emissions from natural marine geological sources and a potential source of risk for marine CO_2 storage sites.

In marine basins, fluid flow is either a diffusive flow through the more permeable sediments close to the surface or occurs in focused flow pathways that penetrate through seals. Such seal bypass systems can occur as geological structures like faults, diapirs, or permeable layers. They can also be formed by fluid migration itself, when the flow rate exceeds the permeability of the overburden. In this case, pore pressure in the rock or sediment increases until hydrofracturing occurs locally and focussed fluid flow pathways form. Such systems are called pipe or chimney structures and are ubiquitous in sedimentary basins (Berndt, 2005; Cartwright, 2007). However, very little is known about their nature, internal architecture, and physical properties, especially their permeability (Karstens et al., 2017). Pipes and chimneys may present a direct connection

from deep reservoirs to the seafloor and feed active seafloor seeps (Hovland & Sommerville, 1985; Schneider vom Deimling et al., 2007; Løseth et al., 2011).

The ubiquity of pipe structures requires their detailed understanding to better estimate the impact of natural emissions of greenhouse gases through pipe structures into ocean and atmosphere and to incorporate them into CCS site selection and CCS site assessment studies. Seismic modelling of ocean-bottom seismometer (OBS) data allows to construct detailed velocity models (Zelt, 1999; Plaza-Faverola et al., 2010) and to put derived velocity anomalies into context with geological and geophysical information to elucidate the functioning of fluid pathways. This thesis is mainly dealing with two fluid flow conduits in sedimentary basins to construct their internal structure and physical properties.

1.1.1. Global warming

Climate change and global warming already have observable effects on the environment and have been in the focus of scientific research over the last decades. Whilst taking natural fluctuations in the climate into account, the average temperature of the Earth is now rising faster than in all other times (Figure 1.1). According to the 'Deutscher Wetterdienst' (DWD), 2020 was the second warmest year in Germany since records have been started (Imbery et al., 2021). It was only 0.1 degree colder than the record years 2022 and 2018, with an average temperature of 10.5 degrees in Germany. Thus, the record years occur in shorter time periods.

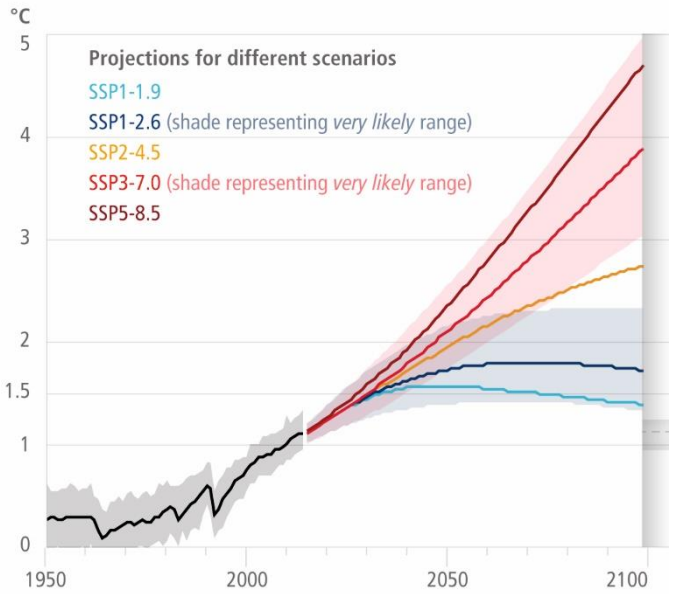

Figure 1.1: Global surface temperature change from 1950 to nowadays and with future projections for different scenarios of the temperature increase (IPPC Summary for Policymakers, 2022).

1. Introduction

Geological records - such as the variations in oxygen ($\delta^{18}O$) and carbon ($\delta^{13}C$) isotopes of deep sediments - show that the earth climate has continuously changed during the last 65 million years (Zachos, 2001). This evolution of the earth climate includes gradual trends of warming and cooling on different time scales (Zachos, 2001). Natural effects on the climate triggered by tectonic processes are on time scales of 10^5 to 10^7 years, rhythmic or periodic cycles driven by orbital processes with durations of 10^4 to 10^6 years and rare rapid aberrant shifts and extreme climate transients with 10^3- to 10^5-year cyclonic (Zachos, 2001). Removing this trend from these natural factors from the ~1000-year time series of the Earth's temperature results in a correlation between anthropogenic greenhouse gas emission and the very large warming of the late 20th century (Crowley, 2000). The main greenhouse gases are carbon dioxide, methane and nitrous oxide. The concentration of these gases in the atmosphere have been reconstructed using ice core records dating back 800,000 years. It shows a significant increase since the beginning of the Industrial era 1750 (Ciais et al., 2014). Worldwide, the ongoing global warming manifested itself in an increase of weather extremes at increasingly shorter intervals as droughts, precipitation deficits, heavy precipitations or floods, an increase of the mean temperature of the atmosphere and the upper surface ocean temperature, partial melting of the Greenland and Antarctic ice sheets, and an average rising of the sea-level of ~ 20 cm (IPCC, 2022). A recent example is that the sea surface temperature rose to 20.96 degrees Celsius on 30 July, according to data from the European Union Climate Observatory.

Due to the extraordinary challenge that society is facing caused by global warming, IPCC was created in 1988 by the World Meteorological Organisation (WMO) and the United Nations Environment Programme (UNEP). The objective of the IPCC is to provide governments at all levels with scientific information, to investigate the correlation between anthropogenic greenhouse gas emissions and global warming, to provide a comprehensive summary of what is known about the drivers of climate change, and to recommend mitigation strategies to society, stakeholder, industry, and policymakers.

According to the IPCC (2022) human activities are estimated to have caused approximately 1.0°C of global warming above pre-industrial levels and the global warming is likely to reach 1.5°C between 2030 and 2063 if it continues to increase at the current rate. The anthropogenic emissions from the pre-industrial period to the present will persist for centuries to millennia and will continue to cause further long-term changes in the climate system (IPCC, 2022).

Even limited global warming of 1.5°C has an impact on terrestrial, freshwater and coastal ecosystems. A sea level rise, caused by the melting ice sheets of Greenland and the Antarctic

of 0.77 m by 2100 amplifies the exposure of small islands, low-lying coastal areas and deltas to risks such as saltwater intrusions, flooding and damage to the human und ecological system (IPCC, 2022). Mitigation pathways to limit global warming to 1.5°C are reaching net zero CO_2 emissions and total emissions of methane, black carbon and nitrous oxide, require a combination of different strategies and technologies. One of these key mitigation technologies is carbon dioxide removal via carbon dioxide capture and storage (CCS) (IPCC, 2022). CCS has the potential to reduce CO_2 emissions in the atmosphere separating of CO_2 from industrial and energy-related sources, by transporting it to storage locations and isolating it from the atmosphere in the long term (Metz et al., 2005). However, CCS is not the solution to reduce CO_2 in the atmosphere to a tolerable amount, but this technology may bridge the time between now and a net-zero carbon emission economy.

1.1.2. Carbon capture and storage

The increasing concentration of greenhouse gases in our atmosphere is one of the major challenges for the global community. The Paris Agreement's central aim is to strengthen the global response to the threat of climate change by keeping the global temperature rise below 2 °C above pre-industrial levels. To reach these ambitious goals, CCS has proven to be a key technology for reducing the emission of carbon CO_2 into the atmosphere and to combat the increase of potential greenhouse gases. Nearly all 1.5°C-pathways require the rapid deployment of industrial-scale CCS (IPCC, 2018).

The aim of CCS is to capture CO_2 from large emission sources such as power stations and industrial facilities, to transport it to a storage site and to permanently lock it away for long-term isolation from the atmosphere (IPCC Special Report on Carbon Dioxide Capture and Storage, 2005).

Since capturing CO_2 directly from small and mobile sources is expected to be more difficult and expensive, the main application of CO_2 capture is likely to be at large point sources (IPCC Special Report on Carbon Dioxide Capture and Storage, 2005). There are four main systems for capturing CO_2 (Metz et al., 2005):

1. Capture from industrial process streams
2. Post-combustion capture
3. Oxy-fuel combustion capture
4. Pre-combustion capture

Transport is that stage of CCS that links sources and storage sites and is an important factor of CCS. Due to the fact that not all power plants are located above geological storage sites and the associated context of long-distance movement of large quantities of carbon dioxide, pipeline transport is part of current practice (IPCC Special Report on Carbon Dioxide Capture and Storage, 2005). Pipelines routinely carry large volumes of natural gas, oil, condensate and water over distances of thousands of kilometres, both on land and in the sea. They are located in deserts, mountain range, heavy populated areas, in the Artic and in seas and oceans up to 2200 m deep. Offshore, an alternative is the transportation via ship (e.g. "Northern Lights" full-scale CCS project in Norway; Global CCS Institute, 2018). In October 2019, the London Protocol Parties provisionally solved one problem during the transportation of CO_2 by the amendment of Article 6 of the Protocol to allow sub-seabed geological formations for sequestration projects to be shared across national boundaries. The London Protocol administers the legal framework for effectively preventing the pollution of the sea caused by dumping or the incineration of waste at sea. CO_2, as an industrial waste product, now can be transported in terms of CCS projects.

Several geological formations have the potential for storing CO_2 (deep saline aquifers, depleted oil and gas reservoirs, etc.). One focus is the ocean storage, as social acceptance in many countries, such as Germany, is greater for offshore projects than onshore storage. Captured CO_2 is injected into the seafloor at great depth, where most of it remains isolated from the atmosphere for centuries (IPCC Special Report on Carbon Dioxide Capture and Storage, 2005). The safe storage of CO_2 in the pore space of the storage formation requires impermeable seals (cap rock) above. The integrity of the cap rock is a crucial requirement for CO_2 storage.

Potential geological storage sites offshore include marine saline aquifers, basalt layers, discharged gas and oil reservoirs, deep unmineable coal beds, salt caverns, or abandoned mines (Metz et al., 2005). So far, deleted oil and gas reservoirs and saline aquifers are the most favoured storage formations, because most operating CO_2 storage sites make use of these storage opportunities and may present the most favourable geological storage opportunity (Michael et al., 2010; Global CCS Institute, 2018). The volume of sedimentary basins in Europe might allow for over 360 Gt of CO_2 to be stored in saline aquifers, 32 Gt in deleted gas and oil reservoirs (Vangkilde-Pedersen et al, 2009).

Saline aquifers are deep, highly permeable and contain large quantities of brines that are not usable for human consumption or agriculture (Metz et al., 2005). Sleipner (1 Mt/a) and Snøhvit (0.7 MT/a), two of Europe's large-scale CCS projects, make use of saline aquifers. One of the

biggest storage formations in the North Sea is the Utsira Formation, a marine saline aquifer with a storage potential of 20 to 60 Gt (Lindeberg et al., 2009). Since 2006, the Sleipner CCS site has already injected 18 Mt of CO_2 into this formation (Furre et al., 2017). A possible conflict concerning carbon storage in saline aquifers may be the interference with the usage of groundwater, hydrocarbon production, and numerous other uses of the subsurface depending on the geological settings.

Fluid traps safely store hydrocarbons over millions of years and have been studied in great detail by hydrocarbon exploration (Metz et al., 2005). These traps can be used for the storage of CO_2 within deleted oil and gas reservoirs. However, the storage capacity of those reservoirs is comparably small and wells of the hydrocarbon exploration may have affected the integrity of the cap rock (Metz et al., 2005).

An alternative place for CO_2 storage might be injected into submarine basalts to form immobile carbonate through the reaction of CO_2 with the host rock. On the European continental margin, basalt provinces have a volume of about 1.2 million km^3. There are virtually no conflicts between CCS in basalt and other industries: there is no hydrocarbon production in basalt provinces, no connection to exploitable freshwater resources and only limited fishery activities. An additional advantage is that the carbonate is immobile. First projects about carbon storage in basalt, i.e. the CarbFix project in Iceland, show the efficiency of carbonation. By injection of CO_2 into these rocks with a depth of more than 1000 m within the clathrate stability zone, carbon storage in basalt provides an additional trap for any CO_2 that could potentially escape from the storage site (Snæbjörnsdóttir, et al., 2020). However, carbon storage sites in basalt are still sparsely explored and there are only a few initial projects like CarbFix in Iceland and PERBAS, a consortium from industry and research investigating technologies for the storage of CO_2 in marine basalt structures.

With all these different geological settings for carbon storage, the integrity of the cap rock and the evaluation of possible leakage pathways requires a careful evaluation. Accumulation of CO_2 beneath the cap rock may lead to critical overpressure and fracturing of the cap rock. Pore fluids may form due to overpressure focused fluid conduits that breach the sealing cap rock and transport fluids and overpressure towards shallower reservoirs or the seafloor (Berndt 2005; Karstens and Berndt, 2015). Very little is known about the physical properties especially the permeability of these focused fluid conduits. If these geological structures can efficiently transfer CO_2, they affect potential carbon storage sites and are a potential risk for the long-term integrity of the storage formation (Karstens et al., 2017).

1.1.3. STEMM-CCS

The Strategies for Environmental Monitoring of Marine Carbon Capture and Storage (STEMM-CCS) project was funded under the European Union's Horizon 2020 programme and was conceived to address the knowledge and capability gaps in methodologies, approaches and technology for an effective environmental monitoring of offshore CCS storage sites.

The key project objectives were to develop:

- Cost-effective tools to identify, detect, and quantify CO_2 leakage from sub-seafloor CCS reservoirs.
- Robust methodology for establishing environmental and ecological baselines.
- Methods for assessing the ability of CO_2 to migrate through leakage pathways to the overburden seafloor at offshore CCS sites.

One keystone of STEMM-CCS was the field experiment to simulate a sub-seafloor CO_2 leak under real-life conditions near the Goldeneye complex in the North Sea.

The STEMM-CCS project consists of seven work packages. Work package 1 coordinated and developed the technical logistics of the STEMM-CCS controlled release experiment, especially the necessary baseline lander for monitoring the background environmental conditions, the drill rig used to emplace the gas pipe, and the CO_2 injection system. Work package 2 established the effective environmental baseline survey at the STEMM-CCS experimental site to identify appropriate biological and chemical indices.

Work package 3 dealt with the location and the expected intensity of CO_2 leakage from CCS sites. The key objectives of this work package are to determine (1) the efficiency of leakage pathways for CO_2 transfer, (2) the CO_2 permeability of fluid flow structures like pipes and chimneys, (3) how long pipe and chimney structures remain open for CO_2 transfer, and (4) the physical properties of pipes and chimney structures.

The primary task of work package 4 was the detection, localisation, and quantification of CO_2 leakage from the controlled CO_2 release experiment. A secondary task was the development of effective methodologies for quantifying of CO_2 fluxes across the seabed and dispersion in the water column as well as coupled and nested model systems to assess CO_2 and tracer dispersion in sediments and the water column for a range of leakage scenarios. Work package 5 dealt with the development of new technologies for the location, detection and quantification of CO_2 leakage. The technology devices should be cost-effective during the measurement of biological

and chemical parameters, including natural variability. The last two work packages, 6 and 7, referred to international collaboration and knowledge sharing. Work package 6 focussed on the collaborative interactions of CCS stakeholders including industry, regulators, governments and researchers. One additional part of work package 7 was the establishment of training programmes for the community of postgraduate and postdoctoral researches involved in this project as well as industry and regulatory stakeholders.

My thesis was conducted in the framework of work package 3 focussing on the physical properties of pipe and chimney structures.

1.2. Fluid flow in marine sediments

1.2.1. Mechanism of fluid flow in marine sediments

Fluid flow in marine sediments occurs all over the world in the marine environment. The transport of fluids through marine sediments is mainly driven by pressure gradients and the permeability contrast (Berndt, 2005), and is defined by Darcy's law, a specific solution of the Navier-Stokes-equation. Darcy's law describes the effective transport of fluids through sedimentary basins (Whitaker, 1986). Depending on the permeability (k) of the rocks, the viscosity of the fluids (μ), and the driving pressure gradient (Δp), it illustrates the effective transport of fluid phases through permeable beds from deeper strata towards:

$$q = -\frac{k}{\mu}\Delta \mathrm{p}.$$

The permeability describes the ability of a porous rock or sediment to allow fluids to migrate through its pore spaces. There are two types of fluid flow: diffuse and focussed fluid flow. Most of the fluid flow in the marine sediments formed by diffusive flow through permeable beds is described by Darcy's law (Løseth et al., 2009). However, seismic data has revealed the presence of focused fluid flow in marine environment. It occurs all over the world and manifests itself in seismic data as a wide range of seismic anomalies (Cartwright et al., 2007; Løseth et al., 2011; Karstens & Berndt, 2015). The type of fluid flow that occurs is related to the permeability of the beds. Lithological units with a low permeability impede or retard the fluid flow to the surface. These impermeable layers are defined as seals (Cartwright et al., 2007). These seals could generate overpressures in the pore space of the underlying sediments. Pore pressure is increased by compaction, hydrothermal activity, rapid loading, or diagenetic processes (Berndt, 2005). Focussed fluid conduits occur when the pore overpressure exceeds the permeable barrier's resistance against the capillary or fracture failure (Clayton & Hay, 1994). The

formation of fractures caused by a high pore fluid overpressure is called hydro-fracturing for water as fluid or pneumatic fracturing for gas.

In marine sediments, the sources of the migrating fluids are various, as are the controlling processes of the propagation of fluids (Berndt, 2005). Focussed fluid flow systems could appear controlled by compactions (Berndt, 2005), hydrothermal venting from volcanic activity (Kulm & Suess, 1990), tectonic compression (Saffer & Tobin, 2011), dissociation of gas hydrates (Kvenvolden, 1993), or burial of seawater (Durgan & Flemings, 2000). Another class of focused fluid flow systems is located close to coastal regions where aquifers conduct freshwater to the shelfs (Berndt, 2005).

The migration of fluids in marine sediments is an important geological process and has great influence on the global carbon cycle, the Earth climate (Svensen et al., 2004), water and hydrocarbon resources, benthic and sub-seafloor ecosystems (Dando et al., 1991; Hovland et al., 2002), or natural and exploration-related geohazards. Furthermore, focussed fluid flow systems could be a trigger mechanism for submarine landslides and associated tsunamis (Bugge et al., 1987).

1.2.2. Focused fluid flow manifestation on the seafloor

Signs for focussed fluid flow manifestations occur in several different ways on the seafloor and have an impact on geology, biology, and the marine environment. Manifestations at the seafloor include pockmarks, carbonates, mud and asphalt volcanos, seafloor fractures, gas hydrates, and biological communities including clams, crabs, and tube worms (Judd & Hovland, 2009). In combination with black smokers, these features can be found even several kilometres below the sea surface at temperatures around 380°C (Baross & Hoffman, 1985). Often, bacterial mats are associated with hydrocarbon seepage (e.g. Santa Barbara Channel offshore California; Spies & Davis, 1979).

The release of big amounts of fluids can cause the mobilisation of the seafloor resulting in the formation of crater-like depression known as pockmarks (Judd & Hovland, 2009). The term pockmark was first used by King and MacLean in 1970 talking about a cone-like depression on the Scotian shelf, but since then, pockmarks have been found all over the world (Judd & Hovland, 2009). They can be identified by sidescan-sonar, seismic and echosounder surveys. Pockmarks are indicators of gas-escape events, but not all pockmarks are actively seeping gas (Judd & Hovland, 2009; Karstens & Berndt, 2015). Pockmarks are frequently associated with carbonate precipitates and unusual biological activity (Judd & Hovland, 2009). The

morphology of the most common pockmarks is standard circular or elliptical, but there are also composite and asymmetric pockmarks, pockmark strings and elongated pockmarks and troughs, unit pockmarks (seabed depression < 5 m) and giant pockmarks (Judd & Hovland, 2009).

1.2.3. Fluid flow manifestation in seismic data

Seismology is a widely used tool to understand the structure of the earth, its dynamic and geological processes, as well as the physical properties of the subsurface. Primarily, seismology depends on the acoustic impedance, which controls the seismic reflection process in sense that only seismic energy is reflected at interfaces in which there are changes in impedance across the interface. Acoustic impedance is defined as the product of density and seismic velocity. Therefore, seismic reflectivity is very sensitive to fluids in the pore space of marine sediments and rocks. Especially gas, with its lower density, has a strong influence on seismic data, seismic velocities and the energy absorption of seismic waves (White, 1975). This effect causes clear anomalies in seismic data, which are summarized by Løseth et al. (2009):

- Acoustic blanking and dim spots are seismic reflections with weak amplitudes and appear as a result of the energy absorption of the seismic waves due to the presence of gas.
- Bright spots are seismic reflections with a high amplitude. They often appear in combination with a polarity reversal, which is an indication of free gas in the pore space (White, 1975).
- Phase reversals result from the change in polarity of the seismic response when a zone with a lower acoustic impedance is overlaid by a high acoustic impedance zone.
- Push-downs or pull-ups of seismic reflections generated by seismic velocity changes.
- Bottom-simulating reflections (BSR) are non-lithological reflections that are broadly parallel to the seafloor and can crosscut sedimentary strata. BSRs can be related to gas hydrates or diagenesis (Shipley at al., 1979; Holbrook et al., 1996; Berndt at al., 2004). In most cases, they appear in combination with a negative polarity caused by the contrast between the overlying gas hydrates and the underlying gas-saturated sediments (Bangs et al., 1993). The depth of the BSR depends on the temperature-depth ratio under which gases (e.g. methane) and water form stable hydrates.
- Breaks in continuous seismic reflections.

These are direct hydrocarbons indicators (DHI), which highlight gas accumulation of fluids (e.g. oil or gas) in the subsurface.

Focussed fluid flow only occurs when fluids from a deeper source focus through a seal-bypass system and escape vertically by seepage to shallow strata (Cartwright et al., 2007). These focused fluid flow systems are typically associated with vertical fluid conduits (Berndt et al., 2003; Løseth et al. 2011), wells from hydrocarbon exploration and other subsurface operations (Gurevich et al., 1993; Vielstädte et al., 2017), or structure-controlled fluid flow along fractured zones or faults (Behrmann, 1991; Cartwright et al., 2007).

However, the interpretation of fluid flow structures, especially if they are vertically orientated, is ambiguous (Karstens & Berndt, 2015) and must include a careful evaluation if there is a real fluid flow structure or if the seismic anomaly is just an imaging artefact. Often, effects such as blanking beneath gas accumulations, migration artefacts due to insufficiently resolved lateral velocity variations at shallow depth or bad seismic traces may lead to misinterpretations as fluid flow conduits (Karstens & Berndt, 2015). The internal architecture and physical properties of fluid flow systems are poorly understood and may vary in time and space (Clayton & Dando, 1996; Moss & Cartwright, 2010; Chand et al., 2012; Kartstens et al., 2018). Certainly, in both cases seismic tomography using ocean bottom seismometer data could help. Seismic tomography is used to determine velocity anomalies of seismic wave propagation in the earth's interior. The seismic velocities provide information about the physical properties of the fluid flow system and are highly sensitive to gas accumulation. For this reason, seismic tomography is a powerful and useful technique to analyse focused fluid flow systems.

1.2.4. Pipes and chimneys

Vertical gas accumulation can be observed in seismic data as columnar vertical amplitude anomalies known as pipes or chimneys (Cartwright et al., 2007; Løseth et al., 2011, Andresen 2012; Karstens and Berndt. 2015). These vertical focused fluid conduits are interpreted as a hydraulic connection between deeper stratigraphic layers with the sediment overburden. They form where localized overpressure breaches the sealing cap rock and fluids migrate upwards. Pipes and chimneys occur in sediment basins all over the world, often above hydrocarbon reservoirs (Heggland, 1997; Karstens et al., 2018) and can reach from a few tens of meters in diameter to more than 2 km in diameter. In literature, different definitions regarding the use of the terms chimneys or pipes can be found. Hereinafter, I use the classification of Karstens & Berndt (2015), which classified dimmed or wiped-out zones as seismic chimney. Chimneys are

wider than pipes and have diameters of several kilometres and their boundaries are often not formed by straight vertical lines (Figure 1.2.a). Seismic chimneys have been described for example in the North Sea in combination with the hydrocarbon reservoirs Ekofisk (Hovland & Sommerville 1985), Hild (Lønøy et al., 1986) or Tommeliten (Granli et al., 1999). Seismic pipes are comparably narrow and have sharp vertical boundaries to the host rock (Figure 1.2.b). They are characterised by broken and bent reflections and bright spots. Examples for pipes are found offshore Angola (Løseth et al., 2011), the Nyegga area, offshore Norway (Plaza-Faverola et al., 2011, Figure 1.2.b), the Danube delta (Hillman et al., 2018) or the Scanner Pockmark in the North Sea (Böttner et al., 2019).

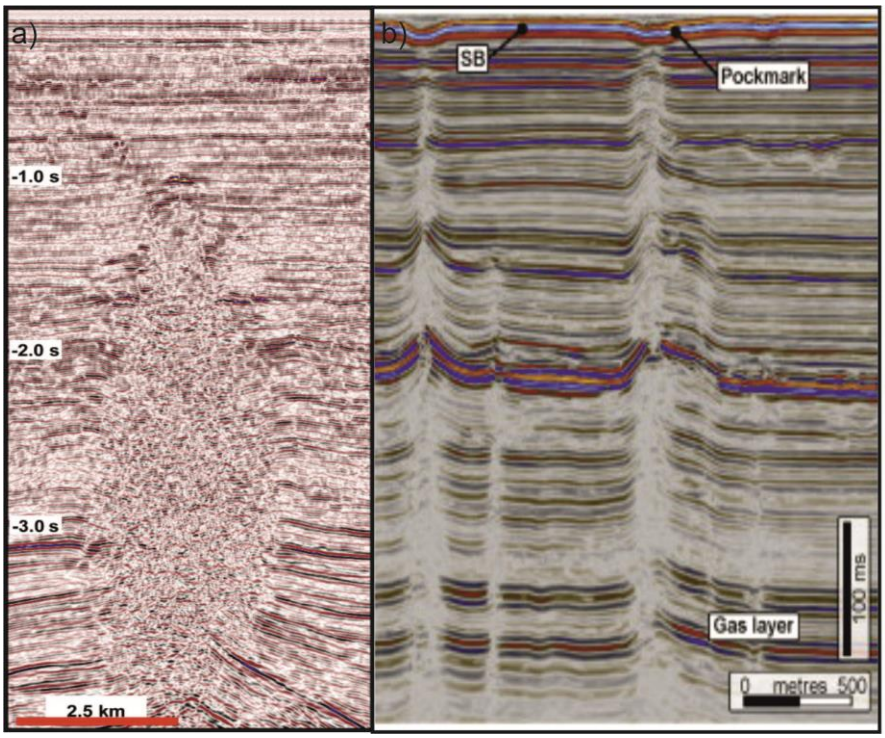

Figure 1.2: a) Seismic characteristics of a chimney structure above the Tommeliten field (Løseth et al., 2009) and a pipe structure offshore Norway (Plaza-Faverola et al., 2011).

Conventional 3D Multichannel Seismic (MCS) data is good in imaging horizontal and gently dipped reflectors in the subsurface, but less conductive in imaging vertical structures such as pipes or chimneys. Often, fluid flow is associated with the accumulation of free gas, which causes high-amplitude reflections and is connected with a loss of seismic energy or scattering. Free gas reduces the seismic imaging of the underlying structures. Effects like blanking beneath gas accumulations, migration artefacts due to insufficiently resolved lateral velocity variations at shallow depth or bad seismic traces may lead to misinterpretation as seismic pipes (Karstens & Berndt, 2015). All of these effects could manifest in MSC data as a seismic artefact and need a careful consideration by distinguishing between seismic artefacts and fluid flow conduits. In

differentiating between real geological structures and imaging artefacts in such settings, seismic velocity models may be a powerful tool to identify real vertical fluid flow conduits. The presence of fluids in the pores affects seismic velocities. Often, seismic velocity models are based on OBS data. These have the advantage to record shots from all directions with a long offset, showing a good signal-noise ratio. Due to the long offset, gas accumulation can be undershot and the wide-angle transmission regime involved in OBS methods can assist in resolving the issue of acoustic blanking due to the present of free gas.

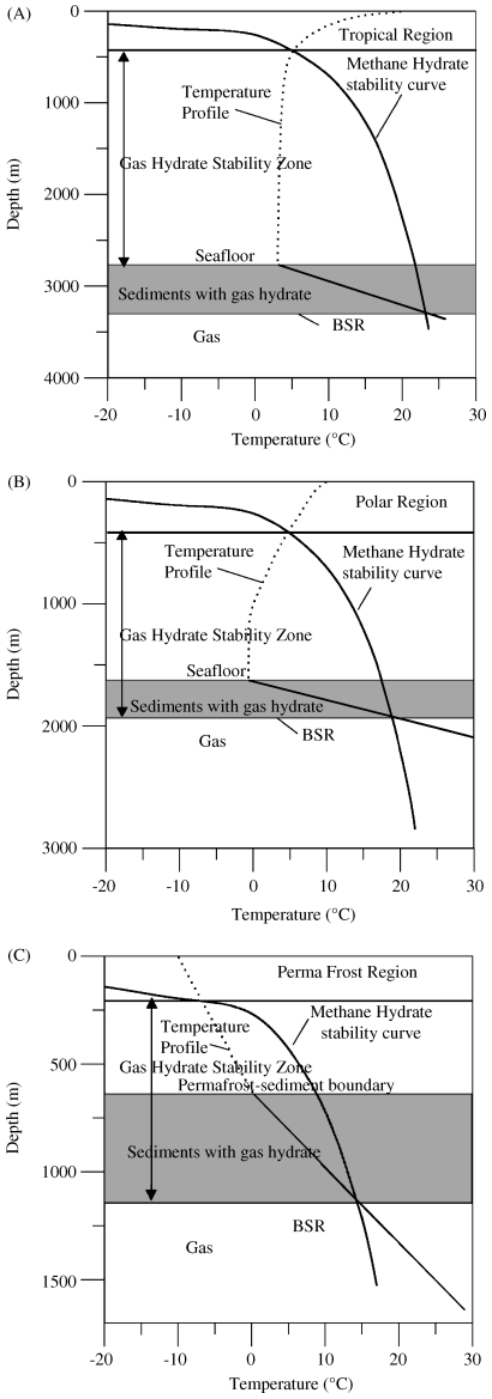

Figure 1.3: The hydrate stability field in different tectonic settings as in a) tropical temperature conditions, b) polar conditions and c) permafrost conditions (Chand and Minshull, 2003).

1.2.5. Gas and gas hydrates in marine sediments

Gas in marine sediments is dominated by methane, which appears as free gas, gas hydrates or dissolved in porewater. Methane in marine sediments originates from biogenic sources, derived from microbial degradation of organic matter, or thermogenic sources, generated in deep hydrocarbon reservoirs by thermal cracking of kerogens (Whiticar, 2000). With help of the carbon and hydrogen isotope signatures and the relative proportions of the methane and other

nature hydrocarbons (e.g. ethane, propane, butane) the two different sources can be distinguished (Whiticar, 2000).

A large amount of methane in marine sediments is stored as gas hydrates. Gas hydrate or gas clathrate is composed of water molecules, which form a rigid lattice of cages, where most cages contain a molecule of natural gas, e.g. methane. Gas hydrates occurs worldwide, but gas hydrates are just stable under high-pressure and low temperatures (Figure 1.3), and their occurrence is restricted to two regions: polar regions and continental margins (Kvenvolden, 1988). Estimations of the amount of gas hydrates are poorly constrained and range from 3 to 400,000 GT of carbon (Kvenvolden, 1988; Kvenvolden, 1993; Milkov, 2004; Burwicz et al., 2011; Piñero et al., 2013). Natural gas hydrates are metastable and affected by change in pressure or temperature. Destabilized gas hydrates may affect the global climate through the release of methane, which enhances the climate change. To understand the dynamic of the system and to make realistic estimation of the natural methane emission from the ocean, a profound understanding of the fluid flow system, especially the internal architecture and preferential migration pathways through the overburden, is necessary.

Gas and gas hydrates have a strong effect on the sediment acoustic properties, especially on the seismic velocity. The presence of gas hydrates in the sediments increase their seismic velocities, while the presence of gas, even with a few percent, decreases the seismic velocities (Figure 1.4). A detailed knowledge of the compressional and/ or shear wave velocity distribution are essential for a estimation of free gas or gas hydrates saturation in the pore space, epically while no direct measurements (e.g. drilling campaigns) or other geophysical data (e.g. electromagnetic data) are available.

Beside the seismic velocities, bottom simulating reflectors (BSRs) are widely used indicators for the presence of gas hydrate in marine sediments. A BSR marks the base of the hydrate stability zone, where pressure and temperature conditions are at the phase boundary between gas hydrates and free gas below. A BSR is more sensitive to temperature than to pressure. Since the temperature in undisturbed sediments usually decreases with depth, a BSR mimics the seafloor.

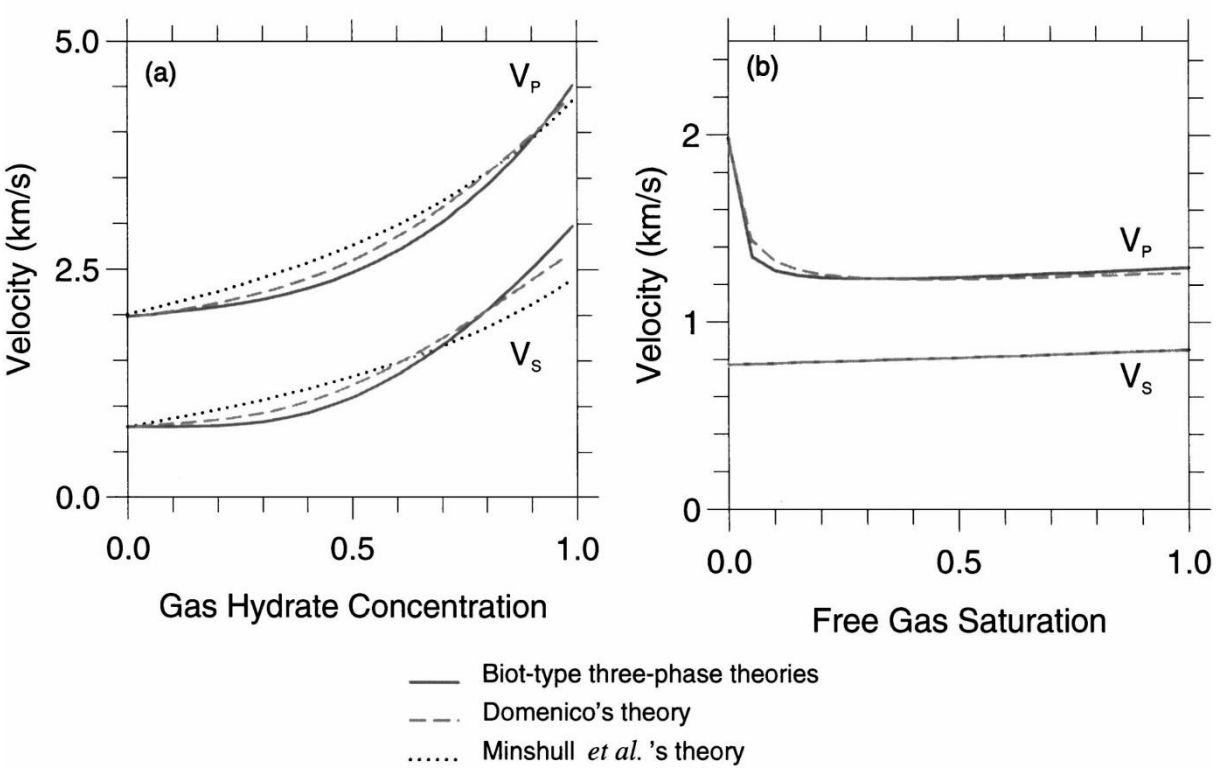

Figure 1.4: Seismic compressional (Vp) and shear (Vs) wave velocities for gas hydrate bearing sediments and free gas bearing sediments (Carcione and Tinivella, 2000).

1.3. Aims of this thesis

In order to mitigate the consequences of climate change, the exploration of CO_2 storage sites becomes increasingly important. One focus of this work is to determine how the geological strata between the reservoir rock and the surface (the overburden) can act as a seal for the reservoir that keeps the CO_2 in place and particularly, whether pipes and chimneys could be a potential pathway for CO_2 through the subsurface. Therefore, this thesis deals with the impact of fluid flow conduits in marine sediments. In order to characterize these fluid flow conduits, I constrain the geophysical nature of pipes and chimneys, and provide new insight for the following questions:

1. What is the internal structure of pipes and chimneys and what are their physical properties?
2. How can seismic P-wave velocity tomographies in combination with other geological and geophysical information elucidate the material inside fluid flow conduits?
3. How can OBS data be used to determine the distribution of gas hydrate, free gas, and carbonates within the gas chimneys and pipes without costly drilling campaign?

4. How can OBS data contribute to the localization of potential CCS sites?

1.4. Thesis outline

This thesis consists of eight chapters including an introduction, the methodical background, five articles or research manuscripts dealing with focussed fluid flow in marine sediments, and a concluding chapter. I authored the article and manuscript presented in chapters 4 and 5, and contributed relevant scientific input to the other articles or manuscripts (chapters 3, 6 and 7). All manuscripts have been published, submitted, or are planned to submitted to peer-review journals.

Chapter 1 introduces this thesis. It describes the motivation for this thesis and gives an overview of the current state of knowledge.

Chapter 2 outlines the concept of tomographic inversion and seismic modelling. Furthermore, I compare the two modelling codes FAST and Jive3D and give a recommendation on their application.

Chapter 3 is the article Böttner et al. (2019) published in Geochemistry, Geophysics, Geosystems. We investigated the fluid migration along pipe structures in the Central North Sea and emphasized the correct attribution of fluids involved in pockmark formation. We combined 2D and 3D multi-channel seismic data, multibeam bathymetric, geochemical, and sedimentological data to characterize pockmarks in the Witch Ground Basin and analyse the related methane release. Additionally, we defined two classes of pockmarks based on morphology and structure. We concluded that greenhouse gas emissions from pockmark fields cannot be based on pockmark numbers and present-day fluxes, but require an analysis of the pockmark forming processes through geological time.

Böttner, C., Berndt, C., Reinardy, B. T., Geersen, J., Karstens, J., Bull, J. M., Callow, B. J., Lichtschlag, A., Schmidt, M., Elger, J., Schramm, B., Haeckel, M. (2019). Pockmarks in the Witch Ground Basin, Central North Sea. *Geochemistry, Geophysics, Geosystems*, *20*(4), 1698-1719. https://doi.org/10.1029/2018GC008068

Chapter 4 is the article Schramm et al. (2021) published in Marine and Petroleum Geology and examines natural fluid migration structures like pipes and chimneys close to CCS deposits, which are potentially suitable for CCS. The detailed structures of such fluid flow conduits are poorly understood and may be very variable. In this article we present the results of a high-resolution 3D seismic refraction tomography of a pipe structure beneath the Scanner Pockmark

in the central North Sea. We show that the conduit, which manifests as a pipe structure in seismic data, is separated into two parts. The upper part is characterized by a negative seismic anomaly that represents a network of open fractures, partly filled with free gas. The deeper part is characterized by a positive seismic anomaly. However, the nature of the deeper part is less clear, but probably a result of calcite precipitation or an overprinting of the original sediment texture by fluid migration. These observations suggest that active pipes can be internally heterogeneous with some intervals probably being open fluid pathways and other intervals being closed. This study highlights the complexity in evaluating focused fluid conduits and the necessity of their detailed assessment when selecting CO_2 storage sites. In this article I deal with the questions 1, 2, 3, and 5 of my aims.

Schramm, B., Berndt, C., Dannowski, A., Böttner, C., Karstens, J., & Elger, J. (2021). Seismic imaging of an active fluid conduit below Scanner Pockmark, Central North Sea. *Marine and Petroleum Geology*, *133*, 105302. https://doi.org/10.1016/j.marpetgeo.2021.105302

Chapter 5 is a manuscript, which yields to characterize the seismic p-wave velocity anomaly beneath the Lunde Pockmark at the Vestnesa Ridge, Svalbard Margin. Such seismic anomalies are widely believed to represent natural fluid migration pathways, yet their physical properties are poorly constrained. In this article we present a high-resolution 3D seismic travel time tomography using OBS and 3D multi-channel seismic data. The model shows a high velocity anomaly beneath the actively seeping Lunde Pockmark caused by gas hydrates and carbon cementations overprinting the velocity decrease of upcoming gas. The results of our study, together with the results of other seismic tomographies, indicate a wide and notable diversity of such fluid flow related structures and their characteristics. This underlines the importance of studying such structures to better understand fluid migration behaviour in marine sediment basins. Chapter 5 is submitted to Geophysical Research Letters and focuses on questions 1, 2, 3 and 4 of my aims.

Schramm, B., Singhroha, S., Plaza-Faverola, A., Dannowski, A., Berndt, C., Bünz, S., (submitted). Characterization of an active gas chimney using seismic velocity analysis, west-Svalbard Margin. *Geophysical Research Letters.*

Chapter 6 examines the stress constraints from shear-wave splitting through shallow sediments at the actively seeping Lunde Pockmark on the Svalbard margin. The article has been accepted by Sunny Singhroha as first author in Earth and Space Science. We investigated differences in S-wave splitting behaviour by estimating symmetry plane directions in anisotropic media using

S-wave null energy directions in transverse components. Subsurface stress distribution affects S-wave splitting behaviour using OBS data. We use S-wave data to infer the stress regime in and around the active seep site and study the effect of stresses on seepage. We observe changes in horizontal stresses in and around Lunde Pockmark. Our analysis indicates a potential correlation of hydrofractures and horizontal stresses, with up to ~32% higher probability of alignment of hydrofractures and faults perpendicular to the minimum horizontal stress below the Lunde Pockmark area.

Singhroha, S., Schramm, B., Plaza-Faverola, A., Domel, P., Bünz, S., Dannowski, A. (2023, accepted). Stress constraints from shear-wave splitting in shallow sediments at an actively seeping pockmark on the W-Svalbard Margin. *Earth and Space Science.*

Chapter 7 is the article Böttner et al. (2021), which presents our study of an onshore outcrop of a focused fluid flow conduit in Varna, Bulgaria. The examined outcrop pipes are the largest known hydrocarbon-derived carbonate conduits. The structures are well-exposed in unconsolidated sand and sandstones. An uncrewed aerial vehicle with an RGB sensor camera produced ortho-rectified image mosaics, digital elevation models and point clouds of the two kilometre-scale outcrop areas. Based on these data, geological field observations and petrological analysis of rock/core samples, fractures and vertical fluid conduits were mapped and analysed with centimetre accuracy. The results indicate that both outcrops comprise several hundred carbonate-cemented fluid conduits (pipes), which are oriented perpendicular to bedding, and at least seven bedding-parallel calcite cemented interbeds which differ from the hosting sand formation only by their increased amount of cementation. Similar structures may also form in modern settings where focused fluid flow advects fluids into overlying sand-dominated formations, which has wide implications for the understanding of how focusing of fluids works in sedimentary basins with broad consequences for the migration of water, oil and gas.

Böttner, C., Callow, B. J., Schramm, B., Gross, F., Geersen, J., Schmidt, M., Vasilev, A., Petsinski, P., Berndt, C. (2021). Focused methane migration formed pipe structures in permeable sandstones: Insights from uncrewed aerial vehicle-based digital outcrop analysis in Varna, Bulgaria. *Sedimentology*, *68*(6), 2765-2782. https://doi.org/10.1111/sed.12871

Chapter 8 compares and discusses the results of the presented studies of the Scanner and Lunde Pockmarks, as well as a study of Plaza-Faverola et al. (2010). All of these studies use high-resolution seismic P-wave tomographies to characterise fluid migration structures in sediment

basins. Finally, Chapter 8 gives an outlook as well as recommendations for future studies in this field.

References

Andresen, K.J. (2012). Fluid flow features in hydrocarbon plumbing systems: What do they tell us about the basin evolution?. Marine Geology, 332, pp.89-108. https://doi.org/10.1016/j.margeo.2012.07.006

Bangs, N.L., Sawyer, D.S., Golovchenko, X. (1993). Free gas at the base of the gas hydrate zone in the vicinity of the Chile triple junction. Geology, 21(10), pp.905-908. https://doi.org/10.1130/0091-7613(1993)021%3C0905:FGATBO%3E2.3.CO;2

Baross, J.A. and Hoffman, S.E. (1985). Submarine hydrothermal vents and associated gradient environments as sites for the origin and evolution of life. Origins of Life and Evolution of the Biosphere, 15(4), pp.327-345. https://doi.org/10.1007/BF01808177

Behrmann, J.H. (1991). Conditions for hydrofracture and the fluid permeability of accretionary wedges. Earth and Planetary Science Letters, 107(3-4), pp.550-558. https://doi.org/10.1016/0012-821X(91)90100-V

Berndt, C. (2005). Focused fluid flow in passive continental margins. Philosophical Transactions of the Royal Society A: Mathematical, Physical and Engineering Sciences, 363(1837), 2855-2871. https://doi.org/10.1098/rsta.2005.1666

Berndt, C., Bünz, S. and Mienert, J. (2003). Polygonal fault systems on the mid-Norwegian margin: a long-term source for fluid flow. Geological Society, London, Special Publications, 216(1), pp.283-290. https://doi.org/10.1144/GSL.SP.2003.216.01.18

Berndt, C., Bünz, S., Clayton, T., Mienert, J., Saunders, M. (2004). Seismic character of bottom imulating reflectors: examples from the mid-Norwegian margin. Marine and Petroleum Geology, 21(6), 723-733. https://doi.org/10.1016/j.marpetgeo.2004.02.003

Böttner, C., Berndt, C., Reinardy, B.T., Geersen, J., Karstens, J., Bull, J.M., Callow, B.J., Lichtschlag, A., Schmidt, M., Elger, J. and Schramm, B. (2019). Pockmarks in the Witch Ground Basin, Central North Sea. Geochemistry, Geophysics, Geosystems, 20(4), pp.1698-1719. https://doi.org/10.1029/2018GC008068

Böttner, C., Callow, B. J., Schramm, B., Gross, F., Geersen, J., Schmidt, M., Vasilev, A.,Petsinski, P., Berndt, C. (2021). Focused methane migration formed pipe structures in permeable sandstones: Insights from uncrewed aerial vehicle-based digital outcrop analysis in Varna, Bulgaria. Sedimentology, 68(6), 2765-2782. https://doi.org/10.1111/sed.12871

Bugge, T., Befring, S., Belderson, R.H., Eidvin, T., Jansen, E., Kenyon, N.H., Holtedahl, H., Sejrup, H.P. (1987). A giant three-stage submarine slide off Norway. Geo-marine letters, 7(4), pp.191-198. https://doi.org/10.1007/BF02242771

Burwicz, E.B., Rüpke, L.H., Wallmann, K. (2011). Estimation of the global amount of submarine gas hydrates formed via microbial methane formation based on numerical reaction-transport modeling and a novel parameterization of Holocene sedimentation. Geochimica et Cosmochimica Acta, 75(16), pp.4562-4576. https://doi.org/10.1016/j.gca.2011.05.029

Carcione, J. M., Tinivella, U. (2000). Bottom-simulating reflectors: Seismic velocities and AVO effects. *Geophysics*, *65*(1), 54-67. https://doi.org/10.1190/1.1444725

Cartwright, J. (2007). The impact of 3D seismic data on the understanding of compaction, fluid flow and diagenesis in sedimentary basins. Journal of the Geological Society, 164(5), pp.881-893. https://doi.org/10.1144/0016-76492006-143

Chand, S., Minshull, T. A. (2003). Seismic constraints on the effects of gas hydrate on sediment physical properties and fluid flow: a review. *Geofluids*, *3*(4), 275-289. https://doi.org/10.1046/j.1468-8123.2003.00067.x

Chand, S., Thorsnes, T., Rise, L., Brunstad, H., Stoddart, D., Bøe, R., Lågstad, P, Svolsbru, T. (2012). Multiple episodes of fluid flow in the SW Barents Sea (Loppa High) evidenced by gas flares, pockmarks and gas hydrate accumulation. Earth and Planetary Science Letters, 331, 305-314. https://doi.org/10.1016/j.epsl.2012.03.021

Ciais, P., Sabine, C., Bala, G., Bopp, L., Brovkin, V., Canadell, J., Chhabra, A., DeFries, R., Galloway, J., Heimann, M. and Jones, C. (2014). Carbon and other biogeochemical cycles. In Climate change 2013: the physical science basis. Contribution of Working Group I to the Fifth Assessment Report of the Intergovernmental Panel on Climate Change (pp. 465-570). Cambridge University Press.

Clayton, C.J. and Dando, P.R. (1996). Comparison of seepage and seal leakage rates.

Clayton, C.J. and Hay, S.J. (1994). Migration mechanisms from accumulation to surface. Bulletin of the Geological Society of Denmark, 41, pp.12-23.

Crowley, T.J. (2000). Causes of climate change over the past 1000 years. Science, 289(5477), pp.270-277. https://doi.org/10.1126/science.289.5477.270

Dando, P.R., Austen, M.C., Burke Jr, R.A., Kendall, M.A., Kennicutt, M.C., Judd, A.G., Moore, D.C., O'Hara, S.C.M., Schmalijohann, R. and Southward, A.J. (1991). Ecology of a North Sea pockmark with an active methane seep. Marine Ecology Progress Series, pp.49-63.

Dugan, B. and Flemings, P.B. (2000). Overpressure and fluid flow in the New Jersey continental slope: Implications for slope failure and cold seeps. Science, 289(5477), pp.288-291. https://doi.org/10.1126/science.289.5477.288

European Union Climate Observatory (2023,July). Tracking breaches of the 1.5ºC global warming threshold | Copernicus. https://climate.copernicus.eu/tracking-breaches-150c-global-warming-threshold

Furre, A.K., Eiken, O., Alnes, H., Vevatne, J.N. and Kiær, A.F. (2017). 20 years of monitoring CO2-injection at Sleipner. Energy procedia, 114, pp.3916-3926. https://doi.org/10.1016/j.egypro.2017.03.1523

Global CCS Institute (2018). The Global Status of CCS: 2018, Melbourne, Australia. Retrieved from https://www.globalccsinstitute.com/resources/global-status-report/.

Granli, J.R., Arntsen, B., Sollid, A. and Hilde, E. (1999). Imaging through gas-filled sediments using marine shear-wave data. Geophysics, 64(3), pp.668-677. https://doi.org/10.1190/1.1444576

Gurevich, A.E., Endres, B.L., Robertson Jr, J.O. and Chilingar, G.V. (1993). Gas migration from oil and gas fields and associated hazards. Journal of Petroleum Science and Engineering, 9(3), pp.223-238. https://doi.org/10.1016/0920-4105(93)90016-8

Haszeldine, R. S. (2009). Carbon capture and storage: how green can black be? Science 325.5948: 1647-1652. https://doi.org/10.1126/science.1172246

Heggland, R. (1997). Detection of gas migration from a deep source by the use of exploration 3D seismic data. Marine Geology, 137(1-2), 41-47. https://doi.org/10.1016/S0025-3227(96)00077-1

Hillman, J.I., Burwicz, E., Zander, T., Bialas, J., Klaucke, I., Feldman, H., Drexler, T. and Awwiller, D. (2018). Investigating a gas hydrate system in apparent disequilibrium in the Danube Fan, Black Sea. Earth and Planetary Science Letters, 502, pp.1-11. https://doi.org/10.1016/j.epsl.2018.08.051

Holbrook, W.S., Hoskins, H., Wood, W.T., Stephen, R.A. and Lizarralde, D. (1996). Methane hydrate and free gas on the Blake Ridge from vertical seismic profiling. Science, 273(5283), pp.1840-1843. https://doi.org/10.1126/science.273.5283.1840

Hovland, M., Gardner, J.V. and Judd, A.G. (2002). The significance of pockmarks to understanding fluid flow processes and geohazards. Geofluids, 2(2), pp.127-136. https://doi.org/10.1046/j.1468-8123.2002.00028.x

Hovland, M. and Sommerville, J.H. (1985). Characteristics of two natural gas seepages in the North Sea. Marine and Petroleum Geology, 2(4), pp.319-326. https://doi.org/10.1016/0264-8172(85)90027-3

Imbery, F., Kaspar, F., Friedrich, K., & Plückhahn, B. (2021). Klimatologischer Rückblick auf 2020: Eines der wärmsten Jahre in Deutschland und Ende des bisher wärmsten Jahrzehnts. Report of the German Weather service (DWD). Available online at: https://www. dwd. de/DE/leistungen/besondereereignisse/temperatur/20210106_rueckblick_jahr_2020. pdf.

IPCC (2005) – Bert Metz, Ogunlade Davidson, Heleen de Coninck, Manuela Loos and Leo Meyer (Eds.) Cambridge University Press, UK. pp 431. Available from Cambridge University Press, The Edinburgh Building Shaftesbury Road, Cambridge CB2 2RU ENGLAND

IPCC: Allen, M. R., Babiker, M., Chen, Y., de Coninck, H., Connors, S., van Diemen, R., ... & Zickfeld, K. (2018). Summary for policymakers. In Global Warming of 1.5: An IPCC Special Report on the impacts of global warming of 1.5\C above pre-industrial levels and related global greenhouse gas emission pathways, in the context of strengthening the global response to the threat of climate change, sustainable development, and efforts to eradicate poverty. IPCC.

IPCC (2022): *Climate Change 2022: Impacts, Adaptation, and Vulnerability.* Contribution of Working Group II to the Sixth Assessment Report of the Intergovernmental Panel on Climate Change [H.-O. Pörtner, D.C. Roberts, M. Tignor, E.S. Poloczanska, K. Mintenbeck, A. Alegría, M. Craig, S. Langsdorf, S. Löschke, V. Möller, A. Okem, B. Rama (eds.)]. Cambridge University Press. Cambridge University Press, Cambridge, UK and New York, NY, USA, 3056 pp., doi:10.1017/9781009325844.

IPCC (2022): Summary for Policymakers [H.-O. Pörtner, D.C. Roberts, E.S. Poloczanska, K. Mintenbeck, M. Tignor, A. Alegría, M. Craig, S. Langsdorf, S. Löschke, V. Möller, A. Okem (eds.)]. In: *Climate Change 2022: Impacts, Adaptation, and Vulnerability.* Contribution of Working group II to the Sixth Assessment Report of the Intergovernmental Panel on Climate Change [H.-O. Pörtner, D.C. Roberts, M. Tignor, E.S. Poloczanska, K. Mintenbeck, A. Alegría, M. Craig, S. Langsdorf, S. Löschke, V. Möller, A. Okem, B. Rama (eds.)]. Cambridge University Press, Cambridge, UK and New York, NY, USA, pp. 3-33, doi:10.1017/9781009325844.001

Judd, A. and Hovland, M. (2009). Seabed fluid flow: the impact on geology, biology and the marine environment. Cambridge University Press.

Karstens, J. and Berndt, C. (2015). Seismic chimneys in the Southern Viking Graben–Implications for palaeo fluid migration and overpressure evolution. Earth and Planetary Science Letters, 412, pp.88-100. https://doi.org/10.1016/j.epsl.2014.12.017

Karstens, J., Ahmed, W., Berndt, C. and Class, H. (2017). Focused fluid flow and the sub-seabed storage of CO2: Evaluating the leakage potential of seismic chimney structures for the Sleipner CO2 storage operation. Marine and Petroleum Geology, 88, pp.81-93. https://doi.org/10.1016/j.marpetgeo.2017.08.003

Karstens, J., Haflidason, H., Becker, L.W., Berndt, C., Rüpke, L., Planke, S., Liebetrau, V., Schmidt, M. and Mienert, J. (2018). Glacigenic sedimentation pulses triggered post-glacial gas hydrate dissociation. Nature communications, 9(1), pp.1-11. https://doi.org/10.1038/s41467-018-03043-z

King, L. H., MacLean, B. (1970). Pockmarks on the Scotian shelf. Geological Society of America Bulletin, 81(10), 3141-3148. https://doi.org/10.1130/0016-7606(1970)81[3141:POTSS]2.0.CO;2

Kulm, L. D., Suess, E. (1990). Relationship between carbonate deposits and fluid venting: Oregon accretionary prism. Journal of Geophysical Research: Solid Earth, 95(B6), 8899-8915. https://doi.org/10.1029/JB095iB06p08899

Kvenvolden, K.A. (1988). Methane hydrate—a major reservoir of carbon in the shallow geosphere?. Chemical geology, 71(1-3), pp.41-51. https://doi.org/10.1016/0009-2541(88)90104-0

Kvenvolden, K.A. (1993). Gas hydrates—geological perspective and global change. Reviews of geophysics, 31(2), pp.173-187. https://doi.org/10.1029/93RG00268

Lindeberg, E., Vuillaume, J.F. and Ghaderi, A. (2009). Determination of the CO2 storage capacity of the Utsira formation. Energy Procedia, 1(1), pp.2777-2784. https://doi.org/10.1016/j.egypro.2009.02.049

Lønøy, A., Akselsen, J., Rønning, K. (1986). Diagenesis of a deeply buried sandstone reservoir: Hild Field, Northern North Sea. Clay Minerals, 21(4), 497-511. https://doi.org/10.1180/claymin.1986.021.4.06

Løseth, H., Gading, M., & Wensaas, L. (2009). Hydrocarbon leakage interpreted on seismic data. Marine and Petroleum Geology, 26(7), 1304-1319. https://doi.org/10.1016/j.marpetgeo.2008.09.008

Løseth, H., Wensaas, L., Arntsen, B., Hanken, N.M., Basire, C. and Graue, K. (2011). 1000 m long gas blow-out pipes. Marine and Petroleum Geology, 28(5), pp.1047-1060. https://doi.org/10.1016/j.marpetgeo.2010.10.001

Metz, B., Davidson, O., De Coninck, H.C., Loos, M. and Meyer, L. (2005). IPCC special report on carbon dioxide capture and storage. Cambridge: Cambridge University Press.

Michael, K., Golab, A., Shulakova, V., Ennis-King, J., Allinson, G., Sharma, S., Aiken, T. (2010). Geological storage of CO2 in saline aquifers—A review of the experience from existing storage operations. International journal of greenhouse gas control, 4(4), 659-667. https://doi.org/10.1016/j.ijggc.2009.12.011

Milkov, A.V. (2004). Global estimates of hydrate-bound gas in marine sediments: how much is really out there?. Earth-science reviews, 66(3-4), pp.183-197. https://doi.org/10.1016/j.earscirev.2003.11.002

Moss, J.L. and Cartwright, J. (2010). The spatial and temporal distribution of pipe formation, offshore Namibia. Marine and Petroleum Geology, 27(6), pp.1216-1234. https://doi.org/10.1016/j.marpetgeo.2009.12.013

PERBAS, Bialas, J., (2023, August). PERBAS – Dauerhafte Speicherung von CO2 in gigatonnen Volumina in Basaltkomplexen an kontinentalen Rändern. https://www.geomar.de/fb4-gdy/projekte/perbas

Piñero, E., Marquardt, M., Hensen, C., Haeckel, M. and Wallmann, K. (2013). Estimation of the global inventory of methane hydrates in marine sediments using transfer functions. Biogeosciences, 10(2), pp.959-975. https://doi.org/10.5194/bg-10-959-2013

Plaza-Faverola, A., Westbrook, G.K., Ker, S., Exley, R.J., Gailler, A., Minshull, T.A., Broto, K. (2010). Evidence from three-dimensional seismic tomography for a substantial accumulation of gas hydrate in a fluid-escape chimney in the Nyegga pockmark field, offshore Norway. Journal of Geophysical Research: Solid Earth, 115(B8). https://doi.org/10.1029/2009JB007078

Plaza-Faverola, A., Bünz, S. and Mienert, J. (2011). Repeated fluid expulsion through sub-seabed chimneys offshore Norway in response to glacial cycles. Earth and Planetary Science Letters, 305(3-4), pp.297-308. https://doi.org/10.1016/j.epsl.2011.03.001

Saffer, D.M. and Tobin, H.J. (2011). Hydrogeology and mechanics of subduction zone forearcs: Fluid flow and pore pressure. Annual Review of Earth and Planetary Sciences, 39, pp.157-186. https://doi.org/10.1146/annurev-earth-040610-133408

Saunois, M., Jackson, R. B., Bousquet, P., Poulter, B., Canadell, J. G. (2016). The growing role of methane in anthropogenic climate change. Environmental Research Letters, 11(12), 120207. https://doi.org/10.1088/1748-9326/11/12/120207

Schneider von Deimling, J., Brockhoff, J., Greinert, J. (2007). Flare imaging with multibeam systems: Data processing for bubble detection at seeps. Geochemistry, Geophysics, Geosystems, 8(6). https://doi.org/10.1029/2007GC001577

Schramm, B., Berndt, C., Dannowski, A., Böttner, C., Karstens, J., Elger, J. (2021). Seismic imaging of an active fluid conduit below Scanner Pockmark, Central North Sea. Marine and Petroleum Geology, 133, 105302. https://doi.org/10.1016/j.marpetgeo.2021.105302

Schramm, B., Singhroha, S., Plaza-Faverola, A., Dannowski, A., Berndt, C., Bünz, S., (submitted). Characterization of an active gas chimney using seismic velocity analysis, west-Svalbard Margin. *Geophysical Research Letters.*

Shipley, T. H., Houston, M. H., Buffler, R. T., Shaub, F. J., McMillen, K. J., Ladd, J. W., Worzel, J. L. (1979). Seismic evidence for widespread possible gas hydrate horizons on continental slopes and rises. *AAPG bulletin*, *63*(12), 2204-2213. https://doi.org/10.1306/2F91890A-16CE-11D7-8645000102C1865D

Singhroha, S., Schramm, B., Plaza-Faverola, A., Domel, P., Bünz, S., Dannowski, A. (2023, accepted). Stress constraints from shear-wave splitting in shallow sediments at an actively seeping pockmark on the W-Svalbard Margin. *Earth and Space Science.*

Snæbjörnsdóttir, S. Ó., Sigfússon, B., Marieni, C., Goldberg, D., Gislason, S. R., Oelkers, E. H. (2020). Carbon dioxide storage through mineral carbonation. Nature Reviews Earth & Environment, 1(2), 90-102. https://doi.org/10.1038/s43017-019-0011-8

Spies, R.B.and Davis, P.H. (1979). The infaunal benthos of a natural oil seep in the Santa Barbara channel. Marine Biology 50, 227–237. https://doi.org/10.1007/BF00394204

Svensen, H., Planke, S., Malthe-Sørenssen, A., Jamtveit, B., Myklebust, R., Rasmussen Eidem, T., Rey, S. S. (2004). Release of methane from a volcanic basin as a mechanism for initial Eocene global warming. Nature, 429(6991), 542-545. https://doi.org/10.1038/nature02566

Vangkilde-Pedersen, T., Anthonsen, K. L., Smith, N., Kirk, K., van der Meer, B., Le Gallo, Y., Bossie-Codreanu, D., Wojcicki, A., Le Nindre, Y., Hendriks, C., Dalhoff, F., Christensen, N. P. (2009). Assessing European capacity for geological storage of carbon dioxide–the EU GeoCapacity project. Energy Procedia, 1(1), 2663-2670. https://doi.org/10.1016/j.egypro.2009.02.034

Vielstädte, L., Haeckel, M., Karstens, J., Linke, P., Schmidt, M., Steinle, L., Wallmann, K. (2017). Shallow gas migration along hydrocarbon wells–An unconsidered, anthropogenic source of biogenic methane in the North Sea. Environmental science & technology, 51(17), 10262-10268. https://doi.org/10.1021/acs.est.7b02732

Whitaker, S. (1986). Flow in porous media I: A theoretical derivation of Darcy's law. Transport in porous media, 1(1), 3-25. https://doi.org/10.1007/BF01036523

White, J. E. (1975). Computed seismic speeds and attenuation in rocks with partial gas saturation. Geophysics, 40(2), 224-232. https://doi.org/10.1190/1.1440520

Whiticar, M. J. (2000). Can stable isotopes and global budgets be used to constrain atmospheric methane budgets?. In Atmospheric methane (pp. 63-85). Springer, Berlin, Heidelberg. https://doi.org/10.1007/978-3-662-04145-1_5

Zachos, J., Pagani, M., Sloan, L., Thomas, E., Billups, K. (2001). Trends, rhythms, and aberrations in global climate 65 Ma to present. science, 292(5517), 686-693. https://doi.org/10.1126/science.1059412

Zelt, C. A. (1999). Modelling strategies and model assessment for wide-angle seismic traveltime data. Geophysical Journal International, 139(1), 183-204. https://doi.org/10.1046/j.1365-246X.1999.00934.x

2. Tomographic inversion and seismic modelling

2.1. Seismic travel time forward modelling and inversion

One of the major goals of geology and geophysics is to gain knowledge on the internal structure of the Earth. Seismic tomography is a data inference technique that uses information provided in seismic records of ocean bottom seismometers to constrain 2D and 3D models of the Earth's interior. There are several forms of seismic tomography like full waveform, shear waves, anisotropy or attenuation, but the most common is one based on seismic compressional waves (P-waves) travel time.

Seismic travel time tomographies base on the concept of forward modelling and inversion. During forward modelling, real or synthetic experimental setups are combined with a model of the structure under scrutiny, and a set of synthetic data is sought that simulates the results of the experiment conducted with that model (Hobro, 1999). The task of generating these synthetic data from the given model and the experimental setup is called the forward problem (Hobro, 1999). The convers process is defined as inversion. During an inversion, a model is sought from a set of real or synthetic data, which is able to produce theses data through forward modelling (Figure 2.1; Hobro, 1999). The task of finding a model is called the inverse problem. Tomographic modelling of seismic travel times is a non-linear problem.

The 2D modelling of seismic refraction and wide-angle reflection travel time data began with one of the first travel time tomography algorithms for first arrivals by Firbas (1981) and White (1989) for regular grid parametrisation. With the rising of computational capability, more computationally intensive travel time inversion algorithms came up, e.g. Lutter and Nowack (1990) facilitate inversion of first arrivals and reflections for velocity and interface independently with regular grid parametrisation or Zelt and Smith (1992) developed inversion of many type pf the arrivals. More recently, 3D codes exit to perform joint refraction and reflection travel time tomography (e.g. Hobro et al., 2003; Rawlinson et al., 2008; Meléndez et al., 2015).

Inverse approaches have been developed (Zelt, 1999) to:

1. Quickly obtain a final model.
2. Model large datasets.
3. Derive simpler models for a given level to fit to the data.
4. To fit data according to a specific norm, without over-fitting.

5. Generate a final model in terms of resolution, errors and non-uniqueness.

One primary objective of the inversion of wide-angle seismic data is to obtain a velocity model that predicts the observed travel times. These velocity models not just provide physical properties of the subsurface, they also improve the processing of MCS data. An accurate method of measuring in situ-seismic velocities is logging during drilling operations. However, drilling operations are very expensive and only provide information for a single point, not for the complete subsurface. Drill holes can be used to calibrate seismic velocity models obtained by travel time tomography.

The following chapters describe the basic approach of 3D seismic travel time modelling. I present two modelling codes, which I used during my doctoral research project for the modelling of P-wave velocities: Jive3D and FAST. FAST is a 2D and 3D first arrival travel time tomography package, including forward modelling and inversion (Zelt and Barton, 1998). Jive3D is a forward-modelling and tomographic inversion package that produces 3D seismic velocity models, which theoretically could contain any combination of reflected and refracted seismic arrivals at near and far offsets (Hobro et al., 2003).

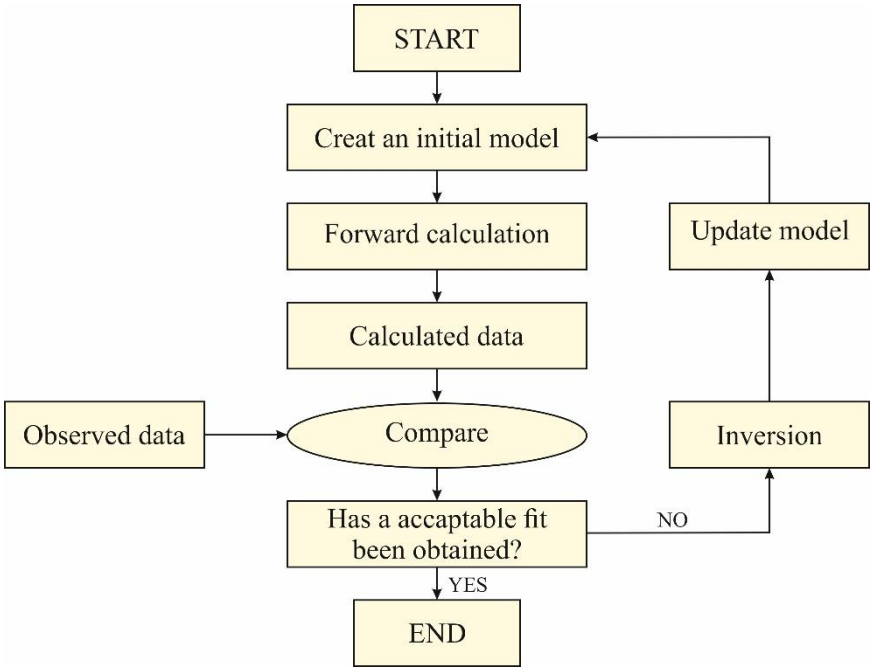

Figure 2.1.: Schema on forward and inversion modelling.

2.1.1. Model parameterisation

An important feature of any tomographic inversion method is the model parametrisation. The parameterisation has implications for the forward and inversion problem in the inversion

algorithm and by balancing the conventional layer-interface formalism and an arbitrary degree of complexity to emerge the model, which is constrained only by the given data and the chosen smoothing criteria.

In some schemes (e.g. Zelt and Smith, 1992), the layer-interface formalism is retained and the density of the model parametrisation is variable, so the user can order to match the structure observed in the data. Especially, the computational time can be reduced by using an irregular grid with a denser mesh in areas of high interest or strong variations in seismic velocities or geology.

Another common tomographic approach is to use a single regular velocity grid to model structures from seismic refraction or reflection data (e.g. Zelt and Barton, 1998). Overall, the grid size should be finer than the expected velocity variation, to avoid any bias.

2.1.2. Forward calculation

A ray tracing method suited to the forward step of the inverse approach is adopted to calculate the model data, i.e. travel times, using a set of values for the model parameters and calculating the source-receiver raypaths. In the forward problem, the wave equation solution from numerical methods produces synthetic data. Numerical methods provide approximate solutions to the equation of motion for any model of the Earth's interior (Sain and Nara, 2023). There are different classes for solving the wave equation including ray tracing methods, direct methods, and integral equation methods (Carcione et al., 2002).

The common method to compute travel times and their partial derivatives with respect to velocity during raytracing is the efficient finite-difference numerical solution of eikonal equations for raytracing (Vidale, 1990; Hole and Zelt, 1995; Sain and Nara, 2023).

2.1.3. Inversion

The inversion method automatically updates the model parameters for a better fit of the model data to the observed data, which is subjected to an adopted regularization procedure. The inverse step of adjusting model parameter is solved with the back projection method (Hole, 1992; Zelt and Barton, 1998; Sain and Nara, 2023). The travel times and the raypaths are recalculated iteratively by the updated model until a satisfactory fit between the observed and the modelled data is achieved, corresponding to a normalized chi-squared value of close to one (Zelt and Barton, 1998; Sain and Nara, 2023).

2.1.4. Resolution and error analysis / Assessment of uncertainty

In 1968, Backus and Gilbert first showed that a solution of an inverse problem must be evaluated with an error analyses and the inverted result becomes valuable only after its resolution and error are evaluated properly. However, even with acceptable χ^2 values (χ^2 is a common test for goodness of fit of an observed distribution to a theoretical and should be ~1), an infinite number of models will fit the data at this misfit level and therefore the resolution needs to be tested. To know how the true structure is reconstructed by the tomography, there are following operations (Zhao, 2015):

1. Create a synthetic input model containing assigned velocity anomalies.
2. Calculate a set of synthetic travel-time data resulting from ray tracing of an actual set of data for the synthetic model.
3. Add random noise to the synthetic data to simulate the picking errors of the observed data.
4. Invert the synthetic data using the same method as for the observed data.
5. Compare the inversion result with the synthetic input model and examine how well or poorly the assigned velocity anomalies are recovered.

The following two kinds of resolution tests are the most common used, being basically the same except for the input synthetic model:

1. Checkerboard test (Humphreys and Clayton, 1988; Zhao, 2015): positive and negative velocity perturbations are assigned alternatively to a 3D grid arrange in an uniform modelling space allowing easy identification of well- and poorly-resolved regions of the model.
2. Restoring test (Zhao, 2015): For a synthetic input model, which contains the main features of the obtained tomographic model, synthetic rays are generated and used as the input for the tomography. This test shows how well the main features of the obtained tomographic image are restored.

2.2. Jive3D and FAST

Seismic tomography is one of the most common methods to calculate seismic velocities (Scott et al., 2009). I used the **F**irst **A**rrival **S**eismic **T**omography (FAST) program (Zelt and Barton, 1998) to create a 3D seismic P-wave velocity model of the pipe structure beneath the Scanner Pockmark (Chapter 4) and the tomographic code Jive3D (**J**oint **I**nterface and **V**elocity **E**stimation in **Three D**imensions; Hobro, 1999) to build up a seismic P-wave velocity model

of the chimney structure beneath the Lunde Pockmark (Chapter 5). The following chapter describes the concept of seismic travel time tomography. I summarize and compare the functionality of FAST and JIVE and compare advantages and disadvantages of each modelling code.

The creation of seismic tomographies based on an inverse or forward modelling of the travel times using the ray theory approach. However, the modelling codes differ, e.g. in terms of model parametrisation, data used for modelling or regularisation (Janik et al., 2016). In order to assess the results of seismic tomographies, it is helpful to know the capabilities and limitations of the used codes compared to others. FAST and Jive3D are popular 3D tomography codes. The tomography package FAST bases on first arrivals. The Jive3D code can model first arrivals, but also refracted arrivals and reflections.

2.2.1. FAST

By using FAST and Jive3D, the models are parametrised on a uniform square grid. The FAST code used a grid with constant cell size in each direction, but the sizes may be different in the x, y, and z directions (Zelt, 1999).

I used FAST (Zelt and Barton, 1998) to invert first arrivals of refracted waves from the upper crustal sedimentary layers only, but in theory FAST can invert as well waves from the upper/middle crystalline crust and phases from the upper mantle (Janik et al., 2016). FAST is based on the Hole and Zelt (1995) improvement of Vidale's scheme for forward modelling and uses an eikonal solver in the forward step to create ray paths and travel times for an initial model:

$$(\delta t/\delta x)^2 + (\delta t/\delta y)^2 + (\delta t/\delta z)^2 = s^2(x,y,z)$$

where t is the travel time and s is the slowness (inverse of velocity) of the media. Travel times are calculated progressively away from the source on the sides of an expanding cube, completing one side at a time. From the travel time field, the ray paths are calculated.

In the following inverse step, a regularized inversion based on the least squares (LSQR) variant of the conjugate gradient technique is used to obtain velocity perturbations from the residuals of travel times (Janik et al., 2016). LSQR is a conjugate gradient method and based on the Lanczos bi-diagonalization process (Paige and Saunders, 1982).

The function to minimize is

$$\Phi(\delta s)=\delta t^T C_d^{-1}\delta t+\lambda[\alpha(\delta s^T W_h^T W_h \delta s+s_z \delta s^T W_v^T W_v \delta s)+(1-\alpha)\delta s^T W_p^T W_p \delta s]$$

where δt is the travel time residual vector, δs is the slowness perturbation vector or $s-s_o$, s_o is the starting model vector. C_d is the data covariance matrix that contains the estimated travel time pick errors. W_p is the perturbation-weighting matrix and W_h and W_v are the horizontal and vertical roughness matrices, respectively. Each row of W_h contains the five non-zero elements of the Laplacian operator corresponding to the centre cell and the four adjacent cells in the x and y direction. These are normalized by the prior slowness of the centre cell. Similarly, each row of W_v contains three non-zero elements corresponding to three adjacent cells in the z direction normalized by the prior slowness of the centre cell. The normalization by the prior slowness is applied to avoid a bias towards a greater level of model roughness in regions of high velocity (Zelt and Barton, 1998) The perturbation-weighting matrix W_p is an identity matrix normalized by the model slowness values that measures the perturbation of the current model from the starting model. Lambda (λ) is a trade-off parameter that controls the weight of fitting the data vs. the solution constraints. Alpha (α) is a trade-off parameter that determines the relative weight of fitting the smallest perturbation vs. the smoothest/flattest constraint equations. s_z controls the importance of maintaining vertical vs. horizontal smoothness/ flatness.

The user can constrain the flatness and smoothness of the slowness perturbations. To linearize the non-linear problem and solve the linear system in multiple iterations, velocity calculations are organized in iterative form to minimize the root mean square residual difference between the calculated and observed travel times. A drawback of FAST is in the smoothing of potentially real velocity anomalies in the resulting model, which is characteristic of all tomographic inversion methods and is similar to all seismic travel time tomographic codes. To ensure the stability of the entire calculation, each inversion involves a smoothing of the results. In addition, the velocity model of FAST is parametrized on a rectangular equidistant grid without the existence of velocity discontinuities representing geological boundaries or fault zones.

Another drawback of FAST is the influence of the initial model on the resulting model. This issue, that the final model is strongly dependent on the initial one, is common to most inversion codes. In case of the Scanner Pockmark, I tested 100 initial models in which I introduced up to ± 100 m/s seismic velocity anomalies on a regional North Sea background model and analysed the results in terms of small χ^2 values, producing similar anomalies to the majority of other starting models and comparability with MCS data (Chapter 3). In general, a formal criterion to stop the iterative inversion process is reaching $\chi^2 \sim 1$, which means the difference

between the observed and the calculated travel times are comparable to data uncertainty. Commonly, we look for models with an acceptable fit and the simplest possible velocity structure, with "minimum structures", and accept usually smoothing of the velocity field (Scales et al., 1990). Generally, it requires the solution of an inverse problem to obtain a heterogeneous seismic model that is consistent with the observations (Rawlinson et al., 2010).

2.2.2. Jive3D

I used the tomographic code Jive3D to build up a seismic p-wave velocity model of the chimney structure beneath the Lunde Pockmark (Chapter 5). The Jive3D tomographic software package (Hobro, 1999; Hobro et al., 2003) is based not on first arrivals only, but can additionally use later refracted phases and reflected arrivals to build a layered seismic velocity model. The code is based on the regularized least squares inversion approach. The model is built as a stack of layers separated by interfaces which represent velocity discontinuities based on geological layers. Jive3D used a grid with constant cell size in each direction, but the sizes may be different in the different layers (Hobro et al., 2003). In the forward step, Jive3D uses the ray theory and ray perturbation method for the calculation of source-receiver synthetic travel times and their partial derivatives with respect to each model parameter (Hobro et al., 2003). In the inverse step, the code used the iterative regularized least-squares method that contains data misfit and model roughness terms (Scott et al., 2009).

This function is

$$F(\delta m) = \| r - A\,\delta m \|_D^2 + \beta \| m + \delta m \|_M^2$$

where m is the model, δm is the model perturbation, r represents the travel time residuals and A is a matrix containing the Frechet derivatives associated with the synthetic travel times. $\|.\|_D$ weights each residual according to its corresponding travel time uncertainty while $\|.\|_M$ describes the roughness of each layer and interface. β is a scalar known as regularization strength, and it controls the amount of model roughness that is permitted to develop during the minimizing of the objective function.

Each layer and interface can be modelled individually or jointly. Usually, I model the upper part first and then successively resolve the deeper layers and interfaces. The previously, shallower modelled layers and interfaces can be fixed during the following inversion of the deeper part of the model, in order to focus the algorithm on the deeper layer and interface only. Therefore, the number of model parameters can be reduced and it stabilizes the inversion procedure. This is particularly important due to the high computing power required by Jive3D,

which is an overall drawback of the code. Another drawback is the high smoothing level of the velocity field by Jive3D, which creates very smooth, homogeneous seismic velocity models. It produces a very smooth model first, before it allows structures to emerge in the model. As a consequence, models created with the Jive3D code contain the minimum degree of structure that is required to fit the data and have sometimes obtained an unreasonable high degree of smoothing. However, the final model produced by Jive3D does less depend on the initial model than other codes, e.g. FAST. To test this, I used a range of initial velocity models of the chimney beneath Lunde Pockmark and Jive3D consistently produces a similar end model. In theory, Jive3D can handle any combination of reflected and refracted seismic arrivals at near and far offsets, but most studies are based either on reflections or refractions as Jive3D produces unrealistic models when jointly inverting for reflections and refractions.

2.2.3. Comparison of Jive3D and FAST

Both software packages allow to model fluid flow conduits below pockmarks. FAST produces a more detailed seismic velocity model with less smoothing effects, especially on the background model. In case of Scanner Pockmark, both software packages were tested with the same input of first arrivals. FAST was able to image more distant seismic velocity structures, such as the velocity anomaly beneath the Scotia Pockmark (Chapter 4), while Jive3D produced less velocity anomalies and a smoother velocity model (Figure 2.2). In case of Lunde Pockmark, a similar seismic structure, the Lomvi Pockmark, was within the model (Chapter 5). However, this seismic structure could not be imaged by Jive3D since Jive3D smooths the background velocity field much more and smears anomalies, especially with scarcely spaced OBS instruments directly above the anomaly. This strong smoothing of the data is a drawback of Jive3D especially for vertical structures. The algorithm of Jive3D is designed to produce a minimum-structure model that is able explain the given travel time data using the simplest model possible (Hobro, 1999). The data quality of the Lunde Pockmark study is much higher than the Scanner Pockmark study due to good weather conditions, higher shot coverage and accurate positioning of the shot points. Nevertheless, FAST provides the more detailed results. Jive3D has a huge increase of the calculation time. The time consumption necessary for the whole seismic modelling is an important matter. The FAST package is the faster way to model a 3D velocity field compared to Jive3D, although seismic boundaries cannot be represented by first order velocity discontinuities and only first arrival refracted phases can be used. This is one of the reasons why FAST could not be used in the Lunde study. Due to the experiment setup and the geological setting, no refractions but only reflections could be recorded.

The decision which code to use for modelling must depend on the data quality and the study aims. The Jive3D code gives a better fit for layered models based on reflections or refractions, which resulting model is less depend on the initial model. The imaging of vertical structures – the main objective of this thesis - with lower calculation time and computing power is more accurate with the tomographic inversion method FAST.

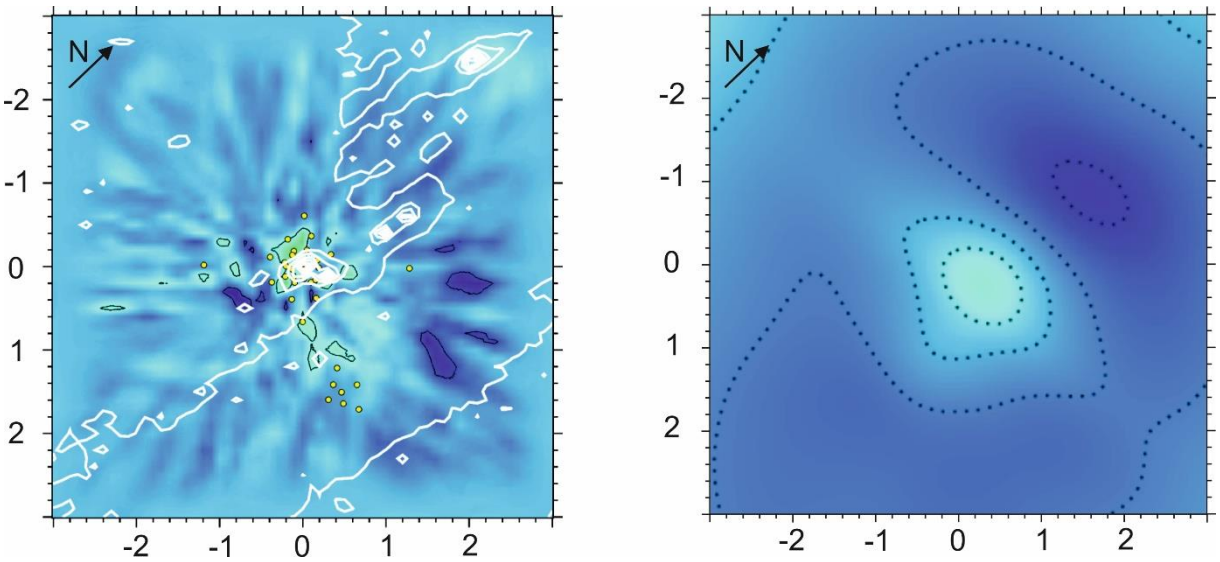

Figure 2.2: P-wave velocity model (same area, same cell size, same initial model, and same depth) beneath the Scanner Pockmark generated with a) FAST (white isolines image the seafloor topography) and b) Jive3D (black dashed lines image velocity gradients).

References

Backus, G., & Gilbert, F. (1968). The resolving power of gross earth data. Geophysical Journal International, 16(2), 169-205. https://doi.org/10.1111/j.1365-246X.1968.tb00216.x

Carcione, J. M., Herman, G. C., & Ten Kroode, A. P. E. (2002). Seismic modeling. Geophysics, 67(4), 1304-1325. https://doi.org/10.1190/1.1500393

Firbas, P. (1981). Inversion of travel-time data for laterally heterogeneous velocity structure—linearization approach. Geophysical Journal International, 67(1), 189-198. https://doi.org/10.1111/j.1365-246X.1981.tb02742.x

Hobro, L. W. D. (1999). Three-dimensional tomographic inversion of combined reflection and refraction seismic travel-time data. Ph.D. Thesis, Department of Earth Sciences, University of Cambridge, Cambridge.

Hobro, J.W., Singh, S.C., Minshull, T.A. (2003). Three-dimensional tomographic inversion of combined reflection and refraction seismic traveltime data. Geophysical Journal International, 152(1), pp.79-93. https://doi.org/10.1046/j.1365-246X.2003.01822.x

Hole, J. A. (1992). Nonlinear high-resolution three-dimensional seismic travel time tomography. Journal of Geophysical Research: Solid Earth, 97(B5), 6553-6562.https://doi.org/10.1029/92JB00235

Hole, J.A. and Zelt, B.C. (1995). 3-D finite-difference reflection traveltimes. Geophysical Journal International, 121(2), pp.427-434. https://doi.org/10.1111/j.1365-246X.1995.tb05723.x

Humphreys, E. and Clayton, R. W. (1988). Adaptation of back projection tomography to seismic travel time problems. Journal of Geophysical Research: Solid Earth, 93(B2), 1073-1085. https://doi.org/10.1029/JB093iB02p01073

Janik, T., Środa, P., Czuba, W. and Lysynchuk, D. (2016). Various Approaches to Forward and Inverse Wide-Angle Seismic Modelling Tested on Data from DOBRE-4 Experiment. Acta Geophysica, 64(6), pp.1989-2019. https://doi.org/10.1515/acgeo-2016-0084

Lutter, W. J. and Nowack, R., (1990). Inversion for crustal structure using reflections from the PASSCAL Ouachita experiment. Journal of Geophysical Research: Solid Earth, 95(B4), 4633-4646. https://doi.org/10.1029/JB095iB04p04633

Meléndez, A., Korenaga, J., Sallarès, V., Miniussi, A. and Ranero, C.R. (2015). TOMO3D: 3-D joint refraction and reflection traveltime tomography parallel code for active-source seismic data—synthetic test. Geophysical Journal International, 203(1), pp.158-174. https://doi.org/10.1093/gji/ggv292

Paige, C. C., & Saunders, M. A. (1982). LSQR: An algorithm for sparse linear equations and sparse least squares. ACM Transactions on Mathematical Software (TOMS), 8(1), 43-71.

Rawlinson, N. and Kennett, B. L. N. (2008). Teleseismic tomography of the upper mantle beneath the southern Lachlan Orogen, Australia. Physics of the Earth and Planetary Interiors, 167(1-2), 84-97. https://doi.org/10.1016/j.pepi.2008.02.007

Rawlinson, N., Pozgay, S., Fishwick, S. (2010). Seismic tomography: a window into deep Earth. Physics of the Earth and Planetary Interiors, 178(3-4), pp.101-135. https://doi.org/10.1016/j.pepi.2009.10.002

Sain, K. and Nara, D. (2023). Active Seismic Tomography: Theory and Applications. John Wiley & Sons.

Scales, J. A., Docherty, P., Gersztenkorn, A. (1990). Regularisation of nonlinear inverse problems: imaging the near-surface weathering layer. Inverse problems, 6(1), 115. https://doi.org/10.1088/0266-5611/6/1/011

Scott, C. L., Shillington, D. J., Minshull, T. A., Edwards, R. A., Brown, P. J., White, N. J. (2009). Wide-angle seismic data reveal extensive overpressures in the Eastern Black Sea Basin. Geophysical Journal International, 178(2), 1145-1163. https://doi.org/10.1111/j.1365-246X.2009.04215.x

Vidale, J. E. (1990). Finite-difference calculation of traveltimes in three dimensions. Geophysics, 55(5), 521-526. https://doi.org/10.1190/1.1442863

White, D. J. (1989). Two-dimensional seismic refraction tomography. Geophysical Journal International, 97(2), 223-245. https://doi.org/10.1111/j.1365-246X.1989.tb00498.x

Zelt, C. A. (1999). Modelling strategies and model assessment for wide-angle seismic traveltime data. Geophysical Journal International, 139(1), 183-204. https://doi.org/10.1046/j.1365-246X.1999.00934.x

Zelt, C. A., Barton, P. J. (1998). Three-dimensional seismic refraction tomography: A comparison of two methods applied to data from the Faeroe Basin. Journal of Geophysical Research: Solid Earth, 103(B4), 7187-7210. https://doi.org/10.1029/97JB03536

Zelt, C. A., Smith, R. B. (1992). Seismic traveltime inversion for 2-D crustal velocity structure. Geophysical journal international, 108(1), 16-34. https://doi.org/10.1111/j.1365-246X.1992.tb00836.x

Zhao, D. (2015). Multiscale Seismic Tomography. Springer Geophysics. https://doi.org/10.1007/978-4-431-55360-1s

3. Pockmarks in the Witch Ground Basin, Central North Sea

Christoph Böttner[1] , Christian Berndt[1] , Benedict T.I. Reinardy[2], Jacob Geersen[1] , Jens Karstens[1] , Jonathan M. Bull[3] , Ben J. Callow[3] , Anna Lichtschlag[4] , Mark Schmidt[1] , Judith Elger[1] , Bettina Schramm[1] ,Matthias Haeckel[1]

[1]*GEOMAR Helmholtz Centre for Ocean Research Kiel, Kiel, Germany*

[2]*Stockholm University and Bolin Centre for Climate Research, Stockholm, Sweden*

[3]*Ocean and Earth Science, University of Southampton, National Oceanography Centre, Southampton, UK*

[4]*National Oceanography Centre, University of Southampton Waterfront Campus, Southampton, UK*

Abstract

Marine sediments host large amounts of methane (CH4), which is a potent greenhouse gas. Quantitative estimates for methane release from marine sediments are scarce, and a poorly constrained temporal variability leads to large uncertainties in methane emission scenarios. Here, we use 2-D and 3-D seismic reflection, multibeam bathymetric, geochemical, and sedimentological data to (I) map and describe pockmarks in the Witch Ground Basin (central North Sea), (II) characterize associated sedimentological and fluid migration structures, and (III) analyze the related methane release. More than 1,500 pockmarks of two distinct morphological classes spread over an area of 225 km^2. The two classes form independently from another and are corresponding to at least two different sources of fluids. Class 1 pockmarks are large in size (>6 m deep, >250 m long, and >75 m wide), show active venting, and are located above vertical fluid conduits that hydraulically connect the seafloor with deep methane sources. Class 2 pockmarks, which comprise 99.5% of all pockmarks, are smaller (0.9–3.1 m deep, 26–140 m long, and 14–57 m wide) and are limited to the soft, fine-grained sediments of the Witch Ground Formation and possibly sourced by compaction-related dewatering. Buried pockmarks within the Witch Ground Formation document distinct phases of pockmark formation, likely triggered by external forces related to environmental changes after deglaciation. Thus, greenhouse gas emissions from pockmark fields cannot be based on pockmark numbers and present-day fluxes but require an analysis of the pockmark forming processes through geological time.

Key Points:

• Marine geophysical data document >1,500 pockmarks of two morphological classes in the Witch Ground Basin, central North Sea

• Class 1 pockmarks are continuously active and supplied through seismic pipe structures by deeply sourced methane

• Class 2 pockmarks form at specific stratigraphic horizons suggesting intermittent venting triggered by pressure and temperature changes

Plain Language Summary

Marine sediments host large amounts of methane (CH4), which is a potent greenhouse gas. The amount of methane released into the atmosphere is, however, largely unknown making it difficult to implement this methane source in climate models. Here we use geophysical, geochemical, and sedimentological data to map the distribution of fluid escape structures in the central North Sea. More than 1,500 pockmarks, which are circular to semicircular depressions of the seafloor, indicate fluid flow from the subsurface. There are two distinct morphological classes of pockmarks corresponding to at least two different fluid sources. Class 1 pockmarks are large, show active venting, and are located above vertical fluid conduits in the subsurface, which feed fluids from deeper strata. Class 2 pockmarks, which comprise 99.5% of all pockmarks, are smaller and limited to the soft sediments directly below the seafloor. Older pockmarks in the subsurface document distinct phases of pockmark formation, likely triggered by external forces after the retreat of ice in the North Sea. The amount of methane released from natural geological sources based on pockmark numbers may be wrong as these do not take into account the origin and composition of released fluids.

3.1. Introduction

Earth's climate is highly sensitive to the release of potent greenhouse gases such as methane (CH_4) into to atmosphere. Methane has been released during climatic changes including the steepest known natural temperature increase on Earth at the Paleocene - Eocene Thermal Maximum around 55.5 Ma ago (Dickens, 2011; Svensen et al., 2004) but also during and after the Younger Dryas - Preboreal abrupt warming event at the beginning of the Holocene (about 11,600 cal. years BP; Petrenko et al., 2017). However, current and future methane emissions remain poorly constrained and bottom up as well as top down approaches for the quantification of methane emissions have large uncertainties (Dean et al., 2018; Petrenko et al., 2017). The global methane emission from natural geological sources shows a wide range in estimates (33-

75 Tg CH_4 per year; Ciais et al., 2013; Etiope et al., 2008), which highlights the large uncertainties involved in attributing and quantifying methane emissions.

Marine sediments host large amounts of methane in the form of free gas, hydrates, or dissolved in porewater. There is evidence for direct contribution of methane from shallow marine sediments to the atmospheric methane budget and hence to climate change (Etiope et al., 2008; Judd et al., 2002). Methane formed in marine sediments may either be biogenic (derived from microbial degradation of organic matter) or thermogenic (generated in deep hydrocarbon reservoirs by thermal cracking of kerogens; Whiticar, 2000). The carbon and hydrogen isotope signatures and the relative proportions of methane and more mature hydrocarbons (e.g.,ethane, propane, butane) can help distinguish between the two sources (Whiticar, 2000). Methane from both onshore and offshore microseep and macroseep contributes to the atmospheric methane budget and can be supplied by geothermal, volcanic, or sedimentary sources (Dean et al., 2018; Etiope et al., 2008; Saunois et al.,2016). In the marine environment, methane may accumulate in the subsurface, when gas pressure exceeds the ambient hydrostatic pressure and the methane forms gas bubbles, which may be released by diffusion or episodic ebullition (Boudreau et al., 2005; Krämer et al., 2017; Maeck et al., 2013). However, the global significance of marine methane sources and their impact on the global methane budget remains poorly constrained (Ciais et al., 2013; Etiope et al., 2008; Petrenko et al., 2017).

One manifestation of focused fluid migration at the seafloor are circular to semicircular depressions known as pockmarks, which may form in response to venting of fluids from the seafloor Hovland & Judd, 1988; King & McLean, 1970). Pockmarks may be meters to hundreds of meters in diameter, meters to tens of meters in depth and affect the local environment, morphodynamics, biochemistry, and ecology (Berndt, 2005; Dando et al., 1991; Judd & Hovland, 2007; Niemann et al., 2005; Wegener et al., 2008). Increasing high - resolution bathymetric data coverage reveals the wide abundance of pockmarks at the seafloor in various structural and geologic settings (e.g., Brothers et al., 2012; Gafeira et al., 2018; Hovland et al., 2002). Understanding the processes that control the formation and activity of pockmarks is crucial to estimate the contribution of methane from natural geological sources to the atmospheric methane budget and its impact on climate change.

Pockmarks often form on top of focused fluid conduits, which manifest in seismic data as seismic chimneys or pipes and are characterized by circular - shaped amplitude anomalies with dimmed reflections and bright spots at different depth levels (Andresen, 2012; Cartwright et al., 2007; Karstens & Berndt, 2015; Løseth et al., 2009). The terms seismic chimneys or pipes and

pockmarks are attributed to the localized release of overpressure in the subsurface through hydraulic connection of deeper strata with the seafloor (Cole et al., 2000; Hustoft et al., 2009). Pockmarks that formed above pipe and chimney structures are observed globally, for example, at the Vestnesa Ridge NW off Svalbard (Hustoft et al., 2009; Plaza - Faverola et al., 2017), in the Nyegga pockmark field on the continental Norwegian margin (Karstens et al., 2018), offshore Nigeria (Løseth et al., 2011), in the Western Nile Deep Sea Fan (Moss et al., 2012), and in the Lower Congo Basin (Gay et al., 2007).

The aim of this study is to analyse pockmark - forming processes in the Witch Ground Basin, central North Sea (Figure 3.1). We first map the abundant pockmarks and characterize them based on their morphology and subsurface preconditions. Second, we determine the source of fluids that contribute to pockmark formation in the Witch Ground Basin and investigate the interrelation of fluid flow and depositional processes during their formation. This includes determining if there are different sources of fluids, if they are located at different depths, and if they provide different types of fluids. Subsequently we constrain the timing and the recurrence rate of pockmark formation in the Witch Ground Basin.

3.2. Regional Setting

3.2.1. Pockmarks in the Central North Sea

The North Sea is affected by focused flow of hydrocarbons from deep thermogenic sources, strongly mixed with microbially formed shallow methane (Chand et al., 2017; Karstens & Berndt, 2015). Three decades of extensive surveying and seafloor mapping in the Witch Ground Basin has revealed abundant “normal” pockmarks and multiple “unusually large” pockmarks. These pockmarks indicate significant flow of fluids from shallow marine sediments (Gafeira et al., 2018; Hovland & Sommerville, 1985; Judd et al., 1994; Pfannkuche, 2005). The term normal pockmark describes pockmarks that are more than 5 m in diameter and found in isolation where free gas pockets in the subsurface degas cyclically (Hovland et al., 2010).

The so - called unusually large pockmarks are complexes of pockmarks that are >100 m in diameter and >10 m deep. They are located in UK block 15/25 and include the Scanner, Scotia, Challenger, and Alkor pockmark complexes, of which Scanner and Scotia comprise two large adjacent pockmarks (Gafeira & Long, 2015; Judd et al., 1994). Ongoing seepage is interpreted from repeated water column imaging (multiple cruises from 1983‑2005; Dando et al., 1991; Judd et al., 1994; Judd & Hovland, 2007; Gafeira & Long, 2015) and visual evidence of

emerging bubbles (Remotely operated vehicles, 1985, 2004; submarine Jago, 1990; Gafeira & Long, 2015). Methane derived - authigenic carbonates (MDACs; Dando et al., 1991; Hovland & Irwin, 1989), bacterial mats (Dando et al., 1991; Pfannkuche, 2005), and seep - associated fauna (Austen et al., 1993; Dando et al., 1991) indicate long - lasting seepage from these unusually large pockmarks.

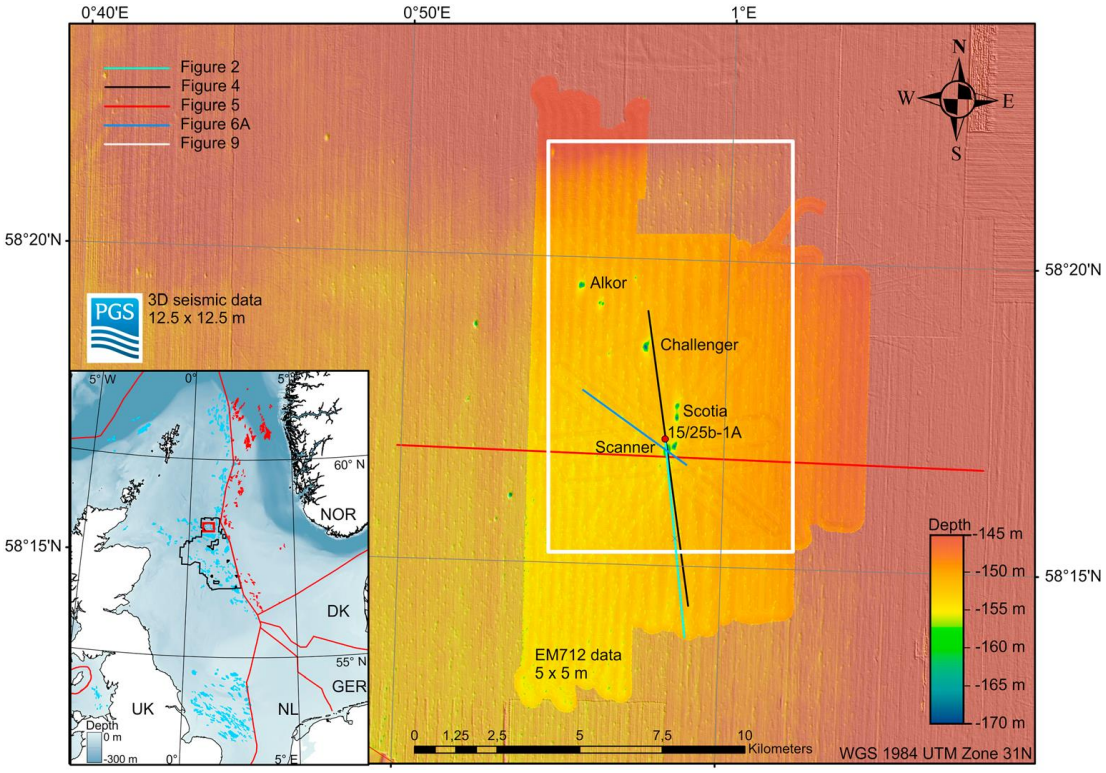

Figure 3.1: Bathymetric grid of the Witch Ground Basin, central North Sea. The shown bathymetry is a compilation of 3-D reflection seismic data (converted with 1,500 m/s constant velocity, 12.5 × 12.5 m lateral resolution) and EM712 (5 × 5mlateral resolution). Locations for additional figures are indicated, turquoise line = Figure 3.2, black line = Figure 3.4c, red line = Figure 3.5b, blue line = Figure 3.6a, white line = Figures 3.9a–9c. The inset shows the location of the study area (red box) within the North Sea (EMODnet bathymetric map projected in UTM zone 31, WGS84). The black line outlines the PGS "CNS MegaSurveyPlus." Colored polygons show Norwegian (red, Norwegian petroleum directorate open data) and UK (blue, oil and gas authority open data) hydrocarbon fields.

The normal pockmarks formed in the soft, fine - grained sediments of the Witch Ground Formation and have been identified across the Witch Ground Basin (Gafeira et al., 2018; Judd et al., 1994; Long, 1992; Sejrup et al., 1994; Stoker & Long, 1984). Their morphometry deviates strongly from the large pockmarks, as they are mostly less than 3 m deep and 20‑40 m wide.

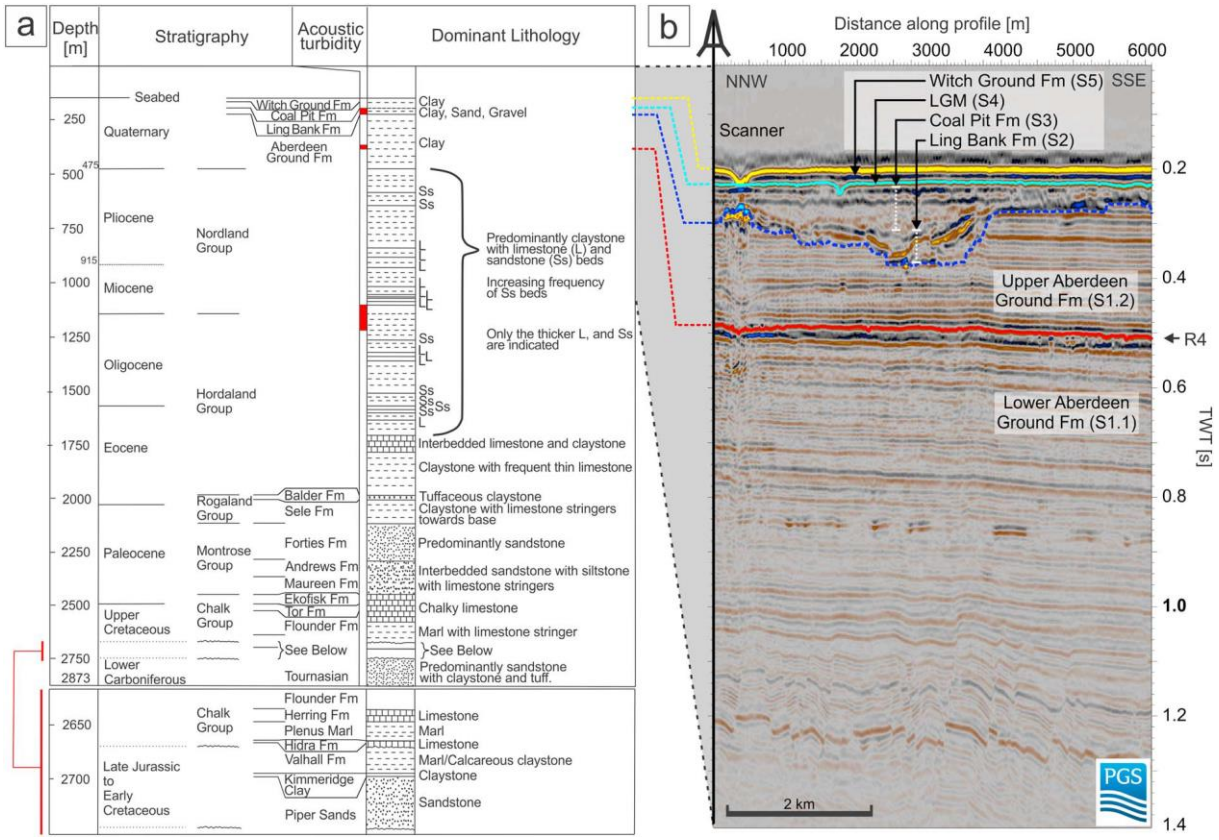

Figure 3.2: (a) Stratigraphic and lithological summary of well 15/25b-1A, located 400 m northwest of the western Scanner pockmark (modified after Judd et al., 1994). (b) 6-km-long representative seismic profile from conventional 3-D seismic data from north-northwest to south-southeast. The seismic profile shows major stratigraphic units lower Aberdeen Ground Formation (S1.1), R4 reflector, upper Aberdeen Ground Formation (S1.2), Ling Bank Formation (S2), Coal Pit Formation (S3), last glacial maximum deposits (LGM, S4) and the Witch Ground Formation (S5). The image shows distance along profile on the x axis and two-way traveltime (TWT) on the y axis. 1.4 s TWT correspond to a minimum depth of 1,050 m (at 1,500 m/s seismic velocity). The location of the profile is given in Figure 3.1.

The density ranges from less than 5 pockmarks per square kilometer at the outer parts of the Witch Ground Basin, to almost 30 pockmarks per square kilometer at the center, where water depth exceeds 150 m (Gafeira et al., 2018). There is seismic evidence that these normal pockmarks occur in tiers at distinct stratigraphic layers and not only at the surface (Figure 3.4a; Stoker & Long, 1984). Previous studies indicate that the density of pockmarks per tier increases with decreasing burial depth (Long, 1992). The lack of evidence for seepage from repeated water column imaging suggests intermittent activity of these normal pockmarks assuming they are formed by seepage (Gafeira & Long, 2015; Judd et al., 1994).

3.2.2. Stratigraphy of the Witch Ground Basin

The Witch Ground Basin is located above the Witch Ground Graben, which is a major structural feature that developed between Triassic and Early Cretaceous times (Andrews et al., 1990). During the Late Jurassic and Early Cretaceous, the basin was a major sediment depo - center (Andrews et al., 1990). Clays with interbeds of sandstone and limestone dominate the Paleogene and Neogene sequences (Figure 3.2). The Witch Ground Basin was again a deposition center during the Quaternary (~600 m of sediment). The shallow sediments and especially the Early Pleistocene sediments of the Aberdeen Ground Formation show evidence for subglacial, glaciomarine, and marine conditions (Buckley, 2012, 2016; Rea et al., 2018; Reinardy et al., 2017; Rose et al., 2016; Sejrup et al., 1987; Stoker & Bent, 1987). On seismic reflection sections, the Aberdeen Ground Formation is characterized by laterally continuous, high amplitude reflections (Ottesen et al., 2014). The top of the Aberdeen Ground Formation is defined by a regional glacial unconformity and dissection by a large number of tunnel valleys. The age of this unconformity is poorly constrained but it is thought to correspond to the advance of grounded ice into the North Sea Basin during the Mid Pleistocene Transition (~1.2-0.5 Ma; further referred to as R4; Reinardy et al., 2017). The tunnel valleys that dissect the unconformity are part of the overlying Ling Bank Formation. This unit comprises a multitude of glacial tunnel valleys with different phases of erosion and deposition with poorly constrained ages. Comparison with tunnel valleys of onshore mainland Europe where the valley infill and associated facies have been dated to the Holsteinian interglacial corresponding toMarine Isotope Stage (MIS) 11 gives a minimum age for formation of the stratigraphically lowest set of tunnel valleys in the North Sea during the Elsterian glaciation (MIS 12; Stewart & Lonergan, 2011). The upper Mid to Late Pleistocene sedimentary succession consists of the Coal Pit, Swatchway, and Witch Ground Formations (Figure 3.2). The Coal Pit Formation comprises glacial till with hard, dark gray to brownish - gray, muddy, pebbly sands or sandy muds deposited between MIS 3 and 6 (Andrews et al., 1990; Graham et al., 2010; Stoker et al., 2011). The Swatchway Formation comprises silty sandy clays with rare pebbles; possibly proximal glaciomarine sediments deposited during MIS2-3. The uppermost finely laminated, glaciomarine sediments of the Witch Ground Formation were deposited during MIS 1-2 (Stoker et al., 2011). The upper part of the Witch Ground Formation comprises Holocene age sediments, which were reworked during the past 8 ka, when sedimentation decreased or ceased to virtually no sediment input into the Witch Ground Basin (Erlenkeuser, 1979; Johnson & Elkins, 1979).

3.3. Methods

3.3.1. Seismic Reflection Data

We used an extensive 3 - D industry seismic data set ("CNS MegaSurveyPlus" provided by PGS) that covers >22,000 km^2 of the central to northern North Sea down to 1.5 s two - way traveltime (TWT, Figure 3.1). The 3 - D pre - stack time - migrated seismic amplitude data (full fold stack) extends approximately 200 km from north to south and 140 km from east to west. The vertical resolution is approximately 20 m with an inline and crossline spacing of 12.5 m. Data sets like this have proven to be useful to identify fluid flow systems, including their geometry, permeability barriers, and fluid accumulations, as they manifest in seismic data as amplitude anomalies (Karstens & Berndt, 2015).

We have used seismic attributes to enhance seismic interpretation including the Kingdom Suite Symmetry attribute, which is a post - stack, post migration structural feature detection tool (e.g., fracture detection) based on a 3 - D log - Gabor filter array (Yu et al., 2015). This attribute is highly sensitive to seismic amplitude variations and therefore correlates with curvatures and discontinuities associated with geological structures, for example, faults, fractures, and discontinuous events (Böttner et al., 2018). In addition, we use the rootmean - square (RMS) amplitude calculated over a time window of ±50 ms around the picked horizon (see horizon in Figure 3.2b, dashed blue line). RMS amplitude is a post - stack attribute that highlights areas with direct hydrocarbon indicators such as bright spots by calculating the root of squared amplitudes divided by the number of samples per specified time window.

In addition, we acquired high - resolution 2 - D seismic reflection data during research cruise MSM63 in April/May 2017 onboard RV Maria S. Merian (Figure 3.1, red/black lines). The aim of the seismic survey was to increase seismic resolution, map the fluid flow systems, and image the presumed subsurface fracture networks. The seismic profiles were acquired with a two - 105/105 - in^3 - GI - Gun - array shot at 210 bar every 5 s and a 150m - long streamer with 96 channels and 1.5625mchannel spacing. The resulting shot point distance is approximately 8.75‑12.5 m at 3.5‑5 kn ship speed. The frequency range of the two - GI - Gun - array is 15‑500 Hz. The processing included geometry and delay corrections, static corrections, binning to 1.5625 m and band - pass filtering with corner frequencies of 25, 45, 420, and 500 Hz. Furthermore, a normal - moveout - correction (with a constant velocity of 1488 m/s calculated from CTD measurements) was applied and the data were stacked and then migrated using a 2 -

D Stolt algorithm (1,500 m/s constant velocity model). The vertical resolution of the processed data is approximately 6–7 m near the seafloor.

3.3.2. Seismostratigraphic Framework

Fluid flow in this area strongly depends on the local and regional stratigraphy and subsequent sediment properties. We have compiled a stratigraphic framework with seismic reflection data, industry well 15/25b - 1A (Figure 3.2a), British Geological Survey boreholes BH77/2, BH86/26, BH04/01 (Figure 3.1), and information from literature (Graham et al., 2010; Holmes, 1977; Judd et al., 1994; Long et al., 1986; Sejrup et al., 2014; Reinardy et al., 2017). We are able to tie most seismostratigraphic units within our stratigraphic framework to previously published lithostratigraphic units (Figure 3.2). Formation names and their ages utilize the North Sea Quaternary lithostratigraphic framework (Stoker et al., 2011). The seismostratigraphic unit S1.1 corresponds to the lower Aberdeen Ground Formation (MIS 100–21); S1.2 to the upper Aberdeen Ground Formation (MIS 21–13); S2 inside the tunnel valleys to the Ling Bank Formation (MIS 12–10), which is unconformably overlain by regional glacigenic sediments deposited during Mid Pleistocene (MIS 6; Reinardy et al., 2017); S3 to the Coal Pit Formation (MIS 6–3); S4 to the upper Swatchway or lower Witch Ground Formation (MIS 3–2); and S5 to the Witch Ground Formation (MIS 2–1). However, previous interpretations and stratigraphic units likely include sediments of different provenance due to lower resolution data. Possible reworking and disturbance by fluvial, glacial, and marine processes further complicate the interpretation of lithostratigraphic units in this part of the Witch Ground Basin (Sejrup et al., 2014).

3.3.3. Hydroacoustic Data

The shallow seismic stratigraphy was imaged by subbottom profiler (SBP) data acquired during cruise MSM63 (Figure 3.1, blue/black line) using Parasound P70 with 4 kHz as the secondary low frequency to obtain seismic images of the upper 100 m below the seafloor with very high vertical resolution (<15 cm). We applied a frequency filter (low cut 2 kHz, high cut 6 kHz, 2 iterations) and calculated the envelope within the seismic interpretation software IHS Kingdom. In addition, further SBP data were acquired during cruise JC152 (onboard RV James Cook in August 2017) using a Chirp. The Chirp SBP produces a sweep, which lasts 0.035 s; the normalized zero - phase Klauder wavelet from the autocorrelation of the sweep shows a temporal length of 0.00075 s, allowing further processing. The bandwidth ranges from 2.8 to 6

kHz, with a central frequency of 4.4 kHz. The combination of both systems and the subsequent integrated data set enables a detailed analysis of the shallow sedimentary succession up to 50 m below the seafloor. Both systems are further referred to as echosounder. Bathymetric data were acquired with the EM712 system mounted to the hull of RV Maria S. Merian (Figure 3.1). The survey was designed to provide high - resolution bathymetry with 5 × 5 m resolution. We processed the data using MB Systems software (Caress & Chayes, 2017) and included statistical evaluation of soundings that increased the signal - to - noise ratio. The sound velocity profile for multibeam processing was measured at the beginning and at the end of the cruise.

3.3.4. Semiautomated Picking of Pockmarks

To delineate pockmarks within the MSM63 bathymetric data we used a workflow that combines multiple ArcGIS geoprocessing tools (also compare Gafeira et al., 2012, Gafeira et al., 2018). In a first step, all depressions shallower than 18 m were filled with the "fill" tool. Subsequently the original grid was subtracted from the filled grid and all areas that have changed vertically by 0.5m or more were classified. The "raster to polygon" tool was then used to draw polygons around the classified areas. Afterward, the areas were calculated for all polygons and those comprising <500 m_2 were deleted. This removed a vast quantity of polygons from the outer regions of single swath transects where the noise level within the multibeam data increased. After this step, the polygon data set was manually inspected and all polygons that did not encircle pockmarks were manually removed. This manual editing step was necessary due to the presence of some large (>500 m^2) noisy regions within the multibeam data. Subsequently all empty areas within individual polygons were removed with the "Eliminate Polygon Part" tool. This removed the bathymetric noise within single pockmarks. The outlines of the polygons were then smoothed with the "smooth polygon" tool using a polynomial approximation with exponential kernel algorithm and a 100 m smoothing tolerance. Finally, the depth, the orientation and length of the longest and shortest axis, the perimeter, and the distance to the closest neighbour pockmarks were calculated for each pockmark defined by a polygon.

3.3.5. Sediment Sampling

Shallow sediment samples were taken at the southwestern edge of the western Scanner pockmark during R/V Poseidon cruise POS518 (Leg2) using a 6m - long gravity corer (Linke & Haeckel, 2018). At the core location, the shallow sedimentary succession thins out, thus

allowing the sampling of the underlying stratigraphic layers. The cores were split in 1 m segments of archive and working halves.

The working halves were sampled for physical sediment properties, element composition of solid phase, and chemical composition of porewater. Porewater was extracted from sediment in 30 cm intervals using Rhizons (0.2 µm, Rhizosphere Research Products, e.g., Seeberg - Elverfeldt et al., 2005). Sulfate and chloride concentrations of sampled porewater were determined by Ion Chromatography equipped with a conductivity sensor (Eco IC, Metrohm; Metrosep A Supp5‑100/4.0). Analytical precision is ~1% (1σ) measured by repeated analysis of IAPSO (International Association for the Physical Sciences of the Oceans). Total organic carbon content (C_{org}), C/N - ratio, and inorganic carbon content ($CaCO_3$) were determined by combustion of sediment samples in a EURO Element Analyzer (C/N/S configuration), prior and after removal of inorganic carbon with 1 M HCl. The analytical data are given in percent of the total weight of dried sediment with an accuracy of 3%. Calculated C/N - ratios are given in atom - ratios. Dissolved methane concentrations were determined by headspace sampling according to Sommer et al. (2009). Three cubic centimeters of sediment are transferred into a 22 ml head space vial and closed with a crimped rubber septum after adding 6 ml of saturated sodium chloride solution. Equilibrated headspace gases were analyzed by injecting 100 µl of headspace gas into a Shimadzu gas chromatograph (GC - 2014) equipped with a packed Haysep - Q (80/100, 8 ft) column and a flame ionization detector. Analytical data are given with 2% (1σ) accuracy. Sediment porosity was determined by weight difference due to loss of water from ~5 cm^3 wet sediment samples during freezedrying.

The archive halves were used to measure the relative abundance of the elements Ca, Fe, S, Rb, Zr, and Cl at the British Ocean Sediment Core Research Facility (Southampton, UK) using the ITRAX core - scanning X - ray fluorescence system (Cox Analytical; Croudace et al., 2006). This was done in 1 - mm intervals using a molybdenum X - ray tube at 30 s measurements time, 30 kV, and 40 mA. Element abundances are presented as total counts normalized to counts per second and a running average of 1 cm was applied to the results. Physical properties (resistivity, magnetic susceptibility, and density) of the sediments were measured on the archive halves using the GEOTEK multisensor core logger at 1 cm intervals.

3.4. Results

3.4.1. Seafloor Morphology

High - resolution bathymetric data reveal abundant depressions of the seafloor in various shapes and sizes in the Witch Ground Basin. These abundant depressions occur in water depths between 120 and 180 m over an area 225 km^2 and we interpret them as pockmarks (Figure 3.3). Where pockmarks are absent, the seafloor is characterized by linear and curvilinear depressions, which we interpret as iceberg plow marks (Figure 3.3a). We identified 1679 individual pockmarks within our bathymetric grid. The derived morphological parameters are summarized in Table 1.

The pockmarks are usually elongated in one direction with a long axis orientation in NNE to SSW direction (Figure 3.3b). The predominant long axis orientations do not align with the orientation of the sail line (20° offset) and are therefore no acquisition artefacts. Based on their depths, widths, and lengths, we separate the pockmarks into two classes: Class 1 pockmarks (n = 9) include the Scanner, Scotia, Challenger, and Alkor pockmark complexes, which are >6 m deep, >75 m wide, and >250 m long (Figure 3.3a); Class 2 pockmarks represent the vast majority of pockmarks with depths between 0.9 and 3.1 m, width between 14 and 57mand length between 26 and 140 m (n = 1670, Table 1).

3.4.2. Seismic Stratigraphy

A3 - D seismic profile shows the major seismostratigraphic units and is centred above the western part of the Scanner Pockmark (Figure 3.4c). Following the local seismostratigraphic framework, unit S1.1 shows laterally highly coherent and finely laminated seismic reflections, with an upper boundary defined by a distinct unconformity (R4), which is characterized by a zone of chaotic incoherent reflections (Figures 3.2b, 3.4c, and 3.5b). Unit S1.2 shows high lateral continuity of seismic reflections cut by numerous glacial tunnel valleys indicating different phases of erosion and deposition. The overlying unit S2 is discordant (erosional surface) and of chaotic to transparent seismic facies (Figures 3.4b and 3.5b). S2 varies in thickness between 0.015 and 0.050 s TWT corresponding to 10‑40 m, and shows high amplitude patches (bright spots) with polarity reversals at stratigraphic highs in between adjacent tunnel valleys (Figures 3.4b and 3.5b), indicating the presence of free gas in pore space (Løseth et al., 2009). In the 3 - D seismic data, unit S3 is characterized by a chaotic to transparent seismic facies at the bottom and laterally continuous, low reflective seismic

reflections at the top (Figure 3.4c). Based on the echosounder and 2 - D seismic data we subdivide this unit into two subunits (S3.1 and S3.2, see Figures 3.4a and 3.4b). S3.2 shows a transparent to chaotic seismic facies at the bottom and a transition to laminated seismic reflections at the top (Figures 3.4a and 3.4b and 3.5). This fine lamination of seismic reflections is also visible below 0.25 s TWT within the echosounder data (Figure 3.4a).

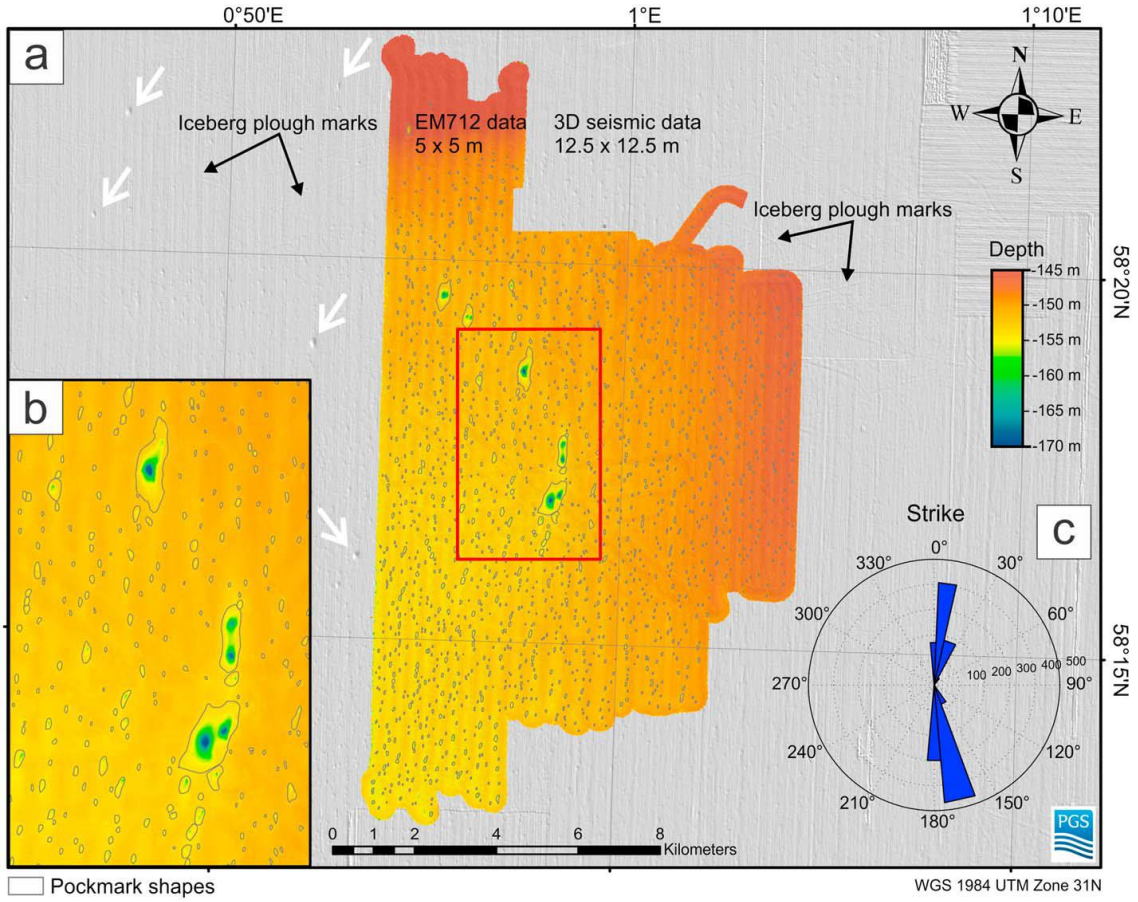

Figure 3.3: (a) Detailed bathymetric map with a compilation of high-resolution multibeam bathymetry (5 × 5 m lateral and up to 10 cm vertical resolution) and depth converted 3-D seismic seafloor horizon in greyscale slope shader (12.5 × 12.5 lateral and ~20 m vertical resolution, converted with constant seismic velocity 1,500 m/s). The semiautomatically picked pockmarks are outlined by black polygons. White arrows highlight class 1 pockmarks outside of the high-resolution bathymetry. (b) Zoom of Scanner, Scotia, and Challenger pockmarks and numerous class 2 pockmarks. Semiautomatedly picked pockmarks are outlined by black polygons. (c) Rose-diagram of pockmark orientation (orientation of a axis).

Figure 35 shows in further detail that unit S4 is discordant to S3.2 and characterized by a transparent to chaotic seismic facies and internal alternating dipping reflections separated by a distinct boundary (Figure 3.5a). Based on the echosounder data and the smeared boundary with high amplitude reflections (Figure 3.5a), we separate unit S4 into subunits S4.1 and S4.2. S4.1

varies in thickness (up to 0.033 s TWT corresponding to 25 m at 1,500 m/s) and thins out eastward toward the Scanner pockmark (Figure 3.5a). Unit S5 shows well - stratified and laterally continuous seismic reflections, which overly the corrugated surfaces of S4.1 and S4.2 (Figure 3.5). Based on the echosounder and 2 - D seismic data, we subdivide S5 into two subunits (S5.1 and S5.2, Figures 3.4a and 3.4b), which will be described in detail below.

3.4.3. Shallow Sedimentary Succession and Water Column Imaging

The high - resolution echosounder data image the very shallow sedimentary succession, including units S4 and S5 (Figure 3.6a). S4.1 is characterized by a chaotic to transparent facies with a highly corrugated surface and internal reflections that show alternating dipping directions. S4.1 is mostly present below 0.23 s TWT and surficially exposed at the center of the western Scanner pockmark (see also inset Figure 3.4a).

Table 3.1: Statistical Analyses of Geomorphological Parameters Derived From 1,679 Individual Pockmarks in our Survey Area Note. Minimum, maximum, mean, standard deviation, and percentage within range of area, length (a axis), width (b axis), maximum depth (from threshold), perimeter, neighboring distance, and water depth at center point of respective pockmark.

Parameter	Min.	Max.	Mean	Std.	Percentage in range
Area [m^2]	503	660,991	7,039	48,998	99% in 503–56,038 m^2
Length [m]	13	1,106	83	57	93% in 26–140 m
Width [m]	6	464	36	22	92% in 14–57 m
Max. depth [m]	0.55	17.77	2.0	1.1	87% in 0.9–3.1 m
Perimeter [m]	32	2439	196	128	94% in 68–324 m
Neighboring distance [m]	0	583	102	60	69% in 42–162 m

Water depth [m]	144	155	151	2	61% in 149–153 m

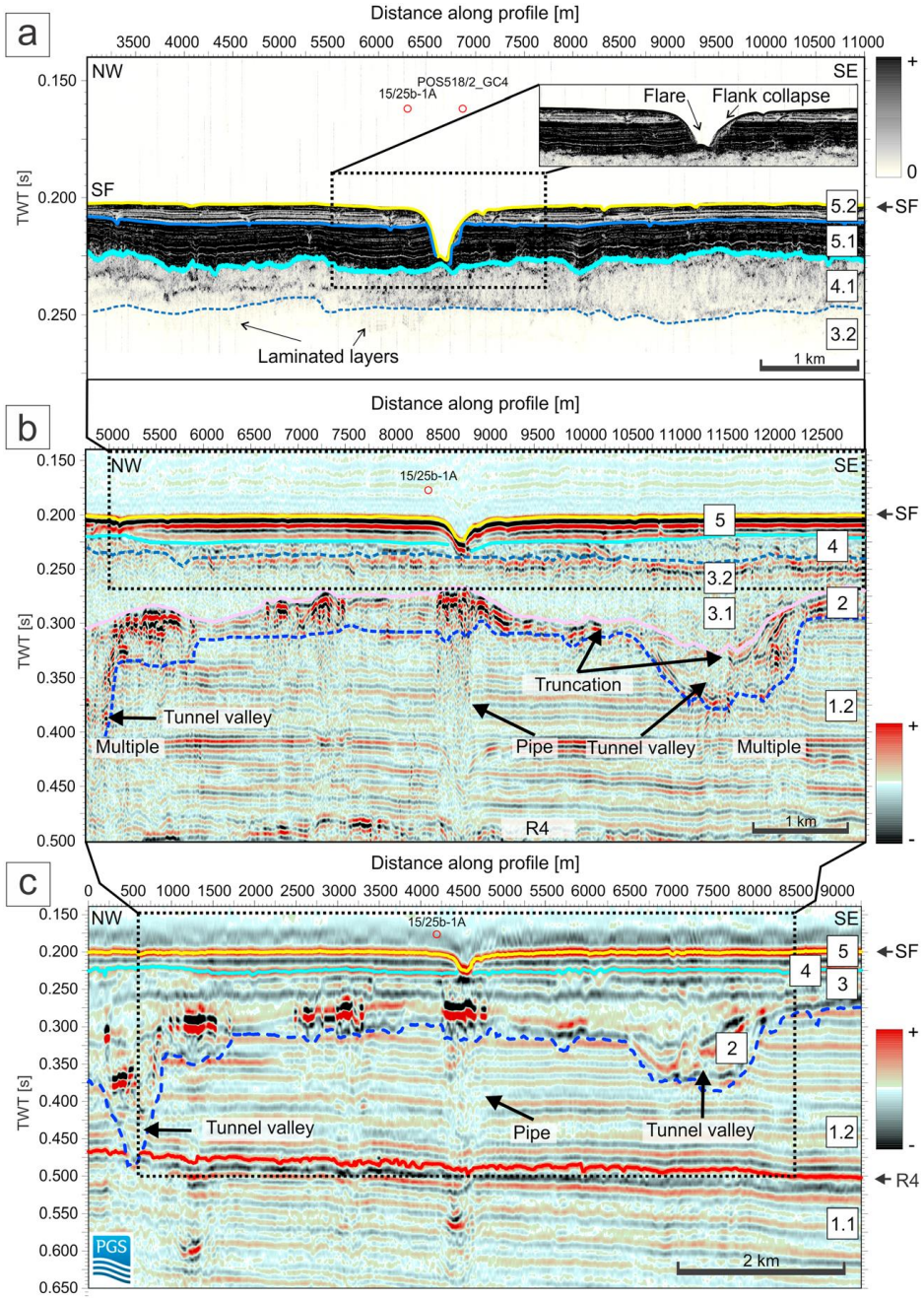

Figure 3.4: Combination of (a) echosounder data, (b) 2-D seismic reflection data, and (c) 3-D seismic reflection data extending from northwest to southeast across the Scanner pockmark showing interpreted horizons, interpreted seismic units S1 to S5 and unconformity R4. The dashed box in (c) shows location of (b), dashed box in (b) shows location of (a) and dashed box in (a) shows location of zoomed section in the right corner. Horizons are as follows: red line = R4; dashed blue line = top S1.2; pink line = top S2; dashed slate blue line = top S3.2; bright blue line = top S4.1; blue line = top S5.1; yellow line = seafloor (SF). Vertical red bar in (c) shows the location of industry well 15/25b-1A. The location of the profile is given in Figure 3,1. TWT = two-way traveltime.

S5.1 lies between 0.212 and 0.230 s TWT and consists of laterally continuous, very well laminated strata and high amplitude response (corresponding to dark colours in the echosounder profile). S5.1 also holds v - shaped amplitude anomalies at specific stratigraphic horizons terminating at two major stratigraphic boundaries (red boxes I and II in Figure 3.6a). On top, S5.2 (0.208–0.215 s TWT) shows lower amplitudes, but a well laminated and lateral coherent stratigraphy. This unit reveals as well v - shaped amplitude anomalies marked with red boxes III and IV. The v - shaped amplitude anomalies show very high amplitudes (black arrows in Figure 3.6a) at their centre. They all terminate at the same stratigraphic horizon. Both S5.1 and S5.2 show local vertical amplitude discontinuities, possibly indicating fractures in the subsurface (Figure 3.6a). The topmost part of unit S5.2 between the seafloor at 0.205–0.207 s TWT is characterized by a high amplitude chaotic seismic facies. Here, the class 2 pockmarks crop out at the seafloor and the unit comprises another set of v - shaped amplitude anomalies, which coincide with the pockmarks at the seafloor. This indicates that the v - shaped amplitude anomalies in the subsurface most probably correspond to previous phases of pockmark formation (further referred to as paleo - pockmarks, red boxes I–IV). If single seep sites would have been active over a long time, this activity would lead to stacked pockmarks (Andresen & Huuse, 2011). However, paleo - pockmarks in the subsurface do not coincide with class 2 pockmarks at the seafloor. The echosounder data allow to determine the thickness of the sediment in unit S5.2, in which the vast majority of pockmarks and paleo - pockmarks are located (Figures 3.6a and 3.7a and 3.7d).

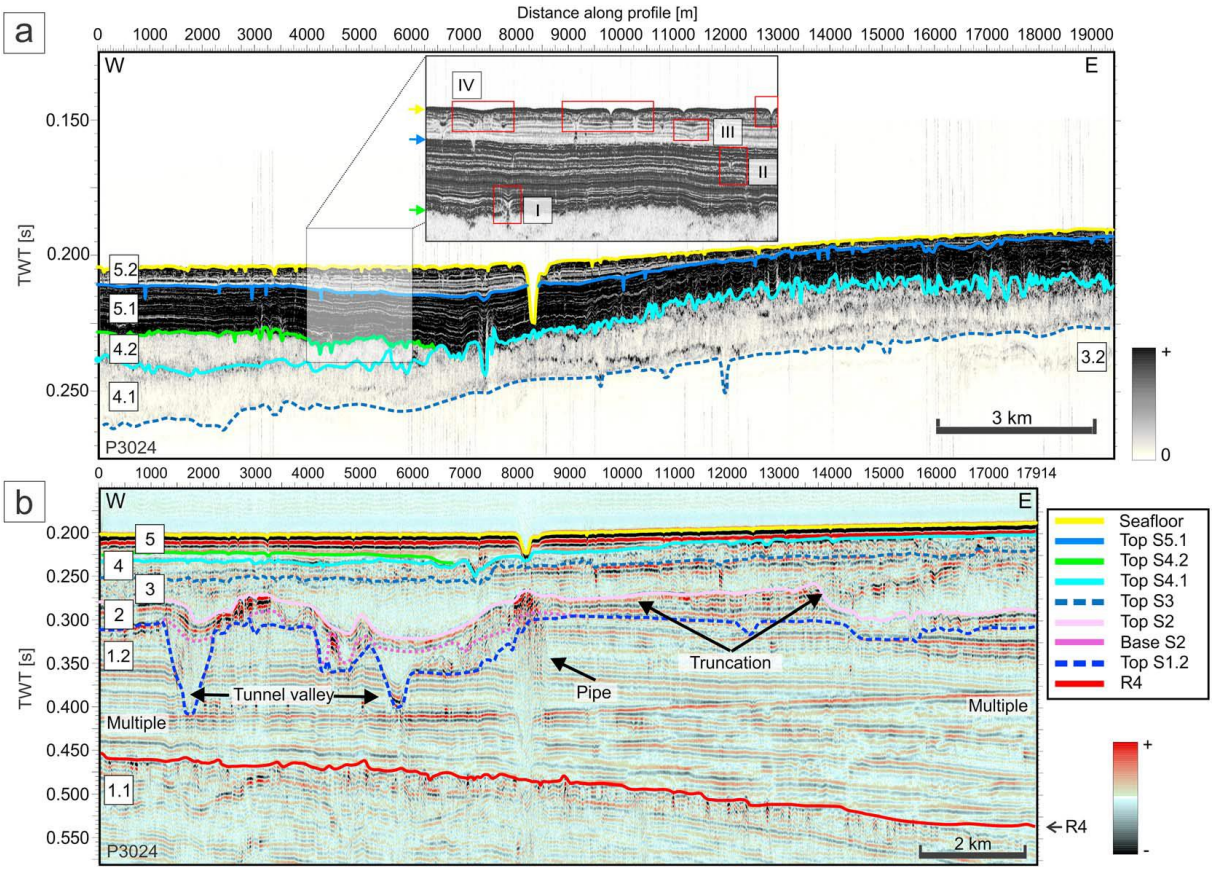

Figure 3.5: (a) ~20-km-long echosounder profile (perpendicular to the profiles shown in Figure 3.4) extending from west to east across the Scanner pockmark. Horizons are base S4.1 (dashed slate blue line), top S4.1 (turquoise line), top S4.2 (green line), top S5.1 (blue reflection), and seafloor (yellow line). The inset shows a part of the echosounder profile for a detailed image of the lower/upper Witch Ground Formation (S5.1, respectively, S5.2; yellow arrow indicates the seafloor, blue arrow top S5.2, and green arrow top 4.2) and to highlight class 2 pockmark formation at distinct stratigraphic horizons (I–IV). (b) Corresponding ~18-km-long 2-D reflection seismic profile across the Scanner pockmark. Horizons are showing S1.1, R4 reflector (red line), top S1.2 (dashed blue line), base MIS 6 till/S2 (dashed purple line), top S2 (pink line), top S3.2 (dashed slate blue line), top S4.1 (turquoise line), top S4.2 (green line), and seafloor (yellow line). The location of the profile is given in Figure 3.1. TWT = two-way traveltime.

We observed no venting from class 2 pockmarks during MSM63 (April/May 2017). However, our backscatter images show high values for class 2 pockmarks around their centre and their rim, of which the latter is most likely related to slope effects (Figure 3.6d). Active venting was limited to the class 1 pockmarks Scanner, Scotia, Challenger, and Alkor confirmed by water column imaging (Berndt et al., 2017). The western Scanner pockmark showed two adjacent flares (Figure 3.6b) that emerged from the centre of the pockmark and extend ~100 m into the water column (water depth 180 m). Similar flare behaviour has been observed at blowout site 22/4b further south, where released methane bubbles emerge in a spiral vortex (Schneider von Deimling et al., 2015). A high backscatter anomaly inside the western Scanner pockmark (Figure 3.6d) indicates a change in lithology probably related to previously identified authigenic

carbonates. In areas where the Witch Ground Formation (S5) is absent and glacial deposits of unit S4.1 are surficial, class 1 pockmarks show a decrease in depth (from >10 to 6‑10 m), width (>300 to ~100 m), and length (>600 to ~300 m) in areas where the Witch Ground Formation is absent (S5).

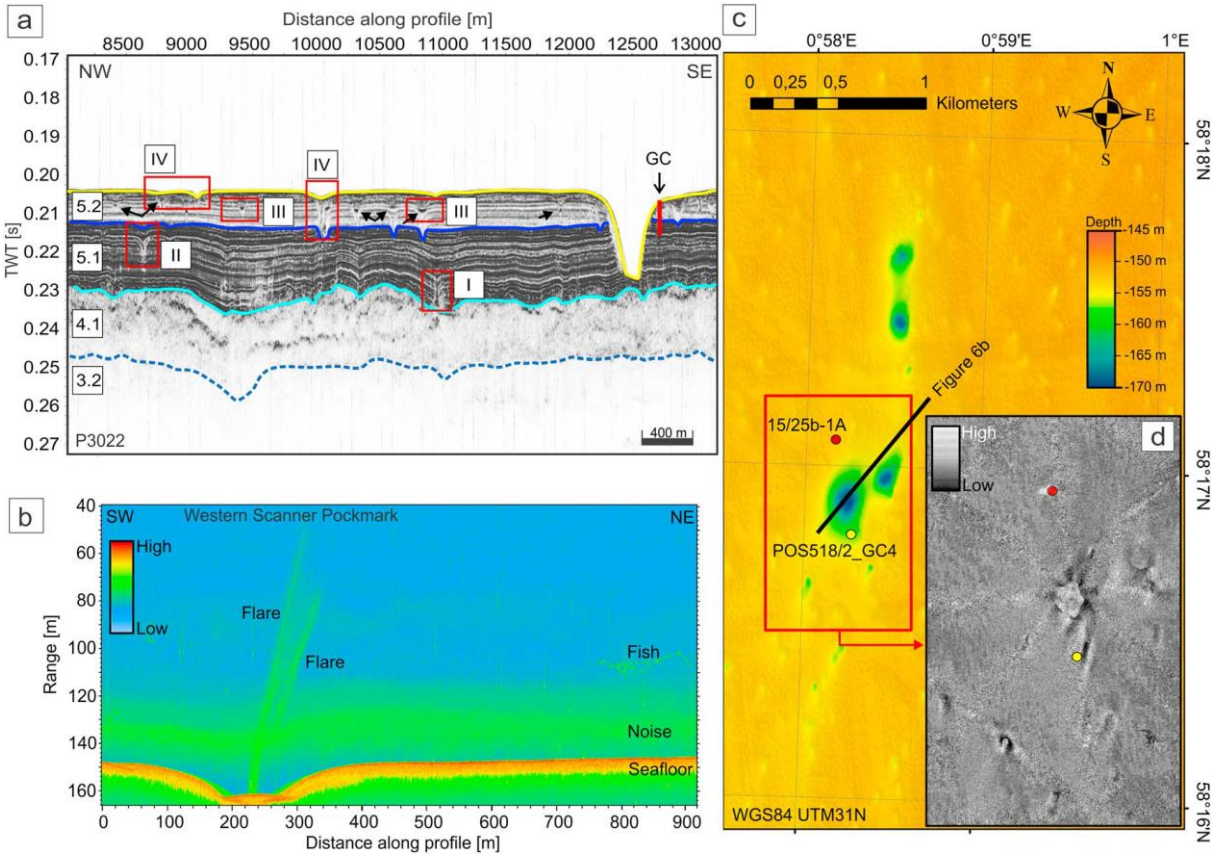

Figure 3.6: (a) ~4 km-long echosounder profile from northwest to southeast showing the shallow sedimentary succession in high-resolution. Horizons include the seafloor (yellow), base S5.2 (blue line), top S4.1 (turquoise line), and base S4.1/top S3.2 (dashed slate blue line). The red boxes highlight specific stratigraphic horizons where pockmarks/paleo-pockmarks occur in at least four phases (I–IV). Black arrows highlight examples of high-amplitude patches (b) 920-m-long EM712 water column imaging range stack perpendicular to (a) across the western part of the Scanner pockmark showing two flares emerging from the centre into the water column (high backscatter = red). Location of the profile given in (c). (c) Bathymetric map showing the location of the Scanner and Scotia pockmark complexes (Class 1 pockmarks) and the location of gravity core POS518/2-GC4 (yellow dot) and industry well 15/25b-1A (red dot). (d) Zoom in bathymetric map within indicated extents (red box) showing backscatter derived from EM712 multibeam data. High backscatter is shown in white and low backscatter in black colours. TWT = two-way traveltime.

The pockmark density correlates with the sediment thickness of the uppermost sedimentary succession. Class 2 pockmarks predominantly occur in areas where seismic unit S5.2 is generally 2‑8 m thick in the surrounding of the pockmarks, while a few pockmarks occur on gentle slopes where seismic unit S5.2 is between 1 and 2 m (Figures 3.7b and 3.7d). We calculated the surrounding sediment thickness by adding the maximum pockmark depth derived

from bathymetric data to the echosounder horizon thickness converted with 1,500 m/s (Figure 3.7a, blue lines P70/black lines SBP). The density of the pockmarks at the seafloor increases with increasing sediment thickness and water depth (1 pockmark per square kilometre at 140 m to 25 per square kilometre at 155 m water depth, see Figure 3.7c).

3.4.4. Sediment Sampling

Gravity core POS518/2 - GC4 shows three lithological units, which we can seismostratigraphically tie to the transition from S5.2 to S5.1 in our echosounder data (Figure 8): Unit 1 (3.4-6 m) comprises very well sorted clay to silty clay with wavy laminations of organic rich material (Figure 3.8). The matrix contains algal remains and shell fragments. The boundary between units 2 and 1 is gradational. Unit 2 (2.9-3.4 m) consists of well - sorted, faintly laminated silty clay with fragments of shale and shells (Figure 3.8). There is a sharp, possibly erosional boundary between units 3 and 2 that corresponds to an increase in density (>2 g/cm$_3$), resistivity (0.6 Ωm), and magnetic susceptibility (50 × 10$_{-5}$). Here, P wave velocity slightly decreases with a subtle increase in CH_4 (Figure 3.8). Furthermore, porewater analyses and ITRAX XRF shows a step increase in SO_4 and solid phase Fe with a step decrease in Cl. The Zr/Rb, Ca/Ti, and Ca/Fe ratios indicate shifts in sediment properties or provenance, also show step decreases between unit 2 and 3. Unit 3 (0-2.9 m) is well - sorted clayey silt to very fine sandy silt with wavy laminations or mottling but otherwise massive. The matrix contains algal remains with shell fragments and even whole shells are present. The lithic grains are subrounded and a dropstone was observed toward the base of the unit. The organic carbon content (C_{org}) is increases from 0.55 wt.% in unit 1 to about 1.5 wt.% in unit 3 (Figure 3.8). $CaCO_3$ shows low values (12 wt.%) in unit 1 with a sharp increase within unit 2 to high values (25 wt.%) in unit 3. SO_4 gradually increases over the whole core length (6 m) from ~10 mmol/L in unit 1 to seawater concentration of ~30 mmol/L in unit 3. CH_4 decreases above 4 m depth from ~10 µmol/L in unit 1 to 0-1 µmol/L in unit 3. Headspace gas analyses of all core segments show that the gas composition is almost purely methane (>99%).

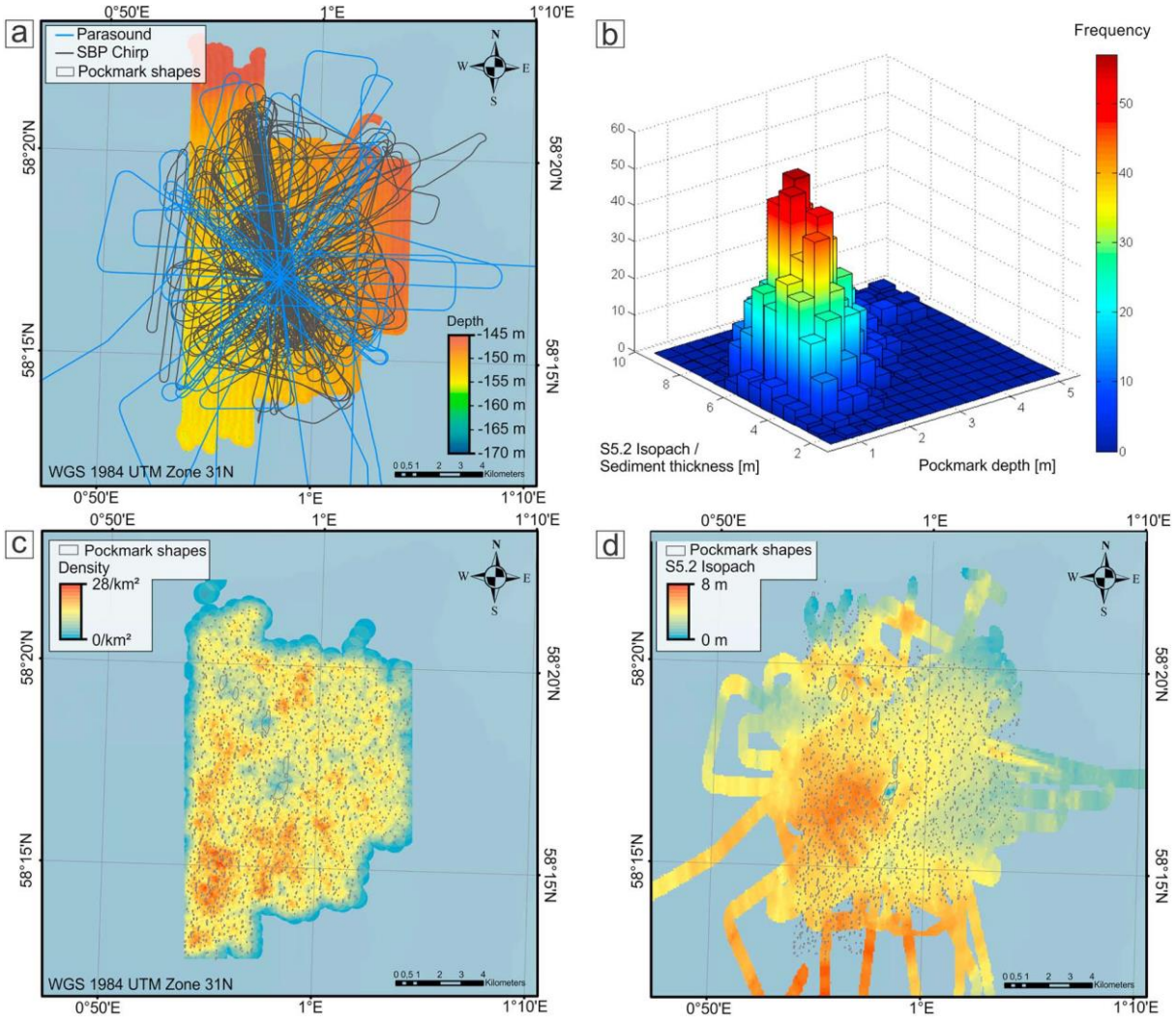

Figure 3.7: (a) Bathymetric map of the survey area showing echosounder profile coverage (Parasound = blue lines, SBP chirp = black lines). (b) 3-D bar plot showing the density of pockmarks, depth versus sediment thickness around the corresponding pockmarks (S5.2 Isopach). (c) Density and semiautomated picked outlines (black polygons) of surface pockmarks derived from high-resolution bathymetric data. (d) Semiautomated picked outlines of surface pockmarks (black polygons) and sediment thickness of unit S5.2 (S5.2 Isopach) derived from echosounder profiles. For echosounder profile coverage see (a).

3.4.5. Subsurface Fluid Migration

In the Scanner pockmark area, the seismostratigraphic layering is disturbed by zones of dimmed reflections and the presence of bright spots at different depth levels (280, 350, 500, 570 ms TWT, Figure 3.4c). This indicates the presence of interstitial fluids that cause a complex wave field propagation by significant changes in acoustic impedance (Domenico, 1977; White, 1975). These amplitude anomalies with bright spots and zones of dimmed amplitudes reach to at least the R4 reflector (Figure 3.4c). Here, we used the seismic symmetry attribute from 3 - D seismic amplitude data to identify the spatial extent of these amplitude anomalies and the subsurface

expression (Figure 3.9c). The time slice of this attribute at 0.4 s TWT shows circular amplitude anomalies with constant diameters in depths ranging from 200 to 600 m beneath the unusually large pockmarks Scanner, Scotia, Challenger, and Alkor (Figure 3.9c). Beneath the Scotia and Alkor pockmark complexes, there are two adjacent amplitude anomalies visible with a spacing of 50‑100 m (Figures 3.9c, 3.9d, and 3.9f).

The 3 - D seismic data show bright spots associated with unit S2 at ~0.3 s TWT in areas, where the tunnel valley erosion formed structural highs (Figures 3.9a and 3.9b). Previous surveys have interpreted these bright spots as free gas bearing layers within the uppermost sedimentary succession that cover the area in between two adjacent tunnel valleys (Judd et al., 1994). The pipe structures link the R4 reflector with the bright spots at the erosional unconformity by zones of dimmed seismic amplitudes. The 2 - D seismic data reveal that unit S2 is highly fractured where bright spots are visible (~0.3 s TWT; 5, 6.5, and 8.5 km distance along profile, Figure 3.4b).

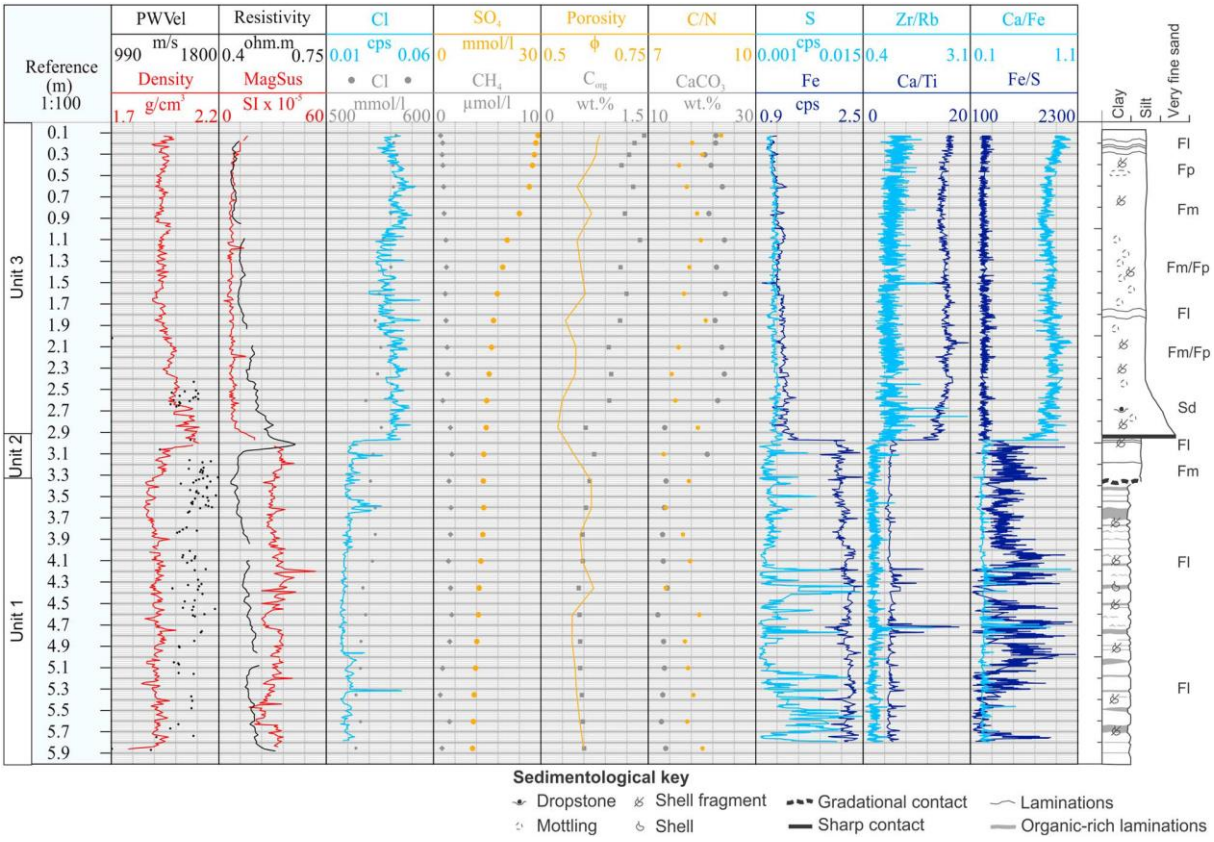

Figure 3.8: Gravity core POS518/2-GC4, subsequent sedimentary units from sedimentological description. The location of the core is given in Figure 3.6a. The graphs show corresponding data retrieved from multisensor core logger data (black and red lines), sediment and porewater analyses (PW, golden lines and gray dots), and ITRAX XRF data (bright and dark blue lines). ITRAX XRF data show abundances of elements averaged over 1 cm normalized in counts per second (cps).

Sedimentological record shows three units. Lithofacies code is given as Sd = sand with dropstones, Fl = silts and clays (laminated), Fm = silts and clays (massive), Fp = silts and clays (lenses/motling).

3.5. Discussion

3.5.1. Fluid Sources for Pockmarks in the Witch Ground Basin

The morphometric analysis of the Witch Ground Basin bathymetry revealed 1,679 individual pockmarks, which can be divided into class 1 and class 2 pockmarks. Pockmark formation and morphometry is highly dependent on the hosting sediments as well as the flux, flux variation, and type of advected fluids (Abegg & Anderson, 1997; Andrews et al., 2010; Boudreau et al., 2001, 2005; Mogollón et al., 2012; Orsi et al., 1996). Predominant strike directions (NNE, SSE) derived from elongated elliptical shapes of the pockmarks may be attributed to local bottom currents shaping the seafloor (Gafeira et al., 2012). As the two types of pockmarks occur in the same sediments, the clear morphological separation between class 1 and 2 (see above) suggests that different fluids possibly sourced from different depth form the two types of pockmarks or that escape of the same fluids was controlled by different processes.

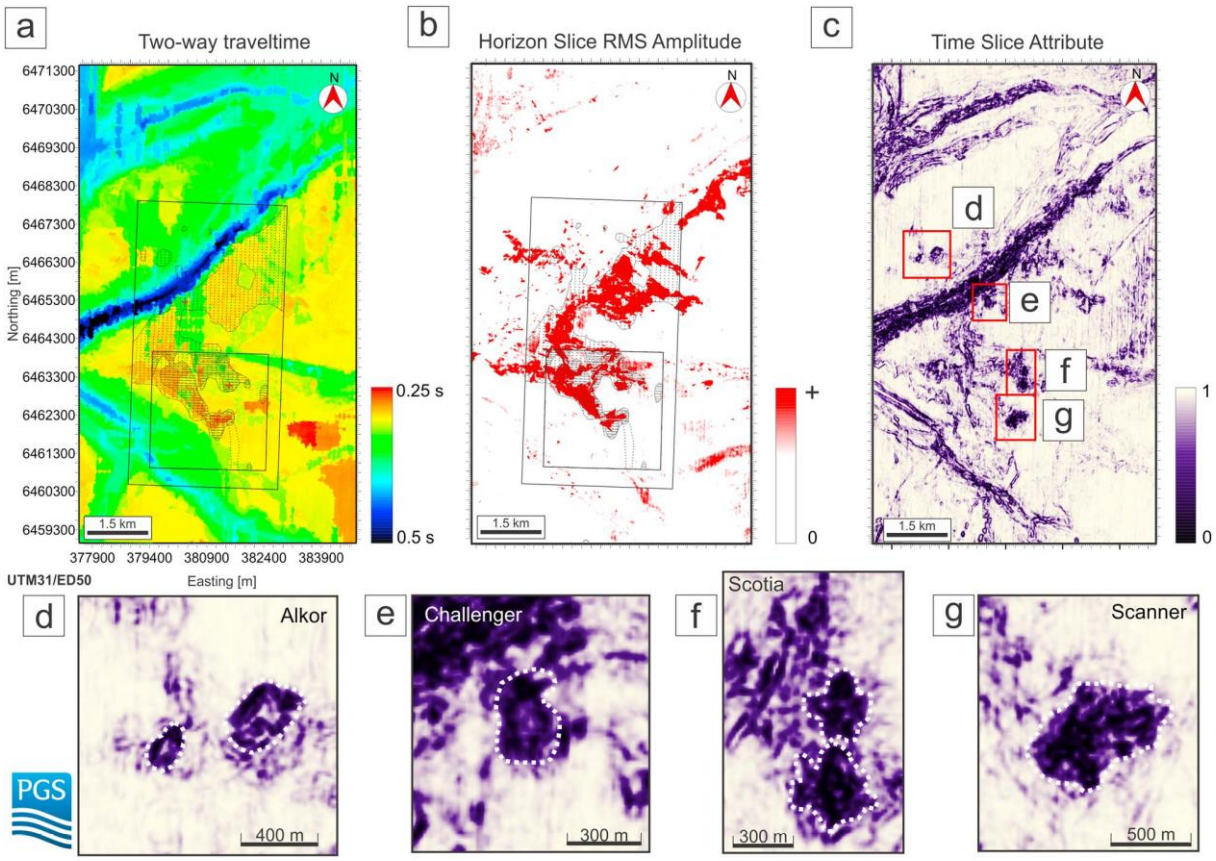

Figure 3.9: 3-D seismic horizon top S1.2/bottom S2. The horizon is given in (a) two-way traveltime, (b) root-mean-square (RMS) amplitude horizon slice over a time window of ±50 ms across the unconformity between units S1.2 and S2 to map the fluids, and (c) symmetry attribute time slice. The slices show the gas accumulation within S2 across stratigraphic highs in between tunnel valleys in comparison to the previous analyses by Judd et al. (1994; see map inset in (a) and (b)). Below are shown close-ups of the

symmetry attribute for the (d) Alkor, (e) Challenger, (f) Scotia, (g) Scanner pockmark complexes (Class 1 pockmarks). White dashed lines outline the pipe structures in the subsurface. The locations of (a), (b), and c are given in Figure 3.1.

3.5.2. Source Depth

The 2 - D and 3 - D seismic data show bright spots within S2, which corresponds to glacigenic sediments deposited during Mid Pleistocene (190–130 ka till from MIS 6; Reinardy et al., 2017). This till unit shows lateral changes in thickness and truncation of reflections to unit S3 indicating an erosional surface (Figure 3.5b). The free gas likely accumulates in the pore space of the glacigenic sediments of S2 rather than in the marine clays of the Aberdeen Ground Formation as previously suggested (Figure 3.4c, S1.2; Andrews et al., 1990; Judd et al., 1994). While the glacial till S2 represents the shallow - most reservoir for the accumulation of free gas within the glacial till, unit 3.2 may act as a seal. S3.2 shows highly continuous reflections corresponding to glaciomarine sediments, which tend to have higher clay contents compared to subglacial sediments and can thus potentially act as a seal.

Horizon slices of RMS amplitudes show patches of bright spots within S2, where stratigraphic highs are present between adjacent tunnel valleys (Figures 3.4b and 3.4c and 3.9a and 3.9b). Previous mapping of these high amplitude patterns (Judd et al., 1994) matches spatially our analysis. The high amplitude patterns are associated with gas in the shallow subsurface. It is likely that the small differences between the two mapping results are due to less complete seismic coverage of previous surveys (Judd et al., 1994) rather than temporal changes in gas distribution.

Below the gas - related bright spots in S2, we interpret the circular - shaped amplitude anomalies with zones of dimmed reflections and bright spots at different depth levels as seismic pipes (Figures 3.4c and 3.9c). Seismic pipes are strictly columnar anomalies with stacks of increased or dimmed amplitudes and are the seismic manifestation of vertical fluid conduits (Cartwright et al., 2007; Karstens & Berndt, 2015; Løseth et al., 2009). However, free gas in unit S2 can cause complex propagation of seismic waves and hence induces seismic artefacts, which may be misinterpreted as seismic pipes. While gas accumulations largely follow the morphology of the stratigraphic highs in between the adjacent tunnel valleys, seismic pipes are not related to any obvious subsurface structures or morphologic patterns. In addition, the circular - shaped amplitude anomalies occupy only a small fraction of the area where free gas accumulates, indicating that the overlying gas induces only minor seismic artefacts (Figures 3.4 and 9). The interpretation of circular - shaped amplitude anomalies as seismic pipes is also

supported by the spatial correlation between seismic pipes in the subsurface and class 1 pockmarks at the seafloor (Figures 3.3a and 3.9c-9g), which indicates their role as fluid migration pathways. We consider the interpretation of the seismic pipe structures robust down to the R4 reflector (Figure 3.4c). Below this reflector, the multiple reflection of the shallow gas bright spots within unit S2 increases interpretation ambiguity.

Unit S2 (intermediate reservoir for the fluids from deeper strata) may be hydraulically connected with the class 1 pockmarks either by a complex fracture network (likely below seismic data resolution), or by flow through unconsolidated sediments. Decompaction weakening may lead to fracture closure after gas bubble release, which would explain the weak seismic response of the fluid conduit beneath the Scanner pockmark complex (Figures 3.4, 3.5, and 3.6a; Räss et al., 2018).

Class 2 pockmark are significantly shallower and have shorter long axes than class 1 pockmarks (Figure 3.3a). Furthermore, our seismic and hydroacoustic data show no evidence for lateral gas migration from class 1 toward class 2 pockmarks identifying them as secondary fluid flow structures, nor for vertical gas migration from deeper strata (Figures 3.6 and 3.7). The apparent differences in morphology and the lack of hydraulic connection suggest the presence of at least two independent sources of fluids in the area.

3.5.3. Class 1 Pockmarks—Timing and Controls of Fluid Venting

Class 1 pockmarks show vigorous venting (Figure 3.6b), indicating vertical fluid migration from deep strata through the pipe structures. Further, high amplitude reflections in echosounder and high backscatter anomalies in multibeam data indicate the precipitation of carbonates at the seafloor (Figures 3.6a and 3.6d). This is consistent with video observations during a previous survey showing MDACs in the central parts of the class 1 pockmarks (Clayton & Dando, 1996; Dando et al., 1991; Gafeira & Long, 2015). Previous geochemical analyses reported carbon isotope ratios ($\delta_{13}C$) of −79‰in gas bubbles emanating from the western Scanner pockmark (Clayton & Dando, 1996) and −53‰ to −36‰ for the carbonate cements and the interstitial gas (Dando et al., 1991; Hovland & Irwin, 1989). Both indicate a biogenic gas origin possibly derived from microbial degradation of organic matter (Judd et al., 1994).

Our geochemical results match the biogenic character of the released methane at class 1 pockmarks (Figure 3.8). Biogenic methane is likely sourced from bright spots at Mid Pleistocene depth (R4) migrating through the pipe (Figure 3.4c). This horizon is primarily associated with biogenic methane (99.9% methane, $\delta_{13}CH_4$ -69‰; Rose et al., 2016). It may act

as a trap focusing and mixing migrating microbial methane from the Quaternary succession with thermogenic methane from deeper sources. Thermogenic fluids may migrate through the overburden from deeper layers (Figure 3.2b), for example, Kimmeridge clay (Judd et al., 1994), along faults (Chand et al., 2017), pipes, or chimneys (Karstens & Berndt, 2015; Räss et al., 2018). This is, however, not corroborated by our geochemical results and the seismic data do not resolve the depth extent of the pipe structures underneath the class 1 pockmarks to the reservoir rocks (e.g., Montrose and Piper sands), but this may be due to imperfect imaging. We conclude that class 1 pockmarks are primarily sourced by biogenic methane from the upper 375 m of the Quaternary succession (corresponding to 500 ms TWT at constant velocity of 1,500 m/s).

The timing of class 1 pockmark formation can be derived from the local stratigraphy. Class 1 pockmarks cut deep into the Witch Ground Formation (S5), truncating the stratigraphic layering of it and expose LGM deposits (S4.1) at their centres (Figures 3.6a and 3.6d). The Witch Ground Formation consists of two individual well - stratified stratigraphic units (S5.1 and S5.2; Figure 3.6a). S5.1 was deposited after 26,595 ± 387 cal. Years BP when grounded ice retreated from the study area (Sejrup et al., 2014). The age of S5.2 is poorly constrained, but it was deposited during some period after 13,165 ± 55 cal. years BP (Sejrup et al., 2014). Furthermore, we observe a gentle shoaling of the Witch Ground Formation toward the class 1 pockmarks while S4.1 slightly dips down (Figure 3.6a), which may indicate sediment doming prior to pockmark formation (Barry et al., 2012; Koch et al., 2015). We therefore conclude that class 1 pockmarks formation initiated between 13,165 ± 55 and 26,595 ± 387 cal. years BP.

The formation of the class 1 pockmarks is related to seismic pipe structures in the subsurface. The formation of two very closely spaced pockmarks at the Scanner, Scotia, and Alkor pockmark complexes are possibly due to two very closely spaced pipes (“twin pockmarks,” Figures 3.9c, 3.9d, and 3.9f). Seismic pipes or chimneys (and ultimately pockmarks) form when (i) pore pressure exceeds the combined least principal stress and tensile strength of the sediment and induces hydrofracturing or (ii) the pore pressure overcomes the capillary entry pressure and capillary failure occurs (Clayton & Hay, 1994; Hubbert & Willis, 1957). Bright spots at the R4 horizon indicate mobile fluids. We suggest that this R4 horizon, which comprises glacigenic sediments, therefore represents a reservoir. The upper Aberdeen Ground Formation (unit S1.2) with high clay content represents a low permeable seal/cap rock, which inhibits pore pressure release via diffusive flow. However, the buoyancy of the gas column itself may not be sufficient

to breach through the overburden (Karstens & Berndt, 2015). To facilitate focused fluid flow through the overlying sediments the system may further need external forcing.

The documented seismic pipes postdate the deposition of the upper Aberdeen Ground Formation (S1.2, MIS 13-21: 474-866 ka). This suggests that they may relate to glacial isostatic and/or glacitectonic mechanisms (e.g., deformation by overriding ice). In glacial environments, overpressure can be generated by rapid sedimentation pulses (Hustoft et al., 2009) or cyclic loading and unloading by ice during the last glacial cycle (Karstens & Berndt, 2015). Gas hydrate dissociation similar to the Troll area further north also represents a possible scenario for gas release (Mazzini et al., 2017). However, the presence of subglacial gas hydrates during the LGM in the Witch Ground Basin remains speculative.

Evidence for class 1 pockmark activity is multifold. First, methane seepage is visible in water column images and second, the presence of MDACs indicate long - lasting seepage (Figures 3.6a and 3.6d). The gas supply is continuous through the colocated pipes. The pockmark activity and flow rates may have been relatively strong at the start with a gradual reduction due to decreasing overpressure in the subsurface. Similar to other seepage sites, current flow rates may also be dependent on tidal pressure changes (Römer et al., 2016).

Class 1 pockmark morphology is likely dependent on the properties of the host sediment (Andrews et al., 2010; Boudreau et al., 2001; Boudreau et al., 2005; Mogollón et al., 2012). We interpret the change in morphometry as a result of the different properties of the outcropping sediments, that is, unit S4.1 comprises overconsolidated subglacial till with hard, muddy, pebbly sands, or sandy muds instead of soft, fine - grained glaciomarine sediments of the Witch Ground Formation (unit S5; Andrews et al., 1990; Long et al., 1986).

Class 1 pockmarks may easily form within the soft, fine - grained sediments of the Witch Ground Formation within the Witch Ground Basin. Elsewhere in the North Sea (e.g., Viking Graben), similar structural and geological conditions may also induce vertical fluid - flow and methane seepage at the seafloor. However, coarser grained sediments, which are present over large areas of the central North Sea (Graham et al., 2010; Reinardy et al., 2017; Sejrup et al., 2014; Stoker et al., 2011), may hinder the formation of pockmarks. Budget calculations of natural geological sources based on pockmark numbers may therefore systematically underestimate the methane flux.

3.5.4. Class 2 Pockmarks—Timing and Controls of Fluid Venting

The timing of class 2 pockmark formation is constrained by the age of the Witch Ground Formation (S5). The Witch Ground Formation was deposited after 26,595 ± 387 cal. years BP. Initially during a transition from glaciomarine to marine environment, the sedimentation rates were very high, that is, up to 50‐100 cm/1,000 years (unit S5, Figures 3.6a and 3.8; Erlenkeuser, 1979; Johnson & Elkins, 1979; Sejrup et al., 2014). Exposed iceberg plow marks at the seafloor indicate very limited input of sediment into the Witch Ground Basin later on during the Holocene (Figure 3.3a). Thus, we can constrain the time of formation of the class 2 pockmarks to between 26,595 ± 387 cal. years BP and the Holocene (8 ka). Class 2 pockmark formation was likely episodic as buried paleo - pockmarks occur at specific stratigraphic horizons within unit S5. If each of these horizons corresponds to their formation time, there have been at least four different phases of pockmark activity (Figure 3.6a). The density of pockmarks per tier is decreasing with increasing burial depth (Figures 3.5a and 3.6a, Long, 1992), which suggests that the late stages of pockmark formation had greater source strength and overpressure than the earlier ones. This is similar to what was proposed for the southern North Sea (Krämer et al., 2017).

Class 2 pockmark formation is likely dependent on the host sediments. They predominantly occur in areas where S5.2 exceeds 2 m thickness and there is a significant correlation of pockmark depth with sediment thickness (Figure 3.7). Neither the abundant iceberg plow marks nor the underlying tunnel valleys seem to play a role for pockmark distribution (Figures 3.3 and 3.7). In this context, the distance between neighbouring pockmarks (Table 1) and the similar appearance of class 2 pockmarks (Figure 3.3 and Table 1) suggest homogeneous preconditions in the subsurface as well as an exclusion zone around each pockmark related to a drainage cell where no other pockmark may form (Maia et al., 2016).

The fluid source of class 2 pockmarks is more difficult to constrain. Similar pockmark occurrences in the North Sea have been associated with methane venting due to post - glacial gas hydrate dissociation (e.g., Troll; Mazzini et al., 2017). However, there are no observations of active gas venting or direct proof of MDACs associating class 2 pockmark formation in the Witch Ground Basin with focused methane release. Furthermore, our results show low methane concentrations, low organic carbon content, and porewater sulfate concentrations that decrease gently with depth indicating no upward migration of methane from below (Figure 3.8). At the same time, there are no direct indications for focused expulsion of porewater or biogenic

activity, which may represent alternative formation processes (Judd & Hovland, 2007). Hence, we are not able to determine the fluids involved in the formation of class 2 pockmarks directly and need to constrain them based on the involved formation processes.

Mechanisms of pockmark formation in the Witch Ground Basin include (1) venting of interstitial biogenic or thermogenic gas (Hovland et al., 2010; Judd & Hovland, 2007; Kilian et al., 2017), (2) porewater escape during compaction (Harrington, 1985). Seepage of thermogenic hydrocarbons has often been proposed for the North Sea. However, we do neither see a hydraulic connection toward deeper strata nor any indication for gas venting into the water column or free gas in the shallow sedimentary successions (S5, Figure 3.6). The low methane concentrations and the downward decreasing sulfate concentrations indicate no upward transport of methane.

Biogenic methane from decomposition of organic material represents another possible source. Microbial methanogenesis may lead to accumulation of free gas due to the soft, cohesive, low permeable sediments of the Witch Ground Basin instead of migrating out of the sediments (Boudreau et al., 2001; Boudreau et al., 2005). Such a scenario has been proposed for organic - rich sediments in the Arkona Basin, Baltic Sea, (Abegg & Anderson, 1997; Mogollón et al., 2012; Orsi et al., 1996), and Belfast Bay, Maine, USA (Brothers et al., 2012). There, pockmark formation is dependent on the sediment thickness, flux of organic matter, and sedimentation rates. The accumulation of free gas depends on the rate of degradation of organic matter and sediment properties, primarily permeability, and occurs where the sediment thickness exceeds 3 m (Boudreau et al., 2001; Boudreau et al., 2005; Mogollón et al., 2012). However, echosounder data for the Witch Ground Basin do not reveal any amplitude blanking indicating free gas within S5. Furthermore, the organic carbon content is not particularly high (~1%) and the methane concentrations too low to generate free gas in the subsurface. In combination, our results indicate that in situ microbial methanogenesis and accumulation of free gas is unlikely the cause for pockmark formation. Unrecognized sources such as gas hydrates or permafrost may provide other possible sources of fluids that may have formed the class 2 pockmarks. However, the presence of subglacial gas hydrates during the LGM remains speculative. The sedimentary succession of the Witch Ground Formation shows high lateral coherence indicating no disturbance due to the dissociation of gas hydrates. Permafrost in the Witch Ground Basin during deposition of the Witch Ground Formation (S5) was not possible as our results show that this unit was deposited in glaciomarine to marine environments (indicated by C/N, Ca/Ti, Zr/Rb, Ca/Fe, and Fe/S ratios and dropstones in unit 1, Figure 3.8, Long et al., 1986).

While pockmarks in the central North Sea are primarily associated with seepage of hydrocarbons, our aforementioned results show no conclusive evidence that class 2 pockmark formation was gas - driven. Therefore, we also consider purely sedimentological mechanisms (Paull et al., 2002). Such a mechanism may be compaction - related dewatering of fast accumulated sediments (disequilibrium compaction, Harrington, 1985). The accumulation rates during the deposition of the Witch Ground Formation are sufficiently high (0.5–1 m/ka) to retain fluids at shallow depth (Mann & Mackenzie, 1990). In this case, the porewater would have been trapped within the soft cohesive sediments of the Witch Ground Formation (clays & silt) and pore pressure would have risen over time releasing fluids. Once vertical pathways are established, they laterally drain the surrounding sediments (Harrington, 1985).

This process broadly agrees with our observations. There is no acoustic turbidity within the Witch Ground Formation that would indicate free gas (Figures 3.4a, 3.5a, and 3.6a). Instead, a transition from glaciomarine to marine sediments is documented by the sediment core (Figure 3.8). The transition from glaciomarine to marine deposition represents a permeability inversion as less permeable distal marine sediments overlie proximal glaciomarine sediments. Because the glaciomarine sediments will continue to compact and dewater after the marine sediments have been emplaced the expelled porewater cannot escape easily, which causes overpressure and focusing of fluid migration. Fractures in the Witch Ground Formation may be the result of this compaction process (Figures 3.5a and 3.6a). Similar compaction - related dewatering and fractures at shallow depth below the seafloor are observed in the Hatton Basin in the northeast Atlantic Ocean (Berndt et al., 2012). The increase in pockmark density per tier with decreasing burial depth indicates an upward increase in source strength (Figure 3.5a). The random distribution instead of aggradation or stacking of pockmarks through time supports the diffusive source character (Figure 3.5a). Both observations match the process of compaction - related dewatering. Sediment compaction as genetic origin for the formation of class 2 pockmarks is further supported by a lower chlorinity at depth in the interstitial water (Figure 3.8). This is indicative for the upward migration of less saline water and would be expected because of the glaciomarine provenance of the lower Witch Ground Formation. Based on the considerations above we propose that class 2 pockmark formation in the Witch Ground Basin is at least partly related to compaction. However, it seems unlikely that this mechanism was dominating the formation of deep pockmarks (>0.5 m) in areas where only 2 m of soft cohesive sediments exist unless there was additional forcing. We also note that the sediment properties are not well constrained.

All evoked models rely on external forcing to release the overpressure in the subsurface and cause pockmark formation, because the tiers of pockmarks and paleo - pockmarks in the subsurface indicate the intermittent nature of seepage events in the Witch Ground Basin. These external forces need to be basin - wide and must have induced sufficient overpressure by a change of subsurface temperature or pressure conditions. In the Witch Ground Basin, temperature conditions may have changed due to warm water inflow from the North Atlantic (e.g., Becker et al., 2018). Pressure conditions may have changed due to rapid sedimentation (Hustoft et al., 2009; Reinardy et al., 2017), disequilibrium compaction (Flemings et al., 2008; Talukder, 2012), tidal currents (Chen & Slater, 2016), large storms (Krämer et al., 2017), or earthquakes (Field & Jennings, 1987; Hasiotis et al., 1996), which may have ultimately led to episodic fluid escape from the shallow marine sediments in the Witch Ground Basin.

3.6. Conclusions

We document >1,500 pockmarks over an area of 225 km^2 within the Witch Ground Basin, northern North Sea. Based on their morphologies we distinguish between two classes of pockmarks. Class 1 pockmarks are >6 m deep, >75 m wide, and >250 m long. Class 2 pockmarks, which represent 99.5% of the overall data set, are much smaller and more uniformly distributed within the study area. Their maximum depth ranges between 0.9 and 3.1 m and their maximum widths and length are 14‑57 and 26‑140 m, respectively. From the structural and morphological analyses, we draw the following conclusions:

· There is no evidence of hydraulic connection between class 1 and class 2 pockmarks. Class 2 pockmarks solely occur in the soft, fine - grained sediments of the Witch Ground Formation, while class 1 pockmarks are colocated with deep fluid accumulations and seismic pipe structures in the subsurface. Together with the lack of intermediate sized pockmarks between the two endmember classes (with respect to pockmark sizes), this indicates the presence of two different fluid sources within the sediments.

· Seismic pipe structures under most class 1 pockmarks, which hydraulically connect deeper strata with the surface, represent vertical conduits for the fluids that formed class 1 pockmarks.

· Class 1 pockmarks relate to biogenic methane sourced from Mid Pleistocene strata (upper 500 ms corresponding to 375mof the sedimentary succession at 1,500 m/s), which migrates through vertical fluid conduits. Mixing of biogenic fluids derived at shallow depths with

thermogenic - derived fluids from deeper sources is, however, possible and may occur episodically.

· The up - bending of Witch Ground Formation sediments toward the pockmark suggests that class 1 pockmarks formed between 13,165 ± 55 and 26,595 ± 387 cal. years BP and present - day activity suggests they may have been active since their formation. Active seepage imaged during the last three decades in combination with indications for long - lasting seepage from MDAC suggests that Class 1 pockmarks may be continuously active over long times.

· In contrast, class 2 pockmarks may only have been active during certain episodes corresponding to the distinct reflectors at which they cluster. During repeated campaign - based water column imaging over the last three decades no seep activity was documented for the class 2 pockmarks at the surface supporting that this type of pockmark is not continuously active. These pockmarks may be sourced by compaction related dewatering. As the pockmarks cluster on distinct stratigraphic levels their formation must have been triggered by externally induced pressure and temperature changes affecting the entire Witch Ground Basin.

References

Abegg, F., & Anderson, A. L. (1997). The acoustic turbid layer in muddy sediments of Eckernfoerde Bay, Western Baltic: Methane concentration, saturation and bubble characteristics. Marine Geology, 137(1–2), 137–147. https://doi.org/10.1016/S0025-3227(96)00084-9

Andresen, K. J. (2012). Fluid flow features in hydrocarbon plumbing systems: What do they tell us about the basin evolution? Marine Geology, 332, 89–108.

Andresen, K. J., & Huuse, M. (2011). 'Bulls-eye' pockmarks and polygonal faulting in the Lower Congo Basin: Relative timing and implications for fluid expulsion during shallow burial. Marine Geology, 279(1–4), 111–127. https://doi.org/10.1016/j.margeo.2010.10.016

Andrews, B. D., Brothers, L. L., & Barnhardt, W. A. (2010). Automated feature extraction and spatial organization of seafloor pockmarks, Belfast Bay, Maine, USA. Geomorphology, 124(1–2), 55–64. https://doi.org/10.1016/j.geomorph.2010.08.009

Andrews, I. J., Long, D., Richards, P. C., Thomson, A. R., Brown, S., Chesher, J. A., & McCormac, M. (1990). The geology of the Moray Firth (Vol. 3). London, UK: HMSO.

Austen, M., Warwick, R., & Ryan, K. (1993). Astomonema southwardorum sp. nov., a gutless nematode dominant in a methane seep area in the North Sea. Journal of the Marine Biological Association of the United Kingdom, 73(3), 627–634. https://doi.org/10.1017/S0025315400033166

Barry, M. A., Boudreau, B. P., & Johnson, B. D. (2012). Gas domes in soft cohesive sediments. Geology, 40(4), 379–382. https://doi.org/10.1130/G32686.1

Becker, L. W., Sejrup, H. P., Hjelstuen, B. O., Haflidason, H., & Dokken, T. M. (2018). Ocean-ice sheet interaction along the SE Nordic Seas margin from 35 to 15 ka BP. Marine Geology, 402, 99–117. https://doi.org/10.1016/j.margeo.2017.09.003

Berndt, C. (2005). Focused fluid flow in passive continental margins. Philosophical Transactions of the Royal Society of London A: Mathematical, Physical and Engineering Sciences, 363(1837), 2855–2871. https://doi.org/10.1098/rsta.2005.1666

Berndt, C., Elger, J., Böttner, C., Gehrmann, R., Karstens, J., Muff, S., et al. (2017). RV MARIA S. MERIAN Fahrtbericht/Cruise Report MSM63-PERMO, Southampton–Southampton (UK) 29.04.-25.05.2017.

Berndt, C., Jacobs, C., Evans, A., Gay, A., Elliott, G., Long, D., & Hitchen, K. (2012). Kilometre-scale polygonal seabed depressions in the Hatton Basin, NE Atlantic Ocean: Constraints on the origin of polygonal faulting. Marine Geology, 332, 126–133.

Böttner, C., Gross, F., Geersen, J., Crutchley, G. J., Mountjoy, J. J., & Krastel, S. (2018). Marine forearc extension in the Hikurangi margin: New insights from high-resolution 3-D seismic data. Tectonics, 37, 1472–1491. https://doi.org/10.1029/2017TC004906

Boudreau, B. P., Algar, C., Johnson, B. D., Croudace, I., Reed, A., Furukawa, Y., et al. (2005). Bubble growth and rise in soft sediments. Geology, 33(6), 517–520. https://doi.org/10.1130/G21259.1

Boudreau, B. P., Gardiner, B. S., & Johnson, B. D. (2001). Rate of growth of isolated bubbles in sediments with a diagenetic source of methane. Limnology and Oceanography, 46(3), 616–622. https://doi.org/10.4319/lo.2001.46.3.0616

Brothers, L. L., Kelley, J. T., Belknap, D. F., Barnhardt, W. A., Andrews, B. D., Legere, C., & Clarke, J. E. H. (2012). Shallow stratigraphic control on pockmark distribution in north temperate estuaries. Marine Geology, 329, 34–45.

Buckley, F. A. (2012). An early Pleistocene grounded ice sheet in the Central North Sea. Geological Society, London, Special Publications, 368, SP368–8(1), 185–209. https://doi.org/10.1144/SP368.8

Buckley, F. A. (2016). A glaciogenic sequence from the Early Pleistocene of the Central North Sea. Journal of Quaternary Science, 32(2), 145–168.

Caress, D. W., & Chayes, D. N. (2017). MB-system: Mapping the seafloor. Retrieved from https://www.mbari.org/products/researchsoftware/mb-system

Cartwright, J., Huuse, M., & Aplin, A. (2007). Seal bypass systems. AAPG Bulletin, 91(8), 1141–1166.

Chand, S., Crémière, A., Lepland, A., Thorsnes, T., Brunstad, H., & Stoddart, D. (2017). Long-term fluid expulsion revealed by carbonate crusts and pockmarks connected to subsurface gas anomalies and palaeo-channels in the central North Sea. Geo-Marine Letters, 37(3), 215–227. https://doi.org/10.1007/s00367-016-0487-x

Chen, X., & Slater, L. (2016). Methane emission through ebullition from an estuarine mudflat: 1. A conceptual model to explain tidal forcing based on effective stress changes. Water Resources Research, 52, 4469–4485. https://doi.org/10.1002/2015WR018058

Ciais, P., Sabine, C., Bala, G., Bopp, L., Brovkin, V., Canadell, J., et al. (2013). Carbon and other biogeochemical cycles. In Climate change 2013: The physical science basis. Contribution of Working Group I to the Fifth Assessment Report of the Intergovernmental Panel on Climate Change (pp. 465–570). UK and New York: Cambridge University Press.

Clayton, C. J., & Dando, P. R. (1996). Comparison of seepage and seal leakage rates. In D. Schumacher & M. A. Abrams (Eds.), Hydrocarbon Migration and Its Near-surface Expression: Outgrowth of the AAPG Hedberg Research Conference. Vancouver, British Columbia, April 24-28, 1994 (No. 66). AAPG.

Clayton, C. J., & Hay, S. J. (1994). Gas migration mechanisms from accumulation to surface. Bulletin of the Geological Society of Denmark, 41(1), 12–23.

Cole, D., Stewart, S. A., & Cartwright, J. A. (2000). Giant irregular pockmark craters in the Palaeogene of the outer Moray Firth basin, UK North Sea. Marine and Petroleum Geology, 17(5), 563–577. https://doi.org/10.1016/S0264-8172(00)00013-1

Croudace, I. W., Rindby, A., & Rothwell, R. G. (2006). ITRAX: Description and evaluation of a new multi-function X-ray core scanner. Geological Society, London, Special Publications, 267(1), 51–63. https://doi.org/10.1144/GSL.SP.2006.267.01.04

Dando, P. R., Austen, M. C., Burke, R. A. Jr., Kendall, M. A., Kennicutt, M. C., Judd, A. G., et al. (1991). Ecology of a North Sea pockmark with an active methane seep. Marine Ecology Progress Series, 70, 49–63. https://doi.org/10.3354/meps070049

Dean, J. F., Middelburg, J. J., Röckmann, T., Aerts, R., Blauw, L. G., Egger, M., et al. (2018). Methane feedbacks to the global climate system in a warmer world. Reviews of Geophysics, 56(1), 207–250. https://doi.org/10.1002/2017RG000559

Dickens, G. R. (2011). Down the rabbit hole: Toward appropriate discussion of methane release from gas hydrate systems during the Paleocene-Eocene thermal maximum and other past hyperthermal events. Climate of the Past, 7(3), 831–846. https://doi.org/10.5194/cp-7-831-2011

Domenico, S. N. (1977). Elastic properties of unconsolidated porous sand reservoirs. Geophysics, 42(7), 1339–1368. https://doi.org/10.1190/1.1440797

Erlenkeuser, H. (1979). Environmental effects on radiocarbon in coastal marine sediments. Berkeley, CA: University of California Press.

Etiope, G., Lassey, K. R., Klusman, R. W., & Boschi, E. (2008). Reappraisal of the fossil methane budget and related emission from geologic sources. Geophysical Research Letters, 35, L09307. https://doi.org/10.1029/2008GL033623

Field, M. E., & Jennings, A. E. (1987). Seafloor gas seeps triggered by a northern California earthquake. Marine Geology, 77(1–2), 39–51. https://doi.org/10.1016/0025-3227(87)90082-X

Flemings, P. B., Long, H., Dugan, B., Germaine, J., John, C. M., Behrmann, J. H., et al. (2008). Pore pressure penetrometers document high overpressure near the seafloor where multiple submarine landslides have occurred on the continental slope, offshore Louisiana, Gulf of Mexico. Earth and Planetary Science Letters, 269(3-4), 309–325. https://doi.org/10.1016/j.epsl.2007.12.005

Gafeira, J., Dolan, M., & Monteys, X. (2018). Geomorphometric characterization of pockmarks by using a GIS-based semi-automated toolbox. Geosciences, 8(5). https://doi.org/10.3390/geosciences8050154

Gafeira, J., & Long, D. (2015). Geological investigation of pockmarks in the Scanner Pockmark SCI area. JNCC Report, (570).

Gafeira, J., Long, D., & Diaz-Doce, D. (2012). Semi-automated characterisation of seabed pockmarks in the central North Sea. Near Surface Geophysics, 10(4), 303–314.

Gay, A., Lopez, M., Berndt, C., & Seranne, M. (2007). Geological controls on focused fluid flow associated with seafloor seeps in the Lower Congo Basin. Marine Geology, 244(1–4), 68–92. https://doi.org/10.1016/j.margeo.2007.06.003

Graham, A. G., Lonergan, L., & Stoker, M. S. (2010). Depositional environments and chronology of Late Weichselian glaciation and deglaciation in the central North Sea. Boreas, 39(3), 471–491.

Harrington, P. K. (1985). Formation of pockmarks by pore-water escape. Geo-Marine Letters, 5(3), 193–197. https://doi.org/10.1007/BF02281638

Hasiotis, T., Papatheodorou, G., Kastanos, N., & Ferentinos, G. (1996). A pockmark field in the Patras Gulf (Greece) and its activation during the 14/7/93 seismic event. Marine Geology, 130(3–4), 333–344. https://doi.org/10.1016/0025-3227(95)00131-X

Holmes, R. (1977). The quaternary geology of the UK sector of the North Sea between 56°N and 58°N. Report of the Institute of Geological Sciences, 77(14), 50–s51.

Hovland, M., Gardner, J. V., & Judd, A. G. (2002). The significance of pockmarks to understanding fluid flow processes and geohazards. Geofluids, 2(2), 127–136.

Hovland, M., Heggland, R., De Vries, M. H., & Tjelta, T. I. (2010). Unit-pockmarks and their potential significance for predicting fluid flow. Marine and Petroleum Geology, 27(6), 1190–1199. https://doi.org/10.1016/j.marpetgeo.2010.02.005

Hovland, M., & Irwin, H. (1989). Hydrocarbon leakage, biodegradation and the occurrence of shallow gas and carbonate cement (pp. 10–11). Stavanger, Norway. Apr: Norwegian Petroleum Society Conf. Shallow Gas and Leaky Reservoirs.

Hovland, M., & Judd, A. (1988). Seabed pockmarks and seepages: Impact on geology, biology, and the marine environment (p. 293). London: Graham & Trotman Ltd.

Hovland, M., & Sommerville, J. H. (1985). Characteristics of two natural gas seepages in the North Sea. Marine and Petroleum Geology, 2(4), 319–326. https://doi.org/10.1016/0264-8172(85)90027-3

Hubbert, M. K., & Willis, D. G. (1957). Mechanic of hydraulic fracturing. Trans. Soc. Pet. Eng. AIME1957 , 153–168.

Hustoft, S., Dugan, B., & Mienert, J. (2009). Effects of rapid sedimentation on developing the Nyegga pockmark field: Constraints from hydrological modeling and 3-D seismic data, offshore mid-Norway. Geochemistry, Geophysics, Geosystems, 10, Q06012. https://doi.org/10.1029/2009GC002409

Johnson, T. C., & Elkins, S. R. (1979). Holocene deposits of the northern North Sea evidence for dynamic control of their mineral and chemical composition. Geologie en Mijnbouw, 58(3), 353–366.

Judd, A., & Hovland, M. (2007). Seabed fluid flow: The impact on geology, biology and the marine environment. Cambridge, UK: Cambridge University Press.

Judd, A. G., Hovland, M., Dimitrov, L. I., Garcia Gil, S., & Jukes, V. (2002). The geological methane budget at continental margins and its influence on climate change. Geofluids, 2(2), 109–126. https://doi.org/10.1046/j.1468-8123.2002.00027.x

Judd, A. G., Long, D., & Sankey, M. (1994). Pockmark formation and activity, UK block 15/25, North Sea. Bulletin of the Geological Society of Denmark, 41(1), 34–49.

Karstens, J., & Berndt, C. (2015). Seismic chimneys in the Southern Viking Graben—Implications for palaeo fluid migration and overpressure evolution. Earth and Planetary Science Letters, 412, 88–100. https://doi.org/10.1016/j.epsl.2014.12.017

Karstens, J., Haflidason, H., Becker, L. W., Berndt, C., Rüpke, L., Planke, S., et al. (2018). Glacigenic sedimentation pulses triggered postglacial gas hydrate dissociation. Nature communications, 9(1), 635. https://doi.org/10.1038/s41467-018-03043-z

Kilian, R., Breuer, S., Behrmann, J. H., Baeza, O., Diaz-Michelena, M., Mutschke, E., et al. (2017). The Seno Otway pockmark field and its relationship to thermogenic gas occurrence at the western margin of the Magallanes Basin (Chile). Geo-Marine Letters, 38, 1–14.

King, L. H., & MacLean, B. (1970). Pockmarks on the Scotian shelf. Geological Society of America Bulletin, 81(10), 3141–3148. https://doi.org/10.1130/0016-7606(1970)81[3141:POTSS]2.0.CO;2

Koch, S., Berndt, C., Bialas, J., Haeckel, M., Crutchley, G., Papenberg, C., et al. (2015). Gas-controlled seafloor doming. Geology, 43(7), 571–574. https://doi.org/10.1130/G36596.1

Krämer, K., Holler, P., Herbst, G., Bratek, A., Ahmerkamp, S., Neumann, A., et al. (2017). Abrupt emergence of a large pockmark field in the German Bight, southeastern North Sea. Scientific reports, 7(1), 5150. https://doi.org/10.1038/s41598-017-05536-1

Linke, P., & Haeckel, M. (2018). Baseline study for the environmental monitoring of subseafloor CO2 storage operations. RV POSEIDON Fahrtbericht/Cruise Report POS518: GEOMAR Report, N. Ser. 040. GEOMAR Helmholtz-Zentrum für Ozeanforschung, Kiel (84 pp.). https://doi.org/10.3289/GEOMAR_REP_NS_40_2018

Long, D. (1992). Devensian late-glacial gas escape in the central North Sea. Continental Shelf Research, 12(10), 1097–1110. https://doi.org/10.1016/0278-4343(92)90071-Q

Long, D., Bent, A., Harland, R., Gregory, D. M., Graham, D. K., & Morton, A. C. (1986). Late Quaternary palaeontology, sedimentology and geochemistry of a vibrocore from the Witch Ground Basin, central North Sea. Marine Geology, 73(1–2), 109–123. https://doi.org/10.1016/0025-3227(86)90114-3

Løseth, H., Gading, M., & Wensaas, L. (2009). Hydrocarbon leakage interpreted on seismic data. Marine and Petroleum Geology, 26(7), 1304–1319. https://doi.org/10.1016/j.marpetgeo.2008.09.008

Løseth, H., Wensaas, L., Arntsen, B., Hanken, N. M., Basire, C., & Graue, K. (2011). 1000 m long gas blow-out pipes. Marine and Petroleum Geology, 28(5), 1047–1060. https://doi.org/10.1016/j.marpetgeo.2010.10.001

Maeck, A., DelSontro, T., McGinnis, D. F., Fischer, H., Flury, S., Schmidt, M., et al. (2013). Sediment trapping by dams creates methane emission hot spots. Environmental Science & Technology, 47(15), 8130–8137. https://doi.org/10.1021/es4003907

Maia, A. R., Cartwright, J., & Andersen, E. (2016). Shallow plumbing systems inferred from spatial analysis of pockmark arrays. Marine and Petroleum Geology, 77, 865–881. https://doi.org/10.1016/j.marpetgeo.2016.07.029

Mann, D. M., & Mackenzie, A. S. (1990). Prediction of pore fluid pressures in sedimentary basins. Marine and Petroleum Geology, 7(1), 55–65. https://doi.org/10.1016/0264-8172(90)90056-M

Karstens, J., & Berndt, C. (2015). Seismic chimneys in the Southern Viking Graben—Implications for palaeo fluid migration and overpressure evolution. Earth and Planetary Science Letters, 412, 88–100. https://doi.org/10.1016/j.epsl.2014.12.017

Karstens, J., Haflidason, H., Becker, L. W., Berndt, C., Rüpke, L., Planke, S., et al. (2018). Glacigenic sedimentation pulses triggered postglacial gas hydrate dissociation. Nature communications, 9(1), 635. https://doi.org/10.1038/s41467-018-03043-z

Kilian, R., Breuer, S., Behrmann, J. H., Baeza, O., Diaz-Michelena, M., Mutschke, E., et al. (2017). The Seno Otway pockmark field and its relationship to thermogenic gas occurrence at the western margin of the Magallanes Basin (Chile). Geo-Marine Letters, 38, 1–14.

King, L. H., & MacLean, B. (1970). Pockmarks on the Scotian shelf. Geological Society of America Bulletin, 81(10), 3141–3148. https://doi.org/10.1130/0016-7606(1970)81[3141:POTSS]2.0.CO;2

Koch, S., Berndt, C., Bialas, J., Haeckel, M., Crutchley, G., Papenberg, C., et al. (2015). Gas-controlled seafloor doming. Geology, 43(7), 571–574. https://doi.org/10.1130/G36596.1

Krämer, K., Holler, P., Herbst, G., Bratek, A., Ahmerkamp, S., Neumann, A., et al. (2017). Abrupt emergence of a large pockmark field in the German Bight, southeastern North Sea. Scientific reports, 7(1), 5150. https://doi.org/10.1038/s41598-017-05536-1

Linke, P., & Haeckel, M. (2018). Baseline study for the environmental monitoring of subseafloor CO2 storage operations. RV POSEIDON Fahrtbericht/Cruise Report POS518: GEOMAR Report, N. Ser. 040. GEOMAR Helmholtz-Zentrum für Ozeanforschung, Kiel (84 pp.). https://doi.org/10.3289/GEOMAR_REP_NS_40_2018

Long, D. (1992). Devensian late-glacial gas escape in the central North Sea. Continental Shelf Research, 12(10), 1097–1110. https://doi.org/10.1016/0278-4343(92)90071-Q

Long, D., Bent, A., Harland, R., Gregory, D. M., Graham, D. K., & Morton, A. C. (1986). Late Quaternary palaeontology, sedimentology and geochemistry of a vibrocore from the Witch Ground Basin, central North Sea. Marine Geology, 73(1–2), 109–123. https://doi.org/10.1016/0025-3227(86)90114-3

Løseth, H., Gading, M., & Wensaas, L. (2009). Hydrocarbon leakage interpreted on seismic data. Marine and Petroleum Geology, 26(7), 1304–1319. https://doi.org/10.1016/j.marpetgeo.2008.09.008

Løseth, H., Wensaas, L., Arntsen, B., Hanken, N. M., Basire, C., & Graue, K. (2011). 1000 m long gas blow-out pipes. Marine and Petroleum Geology, 28(5), 1047–1060. https://doi.org/10.1016/j.marpetgeo.2010.10.001

Maeck, A., DelSontro, T., McGinnis, D. F., Fischer, H., Flury, S., Schmidt, M., et al. (2013). Sediment trapping by dams creates methane emission hot spots. Environmental Science & Technology, 47(15), 8130–8137. https://doi.org/10.1021/es4003907

Maia, A. R., Cartwright, J., & Andersen, E. (2016). Shallow plumbing systems inferred from spatial analysis of pockmark arrays. Marine and Petroleum Geology, 77, 865–881. https://doi.org/10.1016/j.marpetgeo.2016.07.029

Mann, D. M., & Mackenzie, A. S. (1990). Prediction of pore fluid pressures in sedimentary basins. Marine and Petroleum Geology, 7(1), 55–65. https://doi.org/10.1016/0264-8172(90)90056-M

Mazzini, A., Svensen, H. H., Forsberg, C. F., Linge, H., Lauritzen, S. E., Haflidason, H., et al. (2017). A climatic trigger for the giant Troll pockmark field in the northern North Sea. Earth and Planetary Science Letters, 464, 24–34. https://doi.org/10.1016/j.epsl.2017.02.014

Mogollón, J. M., Dale, A. W., Fossing, H., & Regnier, P. (2012). Timescales for the development of methanogenesis and free gas layers in recently-deposited sediments of Arkona Basin (Baltic Sea). Biogeosciences, 9(5), 1915–1933. https://doi.org/10.5194/bg-9-1915-2012

Moss, J. L., Cartwright, J., Cartwright, A., & Moore, R. (2012). The spatial pattern and drainage cell characteristics of a pockmark field, Nile Deep Sea Fan. Marine and Petroleum Geology, 35(1), 321–336. https://doi.org/10.1016/j.marpetgeo.2012.02.019

Niemann, H., Elvert, M., Hovland, M., Orcutt, B., Judd, A., Suck, I., et al. (2005). Methane emission and consumption at a North Sea gas seep (Tommeliten area). Biogeosciences Discussions, 2(4), 1197–1241. https://doi.org/10.5194/bgd-2-1197-2005

Orsi, T. H., Werner, F., Milkert, D., Anderson, A. L., & Bryant, W. R. (1996). Environmental overview of Eckernförde bay, northern Germany. Geo-Marine Letters, 16(3), 140–147. https://doi.org/10.1007/BF01204501

Ottesen, D., Dowdeswell, J. A., & Bugge, T. (2014). Morphology, sedimentary infill and depositional environments of the Early Quaternary North Sea Basin (56–62 N). Marine and Petroleum Geology, 56, 123–146. https://doi.org/10.1016/j.marpetgeo.2014.04.007

Paull, C., Ussler Iii, W., Maher, N., Greene, H. G., Rehder, G., Lorenson, T., & Lee, H. (2002). Pockmarks off Big Sur, California. Marine Geology, 181(4), 323–335. https://doi.org/10.1016/S0025-3227(01)00247-X

Petrenko, V. V., Smith, A. M., Schaefer, H., Riedel, K., Brook, E., Baggenstos, D., et al. (2017). Minimal geological methane emissions during the Younger Dryas–Preboreal abrupt warming event. Nature, 548(7668), 443–446. https://doi.org/10.1038/nature23316

Pfannkuche, O. (2005). Cruise Report ALKOR 259: Methane Cycle at Shallow Gaseous Sediments in the Central North Sea. GEOMAR, Kiel (42 pp.).

Plaza-Faverola, A., Vadakkepuliyambatta, S., Hong, W. L., Mienert, J., Bünz, S., Chand, S., & Greinert, J. (2017). Bottom-simulating reflector dynamics at Arctic thermogenic gas provinces: An example from Vestnesa Ridge, offshore west Svalbard. Journal of Geophysical Research: Solid Earth, 122, 4089–4105. https://doi.org/10.1002/2016JB013761

Räss, L., Simon, N. S., & Podladchikov, Y. Y. (2018). Spontaneous formation of fluid escape pipes from subsurface reservoirs. Scientific Reports, 8(1), 11116.

Rea, B. R., Newton, A. M., Lamb, R. M., Harding, R., Bigg, G. R., Rose, P., et al. (2018). Extensive marine-terminating ice sheets in Europe from 2.5 million years ago. Science Advances, 4(6), eaar8327). https://doi.org/10.1126/sciadv.aar8327

Reinardy, B. T., Hjelstuen, B. O., Sejrup, H. P., Augedal, H., & Jørstad, A. (2017). Late Pliocene-Pleistocene environments and glacial history of the northern North Sea. Quaternary Science Reviews, 158, 107–126. https://doi.org/10.1016/j.quascirev.2016.12.022

Römer, M., Riedel, M., Scherwath, M., Heesemann, M., & Spence, G. D. (2016). Tidally controlled gas bubble emissions: A comprehensive study using long-term monitoring data from the NEPTUNE cabled observatory offshore Vancouver Island. Geochemistry, Geophysics, Geosystems, 17, 3797–3814. https://doi.org/10.1002/2016GC006528

Rose, P., Byerley, G., Vaughan, O., Cater, J., Rea, B. R., Spagnolo, M., & Archer, S. (2016). Aviat: A Lower Pleistocene shallow gas hazard developed as a fuel gas supply for the Forties Field. In Geological society, London, petroleum geology conference series (Vol. 8, pp. PGC8–PGC16). London: Geological Society of London.

Saunois, M., Bousquet, P., Poulter, B., Peregon, A., Ciais, P., Canadell, J. G., et al. (2016). The global methane budget 2000–2012. Earth System Science Data (Online), 8(2), 697–751. https://doi.org/10.5194/essd-8-697-2016

Schneider von Deimling, J., Linke, P., Schmidt, M., & Rehder, G. (2015). Ongoing methane discharge at well site 22/4b (North Sea) and discovery of a spiral vortex bubble plume motion. Marine and Petroleum Geology, 68, 718–730. https://doi.org/10.1016/j.marpetgeo.2015.07.026

Seeberg-Elverfeldt, J., Schlüter, M., Feseker, T., & Kölling, M. (2005). Rhizon sampling of porewaters near the sediment-water interface of aquatic systems. Limnology and Oceanography: Methods, 3(8), 361–371.

Sejrup, H. P., Aarseth, I., Ellingsen, K. L., Reither, E., Jansen, E., Løvlie, R., et al. (1987). Quaternary stratigraphy of the Fladen area, central North Sea: A multidisciplinary study. Journal of Quaternary science, 2(1), 35–58. https://doi.org/10.1002/jqs.3390020105

Sejrup, H. P., Haflidason, H., Aarseth, I., King, E., Forsberg, C. F., Long, D., & Rokoengen, K. (1994). Late Weichselian glaciation history of the northern North Sea. Boreas, 23(1), 1–13.

Sejrup, H. P., Hjelstuen, B. O., Nygård, A., Haflidason, H., & Mardal, I. (2014). Late Devensian ice-marginal features in the central N orth Sea–processes and chronology. Boreas, 44(1), 1–13.

Sommer, S., Linke, P., Pfannkuche, O., Schleicher, T., Schneider, J., Reitz, A., et al. (2009). Seabed methane emissions and the habitat of frenulate tubeworms on the Captain Arutyunov mud volcano (Gulf of Cadiz). Marine Ecology Progress Series, 382, 69–86. https://doi.org/10.3354/meps07956

Stewart, M. A., & Lonergan, L. (2011). Seven glacial cycles in the middle-late Pleistocene of northwest Europe: Geomorphic evidence from buried tunnel valleys. Geology, 39(3), 283–286. https://doi.org/10.1130/G31631.1

Stoker, M. S., Balson, P. S., Long, D., & Tappin, D. R. (2011). An overview of the lithostratigraphical framework for the Quaternary deposits on the United Kingdom continental shelf. Nottingham, UK: British Geological Survey.

Stoker, M. S., & Bent, A. J. (1987). Lower Pleistocene deltaic and marine sediments in boreholes from the central North Sea. Journal of Quaternary Science, 2(2), 87–96. https://doi.org/10.1002/jqs.3390020202

Stoker, M. S., & Long, D. (1984). A relict ice-scoured erosion surface in the central North Sea. Marine Geology, 61(1), 85–93. https://doi.org/10.1016/0025-3227(84)90109-9

Svensen, H., Planke, S., Malthe-Sørenssen, A., Jamtveit, B., Myklebust, R., Eidem, T. R., & Rey, S. S. (2004). Release of methane from a volcanic basin as a mechanism for initial Eocene global warming. Nature, 429(6991), 542–545. https://doi.org/10.1038/nature02566

Talukder, A. R. (2012). Review of submarine cold seep plumbing systems: Leakage to seepage and venting. Terra Nova, 24(4), 255–272. https://doi.org/10.1111/j.1365-3121.2012.01066.x

Wegener, G., Shovitri, M., Knittel, K., Niemann, H., Hovland, M., & Boetius, A. (2008). Biogeochemical processes and microbial diversity of the Gullfaks and Tommeliten methane seeps (Northern North Sea). Biogeosciences Discussions, 5(1), 971–1015. https://doi.org/10.5194/bgd-5-971-2008

White, J. E. (1975). Computed seismic speeds and attenuation in rocks with partial gas saturation. Geophysics, 40(2), 224–232. https://doi.org/10.1190/1.1440520

Whiticar, M. J. (2000). Can stable isotopes and global budgets be used to constrain atmospheric methane budgets? In Atmospheric methane (pp. 63–85). Berlin, Heidelberg: Springer.

Yu, Y., Kelley, C. L., & Mardanova, I. M. (2015). U.S. patent no. 9,105,075. Washington, DC: U.S. patent and Trademark Office.

4. Seismic imaging of an active fluid conduit below Scanner Pockmark, Central North Sea

Bettina Schramm [a], Christian Berndt [a], Anke Dannowski [a], Christoph Böttner [b], Jens Karstens[a], Judith Elger [a]

a GEOMAR Helmholtz Centre for Ocean Research Kiel, Wischhofstraße 1-3, Kiel, Germany

b Christian-Albrechts-Universit¨at zu Kiel, Institute of Geosciences, Christian-Albrechts-Platz 4, Kiel, Germany

Abstract

Subsurface CO_2 storage is a key strategy to reduce greenhouse gas emission, but leakage of CO_2 along natural fluid pathways may affect storage formation integrity. However, the internal structure and the physical properties of these focused fluid conduits are poorly understood. Here, we present a three-dimensional seismic velocity model of an active fluid conduit beneath the Scanner Pockmark in the Central North Sea, derived from ocean-bottom seismometer data. We show that the conduit, which manifests as a pipe structure in seismic data, is separated into two parts. The upper part, extending to 260 m depth, i.e. 110 m below the seafloor, is characterised by seismic velocities up to 100 m/s slower than the surrounding strata. The deeper part is characterized by a 50 m/s seismic velocity increase compared to background velocity. We suggest that the upper part of the pipe structure represents a network of open fractures, partly filled with free gas, while the reason for the velocity increase in the lower part remains speculative. These observations suggest that active pipes can be internally heterogeneous with some intervals probably being open fluid pathways and other intervals being closed. This study highlights the complexity in evaluating focused fluid conduits and the necessity of their detailed assessment when selecting CO_2 storage sites.

Keywords: P wave velocity 3D travel-time tomography Fluid flow Scanner pockmark Ocean-bottom seismometer Wide-angle seismic

4.1. Introduction

The increasing concentration of greenhouse gases in the atmosphere is one of the major challenges of the 21st century. The Intergovernmental Panel on Climate Change (IPCC) identified carbon dioxide capture and storage (CCS) as a key component of mitigation strategies to reduce CO_2 concentration in the atmosphere in order to limit global warming to 1.5 ◦C by the end of this century (IPCC, 2018). Saline aquifers and depleted hydrocarbon reservoirs in the North Sea Basin are the most promising storage formations for the industrial-scale implementation of CCS in Europe (Haszeldine, 2009).

In the North Sea, natural fluid migration structures are commonplace, and manifest in seismic reflection data as pipes and chimneys (Karstens and Berndt, 2015). Pipes and chimneys are the seismic expression of vertical, strata-cutting, focused fluid conduits with chaotic seismic facies and reflections with increased or reduced seismic amplitude (Moss and Cartwright, 2010; Løseth et al., 2011; Andresen, 2012; Cartwright and Santamaria, 2015; Karstens and Berndt, 2015). Both are columnar and can reach from a few tens of meters in diameter to more than 2 km in diameter. We follow the Karstens et al. (2019) nomenclature of calling pipes those structures that are comparably narrow and have sharp vertical boundaries while calling chimneys those with an irregular boundary to the host rock, but we acknowledge that there are different usages of these terms in the literature. Based on the multi-channel seismic (MCS) data presented in this study and the results of Böttner et al. (2019), we will label the focused fluid conduit beneath the Scanner Pockmark as a pipe structure in the following.

Generally, the formation of these pathways is believed to be controlled by overpressure-induced hydrofracturing of an impermeable cap rock (Hubbert and Willis, 1957; Clayton and Hay, 1994; Cathles et al., 2010). However, it is unclear how long these structures remain open for fluid migration after their formation (Karstens and Berndt, 2015). Pipes and chimneys may represent a direct connection from deep reservoirs to the seafloor and feed active seafloor seeps (Hovland and Sommerville, 1985; Schneider von Deimling et al., 2007; Løseth et al., 2011). The internal structure and the physical properties of pipe and chimney structures are poorly understood as they are generally avoided during drilling operations and have rarely been the subject of detailed geophysical studies. Notable exceptions are chimney structures above the Tommeliten Alpha Field (North Sea), where seismic shear wave experiments, numerical simulations and wellbore data revealed a gas-filled fracture network (Granli et al., 1999; Arntsen et al., 2007) and in the Nyegga Region (Norwegian Sea), where the abundance of gas hydrates in the conduit was studied using seismic tomography (Plaza-Faverola et al., 2010).

4. Seismic imaging of an active fluid conduit below Scanner Pockmark, Central North Sea

Seismic reflection profiling is a powerful tool to identify vertical heterogeneities such as pipe structures. However, conventional reflection seismic surveys have significant shortcomings in imaging the internal structure of focused fluid conduits, in differentiating between real geological structures and imaging artefacts in such settings (Løseth et al., 2011; Karstens and Berndt, 2015), and they cannot be used to reconstruct their hydraulic properties. Seismic velocity models may provide valuable information about the internal structure of focused fluid conduits. They can provide information on the type of pore fill, e.g. gas or aqueous fluids, and qualitative information on porosity as it correlates with seismic velocity. Seismic anisotropy and lateral velocity changes that correlate with seismic reflection patterns may also constrain the hydraulic permeability. To derive high-resolution seismic velocity models, we have conducted a three-dimensional (3D) ocean-bottom seismometer (OBS) experiment. The survey layout provided for shots from all directions and long offsets between the shots and the recording instruments. Overall, the data have a good signal-noise ratio.

Seismic forward modelling of OBS data allows to construct detailed velocity models (Zelt, 1998; Plaza-Faverola et al., 2010) as long as the data are sampled densely enough to resolve the velocity variations in the subsurface. Previous studies have mainly used sparse data along 2D seismic lines resulting in rather sparse and undersampled models that may easily be affected by erroneous assignment of arrivals because of side reflections. In this study, we use a very densely sampled 3D OBS data set covering a wide range of offsets and azimuths to derive seismic velocity anomalies within and around the fluid conduit beneath the Scanner Pockmark (Figure 4.1). The objective is to put these derived velocity anomalies into context with other geological and geophysical information to elucidate the functioning of fluid pathways. Furthermore, we investigate the role of free gas in the formation of pipe structures and constrain the source of ascending fluids beneath the Scanner Pockmark.

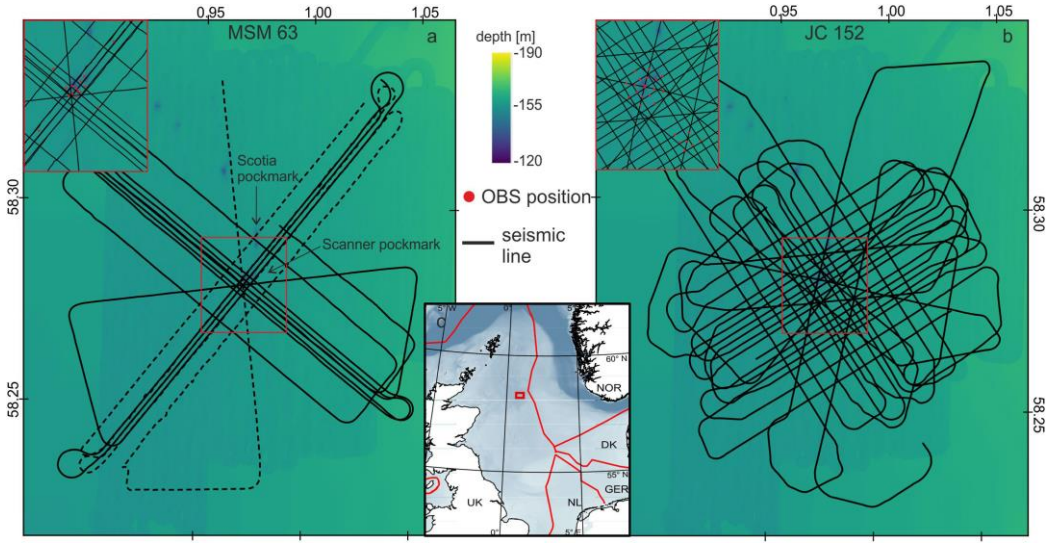

Figure 4.1: Location of the Scanner Pockmark. Map of the seismic experiment and the bathymetry of the Scanner Pockmark, showing the seismic lines (P1000: dashed line; P2000: line drawn through) and the OBS deployment sites (red dots) of research cruises a) MSM 63 and b) JC152. c) Location of the study area block 15/25b in the Central North Sea. The bathymetric data were acquired during this study, while gaps and the surrounding area were filled with bathymetric data from Emodnet-Bathymetry (Schapp and Schmitt, 2017).

4.2. Geological setting

The Scanner Pockmark Field is located within the Witch Ground Graben (Figure 4.2), which developed from the Triassic to the early Cretaceous as part of the North Sea Basin failed rift system (Judd et al., 1994; Glennie, 1998). The basin was a major centre of deposition during the late Jurassic and in the early Cretaceous, as well as during the Quaternary (Judd et al., 1994). Clays with interbedded sandstones and limestones dominate the Paleogene and Neogene sequences. The shallow sediments of the Early Pleistocene Aberdeen Ground Formation show evidence for subglacial, glaciomarine and marine deposition (Sejrup et al., 1987; Reinardy et al., 2017; Rea et al., 2018). The top of the Aberdeen Ground Formation is a regional glacial unconformity, which corresponds to the advance of grounded ice sheets into the North Sea Basin during the Mid-Pleistocene (Figure 4.2; Reinardy et al., 2017). Many tunnel valleys incise into the Aberdeen Ground Formation and into the overlying Ling Bank Formation, representing different phases of glacial erosion and deposition with poorly constrained ages. The upper Mid to Late Pleistocene sediments consist of the Coal Pit, Swatchway and Witch Ground Formations (Figure 4.2; Böttner et al., 2019). The Coal Pit Formation consists of glacial tills with hard dark grey to brownish-grey, muddy, pebbly sands or sandy muds deposited between Marine Isotope Stage (MIS) 3 and 6 (Andrews et al., 1990; Graham et al., 2010; Stoker et al., 2011). The

Swatchway Formation comprises silty to sandy clays with rare pebbles; these possibly proximal glaciomarine sediments were deposited during MIS 2 and 3. The Witch Ground Formation consists of finely laminated glaciomarine sediments, which were deposited during MIS 1 and 2 (Figure 4.2; Stoker et al., 2011).

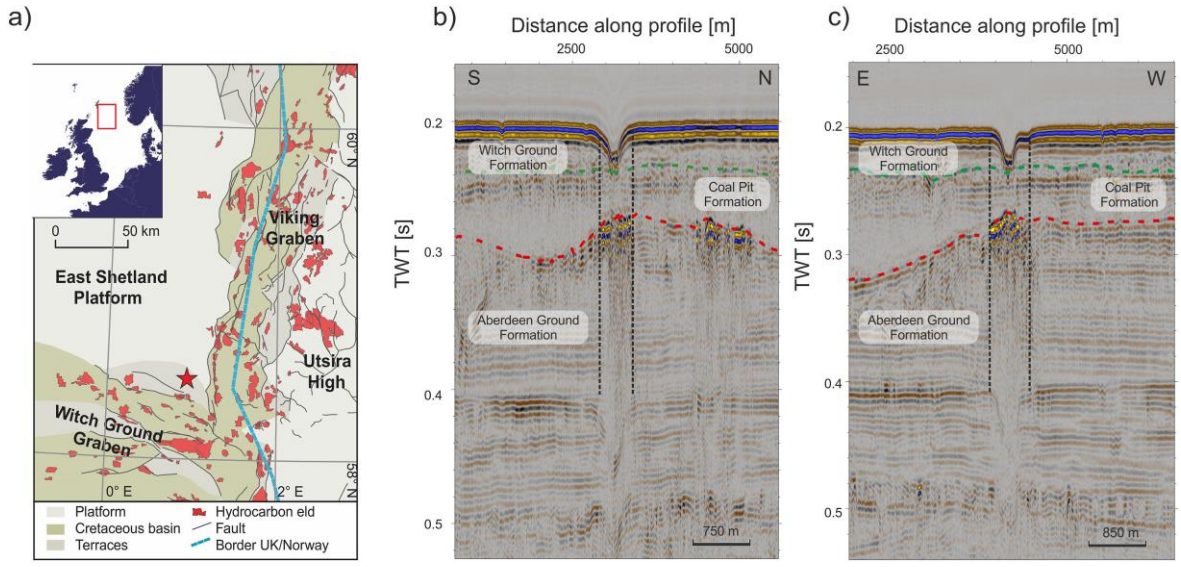

Figure 4.2: Geological setting. a) Geological map of the Central North Sea with the location of the study area (red star). Seismic sections across the Scanner Pockmark b) in South-North and c) East-West direction with the main stratigraphic units.

The entire North Sea Basin is affected by focused flow of hydrocarbons from deep thermogenic sources, strongly mixed with microbially-formed shallow methane (Karstens and Berndt, 2015; Chand et al., 2017). Two types of pockmarks occur in the study area (Hovland et al., 2010; Böttner et al., 2019): smaller pockmarks (0.9–3.1 m deep, 26–140 m long, and 14–57 m wide) that only affect the post-glacial successions, and unusually large pockmarks (>6 m deep, >250 m long, and >75 m wide). The Scanner and Scotia pockmarks (Figure 4.1) are unusually large examples of this second class (Judd et al., 1994; Gafeira and Long, 2015, Böttner et al., 2019). Exploration-type 3D reflection seismic data show almost circular seismic amplitude anomalies below the pockmarks down to a depth of several hundred meters (Böttner et al., 2019). These anomalies do not match the distribution of free gas in the shallow subsurface suggesting that they are not seismic artefacts but caused by real geological structures (Figure 4.2). Persistently observed acoustic anomalies in the water column inside and above the pockmark have be interpreted suggest that the pockmarks continuously release deeply-sourced methane that is advected through the pipe structures (Böttner et al., 2019).

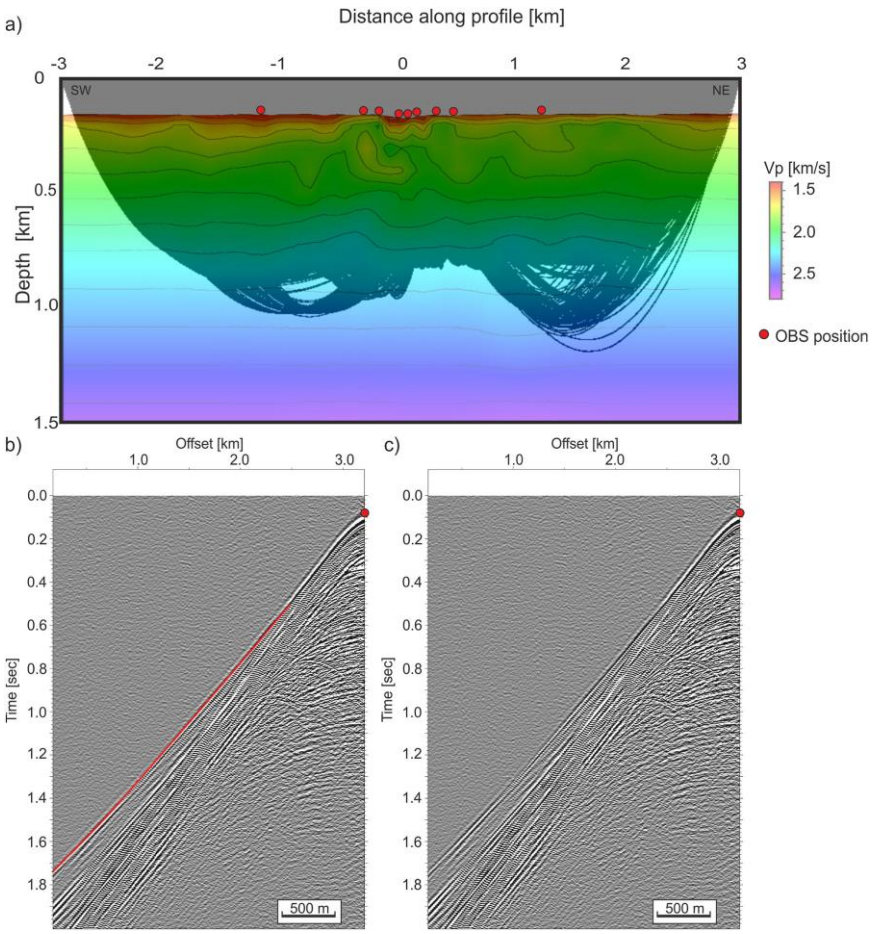

Figure 4.3: Data example. a) Velocity distribution along a SW-NE profile crossing the Scanner Pockmark. The displayed ray paths (black lines) show the zone were the velocity model is well constrained. The red circles mark the OBS positions. b) Seismic section recorded by OBS with the interpreted refractions (red line) used for modelling with FAST and c) without the interpreted refractions.

4.3. Data

We used three different data sets: newly acquired high-resolution 3D OBS and 2D MCS data, and an industry 3D MCS dataset ("CNS MegaSurveyPlus") provided by PGS, Oslo. During research cruise MSM63 in April/May 2017 on board R/V Maria S. Merian, 15 OBSs were deployed around and inside the Scanner Pockmark. The spacing of the OBSs varied between 100 m and 1000 m in water depths between 150 and 170 m (Figure 4.1). A GI-gun array consisting of two 210-inch3-GI-guns (G = 105 in3/I = 105 in3) served as the seismic source. The pressure was kept at 210 bar and the array was towed at 2 m water depth, which provided a frequency band of 15–500 Hz. The shot interval was 10 s (survey P1000). The OBSs recorded continuously for 9 day at a sampling rate of 500 Hz. In general, the data quality was excellent (Figure 4.3). Processing of these data included a minimum phase Ormsby band-pass-filter (15-

20- 200-300 Hz). Due to strong currents, instruments drifted away from their dropping position, on average 30 m. The largest drift was 70 m. The relocation procedure minimized the least square misfit between the observed direct wave arrival and the synthetic arrival calculated based on the bathymetric data collected during the MSM63 survey. For the relocation we used the average velocity of the water column, 1.48 km/s, which was measured by a sound velocity profile at the beginning and at the end of the cruise. The quality of the 3D tomography depends on accurate OBS locations. In this study we were able to obtain an accuracy of about 1 m.

The OBS data were complemented by 2D MCS data (survey P2000) that were recorded during the same research cruise (Figure 4.1a). For the acquisition of the 2D reflection seismic data we used a 150 m-long streamer consisting of 96 channels with a 1.5625 m group spacing. We used the same seismic source and pressure, but the shot interval was reduced to 5 s. Processing of the MCS data included geometry and delay corrections, static corrections, common mid-point binning to 1.5625 m and bandpass filtering with corner frequencies of 25, 45, 420, and 500 Hz. A normal move-out correction with a constant velocity of 1.48 km/s (measured by a water sound velocity probe) was applied and the data were stacked and then migrated using a 2D Stolt algorithm. To compare the reflection seismic image with the velocity model derived from tomographic inversion of the OBS data, we have converted the 2D seismic data from two-way travel time to depth using a single velocity depth function (Table 1). This conversion does not account for lateral velocity variations, but as these velocity variations and layer thickness variations are small, the assumption of a simple velocity field results in a vertical error of less than 10 m at a depth of 300 m. This mismatch is far below the 50 m forward node interval for the tomographic inversion and hence accurate enough for the comparison.

During the same summer season, a second OBS dataset was acquired during RRS James Cook cruise JC152. An array of 25 OBSs was deployed within and around the pockmark and on a reference site southeast of the Scanner Pockmark (Figure 4.1b). The source also consisted of a GI-Gun array of two 210-inch3-GI-guns (G = 105in3/I = 105 in3). It was towed at 2 m water depth behind the vessel with the same configuration as that during MSM63. The shot interval was 8 s and the data were recorded at a sampling rate of 4000 Hz.

The 3D industry seismic data covers more than 22,000 km2 of the central northern North Sea, including the Scanner Pockmark, down to 1.5 s two-way travel time (TWT). This 3D pre-stack time-migrated dataset has a vertical resolution of approximately 20 m with an inline and crossline spacing of 12.5 m (see Böttner et al., 2019).

MCS (depth [m])	MCS (TWT [s])	Interval Velocity (m/s)
0	0	
149	0.2	1490
300	0.37	1798
500	0.56	2073
1000	1	2299
2000	1.63	3155

Table 4.1: Single velocity depth function for converting the 2D seismic data to depth.

4.4. 3D seismic traveltime tomography

First-arrival time tomography aims to reconstruct the P-wave velocities of the Earth's interior. First-arrival times of seismic shots calculated through an initial model are compared to the observed travel times, based on the shortest ray path. The initial model is modified until the best possible fit between model predictions and observed data is found.

To build a detailed 3D seismic velocity model based on the collected OBS data, we used FAST (First Arrival Seismic Tomography), a 2D and 3D first arrival travel time tomography package, including forward modelling and inversion (Zelt and Barton, 1998). The 3D model space is 1.5 km deep and covers an area with a lateral extent of 6 km × 6 km with the Scanner Pockmark at the centre. The grid node spacing for the forward modelling is 10 m in all directions. The grid cell size of the inversion is 100 m in x and y direction and 100 m in depth. Our starting model consists of two layers: the first layer is the water column and has a constant seismic velocity of 1.48 km/s based on sound velocity probe measurements. The seafloor interface and the water velocity were kept fixed during tomographic inversion for the seismic velocities within the subsurface. As FAST is influenced by the initial model it was important to check for the influence of the choice of the second layer, i.e. from the seafloor to the base of the model domain, velocity on the inversion result. Therefore, we tested 100 initial models in which we introduced up to ± 100 m/s seismic velocity anomalies on a regional North Sea background model (Figure 4.4). We analyzed the inversion results and chose a starting model (in the following called the preferred model) that is characterized by small $\chi 2$ values and which is producing similar anomalies to the majority of other starting models. In the following we only discuss seismic velocity anomalies that are produced after 10 iterations and that are independent on the starting model.

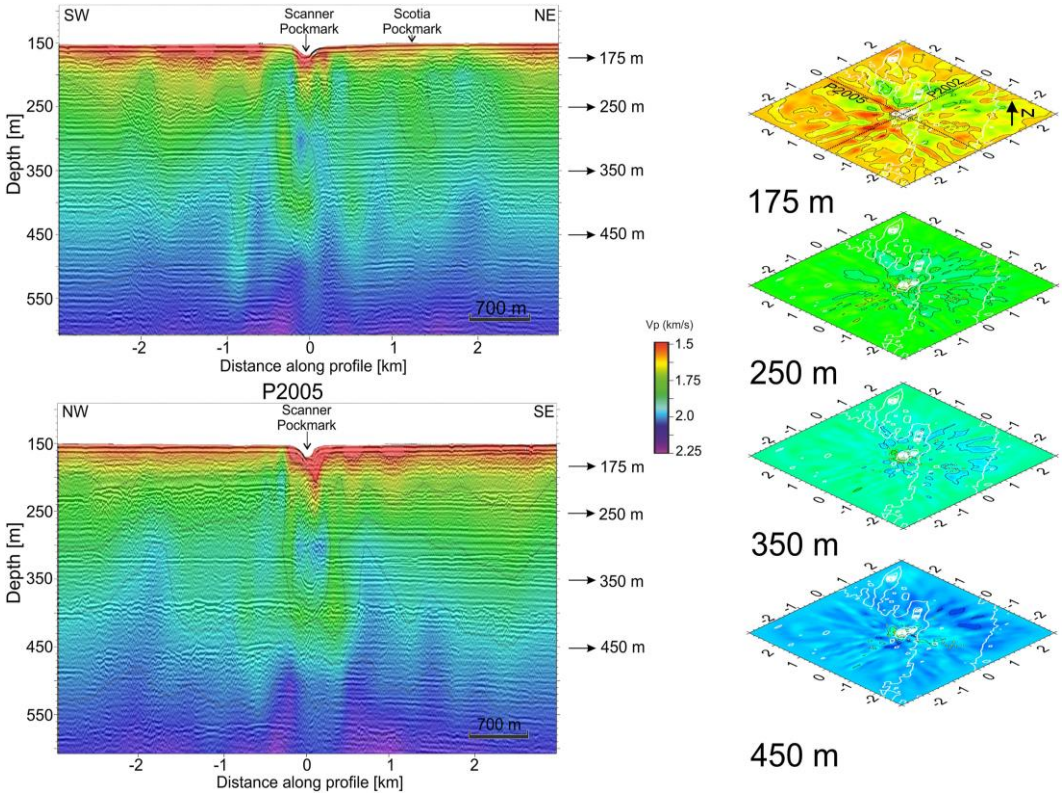

Figure 4.4: Average of 100 inversion runs of the seismic tomography with a random created initial model. Velocity distribution a) in SW-NE direction and b) in NW-SE direction. Each section shows a clear negative seismic velocity anomaly beneath the Scanner pockmark. c) Depth slices of the seismic velocity field for 175 m, 250 m, 350 m and 450 m depth. The white isolines image the seafloor topography.

We picked the seismic first arrivals with the seismic interpretation software IHS Kingdom Suite. Errors resulting from automatic picking were corrected manually. Reflections below the seafloor were difficult to identify due to superposition with multiples below ~300 ms TWT, the effects of blanking inside the pipe, and the ghost signal from the airgun. We assigned the picks an uncertainty of 8 ms. This yielded a $\chi 2$ of 1.0029 and a root-mean-square (RMS) misfit of 8.0115 ms in the best-fitting model, which converged within 10 iterations (initial RMS misfit of 19 ms). The misfits are consistent for the different instruments. Overall, our dataset contains more than 180,000 P-wave first arrival picks with a maximum offset of 3 km.

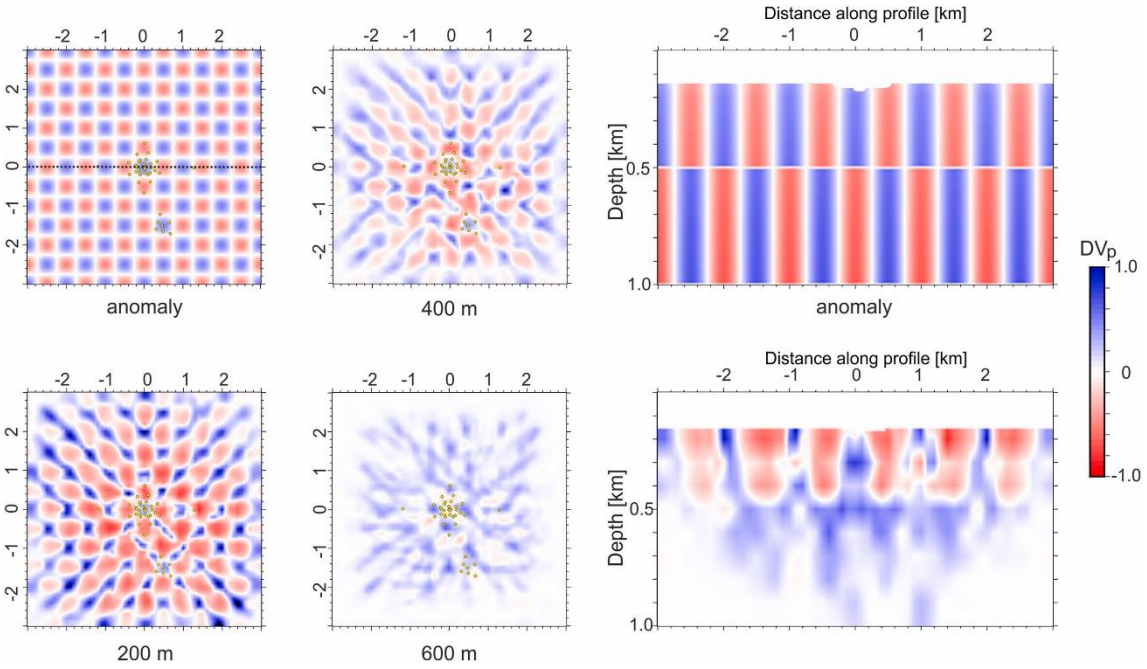

Figure 4.5: Checkerboard test with a synthetic anomaly of 0.5 × 0.5 × 0.5 km in size and a velocity perturbation of 20%. The yellow dots mark the OBS locations.

In order to avoid misinterpretation of structures appearing in the travel time tomography, the lateral resolution of the velocity must be known (Zelt, 1998). Our study region is strongly affected by focused flow of hydrocarbons from deep thermogenic sources, mixed with microbially formed shallow methane, which cause seismic velocity anomalies (Karstens and Berndt, 2015; Chand et al., 2017). To determine the limits of lateral resolution we have conducted a checkerboard test (Figure 4.5) and several characteristic tests (Figure 4.6) (Zelt, 1998; Leveque et al., 1993; Schmelzbach et al., 2008). The checkerboard test was run with a checkerboard pattern of 0.5 × 0.5 × 0.5 km size and 20% of velocity anomalies compared to the preferred model. The results of the checkerboard test show that our tomographic setup allows the recovery of the injected anomalies below the Scanner pockmark and up to a depth of 500 m (Figure 4.5). Satisfactory inversion statistics ($\chi 2$ = 1.8658 and RMS = 12.86795 ms) were obtained at the end of the 5th iterations. All first-arrival tomographies have a lambda of 50 (Zelt, 1998).

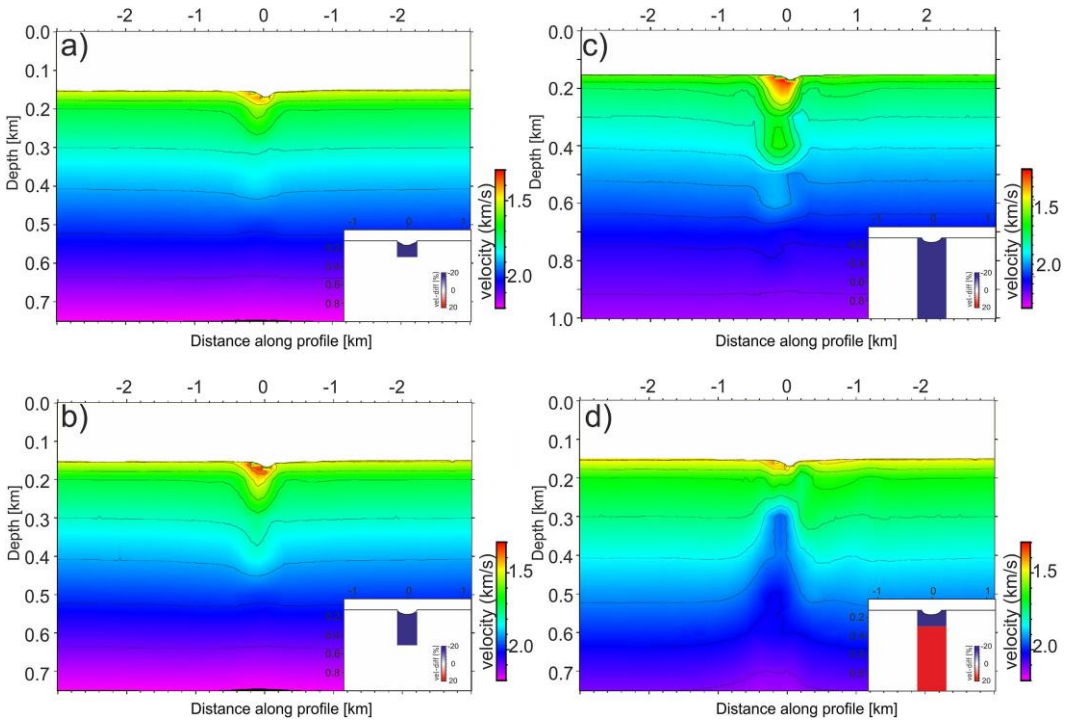

Figure 4.6: Characteristic test with different initial models beneath the Scanner Pockmark. The injected anomaly (insets) is a velocity difference of −20% compared to the initial model of our preferred model. The injected negative anomalies extend to depths of a) 300 m, b) 500 m, c) 1000 m and d) 300 m with a positive anomaly below.

In addition to the checkerboard test, we carried out several characteristic tests. Characteristic tests contain anomalies of similar amplitude as the real one but with different sizes and shapes (Haslinger et al., 1999; Husen et al., 2000). For these tests we introduced single velocity anomalies with a velocity decrease of 20% directly starting beneath the Scanner Pockmark and reaching down to 300, 500, and 1000 m and one with a 20% decreased seismic velocity in the top 300 m and a 20% velocity increase from 300 to 1000 m depth. For these models the rays were calculated by ray tracing and used for tomographic inversion. We analysed the results after 10 iterations. The velocity model for the characteristic tests is based on the width and shape of the seismic anomaly below Scanner Pockmark as observed in the 3D reflection seismic data (Böttner et al., 2019) and has a velocity anomaly which is circular and has a diameter of 200 m. Again, the background model is based on our preferred model. The characteristic tests show that a velocity anomaly beneath the Scanner pockmark can be well resolved by our tomographic setup down to 750 m depth. With greater depth the resolution decreases. These smearing effects are typical for strong lateral velocity variation, when smoothing is applied during the inversion. In addition, the characteristic tests show that no low velocity zones are created as a result of the tomographic inversion. Thus, the inverted velocities allow us to

differentiate between pipe segments with decreased seismic velocities that may reflect increased gas content or disrupted sediments and pipe segments with increased seismic velocities, e.g. due to cementation or different lithologies.

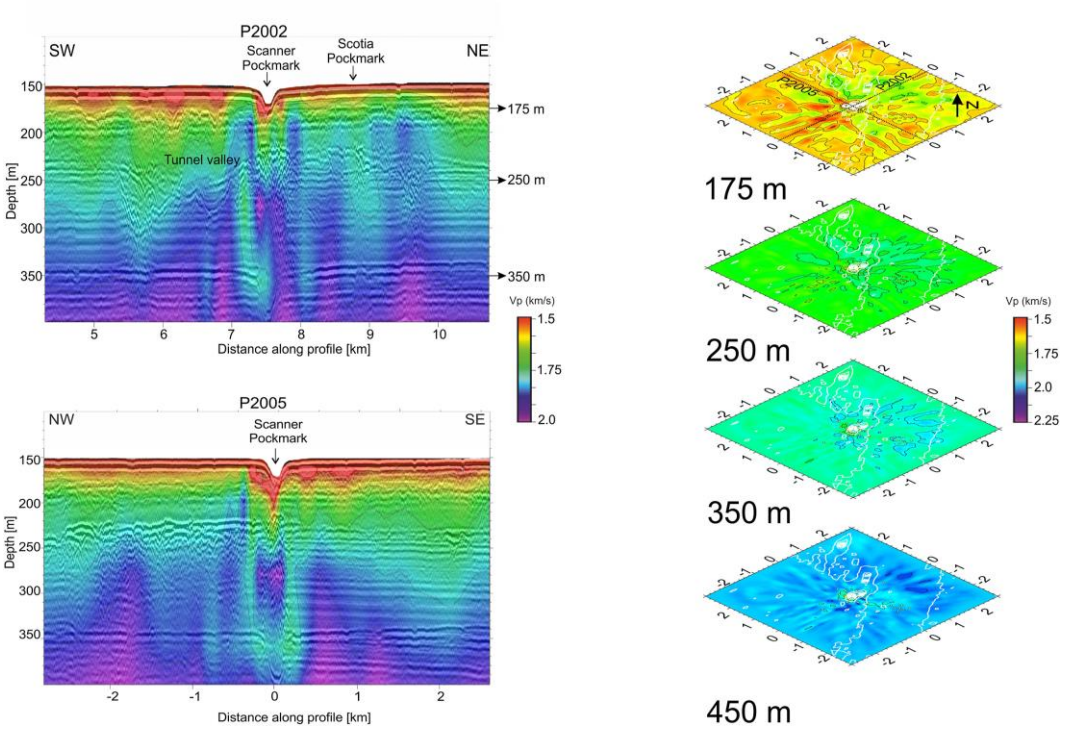

Figure 4.7: Velocity distribution. a) in SW-NE direction and b) in NW-SE direction. Each section shows a clear negative seismic velocity anomaly beneath the Scanner pockmark. c) Depth slices of the seismic velocity field for 175 m, 250 m, 350 m and 450 m depth. The white isolines image the seafloor topography, one isoline is every 2 m.

4.5. Results

4.5.1. P-wave velocity model from FAST

The results of the first arrival travel time tomography show considerable lateral velocity variations in the area beneath the Scanner Pockmark and the surrounding area. The region beneath the pockmark is characterized by a decrease in seismic P-wave velocity (Vp) inside the pipe structure compared to the area surrounding it (Figure 4.7). From the seafloor down to 260 m depth (in the following all depth values refer to depth below sea level), the velocity inside of the pipe is up to 10% lower than in the surrounding background. For example, at 200 m depth the velocity drops from 1.7 km/s outside the pipe structure to 1.55 km/s inside. The velocity decrease coincides with a high-amplitude seismic anomaly in the 2D and 3D MCS data and the velocity anomaly is approximately 370 m wide in all directions. The location, the width and the magnitude of the velocity anomaly are robust for all starting models, i.e. it is reproduced by the

inversion regardless of the chosen starting model and for different subsets of data. Below the Upper Aberdeen Ground Formation, the negative velocity anomaly beneath the Scanner Pockmark turns into a positive velocity anomaly that stretches from about 280 m depth to about 500 m below the sea surface (Figure 4.7c). It is robust in the sense that it is produced by inversion of most starting models. The shape of the anomaly is nearly circular and becomes wider with greater depth, while the velocity difference is up to 0.05 km/s. The deeper part of the pipe structure, which is characterized by a positive seismic velocity anomaly, is surrounded by an area of lower seismic velocities (Figure 4.7b).

Below 260 m depth, the inverted models for all starting models consistently show a velocity drop of about 0.1 km/s for the pipe structure compared to the surrounding formation. These low velocities occur approximately 500 m NW and the SE of the pipe (Figure 4.7b). Average velocities of 1.7–1.8 km/s characterize the tunnel valley in the Southwest of Scanner Pockmark. Only the most deeply incised part of the tunnel valley further in the SW is associated with velocities of 1.8–1.85 km/s. Seismic velocity decreases laterally to 1.8 km/s at 300 m next to the Scotia pockmark to the NE of the Scanner Pockmark (Figure 4.7a). Overall, the results of the travel time tomography show significant seismic velocity variations but the limited extent of the model is insufficient to determine a general background seismic velocity for the Quaternary sediments. Small-scale seismic velocity anomalies are ambiguous, but the low velocity anomalies below Scanner Pockmark and Scotia Pockmark are robust, including the high velocity anomaly below the Scanner Pockmark from 280 m to ~500 m depth and the surrounding, about 400 m-wide zones of slightly reduced velocities (Figure 4.8a). Possibly the offset of the anomaly below Scotia Pockmark is a result of the survey layout with fewer ray paths sampling the subsurface in this region.

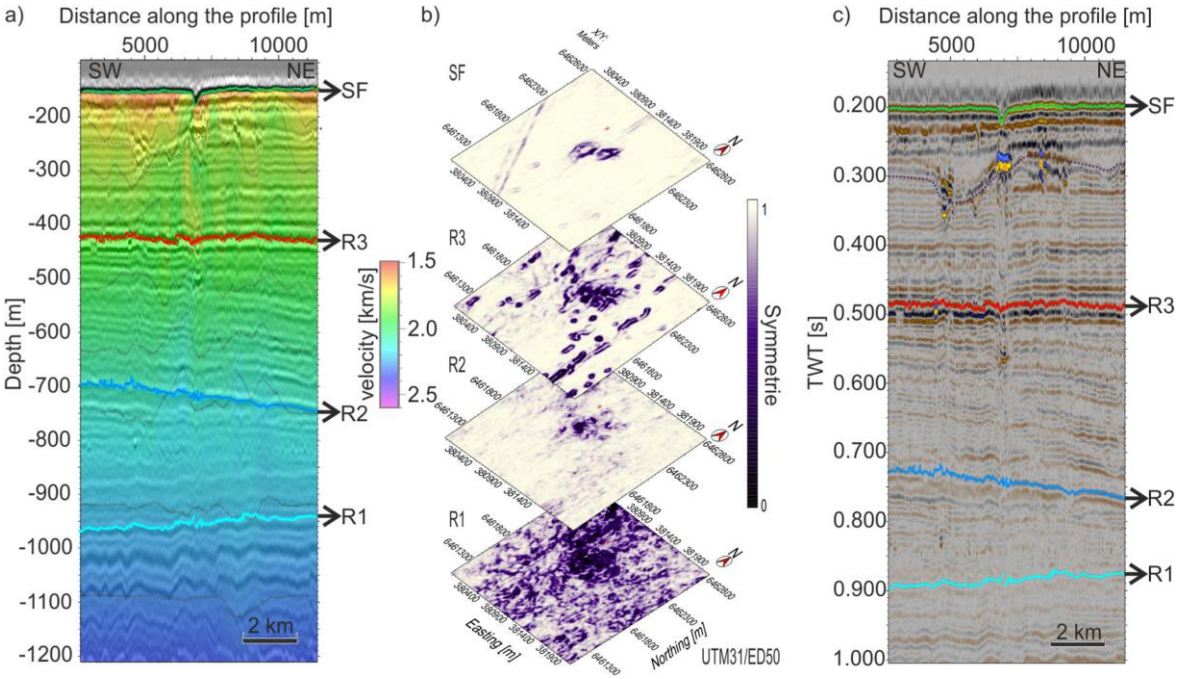

Figure 4.8: Seismic section at the Scanner Pockmark. a) MCS data on which the Vp model has been overlain (profile P2002). b) 3D seismic attribute analysis based on conventional 3D seismic data. The similarity attribute is displayed for four stratigraphic horizons. c) MCS data (profile P2002) with respective seismic horizons with seismic stratigraphy from Böttner et al. (2019).

4.5.2. Correlation between MCS and tomography

To quantify the dimensions of the pipe structure beneath the Scanner Pockmark, we compare the 2D MCS data with the results of the travel time tomography. Beneath the pockmark, the MCS data show amplitude anomalies with zones of dimmed reflections and bright spots at different depth levels, e.g. at 280 ms and 350 ms TWT. The MCS data show increased seismic amplitudes at the lowest glacial incision surface below the Scanner and Scotia pockmarks and along the northern rim of the tunnel valley. In some places (Figure 4.8c), these high-amplitude reflectors have reversed polarity with respect to the seafloor reflection (i.e. reflector at 280 ms TWT depth and 7000 m along the profile). The anomalies are limited to an interval of 20–30 ms TWT and they are commonly underlain by chaotic seismic facies. We used the seismic similarity attribute derived from the 3D seismic amplitude data to identify the spatial extent of these amplitude anomalies and their subsurface expression (Figure 4.8b). The symmetry attribute is a post-stack, post-migration structural feature detection tool based on a 3D log-Gabor filter array (Yu et al., 2015) provided by the IHS Kingdom software. The horizon slices through the similarity volume show the pipe structure as an almost circular amplitude anomaly with a constant diameter at different depth levels. The comparison of the lateral extent of the pipe structure in the two data sets reveals a consistent discrepancy: the area of high amplitudes

in the 3D MCS data is 280 m wide in diameter compared to a width of the velocity anomaly in the OBS tomography models of about 370 m (compare Figures 4.7c and 4.8b).

The 3D MSC seismic data provide important insights into the regional geological setting. High amplitude patches (bright spots) with polarity reversals occur at most stratigraphic highs between the adjacent tunnel valleys that incise the Ling Bank Formation. These anomalies correspond to the low velocities in the tomographic models. A detailed seismic stratigraphic analysis (Böttner et al., 2019) showed that the seismic amplitude anomalies are the seismic expression of shallow free gas accumulations. The 3D seismic data also provide more details on the lateral variation of the tunnel valleys. The deeply incised tunnel valley SW of the Scanner Pockmark is a major structure that can be traced for several tens of kilometres. However, the vicinity of Scanner is different compared to the rest of the tunnel valley as it broadens from about 500 m to about 2500 m with a terrace close to Scanner Pockmark and a deeply incised part only at the SW edge of the tunnel valley (Figure 4.8).

4.6. Discussion

4.6.1. Seismic artefact or geological feature

Seismic interpretation of fluid flow structures, especially when they are vertically orientated, can be ambiguous (Kristensen and Huuse, 2012; Karstens and Berndt, 2015). Further analysis of the pipe structure interpreted underneath the Scanner Pockmark thus requires an assessment to what extent the geophysical observations support the presence of a real geological structure and to what extent the observations are the result of imperfect geophysical imaging. Often, effects like blanking beneath gas accumulations, migration artefacts due to insufficiently resolved lateral velocity variations at shallow depth or bad seismic traces may lead to misinterpretation as seismic pipes (Karstens and Berndt, 2015). Böttner et al. (2019) conclude in their discussion about the limitations of 3D seismic imaging that a geological structure at Scanner exists because the anomaly in the seismic data does not coincide spatially with the seismic evidence of free gas in the subsurface. Furthermore, the structure is associated with distinct seismic observations such as downlaps that cannot be explained by seismic wave propagation artefacts. Our seismic tomography results show a distinct and starting-model-independent seismic velocity anomaly directly beneath the Scanner Pockmark. The reduced seismic velocities down to a depth of about 260 m coincide with the high amplitude, reverse polarities in the 3D seismic data that are commonly reported as evidence for free gas (Figures 4.7 and 4.8). We observe a similar low-velocity anomaly close to the Scotia Pockmark (Figure 4.7a). The seismic velocity below Scotia Pockmark is reduced down to at least 300 m. Thus,

the entire anomaly beneath Scotia Pockmark may be the result of a free gas accumulation at the base of the post-glacial sediments. Due to the nature of the seismic tomography, it is quite likely that the velocity field will be smoothed and smeared out. Therefore, we attribute the mismatch between the width of the pipe structure in the 3D seismic data, i.e. 280 m, and the width of the tomography-derived velocity anomaly, i.e. 370 m, to smoothing caused by the tomographic inversion. Importantly, the velocity anomalies beneath the two pockmarks differ at depths greater than 280 m. There is a change to higher velocities underneath the Scanner Pockmark from 280 m below the surface to about 500 m. This high velocity anomaly for Scanner Pockmark is robust in the sense that almost all tomographic inversion results for different starting models show it and that the inversion result is independent of the choice of OBS ruling out picking or positioning errors. Therefore, we interpret the velocity increase to be caused by a real geological structure with different physical properties than the surrounding rocks. This interpretation matches the findings of 3D seismic attribute analysis (Böttner et al., 2019). The circular shape of the velocity anomaly (Figure 4.7) supports the interpretation of this geological structure as a pipe structure. The tomographic results show that the anomaly is circular beneath the Scanner Pockmark, like other reported pipe and chimney structures (Cartwright et al., 2007; Løseth et al., 2009; Plaza-Faverola et al., 2010; Karstens and Berndt, 2015). It does not follow the shape of the tunnel valley or the distribution of free gas mapped in the 3D seismic data. A similar positive velocity anomaly may exist under Scotia Pockmark, but it is not produced by the inversion possibly because of a more limited ray coverage.

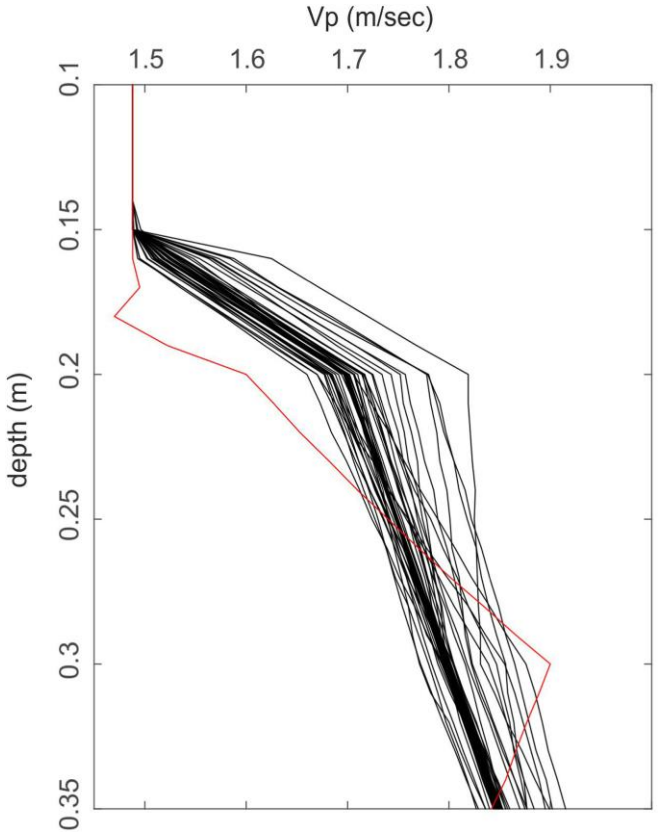

Figure 4.9: Velocity distribution. The lines show Vp against depth. Each line corresponds to one point every 1 km across the model. The red line highlights the seismic velocity in the centre of the model, where the Scanner Pockmark is located.

4.6.2. Nature and size of the pipe structure beneath the Scanner Pockmark

Generally, the detailed structure of pipes is poorly understood and may be variable (Cartwright et al., 2007; Gay et al., 2012). In some cases, pipe structures are associated with a positive velocity anomaly caused by diagenetic overprinting of the host rock, e.g. due to carbonate cementation within fractures (Garten et al., 2008) or gas hydrate accumulation (Plaza-Faverola et al., 2010). In other cases, the velocity anomaly is negative. Arntsen et al. (2007) proposed that such a negative velocity anomaly can be caused by a network of open fractures and ascending gas, which reduces the seismic velocities. In case of the Scanner Pockmark, the smooth 3D tomography shows up to 10% reduced seismic velocity, compared to the surrounding rocks, down to a depth of about 260 m (Figures 4.8 and 4.9). The observation that there is no consistent low velocity anomaly at greater depth suggests that the gas that seeps at the seafloor originates from the accumulation of biogenic methane at the base of the glacial sediments about 50–110 m below the seafloor. Especially, with the observed seepage of gas from the seafloor (Judd et al., 1994) there is little doubt that the high amplitude, reversed-polarity reflections and the low seismic velocities are the result of free gas. It is possible that the gas is hosted in fracture networks that would further reduce the seismic velocity, but the

resolution of our tomography does not allow to quantify the amount of free gas within the pipe structure. The tomographic inversion not only smooths the velocity field spatially but it also smooths the absolute velocity values. Therefore, it is likely that the seismic velocity within parts of the pipe is even more reduced or increased than 10%. The diameter of the pipe-related velocity anomaly in the inversion model is up to 370 m wide, i.e. almost twice as wide than the Scanner Pockmark. As discussed above the broad width may be due to smearing as strong differences of the velocity are smoothed during the inversion. On the other hand, characteristic tests of various possible pipe geometries show that imaging of smaller and shorter pipes is limited by the vertical resolution of the tomography. From this we conclude that the pipe structure must have at least the size of the Scanner Pockmark as smaller structures could not be resolved using our experiment setup (Figure 4.1). Thus, the tomographic modelling is broadly consistent with the interpretation of the 3D seismic data that resulted in a pipe diameter of approximately 280 m (Böttner et al., 2019). The MCS data show bright spots in depths of 0.28 s and 0.35 s TWT, which correspond to glacial sediments deposited during Mid-Pleistocene (Reinardy et al., 2017). Assuming that the 3D seismic data-derived width of the pipe structure is correct, the larger pipe width in the tomographic model than in the 3D seismic data suggests that the true seismic velocity within the pipe may be as low as 150 m/s lower than the surroundings, assuming that the velocity anomaly scales with the width of the pipe.

The interpretation of the deeper part of the pipe structure is more ambiguous. The high-velocity anomaly at the centre of the pipe structure is surrounded by several-hundred-meter wide zones of decreased seismic velocities. Using characteristic tests (Figure 4.6), we can rule out that this observation is caused by topographic effects related to the pronounced seafloor depressions. There is an uncertainty in the lateral extent of the pipe from MCS data and the resolution of the tomography decreases with depth. As a consequence, it is unclear whether the observed velocity anomaly (fast in the centre and slow in the surrounding area) is primarily caused by geological processes leading to an increase of seismic velocity in the centre of the pipe or processes causing a velocity decrease at the edges or the surrounding of the structure. It may be possible that the velocity decrease is a result of gas filled fractures (similar to the upper part of the pipe), which have formed by ascending fluids as the result of clogging of the pipe itself. However, it appears more likely that the low velocity zones represent the undisturbed sediments outside the pipe and the seismic anomaly is the result of increased seismic velocity inside the pipe structure. At Nyegga, gas hydrates cause an increase of seismic velocities within the local pipe structures (Plaza-Faverola et al., 2010). However, the Scanner Pockmark area is outside the gas hydrate stability zone. Alternatively, it is possible that the velocity increases because of calcite cements

in the fracture network. This process has been observed in boreholes (Garten et al., 2008) and in onshore outcrops (Nielsen and Hanken, 2002). It is also possible that the pipe provides a pathway for methane to escape from the sediments, thus increasing the average velocity. In both cases, this would suggest that a fracture network in the pipe structure is not open at present. Nevertheless, even closed fracture networks that open and close episodically may still pose a lower resistance to fluid migration than the surrounding rocks that have not been affected by fluid migration. Although geophysical inversion method commonly result in an overshoot around an anomaly with the opposite sign to the core of the anomaly, the checkerboard tests and the characteristic tests do not show an overshoot (Figures 4.5 and 4.6) suggesting that these anomalies are real and not an artefact due to the FAST algorithm. However, a final explanation for high velocities in the lower parts of the pipe can probably only be derived from drilling this part of the structure.

4.7. Conclusion

From the results of our high-resolution seismic experiment, we conclude that the pipe structure observed in seismic reflection data beneath the Scanner Pockmark is a real geological feature.

The low velocity anomaly in the upper part of the pipe corroborates the presence of free gas and we propose that it is hosted in a network of open fractures in the upper part of the pipe structure.

The nature of the deeper part of the pipe structure is less clear. The trend towards increased seismic velocities in the deep part of the pipe structure may be the result of calcite precipitation or an overprinting of the original sediment texture by fluid migration.

Overall, our study shows that a single pipe structure can be characterized by both positive and negative seismic velocity anomalies at different depths. This strongly suggests different physical properties at different depths along the pipe structure without further complications such as the presence or absence of gas hydrate accumulations (Plaza-Faverola et al., 2010). The hydraulic properties of the pipe structure are likely different than the properties of the surrounding sediments that have not been affected by fluid migration. This may be of relevance for the large-scale implementation of the geological storage of CO_2 in the North Sea Basin. Therefore, we suggest that a detailed, multi-method assessment of specific fluid conduits should be an essential part of CO_2 storage site selection.

With the available seismic data it is not possible to directly derive the hydraulic permeability of pipe structures. The lesson that the evaluation of the OBS data was severely hampered by

seafloor multiples, a surface ghost, and the dimming of reflectors due to gas suggests that future geophysical investigations of pipe structures should also involve detailed tomographic inversion of surface-towed 3D seismic data with long offset streamers. This may get around the multiple and ghost problems and can make use of deeper reflections to generate velocity fields with higher resolution. Also, tomographic inversion of P-to-S converted wave arrivals may provide further insights as it would not be affected by the dimming effect of free gas and because it would provide information on the shear strength of the rocks insight the pipe structure which may reveal further indications for fracturing. Regardless, a thorough assessment of pipe structure permeability in the Central North Sea will require dedicated drilling campaigns that penetrate deeper than the base of the glacial and postglacial deposits.

Data availability

Access to 2D seismic and OBS seismic data through Pangaea data repository (https://doi.org/10.1029/2018GC008068/https://doi.
pangaea.de/10.1594/PANGAEA.915,968/https://doi.pangaea.
de/10.1594/PANGAEA.932,200). Access to 3D seismic data through PGS data library (https://www.pg s.com/data-library/europe/nw-europe/north-sea/cns). Access to Bathymetry data through EMODnet Digital Bathymetry (DTM; http://doi. org/10.12770/c7b53704-999d-4721-b1a3-04ec60c87238).

Declaration of competing interest

The authors declare that they have no known competing financial interests or personal relationships that could have appeared to influence the work reported in this paper.

Acknowledgements

We thank the masters and the crews of R/V Maria S. Merian cruise MSM63 and RRS James Cook cruise JC152. We thank an anonymous reviewer and the editor for their comments helping to improve the manuscript. We thank Gaye Bayrakci, Jonathan M. Bull, Timothy J. Henstock and Tim Minshull for the support during the process of writing this manuscript. We thank PGS, Oslo for access to the MegaSurveyPlus 3D seismic data set. Access to 3D seismic data through PGS data library. (https://www.pgs.com/data-library/europe/nw-europe/north-sea /cns). We are grateful to IHS Markit for providing the KingdomSuite interpretation software within the academic licensing program. We thank the EMODnet Bathymetry Consortium (2016) for

access to the EMODnet Digital Bathymetry (DTM; http://doi.org/10.12770/c7b5370 4-999d-4721-b1a3-04ec60c87238). This research is part of the STEMM-CCS project, which has received funding from the European Union's Horizon 2020 research and innovation program under grant agreement 654462. Additional funding for JC152 was provided by NERC grant NE/ N016130/1.

References

Andresen, K.J., 2012. Fluid flow features in hydrocarbon plumbing systems: what do they tell us about the basin evolution? Mar. Geol. 332, 89–108. https://doi.org/10.1016/j.margeo.2012.07.006

Andrews, I.J., Long, D., Richards, P.C., Thomson, A.R., Brown, S., Chesher, J.A., McCormac, M., 1990. The Geology of the Moray Firth, vol. 3. HMSO.

Arntsen, B., Wensaas, L., Løseth, H., Hermanrud, C., 2007. Seismic modeling of gas chimneys. Geophysics 72 (5), SM251–SM259. https://doi.org/10.1190/1.2749570

Böttner, C., Berndt, C., Reinardy, B.T.I., Geersen, J., Karstens, J., Bull, J.M., Callow, B.J., Lichtschlag, A., Schmidt, M., Elger, J., Schramm, B., Haeckel, M., 2019. Pockmarks in the Witch Ground basin, central north sea. G-cubed 20 (4), 1698–1719. https://doi.org/10.1029/2018GC008068

Cartwright, J., 2007. The impact of 3D seismic data on the understanding of compaction, fluid flow and diagenesis in sedimentary basins. J. Geol. Soc. 164 (5), 881–893. https://doi.org/10.1144/0016-76492006-143.

Cartwright, J., Santamaria, C., 2015. Seismic characteristics of fluid escape pipes in sedimentary basins: implications for pipe genesis. Mar. Petrol. Geol. 65, 126–140. https://doi.org/10.1016/j.marpetgeo.2015.03.023.

Cathles, L.M., Su, Z., Chen, D., 2010. The physics of gas chimney and pockmark formation, with implications for assessment of seafloor hazards and gas sequestration. Mar. Petrol. Geol. 27, 82–91. https://doi.org/10.1016/j.marpetgeo.2009.09.010

Chand, S., Cremiere, A., Lepland, A., Thorsnes, T., Brunstad, H., Stoddart, D., 2017. Long-term fluid expulsion revealed by carbonate crusts and pockmarks connected to subsurface gas anomalies and palaeo-channels in the central North Sea. Geo Mar. Lett. 37 (3), 215–227. https://doi.org/10.1007/s00367-016-0487-x

Clayton, C.J., Hay, S.J., 1994. Gas migration mechanisms from accumulation to surface. Bull. Geol. Soc. Den. 41, 12–23.

Gafeira, J., Long, D., 2015. Geological Investigation of Pockmarks in the Scanner Pockmark SCI Area. JNCC Report, 570.

Garten, P., Houbiers, M., Planke, S., Svensen, H., 2008. Vent Complex at Heidrun, vol. 2008. SEG Technical Program Expanded Abstracts, pp. 809–813. https://doi.org/10.1190/1.3063767

Gay, A., Mourgues, R., Berndt, C., Bureau, D., Planke, S., Laurent, D., Gautier, S., Lauer, C., Loggia, D., 2012. Anatomy of a fluid pipe in the Norway Basin: initiation, propagation and 3D shape. Mar. Geol. 332–334, 75–88. https://doi.org/10.1016/j.margeo.2012.08.010

Glennie, K.W., 1998. Petroleum geology of the north sea: basic concepts and recent advances. https://doi.org/10.1002/9781444313413. Fouth Edition.

Graham, A.G., Lonergan, L., Stoker, M.S., 2010. Depositional environments and chronology of Late Weichselian glaciation and deglaciation in the central North Sea. Boreas 39 (3), 471–491. https://doi.org/10.1111/j.1502-3885.2010.00144.x

Granli, J.R., Arntsen, B., Sollid, A., Hilde, E., 1999. Imaging through gas-filled sediments using marine shear-wave data. Geophysics 64 (3), 659–992. https://doi.org/10.1190/1.1444576

Haslinger, F., Kissling, E., Ansorge, J., Hatzfeld, D., Papadimitriou, E., Karakostas, V., Makropoulos, K., Kahle, G., Peter, Y., 1999. 3-D crustal structure from local earthquake tomography around the Golf of Arta (Ionian-region, NW Greece). Tectonophysics 304, 201–218. https://doi.org/10.1016/S0040-1951(98)00298-4

Haszeldine, R.S., 2009. Carbon capture and storage: how green can black Be? Science 325 (5948), 1647–1652, 25 Sep. 2009. https://doi.org/10.1126/science.1172246

Hovland, M., Sommerville, J.H., 1985. Characteristics of two natural gas seepages in the North Sea. Mar. Petrol. Geol. 2 (4), 319–326. https://doi.org/10.1016/0264-8172(85)90027-3

Hovland, M., Heggland, R., De Vries, M.H., Tjelta, T.I., 2010. Unit-pockmarks and their potential significance for predicting fluid flow. Mar. Petrol. Geol. 27 (6), 1190–1199. https://doi.org/10.1016/j.marpetgeo.2010.02.005

Hubbert, M.K., Willis, D.G., 1957. Mechanic of hydraulic fracturing. Transactions of Society of Petroleum Engineers of AIME 210 (1957), 153–168. https://doi.org/10.2118/686-G

Husen, S., Kissling, E., Flueh, E., 2000. Local earthquake tomography of shallow subduction in north Chile: a combined onshore and offshore study. J. Geophys. Res. 155, 11–32. https://doi.org/10.1029/2000JB900229

IPCC, 2018. Summary for policymakers. In: Masson-Delmotte, V., Zhai, P., P¨ortner, H.- O., Roberts, D., Skea, J., Shukla, P.R. (Eds.), Global Warming of 1.5◦C: an IPCC Special Report on the Impacts of Global Warming of 1.5◦C above Pre-industrial Levels and Related Global Greenhouse Gas Emission Pathways, in the Context of Strengthening the Global Response to the Threat of Climate Change, Sustainable Development, and Efforts to Eradicate Poverty. Intergovernmental Panel on Climate Change, Geneva.

Judd, A.G., Long, D., Sankey, M., 1994. Pockmark formation and activity, UK block 15/ 25, North Sea. Bull. Geol. Soc. Den. 41 (1), 34–49.

Karstens, J., Berndt, C., 2015. Seismic chimneys in the Southern Viking Graben–Implications for palaeo fluid migration and overpressure evolution. Earth Planet Sci. Lett. 412, 88–100. https://doi.org/10.1016/j.epsl.2014.12.017

Karstens, J., Müller, P., Berndt, C., Patruno, S., 2019. Deep-seated focused fluid migration as indicator for hydrocarbon leads in the East Shetland Platform. North Sea Province. https://doi.org/10.1144/SP494-2019-26

Kristensen, T.B., Huuse, M., 2012. Multistage erosion and infill of buried Pleistocene tunnel valleys and associated seismic velocity effects. Geol. Soc. Spec. Publ. 368, 159–172. https://doi.org/10.1144/SP368.15.

Leveque, J., Rivera, L., Wittlinger, G., 1993. On the use of the checker-board test to assess the resolution of tomographic inversions. Geophys. J. Int. 115 (1), 313–318. October 1993. Løseth, H., Gading, M., Wensaas, L., 2009. Hydrocarbon leakage interpreted on seismic data. Mar. Petrol. Geol. 26 (7), 1304–1319. https://doi.org/10.1111/j.1365-246X.1993.tb05605.x

Løseth, H., Wensaas, L., Arntsen, B., Hanken, N.-M., Basire, C., Graue, K., 2011. 1000-m long gas blow-out pipes. Mar. Petrol. Geol. 28 (5), 1047–1060. Moss, J.L., Cartwright, J.A., 2010. The spatial and temporal distribution of pipe formation, offshore Namibia. Mar. Petrol. Geol. 27 (6), 1216–1234. https://doi.org/ 10.1016/j.marpetgeo.2009.12.013. https://doi.org/10.1016/j.marpetgeo.2010.10.001

Nielsen, J.K., Hanken, N., 2002. Late Permian carbonate concentration in the marine siliciclastic sediments of the Ravnefjeld Formarion, East Greenland. Geology of Greenland Survey Bulletin 191, 126–132. https://doi.org/10.34194/ggub.v191.5140

Plaza-Faverola, A., Westbrook, G.K., Ker, S., Exley, R.J.K., Gailer, A., Minshull, T.A., Broto, K., 2010. Evidence from three-dimensional seismic tomography for a substantial accumulation of gas hydrate in a fluid-escape chimney in the Nyegga pockmark field, offshore Norway. J. Geophys. Res.: Solid Earth 115. Issue B8. https://doi.org/10.1029/2009JB007078

Rea, B.R., Newton, A.M., Lamb, R.M., Harding, R., Bigg, G.R., Rose, P., Buckley, F., 2018. Extensive marine-terminating ice sheets in Europe from 2.5 million years ago. Science advances 4 (6), eaar8327. https://doi.org/10.1126/sciadv.aar8327

Reinardy, B.T., Hjelstuen, B.O., Sejrup, H.P., Augedal, H., Jørstad, A., 2017. Late Pliocene-Pleistocene environments and glacial history of the northern North Sea. Quat. Sci. Rev. 158, 107–126. https://doi.org/10.1016/j.quascirev.2016.12.022

Schmelzbach, C., Zelt, C.A., Juhlin, C., Carbonell, R., 2008. P- and SV-velocity structure of the South Portuguese Zone fold-and-thrust belt, SW Iberia, from traveltime tomography. Geophys. J. Int. 175 (2), 689–712. November 2008. https://doi.org/10.1111/j.1365-246X.2008.03937.x

Schneider von Deimling, J., Brockhoff, J., Greinert, J., 2007. Flare imaging with multibeam systems: data processing for bubble detection at seeps. G-cubed 8 (6). https://doi.org/10.1029/2007GC001577

Sejrup, H.P., Aarseth, I., Ellingsen, K.L., Reither, E., Jansen, E., Løvlie, R., Stoker, M., 1987. Quaternary stratigraphy of the Fladen area, central North Sea: a multidisciplinary study. J. Quat. Sci. 2 (1), 35–58. https://doi.org/10.1002/jqs.3390020105

Stoker, M.S., Balson, P.S., Long, D., Tappin, D.R., 2011. An Overview of the Lithostratigraphical Framework for the Quaternary Deposits on the United Kingdom Continental Shelf.

Yu, Y., Kelley, C.L., Mardanova, I.M., 2015. U.S. Patent No. 9,105,075. U.S. patent and Trademark Office, Washington, DC.

Zelt, C.A., 1998. Lateral velocity resolution from three-dimensional seismic refraction data. Geophysical Journal of Geophysical Research 135, 1101–1112. https://doi.org/10.1046/j.1365-246X.1998.00695.x

Zelt, C.A., Barton, P.J., 1998. Three-dimensional seismic refraction tomography: a comparison of two methods applied to data from the Faeroe Basin. J. Geophys. Res.: Solid EarthVolume 103. Issue B4. https://doi.org/10.1029/97JB03536

5. Characterization of an active gas chimney using seismic velocity analysis, west-Svalbard Margin

Bettina Schramm[1,2], Sunny Singhroha[3,4], Anke Dannowski[1], Christian Berndt[1], Andreia Plaza-Faverola[3], Stefan Bünz[3]

[1]*GEOMAR Helmholtz Centre for Ocean Research Kiel, Kiel, Germany*

[2]*Federal Institute for Geosciences and Natural Resources, Hannover, Germany*

[3]*Centre for Arctic Gas Hydrate, Environment and Climate (CAGE), UiT The Arctic University of Norway, Tromsø, Norway*

[4]*Geological Survey of Denmark and Greenland, Aarhus, Denmark*

Abstract

The Lunde Pockmark on the Vestnesa Ridge offshore Svalbard is characterized active seepage of hydrocarbons. The pockmark is underlain by seismic amplitude anomalies interpreted as fluid migration pathways and buried authigenic carbonate occurrences. Despite the crucial role of focused fluid flow systems in several seafloor processes, the detailed geometry and physical properties of such pathways are poorly constrained. Here, we present a P-wave travel time tomography using integrated ocean bottom seismic and high-resolution P-Cable seismic data. The 3D distribution of P-wave velocities shows high seismic velocity anomalies in the chimney interior. Our analysis, combined with earlier datasets provide evidence for redirection of vertical migrating fluids controlled by buried authigenic carbonate concretions and gas hydrates, associated with major past seepage events. This work improves our understanding of the evolution of fluid migration features globally.

Keywords: P wave velocity, travel-time tomography, fluid flow

Plain language summary

Hydrocarbon gases, especially methane, leaking from the seabed into the ocean is a global phenomenon. It is known that these seeps control benthic ecosystems, influence slope stability and may even influence climate. Despite decades of research it is not clear how exactly the gas migrates through the sediments and up to the seafloor. Here, we show with the results from a very sophisticated seismic experiment that there are areas below active seep sites off Svalbard

where seismic waves travel faster and others where they travel slower than in the surrounding rocks. This shows where the gas is rising and that its migration is influenced by the presence of gas hydrate accumulations and dense carbonate accretions in the uppermost sediments.

5.1. Introduction

Pipes and chimneys are imaged in seismic data as sub-vertical zones of chaotic seismic facies and reflections with increased or reduced seismic amplitude disrupting the continuity of seismic reflection (Moss and Cartwright, 2010; Løseth et al., 2011; Andresen, 2012; Cartwright and Santamaria, 2015; Karstens and Berndt, 2015). The release of big amounts of fluids can cause the mobilisation of the seafloor resulting in the formation of these features, often with a depressed seafloor feature known as pockmark (Judd and Hovland, 2009). These fluid flow structures at continental margins are common features and have been documented from compressive as well as from extensive margin settings (e.g., Berndt et al., 2005; Hustoft et al., 2009; Plaza-Faverola et al., 2010; Crutchley et al., 2010; Sun et al., 2012; Cartwright and Santamaria, 2015).

The physical properties, the flow dynamics and the internal structure of pipes and chimneys are still poorly understood. The material stored in their interior as well as the type of deformation the sediment have experienced can vary significantly from one setting to another. Notable studies of such fluid flow structures include: chimneys above the Tommeliten Alpha Field in the southern North Sea, a faulted dome, where seismic shear waves studies, numerical simulations and wellbore data revealed a gas-filled fracture network (Granli et al., 1999); a three-dimensional seismic tomography of a fluid-escape chimney in the Nyegga pockmark field (Norwegian Sea), an area northward from the Storegga slide in the mid-Norwegian margin, where gas hydrate abundance is inferred as explanation for the presence of a high velocity zone inside the chimney (Plaza-Faverola et al., 2010); and the seismic imaging of an active pipe structure below the Scanner Pockmark (North Sea) located within the Witch Ground Graben, a part of the North Sea Basin failed rift system, which is separated in an upper part that represents a network of open, gas filled fractures and a lower part with increased seismic velocities (Schramm et al., 2021).

This study focuses on the chimney structure below the Lunde Pockmark on the Vestnesa Ridge in the eastern Fram Strait, a rifted margin in proximity to glaciated regions (Figure 5.1). The Lunde Pockmark was the subject of various geophysical and geochemical studies including MeBo drilling where 2D and 3D seismic interpretations have been correlated with authigenic

carbonate, gas hydrate and gas sample analyses (Bünz et al., 2012; Panieri et al., 2017; Himmler et al., 2019; Pape et al., 2020; Sauer et al., 2021; Hong et al., 2021; Domel et al., 2022).

Here, we present the results of a detailed 3D P-wave reflection tomography of the chimney below the Lunde Pockmark, using an array of 22 ocean bottom seismometers (OBS) generating a relatively dense (50-300 m separation between instruments) 3D data set covering a range of offsets (up to 2000 m) and azimuths to derive seismic velocity anomalies (Figure 5.1). The objective is to study the derived seismic P-wave velocity (Vp) in the context of a priori geological and geophysical information to characterize the chimney interior and associated fluid pathways. Furthermore, we explore the suitability of high-resolution 3D seismic tomography (i.e., from integration of OBS and high resolution 3D seismic data) to constrain the distribution of gas hydrate, free gas accumulations and carbonate concretions within focused vertical fluid migration pathways without the need of invasive methods.

5.2. Geological Setting

The Vestnesa Ridge is a 100 km-long sediment drift located north of the Molloy transform fault off the west Svalbard coast and bends from SE-NW to E-W direction (Figure 5.1) (Bünz et al., 2012). This ridge is partially located on a relatively young (<20 Ma) and hot (heat flux > 115mW/m²) oceanic crust (Eiken and Hinz, 1993; Engen et al., 2008; Hustoft et al., 2009). It grows due to bottom-current controlled sediment dynamics (Eiken and Hinz, 1993) and the sediment thickness along the Vestnesa Ridge increase from 1 km in the west to more than 2 km at the eastern end (Eiken and Hinz, 1993). Several seismic studies divided the seismic section of the Vestnesa Ridge into three seismic sequences (Figure 10 in Eiken and Hinz, 1993). In addition, several studies revealed the occurrence of a bottom-simulation reflector (BSR) approximately 140-200 mbsf, which covers the whole of the Vestnesa Ridge (Eiken and Hinz, 1993; Posewang and Mienert, 1999; Vanneste et al., 2005; Hustoft et al., 2009; Plaza-Faverola et al., 2017; Singhroha et al., 2019).

The crest of the ridge is studded with numerous pockmarks with a diameter of up to 600 m (Vogt et al., 1994; Hustoft et al., 2009). The eastern sector of the Vestnesa pockmarks have shown periodic active gas discharge in recent years, whereas seepage activity has not been documented from pockmarks on the western sector despite numerous surveys in the area (Bünz et al., 2012; Plaza-Faverola 2015). One of the most active ones is the Lunde Pockmark (Panieri et al., 2017). Numerous studies have investigated the structures and properties of the Lunde Pockmark (e.g. Panieri at al., 2017; Dazinnies et al., 2021; Hong et al., 2021; Sauer et al., 2021).

Panieri et al. (2017) show carbonate formation at the Lunde Pockmark, together with extensive chemosynthetic communities including filaments sulphide-oxidizing bacteria and siboglinid tubeworms. They also document ongoing diffusive and focused fluid flow regimes. Sauer et al. (2021) show bacterial mats within the pockmark and very shallow sulphate methane transition zones. MeBo cores recovered from Lunde Pockmark show the presence of gas hydrates at two depth intervals: 5.80 to 8.28 mbsf and 10.29 to 11.54 mbsf (Hong et al., 2021). The MeBo cores retrieved authigenic carbonate concretions at various depths and some of those concretions correlate with documented high amplitude anomalies within the chimney (Plaza-Faverola et al., 2015; Himmler et al., 2019). Hong et al. (2021) suggest that the decomposition of gas hydrate is as fast as its formation and can attribute this to a relatively low methane supply through the advection of saline formation waters at present. They propose a conceptual evolution for the fluid pumping system characterized by the redirection of flow due to sealing carbonate concretions. In addition, a high-resolution 3D petroleum systems model of the Vestnesa Ridge shows gaseous hydrocarbons, originating from Miocene age terrigenous organic matter, accumulates largely in ~2 million-year-old sediments underneath the Lunde Pockmark (Dumke et al., 2016; Daszinnies et al., 2021). To the present day, these traps are constantly charged and supply free gas to the gas hydrate stability zone (GHSZ), initiating the formation of gas hydrates (Daszinnies et al., 2021).

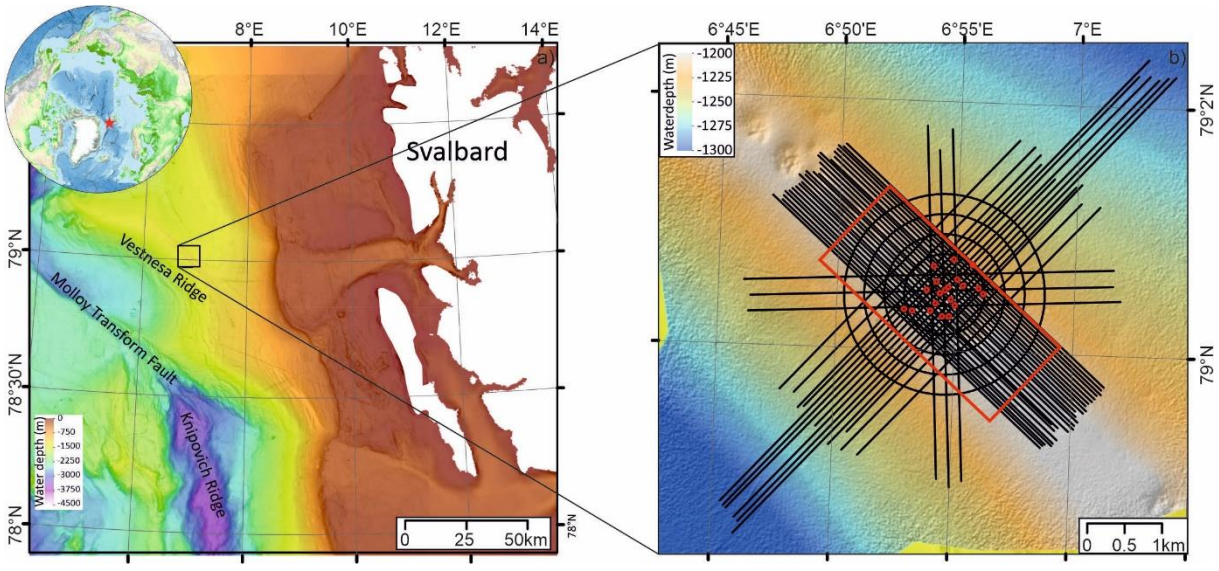

Figure 5.1: (a) Location and (b) bathymetry at the Vestnesa Ridge. Map of the OBS seismic lines (black lines), the OBS deployment (red dots) and the P-Cable cube (red box).

5.3. Experiment and Data

The aim of the high-resolution seismic reflection tomography was to resolve the 3D Vp variations in the chimney beneath the Lunde Pockmark. We used two different seismic data sets: a high-resolution 3D seismic P-Cable dataset (Bünz, 2013; Plaza-Faverola et al., 2015) and high-resolution 2D seismic lines recorded both at the seafloor (OBS data) and at the surface (streamer data). The high-resolution 3D data set was acquired with the P-Cable system on board R/V Helmer Hanssen in July 2013 (Bünz et al., 2013; Plaza-Faverola et al., 2015). The available 3D P-Cable seismic data covers an area of 2x7 km² with using 14,25 m long parallel streamers (Figure 5.1) and details about acquisition and processing can be found in previous publications (Plaza-Faverola et al., 2015; Waage et al., 2019).

In July 2019, we deployed 22 OBSs over Lunde Pockmark. 2D streamer lines and OBS lines with two different orientations plus circles (Figure 5.1b) were collected using a mini GI gun (30/30 in³) that provided a frequency band of 20-400 Hz, with a dominant frequency of 100-150 Hz (Bünz et al., 2019). The pressure was kept at 170 bar and the shooting rate was every five seconds. The mini GI gun was towed at 2 m water depth with a GPS transponder on the gun raft. The OBS instruments were equipped with a 4.5 Hz three-component seismometer and a hydrophone (lobster type of OBSs). The instruments recorded continuously at a sampling rate of 4000 Hz. Processing of these data included a minimum phase Ormsby band-pass-filter (10-20-200-300 Hz).

The OBSs were freely dropped in the water. Due to ~1200 m water depth and ocean currents, the instruments drifted away by up to several hundred meters from their dropping position (Figure 5.1). The relocation procedure minimized the least square misfit between the observed direct wave arrival time and the synthetic arrival time calculated based on the water depth derived from existing multibeam bathymetry data. Due to the large number of shots (>10000) from different directions, we estimate the error in OBS location to be less than 1 m.

The design includes inlines, crosslines and circles over the OBSs to provide a good coverage of rays from all directions (Figure 5.1). A total of 50 seismic profiles and three circular tracks were acquired (Figure 5.1). During the seismic experiment the weather conditions were good (< 1 m high waves) and the data quality of the OBSs is excellent (Figure 5.2).

5.4. 3D seismic travel time tomography

P-wave reflections were identified in all lines on all wide-angle OBSs and in the high-resolution 3D seismic dataset. To ensure that the same reflectors were picked in all datasets, the 3D seismic data and OBS profiles were correlated (Figure 5.2). Due to the higher penetration depth of the OBS data, only the first three prominent reflectors (H50, H80, BSR) could be correlated. The two deeper reflectors H100 and H110 were only identified on the OBS dataset (Figure 5.2c). In total, five reflectors were picked and used as input for the three-dimensional tomography (Figure 5.2). Overall, our dataset contains ~500,000 P-wave arrival picks. We picked these arrivals with the seismic interpretation software IHS Kingdom Suite which ensures that the true peak of any phase is selected. Mispicks by the automatic picker, i.e. instances in which the automatic picker resulted in cycle skips, were visually identified and corrected manually.

To build a detailed 3D seismic velocity model, we used Jive3D (Hobro et al., 2003), a 3D forward-modelling and tomographic inversion package (Scott et al., 2009). Therefore, uncertainties associated with the predicted travel times are primarily associated with the tomography algorithm (i.e., 4-9 ms for all picks of the upper layers) (Table 5.B1 and 5.B2). The 3D model space is 2.5 km deep and covers an area with a lateral extent of 6 km x 6 km with the Lunde Pockmark at its centre. The cubic grid cell size is 50 m in horizontal directions and 25 m in vertical direction. Our model consists of seven layers, with the designation of the shallow reflectors identical to Singhroha et al. (2020) (Figure 5.2): the first layer is the water column with a constant seismic velocity. The base of the second layer is the horizon H50. This horizon is characterized by high seismic amplitude, reverse polarity, and it is visible in most seismic sections. It is at a mean depth of 1.73 s TWT below the seafloor. The base of the third layer is horizon H80, characterised by milder amplitudes compared to H50 and by a normal polarity reflection. We can identify H80 clearly in all OBS and streamer profiles. The base of the fourth layer is the BSR. This reflection has particularly strong amplitudes. In the high-resolution seismic data, it often consists of phases that are laterally discontinuous (Figure 5.2). H100 is the first reflector from the top which can only be observed in the OBS data and is not identified by Singhroha et al. (2020). This reflector constitutes the base of the fifth layer. The base of the sixth layer is defined by reflector H110, which we could only identify in a few profiles and OBS stations. Since the signal-to-noise ratio decreases with depth, the picking uncertainty was higher for these two reflectors and we assigned a more conservative picking error for these two reflectors (Table 1 and 2). The seventh layer is the final layer of our model and comprises the model space below horizon H110.

The Vp for our starting model is taken from the study of Singhroha at el. (2020), which is based on the same high-resolution P-cable dataset used in this study and includes a 1D Vp-model derived from the evaluation of a single OBS. After running the inversion, we converted the resulting velocity model to two-way-travel time (TWT) to facilitate a comparison with the 3D data. The arrival time for each reflector was inverted individually within ten iterations, progressing from top to bottom. Other parameters and the result of the checkerboard test are described in the supplementary material.

5.5. Results

5.5.1. P-wave velocity model from travel time tomography

The Lunde Pockmark shows a complex bathymetry that is underlain by the seismic chimney structure in the 3D seismic data. The chimney extends from the seafloor down to the base of the GHSZ (Figure 5.2). The results of the Vp tomography show considerable lateral velocity anomalies in the area beneath the Lunde Pockmark (Figure 5.2). The region beneath the pockmark is characterized by increased seismic Vp inside the chimney structure compared to the surrounding area (Figure 5.2). From the seafloor down to reflector H50 (~1730 s TWT) the velocity inside of the chimney is up to 12 % higher than the seismic velocity of the surrounding background sediments. For example, at 1700 s TWT, the velocity rises from 1.55 km/s outside the chimney to 1.75 km/s inside. In this layer, the velocity anomaly is moved slightly in NE direction towards the periphery of the chimney, above a zone of high amplitudes in the P-Cable data (Figure 5.2a). The velocity increase coincides with disturbed reflectors and a high-amplitude seismic anomaly in the 3D seismic data. In this layer, the chimney is more ellipsoidal than circular and has a greater extension in east-west than in north-south direction (Figure 5.2c). In the north-south direction the seismic anomaly is ~400 m wide, in the east-west direction it is about 650 m wide. In the third layer down to the horizon H80 (depth ca. 1820 s TWT), the seismic velocity anomaly becomes more circular and smaller in lateral extent and the velocity inside the chimney is only about 10 % higher than the background velocities. Comparison with the overlying layers shows that this is due to an increase of the background velocity – probably due to compaction – while the velocity inside the chimney stays constant (Figure 5.2). In the fourth layer, the contrast between the Vp within the chimney and the background sediments is the highest. At 1830 s TWT the velocity rises from 1.6 km/s outside the chimney up to 1.85 km/s inside and thus it is up to 14 % higher than the background seismic velocity at the same depth. In the fourth layer, the chimney is again more ellipsoidal than circular. It is not possible to trace the chimney in the inverted velocity model deeper down. The 3D seismic data show

very strong amplitudes and the Vp model shows reduced (1.5 km/s) seismic velocities but not only below the Lunde Pockmark but consistently through the entire layer (Figure 5.2). Also, the sixth layer does not show an ellipsoidal- or circular- shaped anomaly in the Vp below the Lunde Pockmark, but the seismic velocity of the entire layer is higher than in layer five.

Overall, the results of the travel time tomography show significant seismic velocity contrasts within the chimney conduit. A similar model is likely to be representative of other active pockmarks adjacent to Lunde along the eastern Vestnesa Ridge segment.

5.5.2. Correlation between P-Cable and traveltime tomography

To quantify the dimensions of the chimney structure below the Lunde Pockmark, we analyse the results of the travel time tomography with the characteristics of the chimney in 3D seismic data. Beneath the Lunde Pockmark, the 3D seismic data show amplitude anomalies with zones of dimmed reflections and bright spots. In some places below the pockmark, the high-amplitude reflectors have reversed polarity with respect to the seafloor reflection (e.g. reflector at 1.7 s TWT depth; Figure 5.2). High amplitudes occur especially between the seafloor and reflector H50 (e.g. 1.66 s TWT; Figure 5.2), but also between the second and third layer and partly down to reflector H80 (Figure 5.2d). These high-amplitude reflections are underlain by chaotic seismic facies. Plaza-Faverola et al. (2015; Figure 5.2b) used structural maps along horizon H80 to constrain the internal structure of the chimney. The maps show the chimney structure as an almost circular anomaly. The chimneys are associated with NW-SE oriented faults and fractures (Plaza-Faverola et al., 2015) which are partly characterized by high velocity anomalies suggested by Singhroha et al. (2020) to be due to plugging of fractured zones with gas hydrate concentrations. Comparison of the lateral extent of the chimney structure in the 3D seismic dataset and the 3D tomography show matching diameters of the chimney structure. In both datasets the chimney is about 300 m wide. Just in the second layer, between the seafloor and H50, the result of the tomography shows a wider seismic velocity anomaly. Additionally, the seismic data show a very straight chimney below H50, while in the tomography model the chimney shifts its position slightly to the northeast (Figure 5.2).

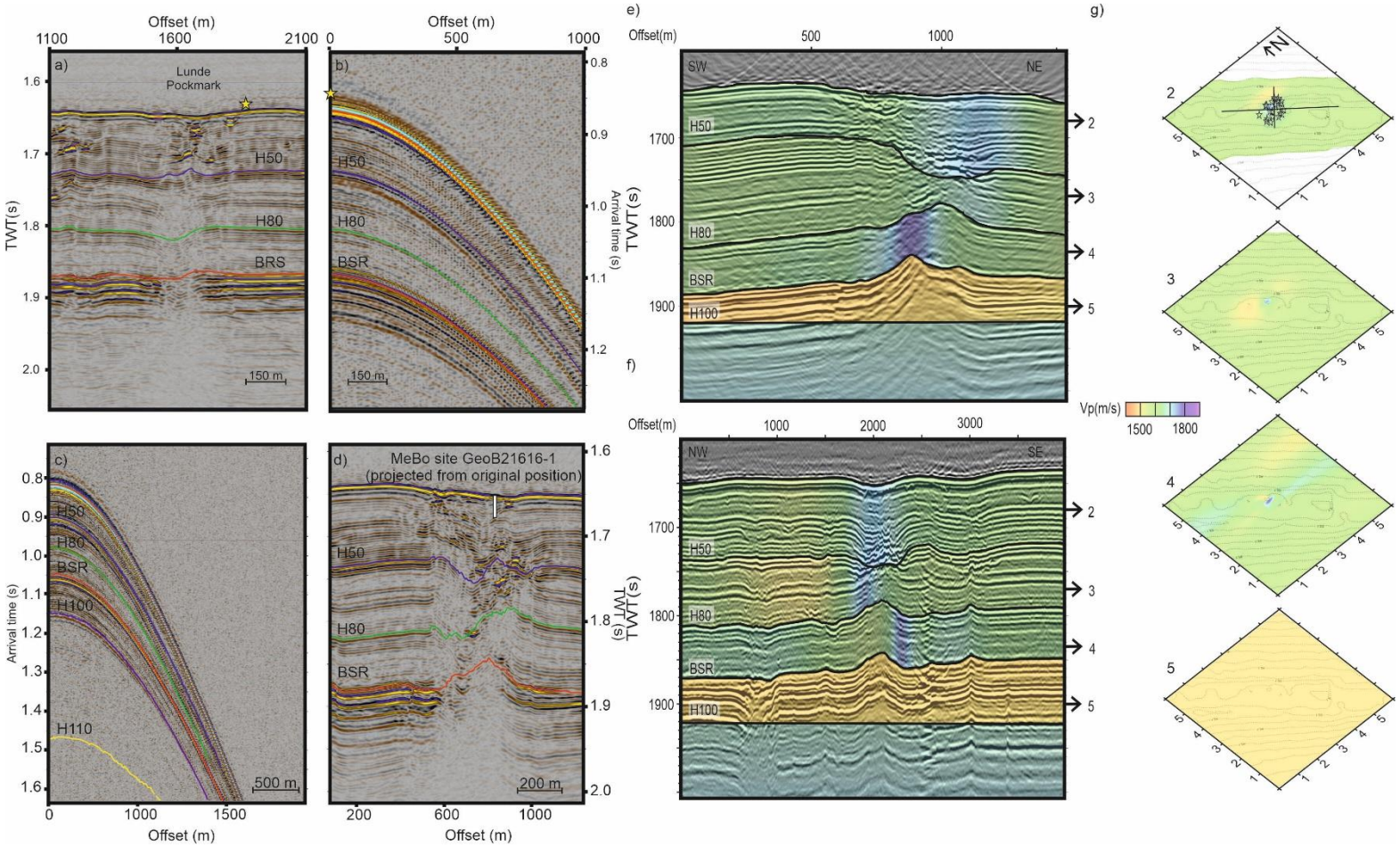

Figure 5.2: Correlation between P-Cable (a) and the OBS data (b). The interpreted reflectors are indicated (lines). (c) All interpreted reflectors identified in the OBS data. (d) Crossline 751 shows high amplitudes between layers H50 and H80, which is just observed on a few profiles. Velocity distribution in e) SW-NE direction and f) in NW-SE direction. Each section shows a clear positive seismic velocity anomaly beneath the Lunde Pockmark. g) Depth slices of the seismic field for layer 2-5(black lines image the seafloor topography).

5.6. Discussion

The detailed structure and geophysical properties of pipes and chimneys are generally poorly understood and may vary significantly from one setting to another (Cartwright, 2007; Gay at al., 2012). In some studies, the seismic velocities of pipe or chimney structures are lower compared to the surrounding sediments. The study of Arntsen et al. (2007) proposed that negative anomalies can be caused by a network of open fractures and ascending gas. In other studies, the chimney structures are associated with a positive seismic velocity anomaly caused by gas hydrate accumulation and/or buried authigenic carbonate concretions (Plaza-Faverola et al., 2011) or due to carbonate cementation within the fractures (Garten et al., 2008). The study of Schramm et al. (2021) shows that a pipe structure can be internally heterogeneous. The study also shows that the conduit below the Scanner Pockmark in the central North Sea is separated into two parts. The upper part of the pipe structure is characterized by a low velocity anomaly and indicates the presence of free gas, which is hosted in a network of open fractures. The deeper part is characterised by a positive seismic velocity anomaly, which may be the result of calcite precipitation or a modification of the original sediment texture by fluid migration (Schramm et al., 2021).

In case of the Lunde Pockmark, the 3D tomography shows up to 14 % increased seismic velocity compared to the surrounding background sediments down to a depth of 1850 TWT s (Figure 5.2). Previous studies of this area document the presence of methane hydrate and free gas (Goswami et al., 2015; Singhroha et al., 2019). Considering the local geological conditions, gas hydrates as well as free gas impact Vp significantly: the presence of gas hydrates may increase Vp up to ~4000 m/s, while free gas may decrease Vp down to less than 1000 m/s (Ecker et al., 2018; Chand et al., 2004; Gei & Carcione, 2003; Song et al., 2018; Waage et al., 2021). The changes in seismic velocity are more sensitive to the presence of gas as ~4% homogeneously distributed gas decrease Vp by up to 0.4 km/s whereas ~16% pore filling gas hydrate increase Vp only by ~0.13 km/s on Vestnesa Ridge (Singhroha et al., 2019). The magnitude of the Vp increase due to hydrates can vary up to 40-50% depending on gas hydrate distribution and morphology and the orientation of gas hydrate filled fractures (Chand et al., 2004; Ghosh et al., 2010) and the magnitude of the Vp decrease can vary up to 500-600% depending on homogeneous vs patchy free gas distribution (Mavko et al., 2020; Waage et al., 2021). Furthermore, other lithological variations like the presence of authigenic carbonates can increase the seismic velocity. The fact that we observe increase in seismic velocities radially inwards towards gas chimney, even though the effect of free gas is much stronger on seismic

velocities, indicates that the gas chimneys are primarily dominated by gas hydrates and carbonates. This interpretation is supported by geochemical analyses and MeBo drilling into the Lunde Pockmark that document both, carbonate cementations and gas hydrates within the chimney (Smith et al., 2014; Himmler et al., 2019). Therefore, we expect that increases of Vp at greater depth probably indicate gas hydrate as supported by the BSR, while high velocities at shallow depth may be caused by both gas hydrate and carbonate. The influence of hydrates on the physical properties such as Vp of the sediments overlying the BSR is dependent on the elastic properties of the sediments and the pore fill (Chand et al., 2004). A comparison of various effective medium theories shows that the variation of velocity with hydrate saturation depends on sediment microstructure as this controls gas hydrate distribution (Chand et al., 2004). Such high velocity anomaly above the BSR has been documented from seepage sites at various margins (e.g., Minshull et al., 1994; Korenaga et al., 1997; Hustoft et al., 2009; Crutchley et al., 2016)

Although Lunde Pockmark is active, the tomography results do not show a velocity inversion or a significant Vp decrease with respect to the surroundings. This could lead to the interpretation that there is no low velocity material (i.e., gas) within the conduit. However, gas accumulations smaller than the resolution of the tomography may remain unrecognized. Moreover, there are significant differences between the magnitudes of high Vp zones within the various layers. Assuming that the high amplitude anomalies are caused by buried carbonates and/or hydrate accumulations, small accumulations of gas would potentially decrease the average velocities documented by the tomography. Small amounts of gas trapped underneath these hard material accumulations cannot be ruled out.

It is very likely that gas hydrates, carbonates, and free gas occur in close (mm-scale) proximity as shown for Hydrate Ridge (Tréhuet al., 2004) or Formosa Ridge in Taiwan (Bohrmann et al., 2023). The tomography results in the average velocity on 10 s of meter scales and does therefore not have the resolution to distinguish between gas and gas hydrates. Since the 3D tomography resolves a positive seismic Vp anomaly beneath the Lunde Pockmark, the increasing effect on the seismic Vp due to gas hydrates in the sediment pore space must be larger than the decreasing effect of free gas. Onshore pipe structures in permeable sandstones in Varna, Bulgaria where gas was transported through carbonate pipes that have a diameter of 0.5-3 m may serve as an analogue (Böttner et al., 2021).

The evidence for the occurrence of gas hydrates in the chimney is stronger at greater depth in the fourth layer of our model. For example, at 1830 s TWT the velocity rises from 1.6 km/s

outside the chimney up to 1.85 km/s inside (Figure 5.2). It is likely that there is a higher gas hydrate saturation near the base of the GHSZ – an observation that has been reported for many gas hydrate systems, (e.g., Minshull et al., 1994; Hustoft et al., 2009; Crutchley et al., 2016). Below the GHSZ, the tomography shows a low velocity zone. In combination with the high amplitudes in 3D seismic data this is an indicator of free gas beneath the gas hydrate satuated sediments. This low velocity zone beneath the BSR has been documented from several gas hydrate systems worldwide as the free gas zone (e.g., Crutchley et al., 2010; Chabert et al., 2011; Plaza-Faverola et al., 2012) and has been in instances confirmed by drilling (Singh et al., 1993; Mackay et al., 1994; Holbrook et al., 1996; Chand et al., 2004). The observation that there is no consistent seismic velocity anomaly at greater depth suggests that the origin of the chimney is at the BSR.

The shape of the seismic Vp anomaly is nearly circular in the chimney, barring the second and fourth layers where it is elliptical (Figure 5.2). However, we cannot identify more internal structures of the chimney in our tomography results. The 3D seismic data and the modelling by Hong et al. (2021) show a potentially internal splitting in the upper part of the chimney. They suggest that a main fluid channel was once blocked by buried pockmarks and seep carbonates deflected the fluid conduit and channeled fluid flow towards a seepage site in the SW (Hong et al., 2021). They propose that this new seepage site was self-sealed by authigenic carbonates (e.g., Hovland and Roy, 2022) which decreases the gas discharges on the seafloor, consistent with the documentation of buried carbonate by Himmler et al. (2019). At the present day, the Lunde Pockmark has a second redirected fluid pathway with active seepage towards the southeast of the pockmark (Hong et al., 2021). The tomographic inversion results show a movement of the seismic Vp anomaly in northeast direction towards the periphery of the chimney. These results are consistent with a process of redirection of migrating fluids. However, the resolution of the velocity field resolved by our approach does not seem to solve individual pathways.

5.7. Conclusion

The high-resolution 3D P-wave reflection tomography from the chimney structure beneath the Lunde Pockmark provides evidence for the presence of gas hydrate and buried authigenic carbonate concretions. Vp increases radially towards the centre of the chimney. The root of the conduit beneath the Lunde Pockmark is likely the base of the hydrate stability zone at the BSR. Beneath the BSR, the velocity distribution in each layer is homogenous with no major radial changes in the velocity.

Overall, our study shows, that a chimney provides a fluid pathway through the GHSZ. Gas hydrates and carbonate cementations overprint the velocity effect of ascending gas resulting in a positive seismic velocity anomaly. The hydraulic properties of the pipe structure are likely different than the properties of the surrounding sediments that have not been affected by fluid migration. Our observations are consistent with a chimney that formed as the result of multiple fracture-controlled seepage events. Each event left a footprint of buried authigenic carbonate concretions and gas hydrate filled fractures that retain fluids (i.e., free gas) for fixed period of times until the pressure in the system triggers redirection of the flow. Such process explains the occurrence of discrete seepage sites within single pockmarks.

The detailed examination of the arrival times shows that the chimney width inverted by Jive3D is probably overestimated due to smearing effects, and that gas hydrates may be more concentrated but less widespread.

The tomographic inversion exercise from this active seepage system in the west Svalbard margin, corroborates that chimney structures play an important role in the transport of carbons into the ocean and are zones of concentrated carbonates and hydrates.

Open Research

This data was acquired on board R/V Helmer Hanssen, and we are thankful to the ship and scientific crew for data acquisition. The research cruise were conducted as part of a scientific collaboration between UiT the Arctic University of Norway and GEOMAR under the SEAMSTRESS project, supported by starting grants from the Tromsø Research Foundation (TFS) and the Research Council of Norway (grant 287865). The study was also supported by the Research Council of Norway through its Centers of Excellence funding scheme, project 223259 (CAGE; culminated 2023). SB and APF are currently affiliated with the new Norwegian Centre of Excellence iC3, project number 332635. We are grateful to IHS Markit for providing the Kingdom Suite interpretation software within the academic licensing program. The data are stored at UiT open research data repository and can be accessed using the weblink (https://doi.org/10.18710/SBR9GJ).

5.8. Supplementary material

5.8.1. Raytracing

5.8.1.1. Results raytracing

During the picking of the OBS data, we detected changes in the slope along some horizons (Figure 5.B1). Usually, these signal shifts are in up to ~100 m-long offset intervals between point of reflection and OBS and the gradient is higher compared to the gradient of the whole reflector. These signal shifts occur only on profiles directly under the pockmark and at near offsets. To understand the origin of these shifts, we modelled the theoretical arrival times in 2D along the profiles with the program Modeling by Fujie Gou (Fujie et al., 2007). Starting with the velocity model provided by the travel time tomography we varied the velocities until the observed and modelled arrival times matched (Figure 5.B1). Generally, the smearing effects in Modeling are smaller than in Jive3D and we assigned thinner anomalies with higher Vp perturbations to the model. This shows that a modelled chimney of 50 m diameter, but a velocity anomaly that is about 0.1 km/s higher than originally assumed would also be consistent with the data. This can be attributed to the uncertainties of the picks and the smearing effects of Jive3D.

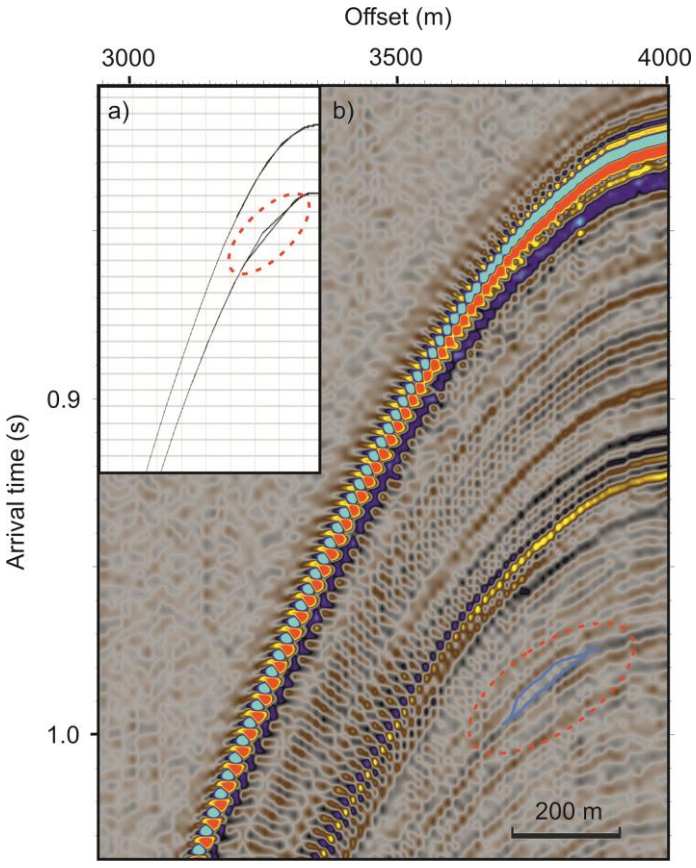

Figure 5.B1: a) With Modeling generated signal and (b) data example with a signal shifts (blue line highlighted with red dashed line/OBS 14).

In addition, we traced the rays in our tomography-derived velocity model to identify the ray paths and locate the source of the velocity anomaly. We observe that the source of the velocity anomalies between the seafloor and H80 horizon is located within the second and third layers and only within the chimney conduit (Figure 5.B2). The impossibility to have rays within the chimney at high contrast between the background and the chimney interior velocity suggests that seismic energy would only propagate through the chimney up to a certain velocity contrast and would either be refracted away from the chimney for larger contrasts or there would be diffraction due to brecciation of sediments, gas hydrates filled fracture zones, and the morphology of the buried authigenic carbonate concretions. As the arrivals in the OBS data are clearly visible and characterized by high seismic amplitudes we surmise that the velocity variations are not as high and the chimney not as narrow as theoretically possible based on the arrival time fit in the ray tracing, and we propose that the velocity anomalies and the chimney widths resulting from the tomographic inversion are realistic.

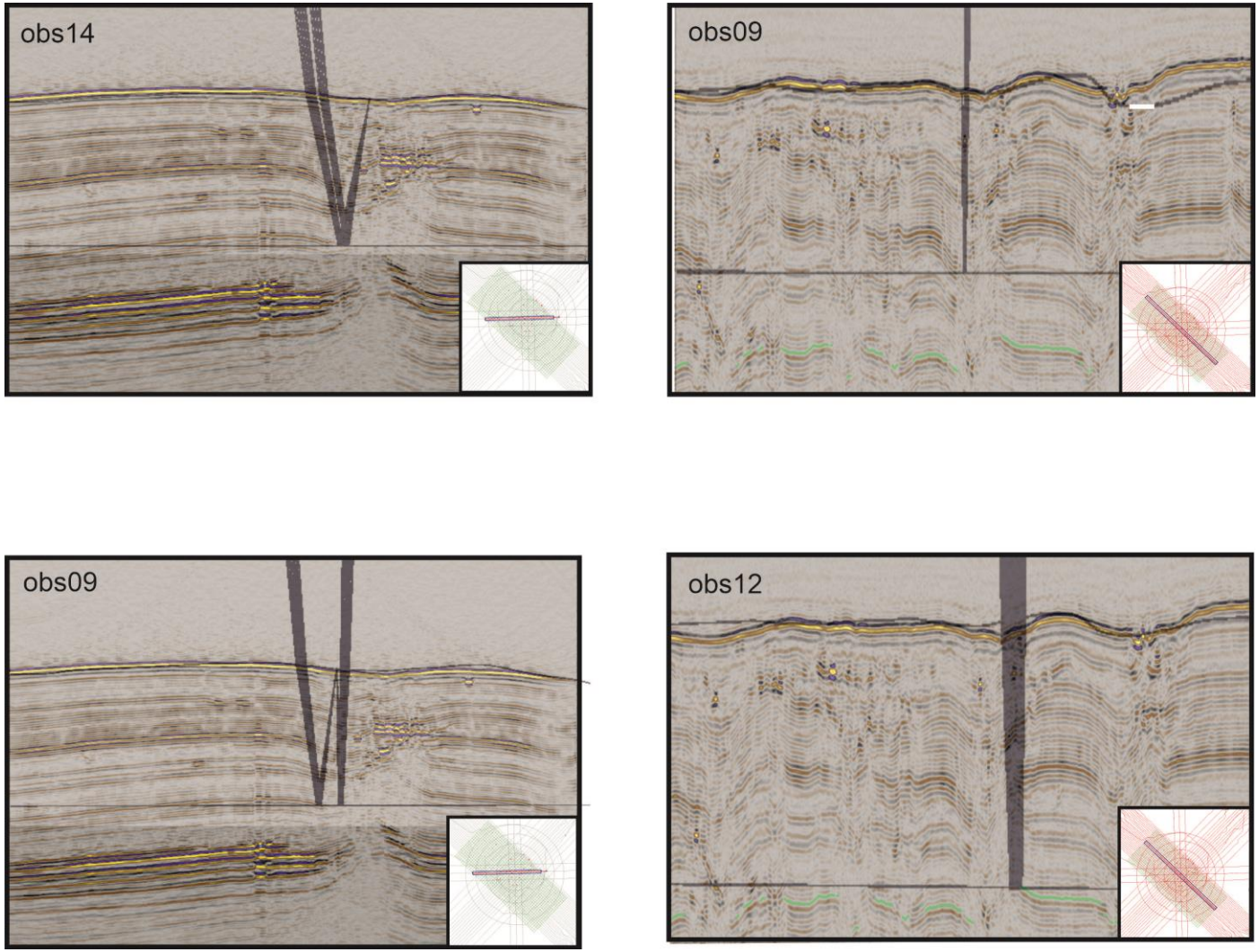

Figure 5.B2: Examples of the traced rays of the signal anomalies of OBS 14 (a), OBS 9 (b and c) and OBS 15 (d).

5.8.1.2. Discussion raytracing

The OBS data provide additional information on the physical properties of the chimney structure. Using the code Modeling by Fujie Gou (Fujie et al., 2007), we were able to replicate the travel time anomalies, and by using the ray tracing of Jive3D with the OBS data, we were able to generate an overview showing the location of such anomalies (Table 5.B1 and 5.B2). We detected shifts in slope along horizons H50 and H80 directly over the pockmark and at near offset. Modelling of the ray paths with synthetic data shows that these anomalies can be caused by very high, sharp positive velocity anomalies. These velocity anomalies are caused by changes in the geophysical properties of the subsurface, most likely by irregular sharped authigenic carbonate concentrations or gas hydrates as they were detected during the drilling campaign (Hong et al., 2021). As drilling only provides information for a very small part of the subsurface it would be beneficial to locate authigenic carbonates and gas hydrates by OBS ray tracing.

5.8.2. Checkerboard-Test

We investigated the solution quality by using the checkboard test approach (e.g., Lévêque et al., 1993; Zelt, 1998; Plaza-Faverola et al., 2010; Schramm et al., 2021) to avoid misinterpretation of velocity variations resulting from the travel time tomography (Figure 5.B1). The checkerboard test was run with a checkerboard pattern of 500 m x 500 m x 500 m and 15 % of velocity perturbation compared to the starting model. The results of the checkerboard test show our tomographic setup allows the recovery of the generated anomalies below the Lunde Pockmark and up to the depth of layer 5 (Figure 5.B1). After 8 inversions, satisfactory inversion statistics were obtained.

Layer	Hit rate	X^2	No. of Rays
Layer2	99 %	5.76	133,563
Layer3	97 %	6.09	125,062
Layer4	99 %	5.85	196,648
Layer5	99 %	10.01	73,541
Layer6	99 %	12.03	16,257

Table B1: List of hit rates, X^2 and numer of rays used for inversion of each leyer in the resulting model.

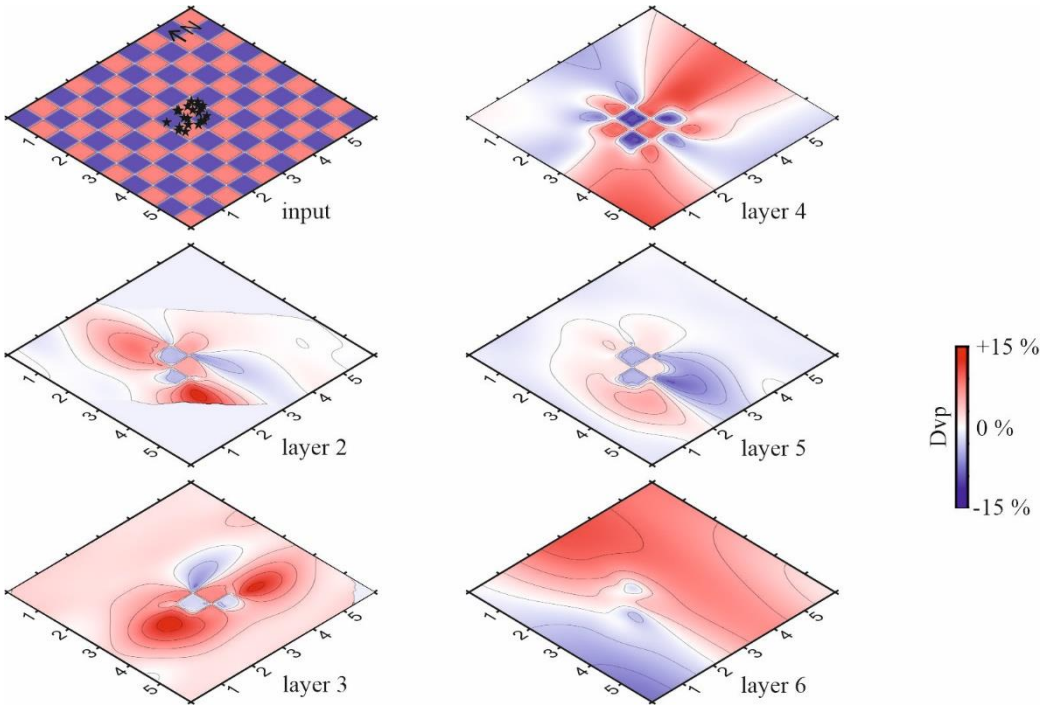

Figure 5.B1: Checkerboard test with synthetic anomaly of 0.5 x 0.5 x 0.5 km in size and a velocity perturbation of 15 %. The stars mark the OBS positions.

Station	Uncertainty Layer 2 / ms	Uncertainty Layer 3 / ms	Uncertainty Layer 4 / ms	Uncertainty Layer 5 / ms	Uncertainty Layer 6 / ms	Overall quality
OBS01	9	9	9	15	15	Bad
OBS02	4	4	4	8	8	Good
OBS03	9	9	9	15	15	Bad
OBS04	7	7	7	10	10	Medium
OBS05	9	9	9	15	15	Bad
OBS06	4	4	4	8	8	Good
OBS07	4	4	4	8	8	Good
OBS08	4	4	4	8	8	Good
OBS09	4	4	4	8	8	Good

OBS10	9	9	9	15	15	Bad
OBS11	4	4	4	8	8	Good
OBS12	4	4	4	8	8	Good
OBS13	4	4	4	8	8	Good
OBS14	4	4	4	8	8	Good
OBS15	4	4	4	8	8	Good
OBS16	4	4	4	8	8	Good
OBS17	4	4	4	8	8	Good
OBS18	7	7	7	10	10	Medium
OBS19	7	7	7	10	10	Medium
OBS20	7	7	7	10	10	Medium
OBS21	7	7	7	10	10	Medium
OBS22	4	4	4	8	8	Good

Table B2: Analysis of recorded dataset from different OBS stations.

References

Andresen, K. J. (2012). Fluid flow features in hydrocarbon plumbing systems: What do they tell us about the basin evolution? Marine Geology, Volumes 332–334, ISSN 0025-3227, https://doi.org/10.1016/j.margeo.2012.07.006.

Arntsen, B., Wensaas, L., Løseth, H., Hermanrud, C. (2007). Seismic modeling of gas chimneys. Geophysics, 72(5), SM251-SM259. https://doi.org/10.1190/1.2749570

Berndt, C. (2005). Focused fluid flow in passive continental margins. Philosophical Transactions of the Royal Society A: Mathematical, Physical and Engineering Sciences, 363(1837), 2855-2871. https://doi.org/10.1098/rsta.2005.1666

Bohrmann, G., Ivanov, M., Foucher, J. P., Spiess, V., Bialas, J., Greinert, J., Weinrebe, W., Abegg, F., Aloisi, G., Artemov, Y., Blinova, V., Drews, M., Heidersdof, F., Krabbenhöft, A., Klaucke, I., Krastel, S., Leder, T., Polikarpov, I., Saburova, M., Schmale, O., Seifert, R., Volkonskaya, A., Zillmer, M. (2003). Mud volcanoes and gas hydrates in the Black Sea: new data from Dvurechenskii and Odessa mud volcanoes. Geo-Marine Letters, 23, 239-249. https://doi.org/10.1007/s00367-003-0157-7

Böttner, C., Callow, B. J., Schramm, B., Gross, F., Geersen, J., Schmidt, M., Vasilev, A., Petsinski, P., Berndt, C. (2021). Focused methane migration formed pipe structures in permeable sandstones: Insights from uncrewed aerial vehicle-based digital outcrop analysis in Varna, Bulgaria. Sedimentology, 68(6), 2765-2782. https://doi.org/10.1007/s00367-003-0157-7

Bünz, S., Polyanov, S., Vadakkepuliyambatta, S., Consolaro, C., Mienert, J. (2012). Active gas venting through hydrate-bearing sediments on the Vestnesa Ridge, offshore WSvalbard. Marine Geology, Volumes 332–334, Pages 189-197, ISSN 0025-3227. https://doi.org/10.1016/j.margeo.2012.09.012.

Bünz, S. (2013). CAGE13-3 Cruise Report: Sub-seabed CO2 Storage: Impact on Marine Ecosystems (ECO2)(A 7th Framework Programme EU project) PART I. CAGE–Centre for Arctic Gas Hydrate, Environment and Climate Report Series, 1. https://doi.org/10.7557/cage.6843

Bünz, S. (2019). CAGE19-1 Cruise Report: Passive and active ocean-bottom seismic surveys at Vestnesa Ridge, west-Svalbard margin within the framework of the SEAMSTRESS project. CAGE–Centre for Arctic Gas Hydrate, Environment and Climate Report Series, 7. https://doi.org/10.7557/cage.6909

Cartwright, J. (2007). The impact of 3D seismic data on the understanding of compaction, fluid flow and diagenesis in sedimentary basins. Journal of the Geological Society, 164(5), 881-893. https://doi.org/10.1144/0016-76492006-143

Cartwright, J., Santamarina, C. (2015). Seismic characteristics of fluid escape pipes in sedimentary basins: Implications for pipe genesis. Marine and Petroleum Geology, Volume 65, Pages 126-140, ISSN 0264-8172, https://doi.org/10.1016/j.marpetgeo.2015.03.023.

Chabert, A., Minshull, T. A., Westbrook, G. K., Berndt, C., Thatcher, K. E., Sarkar, S. (2011). Characterization of a stratigraphically constrained gas hydrate system along the western continental margin of Svalbard from ocean bottom seismometer data. Journal of Geophysical Research: Solid Earth, 116(B12). https://doi.org/10.1029/2011JB008211

Chand, S., Minshull, T. A., Gei, D., Carcione, J. M. (2004). Elastic velocity models for gas-hydrate-bearing sediments—A comparison. Geophysical Journal International, 159(2), 573-590. https://doi.org/10.1111/j.1365-246X.2004.02387.x

Crutchley, G. J., Pecher, I. A., Gorman, A. R., Henrys, S. A., Greinert, J. (2010). Seismic imaging of gas conduits beneath seafloor seep sites in a shallow marine gas hydrate province, Hikurangi Margin, New Zealand. Marine Geology, 272(1-4), 114-126. https://doi.org/10.1016/j.margeo.2009.03.007

Crutchley, G. J., Maslen, G., Pecher, I. A., & Mountjoy, J. J. (2016). High-resolution seismic velocity analysis as a tool for exploring gas hydrate systems: An example from New Zealand's southern Hikurangi margin. Interpretation, 4(1), SA1-SA12. https://doi.org/10.1190/INT-2015-0042.1

Daszinnies, M., Plaza-Faverola, A., Sylta, Ø., Bünz, S., Mattingsdal, R., Tømmerås, A., Knies, J. (2021). The Plio-Pleistocene seepage history off western Svalbard inferred from 3D petroleum systems modelling. Marine and Petroleum Geology, 128, 105023, https://doi.org/10.1016/j.marpetgeo.2021.105023

Domel, P., Singhroha, S., Plaza-Faverola, A., Schlindwein, V., Ramachandran, H., & Bünz, S. (2022). Origin and periodic behavior of short duration signals recorded by seismometers at Vestnesa Ridge, an active seepage site on the west-Svalbard continental margin. Frontiers in Earth Science, 10, 831526. https://doi.org/10.3389/feart.2022.831526

Dumke, I., Burwicz, E. B., Berndt, C., Klaeschen, D., Feseker, T., Geissler, W. H., Sarkar, S. (2016). Gas hydrate distribution and hydrocarbon maturation north of the Knipovich Ridge, western Svalbard margin. Journal of Geophysical Research: Solid Earth, 121(3), 1405-1424. https://doi.org/10.1002/2015JB012083

Ecker, C., Dvorkin, J., Nur, A. (1998). Sediments with gas hydrates: Internal structure from seismic AVO. Geophysics, 63(5), 1659-1669. https://doi.org/10.1190/1.1444462

Eiken, O., Hinz, K. (1993). Contourites in the Fram Strait. Sedimentary Geology, Volume 82, Issues 1–4, 1993, Pages 15-32, ISSN 0037-0738, https://doi.org/10.1016/0037-0738(93)90110-Q.

Engen, Ø., Faleide, J.I., Dyreng, T.K. (2008). Opening of the Fram Strait gateway: a review of plate tectonic constraints. Tectonophysics 450, 51–69, ISSN 0040-1951, https://doi.org/10.1016/j.tecto.2008.01.002.

Fujie, G., Kasahara, J., Murase, K., Mochizuki, K., Kaneda, Y. (2008). Interactive analysis tools for the wide-angle seismic data for crustal structure study (Technical Report). *Exploration Geophysics*, *39*(1), 26-33. https://doi.org/10.1071/EG08006

Garten, P., Houbiers, M., Planke, S., Svensen, H. (2008). Vent complex at Heidrun. In SEG Technical Program Expanded Abstracts 2008 (pp. 809-813). Society of Exploration Geophysicists. https://doi.org/10.1190/1.3063767

Gay, A., Mourgues, R., Berndt, C., Bureau, D., Planke, S., Laurent, D., Gautier, S., Lauer, C., Loggia, D. (2012). Anatomy of a fluid pipe in the Norway Basin: Initiation, propagation and 3D shape. Marine Geology, 332, 75-88. https://doi.org/10.1016/j.margeo.2012.08.010

Gei, D., & Carcione, J. M. (2003). Acoustic properties of sediments saturated with gas hydrate, free gas and water. Geophysical prospecting, 51(2), 141-158. https://doi.org/10.1046/j.1365-2478.2003.00359.x

Ghosh, R., Sain, K., & Ojha, M. (2010). Effective medium modeling of gas hydrate-filled fractures using the sonic log in the Krishna-Godavari basin, offshore eastern India. Journal of Geophysical Research: Solid Earth, 115(B6). https://doi.org/10.1029/2009JB006711

Goswami, B.K., Weitemeyer, K.A., Minshull, T.A., Sinha, M.C., Westbrook, G.K., Chabert, A., Henstock, T.J., Ker, S. (2015). A joint electromagnetic and seismic study of an active pockmark within the hydrate stability field at the Vestnesa Ridge, West Svalbard margin Journal of Geophysical Research: Solid Earth, 120(10), 6797-6822. https://doi.org/10.1002/2015JB012344

Granli, J. R., Arntsen, B., Sollid, A., Hilde, E. (1999). Imaging through gas-filled sediments using marine shear-wave data. Geophysics, 64(3), 668-677. https://doi.org/10.1190/1.1444576

Himmler, T., Sahy, D., Martma, T., Bohrmann, G., Plaza-Faverola, A., Bünz, S., Condon, D. J., Knies, J., Lepland, A. (2019). A 160,000-year-old history of tectonically controlled methane seepage in the Arctic. Science advances, 5(8), eaaw1450. https://doi.org/10.1126/sciadv.aaw1450

Hobro, J. W., Singh, S. C., Minshull, T. A. (2003). Three-dimensional tomographic inversion of combined reflection and refraction seismic traveltime data. Geophysical Journal International, 152(1), 79-93. https://doi.org/10.1046/j.1365-246X.2003.01822.x

Holbrook, W. S., Hoskins, H., Wood, W. T., Stephen, R. A., & Lizarralde, D. (1996). Methane hydrate and free gas on the Blake Ridge from vertical seismic profiling. Science, 273(5283), 1840-1843. https://doi.org/10.1126/science.273.5283.1840

Hong, W. L., Pape, T., Schmidt, C., Yao, H., Wallmann, K., Plaza-Faverola, A., Rae, J.W.B., Lepland, A., Bünz, S., Bohrmann, G. (2021). Interactions between deep formation fluid and gas hydrate dynamics inferred from pore fluid geochemistry at active pockmarks of the Vestnesa Ridge, west Svalbard margin. Marine and Petroleum Geology, 127, 104957, https://doi.org/10.1016/j.marpetgeo.2021.104957

Hovland, M. T., & Roy, S. (2022). Shallow Gas Hydrates Near 64° N, Off Mid-Norway: Concerns Regarding Drilling and Production Technologies. World Atlas of Submarine Gas Hydrates in Continental Margins, 15-32. https://doi.org/10.1007/978-3-030-81186-0_2

Hustoft, S., Bünz, S., Mienert, J., Chand, S. (2009). Gas hydrate reservoir and active methane-venting province in sediments on< 20 Ma young oceanic crust in the Fram Strait, offshore NW-Svalbard. Earth and Planetary Science Letters, Volume 284, Issues 1–2, Pages 12-24, ISSN 0012-821X, https://doi.org/10.1016/j.epsl.2009.03.038.

Judd, A., Hovland, M. (2009). Seabed fluid flow: the impact on geology, biology and the marine environment. Cambridge University Press.

Karstens, J., Berndt, C. (2015). Seismic chimneys in the Southern Viking Graben–Implications for palaeo fluid migration and overpressure evolution. Earth and Planetary Science Letters, 412, 88-100. ISSN 0012-821X, https://doi.org/10.1016/j.epsl.2014.12.017.

Korenaga, J., Holbrook, W. S., Singh, S. C., & Minshull, T. A. (1997). Natural gas hydrates on the southeast US margin: Constraints from full waveform and travel time inversions of wide-angle seismic data. Journal of Geophysical Research: Solid Earth, 102(B7), 15345-15365. https://doi.org/10.1029/97JB00725

Lévêque, J. J., Rivera, L., & Wittlinger, G. (1993). On the use of the checker-board test to assess the resolution of tomographic inversions. Geophysical Journal International, 115(1), 313-318. https://doi.org/10.1111/j.1365-246X.1993.tb05605.x

Løseth, H., Wensaas, L., Arntsen, B., Hanken, N., Basire, C., Graue, K. (2011). 1000 m long gas blow-out pipes. Marine and Petroleum Geology, Volume 28, Issue 5, Pages 1047-1060, ISSN 0264-8172, https://doi.org/10.1016/j.marpetgeo.2010.10.001.

MacKay, M. E., Jarrard, R. D., Westbrook, G. K., Hyndman, R. D. (1994). Origin of bottom-simulating reflectors: geophysical evidence from the Cascadia accretionary prism. Geology, 22(5), 459-462. https://doi.org/10.1130/0091-7613(1994)022%3C0459:OOBSRG%3E2.3.CO;2

Mavko, G., Mukerji, T., Dvorkin, J., 2020. The Rock Physics Handbook. Cambridge university press.

Minshull, T. A., Singh, S. C., & Westbrook, G. K. (1994). Seismic velocity structure at a gas hydrate reflector, offshore western Colombia, from full waveform inversion. Journal of Geophysical Research: Solid Earth, 99(B3), 4715-4734. https://doi.org/10.1029/93JB03282

Moss, J.L., Cartwright, J. (2010). The spatial and temporal distribution of pipe formation, offshore Namibia. Marine and Petroleum Geology, Volume 27, Issue 6, Pages 1216-1234, ISSN 0264-8172, https://doi.org/10.1016/j.marpetgeo.2009.12.013.

Panieri, G., Bünz, S., Fornari, D.J., Escartin, J., Serov, P., Jansson, P., Torres, M.E., Johnson, J.E., Hong, W., Sauer, S., Garcia, R., Gracias, N. (2017). An integrated view of the methane system in the pockmarks at Vestnesa Ridge, 79◦N. Marine Geology, Volume 390, Pages 282-300, ISSN 0025-3227,

https://doi.org/10.1016/j.margeo.2017.06.006.

Pape, T., Bünz, S., Hong, W.-L., Torres, M. E., Riedel, M., Panieri, G., Lepland, A., Hsu, C.-W., Wintersteller, P., Wallmann, K., Schmidt, C., Yao, H., Bohrmann, G. (2020). Origin and transformation of light hydrocarbons ascending at an active pockmark on Vestnesa Ridge, Arctic Ocean. Journal of Geophysical Research: Solid Earth, 125(1), e2018JB016679. https://doi.org/10.1029/2018JB016679

Posewang, J., Mienert, J. (1999). High-resolution seismic studies of gas hydrates west of Svalbard. Geo-Marine Letters 19, 150-156. https://doi.org/10.1007/s003670050102

Plaza-Faverola, A., Westbrook, G. K., Ker, S., Exley, R. J., Gailler, A., Minshull, T. A., Broto, K. (2010). Evidence from three-dimensional seismic tomography for a substantial accumulation of gas hydrate in a fluid-escape chimney in the Nyegga pockmark field, offshore Norway. Journal of Geophysical Research: Solid Earth, 115(B8). https://doi.org/10.1029/2009JB007078

Plaza-Faverola, A., Bünz, S., Mienert, J. (2011). Repeated fluid expulsion through sub-seabed chimneys offshore Norway in response to glacial cycles. Earth and Planetary Science Letters, Volume 305, Issues 3–4, Pages 297-308, ISSN 0012-821X, https://doi.org/10.1016/j.epsl.2011.03.001.

Plaza-Faverola, A., Klaeschen, D., Barnes, P., Pecher, I., Henrys, S., Mountjoy, J. (2012). Evolution of fluid expulsion and concentrated hydrate zones across the southern Hikurangi subduction margin, New Zealand: An analysis from depth migrated seismic data. Geochemistry, Geophysics, Geosystems, 13(8). https://doi.org/10.1029/2012GC004228

Plaza-Faverola, A., Bünz, S., Johnson, J. E., Chand, S., Knies, J., Mienert, J., Franek, P. (2015). Role of tectonic stress in seepage evolution along the gas hydrate-charged Vestnesa Ridge, Fram Strait. Geophysical Research Letters, 42(3), 733-742. https://doi.org/10.1002/2014GL062474

Plaza-Faverola, A., Vadakkepuliyambatta, S., Hong, W. L., Mienert, J., Bünz, S., Chand, S., & Greinert, J. (2017). Bottom-simulating reflector dynamics at Arctic thermogenic gas provinces: An example from Vestnesa Ridge, offshore west Svalbard. Journal of Geophysical Research: Solid Earth, 122(6), 4089-4105. https://doi.org/10.1002/2016JB013761

Sauer, S., Hong, W., Yao, H., Lepland, A., Klug, M., Eichinger, F., Himmler, T., Crémière, A., Panieri, G., Schubert, C. J., Knies, J. (2021). Methane transport and sources in an Arctic deep-water cold seep offshore NW Svalbard (Vestnesa Ridge, 79°N). Deep Sea Research Part I: Oceanographic Research Papers, Volume 167, 103430, ISSN 0967-0637, https://doi.org/10.1016/j.dsr.2020.103430.

Schramm, B., Berndt, C., Dannowski, A., Böttner, C., Karstens, J., Elger, J. (2021). Seismic imaging of an active fluid conduit below the Scanner Pockmark, Central North Sea. Marine and Petroleum Geology, Volume 133, ISSN 0264-8172, https://doi.org/10.1016/j.marpetgeo.2021.105302.

Scott, C. L., Shillington, D. J., Minshull, T. A., Edwards, R. A., Brown, P. J., & White, N. J. (2009). Wide-angle seismic data reveal extensive overpressures in the Eastern Black Sea Basin. Geophysical Journal International, 178(2), 1145-1163. https://doi.org/10.1111/j.1365-246X.2009.04215.x

Singh, S. C., Minshull, T. A., Spence, G. D. (1993). Velocity structure of a gas hydrate reflector. Science, 260(5105), 204-207. https://doi.org/10.1126/science.260.5105.204

Singhroha, S., Chand, S., Bünz, S. (2019). Constraints on gas hydrate distribution and morphology in Vestnesa Ridge, western Svalbard margin, using multicomponent ocean-bottom seismic data. Journal of Geophysical Research: Solid Earth, 124(5), 4343-4364. https://doi.org/10.1029/2018JB016574

Singhroha, S., Bünz, S., Plaza-Faverola, A., Chand, S. (2020). Detection of gas hydrates in faults using azimuthal seismic velocity analysis, Vestnesa Ridge, W-Svalbard Margin. Journal of Geophysical Research: Solid Earth, 125(2), e2019JB017949. https://doi.org/10.1029/2019JB017949

Smith, A. J., Mienert, J., Bünz, S., & Greinert, J. (2014). Thermogenic methane injection via bubble transport into the upper Arctic Ocean from the hydrate-charged Vestnesa Ridge, Svalbard. Geochemistry, Geophysics, Geosystems, 15(5), 1945-1959. https://doi.org/10.1002/2013GC005179

Song, S., Tinivella, U., Giustiniani, M., Singhroha, S., Bünz, S., Cassiani, G. (2018). OBS data analysis to quantify gas hydrate and free gas in the South Shetland margin (Antarctica). Energies, 11(12), 3290. https://doi.org/10.3390/en11123290

Sun, Y., Wu, S., Dong, D., Lüdmann, T., & Gong, Y. (2012). Gas hydrates associated with gas chimneys in fine-grained sediments of the northern South China Sea. Marine Geology, 311, 32-40. https://doi.org/10.1016/j.margeo.2012.04.003

Tréhu, A. M., Flemings, P. B., Bangs, N. L., Chevallier, J., Gràcia, E., Johnson, J. E., Liu, C.-S., Liu, X., Riedel, M., Torres, M. E. (2004). Feeding methane vents and gas hydrate deposits at south Hydrate Ridge. Geophysical Research Letters, 31(23). https://doi.org/10.1029/2004GL021286

Vanneste, M., Guidard, S., Mienert, J. (2005). Bottom-simulating reflections and geothermal gradients across the western Svalbard margin. Terra Nova 17, 510-516. **https://doi.org/10.1111/j.1365-3121.2005.00643.x**

Vogt, P.R., Crane, K., Sundvor, E., Max, M.D., Pfirman, S.L. (1994). Methane-generated(?)

pockmarks on young, thickly sedimented oceanic crust in the Arctic: Vestnesa ridge,

Fram strait. Geology 22, 255–258. https://doi.org/10.1130/0091-613(1994)022<0255:MGPOYT>2.3.CO;2

Waage, M., Singhroha, S., Bünz, S. ,Planke, S., Waghorn, K.A., Bellwald B. (2021).

Feasibility of using the P-Cable high-resolution 3D seismic system in detecting and monitoring CO2 leakage. Int. J. Greenh. Gas Control, 106, Article 103240. https://doi.org/10.1190/geo2018-0099.1

Zelt, C. A. (1998). Lateral velocity resolution from three-dimensional seismic refraction data. Geophysical Journal International, 135(3), 1101-1112. https://doi.org/10.1046/j.1365-246X.1998.00695.x

6. Stress constraints from shear-wave analysis in shallow sediments at an actively seeping pockmark on the W-Svalbard Margin

Sunny Singhroha[1,3], Bettina Schramm[2, 4], Andreia Plaza-Faverola[1], Przemyslaw Domel[1], Anke Dannowski[2], Frances Cooke[1], Stefan Bünz[1]

[1]*Centre for Arctic Gas Hydrate, Environment and Climate (CAGE), UiT The Arctic University of Norway, Tromsø, Norway*

[2]*GEOMAR Helmholtz Centre for Ocean Research Kiel, Kiel, Germany*

[3]*Geological Survey of Denmark and Greenland, Universitetsbyen 81, Building 1872, DK-8000 Aarhus, Denmark*

[4]*Federal Institute for Geosciences and Natural Resources, Hannover, Germany*

Abstract

Mechanisms related to sub-seabed fluid flow processes are complex and inadequately understood. Petrophysical properties, availability of gases, topography, stress directions, and various geological parameters determine the location and intensity of leakage which change over time. From tens of seafloor pockmarks mapped along Vestnesa Ridge on the west-Svalbard margin, only six show persistent present-day seepage activity in sonar data. To investigate the causes of such restricted gas seepage, we conducted a study of anisotropy within the conduit feeding one of these active pockmarks (i.e., Lunde Pockmark). Lunde is ~400-500 m in diameter, and atop a ~300-400 m wide seismic chimney structure. We study seismic anisotropy using converted S-wave data from 22 ocean-bottom seismometers (OBSs) located in and around the pockmark. We investigate differences in symmetry plane directions in anisotropic media using null energy symmetries in transverse components. Subsurface stress distribution affects fault/fracture orientations and seismic anisotropy, and we use S-wave and high-resolution 3D seismic data to infer stress regimes in and around the active seep site and study the effect of stresses on seepage. We observe the occurrence of changes in dominant fault/fracture and

horizontal stress orientations in and around Lunde Pockmark and conclude minimum (NE-SW) and maximum (SE-NW) horizontal stress directions. Our analysis indicates a potential correlation between hydrofractures and horizontal stresses, with up to a ~32% higher probability of alignment of hydrofractures and faults perpendicular to the inferred minimum horizontal stress direction beneath the Lunde Pockmark area.

Key points

- The S-wave analysis using ocean-bottom seismic (OBS) data indicates seismic anisotropy around a seeping Pockmark on the W-Svalbard Margin.
- The occurrence and orientation of symmetry planes in shallow anisotropic sediments vary across the pockmark.
- Combined analyses using S-wave and 3-D Seismic data suggest that preferred fault and fracture orientations follow local stress conditions.

Plain language summary

Hydrocarbon gases, mostly methane, leak from the seabed into the ocean at different locations worldwide. Methane is a potent greenhouse gas, therefore understanding the natural processes of methane release has important implications for climate research. We investigate the role of regional and local stresses in controlling an ongoing gas leakage at Vestnesa Ridge, offshore west-Svalbard. For this, we study the behavior of shear (S)-waves, recorded by 22 sensors on the seabed, around a geological feature (pockmark) that releases methane at the present day. S-waves propagate in relation to the orientation of subsurface faults, fractures and stresses. S-wave data analysis indicates a change of stress in shallow (<150-200 m below the seafloor) sediments across the pockmark. We observe that the preferred orientation of fractures releasing methane into the ocean, matches the orientation of the stresses predicted from the wave analysis. This study advances our understanding of the influence of local and regional geological processes on the release of methane from the seabed.

Keywords: S-wave analysis, converted shear (PS) waves, ocean-bottom seismometer (OBS), fluid seepage, anisotropy, stress, fault analysis.

6.1. Introduction

Fluid leakage occurs in different sedimentary basins and various geological settings globally and is often facilitated by vertical columnar zones, commonly known as e.g., gas chimneys, vent pipes or mud volcanoes (e.g., Bünz et al., 2003, 2012; Cartwright et al., 2007; Cole et al., 2000; Gay et al., 2007; Hovland & Sommerville, 1985; Karstens & Berndt, 2015; Løseth et al., 2011; Moss & Cartwright, 2010a,b). In places where fluids reach the seabed, they may seep into the water column. Such active fluid seepage, consisting mostly of methane, occurs at various locations in the Arctic, and it has special importance due to elevated impacts of global warming and increasing ocean-water temperatures, that in turn affect the stability of gas hydrates and free gas reservoirs (Ketzer et al., 2020; Phrampus & Hornbach, 2012; Portnov et al., 2016; Westbrook et al., 2009). Recurrent seafloor seepage leads to the formation of seafloor depressions, known as pockmarks (Hovland et al., 2005; Sultan et al., 2010, 2014). Several tens of pockmarks occur at the crest of Vestnesa Ridge, a sedimentary drift on the western-Svalbard Margin (Figure 1b-c and 2; Vogt et al., 1994; Bünz et al., 2012). Many of the pockmarks on the eastern segment of Vestnesa Ridge actively seep gas into the water column and show gas-chimney features in subsurface data below them (Vogt et al., 1994; Bünz et al., 2012; Plaza-Faverola et al., 2015). Why seepage is sustained exclusively at few pockmarks on the eastern Vestnesa Ridge segment is the question that motivates our study of shallow stress and anisotropy. Previous studies have hypothesized that the eastern Vestnesa Ridge segment is under an extensional stress regime that facilitates fracture/fault dilation and favors gas release via fluid advection (Plaza-Faverola et al., 2015; Plaza-Faverola & Keiding, 2019). However, the western segment may be under a more compressive regime, where any potential gas release

would occur at lower rates, for example, via diffusion (Plaza-Faverola & Keiding, 2019; Ramachandran et al., 2022).

Permeability, availability of gases along with various other factors (e.g., topography, stress directions, hydrate formation, pore pressure and other petrophysical properties like porosity, grain size, etc.) control the seepage through a gas chimney (Liu et al., 2019; Ramachandran et al., 2022). Chimneys have a higher secondary permeability (i.e., one created by faults/fractures/cracks) compared to surrounding sediments, mainly due to a series of interconnected subvertical or radial fractures, which facilitate the vertical flow of gas as well as gas hydrate accumulations in the shallow subsurface (Liu & Flemings, 2007; Cartwright et al., 2007; Cartwright & Santamarina, 2015). Gas overpressure forms self-enhanced hydrofractures, which are a major cause of secondary permeability in gas chimneys (Daigle et al., 2011; Ramachandran et al., 2022). Permeability, especially one driven by faults and fractures, is dependent on stress orientations and often changes with a change in stress direction (Rutqvist, 2015; Zheng et al., 2015). The present-day effective stress fields might help with opening or closing of pre-existing faults and fractures, depending on orientations of stress fields and faults/fractures. Gravitational stress due to seafloor topography is a particularly important contributor in the overall stress field at shallow depths. It is also important to study at which depths tectonism-related stresses dominate over gravitational/slope related stresses (Haacke et al., 2009). The in-situ measurement of stress in marine sediments is expensive and instruments do not penetrate very deeply (>5 m) (Lunne et al., 1997; Boggess & Robertson, 2011). Therefore, remote methods are necessary to study stress fields in sediments. The most conventional approach relies on subsurface seismic imaging of faults and fractures, developing tectonic stress models and linking them together to get a comprehensive understanding of the subsurface stress field.

6. Stress constraints from shear-wave analysis in shallow sediments at an actively seeping pockmark on the W-Svalbard Margin

Seismic anisotropy affects shear (S)-wave propagation in the subsurface (e.g., Hudson, 1981; Crampin, 1981, 1984, 1985, 1993a; Willis et al., 1986; Schoenberg & Douma, 1988; Simmons, 2009). The Study of fault/fracture properties and stress orientations by analyzing S-waves has been implemented successfully at different continental margins (Evans et al., 1987; Zinke & Zoback, 2000; Haacke et al., 2009; Exley et al., 2010; Pastori et al., 2019; Robinson et al., 2022). The intensity of seismic anisotropy is mostly related to the fault/fracture density and their alignment (e.g., Leary et al., 1987; Mueller, 1992). S-waves split into fast- and slow-propagating components in an anisotropic medium, with fast S-wave polarization preferentially aligned parallel to fault/fracture/cracks/maximum principal horizontal stress direction, (Crampin, 1985; Li, 1997; Crampin, & Peacock, 2008; Robinson et al., 2022). In shallow sediments, where vertical stress dominates over horizontal stresses, the directions of maximum and minimum horizontal principal stresses are often aligned parallel and perpendicular with the primary linear fabric (e.g., cracks, fractures, faults, crystal preferred orientation) of a medium, respectively (Hubbert & Willis 1957; Evans & Brereton, 1990). The analysis of azimuthal variations of S-waves amplitudes using recorded seismographs can help us to identify the polarizations of the fast- and slow-S-waves, and, hence, constrain fault/fracture and stress properties in shallow sediments (Haacke & Westbrook, 2006; Exley et al., 2010).

By implementing integrated S-wave and 3D seismic data analysis, our aim is to study subsurface anisotropy in shallow (< 250-300 m) sediments below the seafloor at an active seep site on Vestnesa Ridge. Concretely, we are interested in understanding the relationship between anisotropy, the orientation of faults and fractures and seepage distribution through vertical pathways. We discuss our observations in relation to processes that exert a control on gas seepage activity in this deep marine Arctic setting (e.g., topography, sediment cohesion, gas saturation and distribution, pore pressure, lithology, etc.).

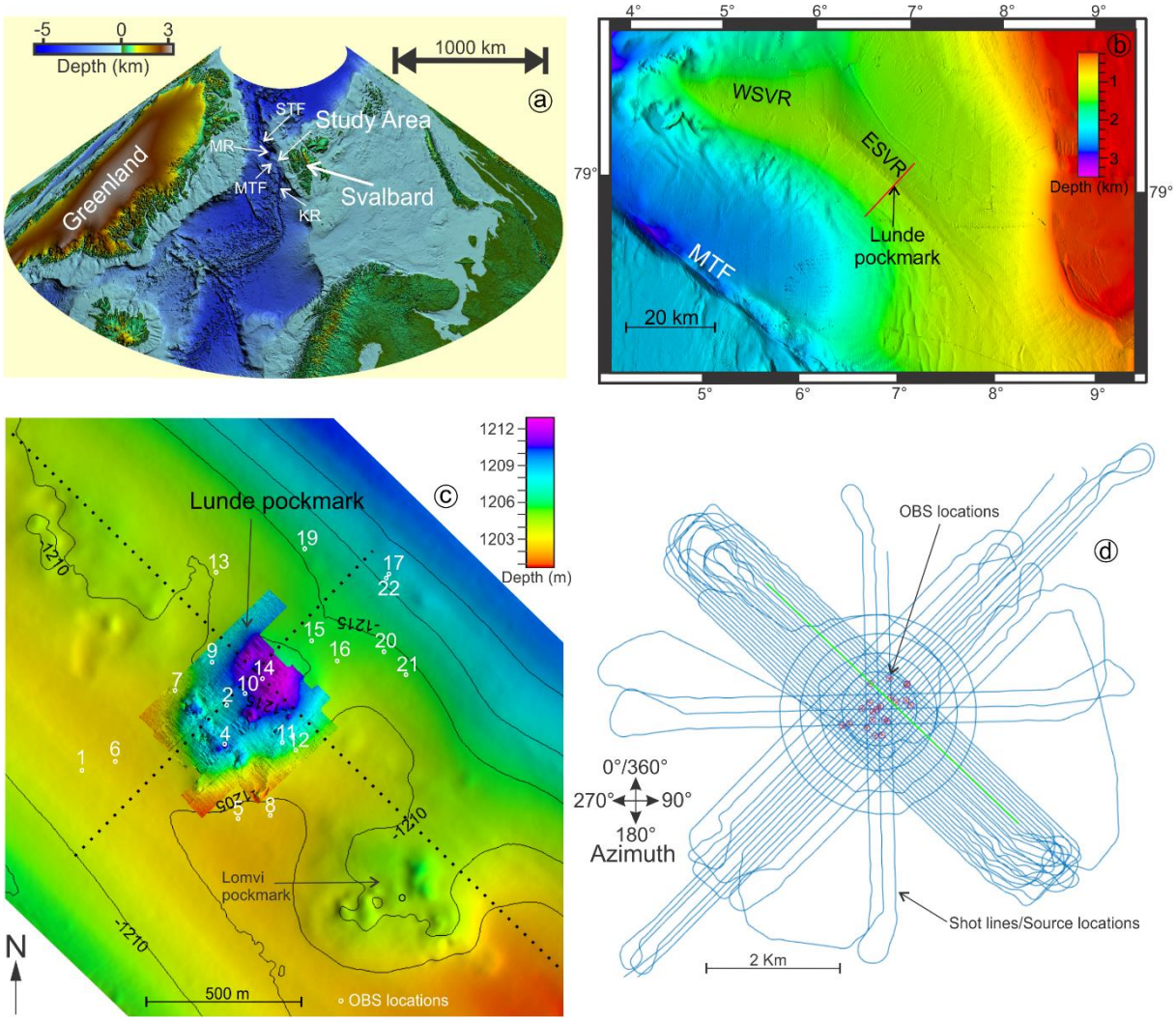

Figure 6.1: a) Regional map showing the location of the study area along with Knipovich Ridge (KR), Molloy Transform Fault (MTF), Molloy Ridge (MR), Spitsbergen Transform Fault (STF). b) Bathymetry map showing various pockmark features along Vestnesa Ridge (ESVR-eastern segment of Vestnesa Ridge and WSVR-western segment of Vestnesa Ridge) and the location of Lunde Pockmark on Vestnesa Ridge. c) Relocated OBS positions (shown in white circles) are laid over the seafloor map picked from 3-D seismic data and high-resolution bathymetry map of Lunde Pockmark. Dotted lines show location of inline and crosslines seismic sections in Figure 2. d) Location of different shots fired using seismic source and red points show the relocated OBS positions. The green line shows shot locations for data shown in Figure 3.

6.2. Study Area

Vestnesa Ridge is a contourite sedimentary drift in the western Svalbard margin and northeast to the Molloy Transform Fault in ~79° N (Eiken and Hinz, 1993; Vogt et al., 1994; Figure 1b-c). The ridge is at a water depth of ~1000 m to ~1700 m and has up to ~100 m elevation

relative to the deeper side towards the continental shelf (Figure 1b). The sediment drift bends anticlockwise from SE-NW to ESE-WNW in the north (Figure 1b) where it terminates at the Molloy Ridge. In previous studies, the SE-NW and ESE-WNW oriented segments are referred as the eastern and western segments, respectively; and we will also follow the same naming convention (Figure 1b). The occurrence of contourite mounds, moats and migrating wave features in the region indicate sedimentation under the influence of bottom water contour currents (Eiken & Hinz, 1993; Ottesen et al., 2005; Stein et al., 2005). Sedimentary deposits along the western Svalbard margin slope consist mostly of turbiditic, glaciomarine and hemipelagic sediments (Howe et al., 2008). Sediment core analyses from nearby ODP wells reveal a high (~105 cm/yr) sedimentation rate, mostly of silty turbidites, from the mid Weischselian to the Last Glacial Maximum (LGM) and followed by a relatively slow (<10 cm/yr) sedimentation rate, mostly of muddy-silty contourites with abundant ice-rafted debris, from the LGM to the early Holocene (Forsberg et al., 1999; Eiken & Hinz, 1993; Howe et al., 2008).

Acoustic flares from six pockmarks on the eastern segment of the ridge are profusely evident (up to 400 m water depth from the seafloor) in sonar data (Smith et al., 2014). Lunde Pockmark is one of them (Panieri et al., 2017; Figure 1c and 2). It is a ~400-500 m wide complex structure, with small- (~0-10 m) to medium-scale (~10-50 m) depression features, referred to as pits, within the overall perimeter of the pockmark (Figure 1c; Panieri et al., 2017; Himmler et al., 2019). Hydroacoustic and seismic data show an intense advective gas release occurring through these pits, whereas slow diffusive gas release is more likely to dominate elsewhere within the pockmark (Panieri et al., 2017; Hong et al., 2016, 2021). Present-day seepage is not evident from sonar data in the western segment of the ridge; however, the occurrence of pockmarks and gas chimney features indicate fluid seepage activity in the past (Plaza-Faverola et al., 2015). Even at the Lunde Pockmark site, seepage activity has changed over time scales of thousands

of years; and several methane seepage episodes have been documented via sampling and dating of authigenic carbonate for the last ca. 160,000 years (Himmler et al., 2019).

The gas hydrate stability zone (GHSZ) in marine sediments along Vestnesa Ridge is ~140-200 m thick (i.e., from seafloor to ~140-200 m below the seafloor (bsf)) (Plaza-Faverola et al., 2017; Singhroha et al., 2019). Ideally, hydrocarbon gases in the presence of water should form hydrates in the GHSZ. However, if the gas supply and pressure is above a certain point, seepage occurs even if gas hydrate stability conditions are met (Ramachandran et al., 2022; Domel et al., 2022). Gas hydrates have been recovered through drilling (Himmler et al., 2019), as well as sampling of near seafloor sediments (Panieri et al., 2017) from Lunde Pockmark. Seismic studies suggest a ~190-195 m thick GHSZ below Lunde Pockmark (Bünz et al., 2012; Singhroha et al., 2019).

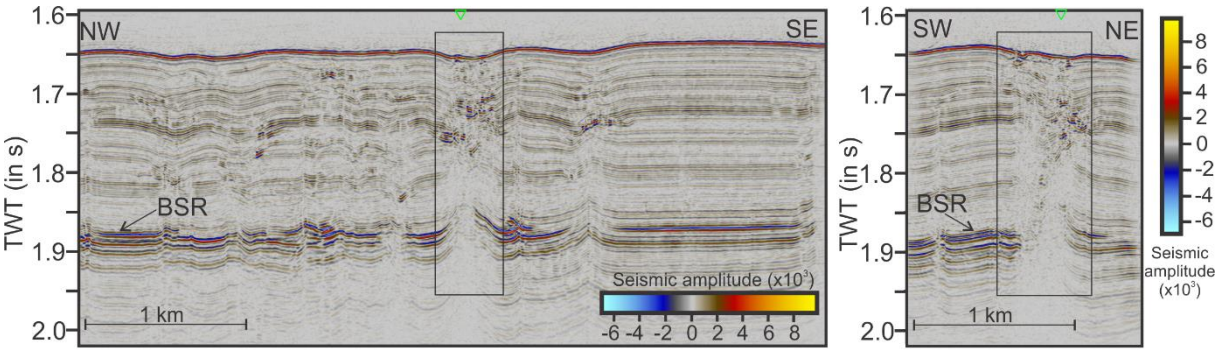

Figure 6.2: Inline and crossline seismic sections imaging the Lunde Pockmark (inside the rectangle). Inline and crossline locations are shown by black dotted lines in Figure 1c. Locations at the top (marked in green) show the intersection of the inline and crossline.

Structural background

The continental break-up and seafloor spreading in the early Eocene along Reykjanes, Aegir, and Mohns Ridges, followed by a change in the plate motion (~33 Ma) between Svalbard and Greenland from strike slip to oblique divergence, led to the initial formation of Fram Strait (Demenitskaya & Karasik, 1969; Talwani & Eldholm, 1977; Eldholm et al., 1987; Vogt, 1986;

Myhre & Eldholm, 1988). The shearing along faults between Greenland and Svalbard resulted in the Western Spitsbergen Orogeny, which continued until the early Oligocene, when the spreading direction changed from NNW-SSE to NW-SE (Harland et al. 1974, Steel et al. 1985).

The opening formed Spitsbergen Shear Zone, which developed into an asymmetric, ultra-slow and obliquely spreading ridge system in the region. This rifting system continued as an asymmetric pure shear or a high angle simple shear mode, pivoted around a system of faults adjacent to the continental margins of Svalbard (Johnson et al., 1972; Vogt et al., 1982; Kovacs & Vogt, 1982; Nunns & Peacock, 1983; Nunns, 1983). By the end of the Oligocene (~23 Ma), rifting shifted northwards along Molloy Ridge. The process of continental break-up continued, opening up Fram Strait by 10-15 Ma for deep water circulation, establishing bottom water-current driven sedimentary drifts (Jakobsson et al., 2007; Ehlers & Jokat, 2009; Johnson et al., 2015).

At present, shearing along Spitsbergen Transform Fault and rifting at Knipovich and Molloy Ridges influence overall stresses at a regional scale. The effect of these forces can also be seen in the formation of half graben structures with bounding faults rooted deep in the basement and dipping towards the ridge axis (Amundsen et al., 2011). These deep-rooted faults in the region provide pathways for fluid flow and bring deep crustal fluids into the sedimentary cover (Waghorn et al., 2018; Madrussani et al., 2010). Analytical tectonic stress modeling predicts an extensional stress, due to oblique spreading, in an area extending northward from Knipovich Ridge, encompassing the eastern Vestnesa Ridge segment (Plaza-Faverola & Keiding, 2019). Glacial stress modelling predicts low magnitudes (<6 MPa) of maximum and minimum horizontal stresses in the region comprising the eastern Vestnesa Ridge segment due to isostatic adjustment of the ice-sheets forebulges (Vachon et al., 2022). Glacial stresses are in addition to the background tectonic stresses, whose magnitudes at Vestnesa Ridge are unknown. A northward progradation of the extensional stress regime from Knipovich Ridge affects fault

behavior in the eastern segment of Vestnesa Ridge (Crane et al., 2001; Vanneste et al., 2005; Plaza-Faverola & Keiding, 2019). NW-SE trending sedimentary faults are aligned nearly parallel to the modeled maximum tectonic stress direction in the eastern segment of Vestnesa Ridge, which favors the occurrence of seepage (Plaza-Faverola et al., 2015; Plaza-Faverola & Keiding, 2019). However, whether overpressured fluids create faults and fractures or pre-existing faults and fluids act as pathways for the upward migration of fluid is still an unanswered question in this area. An upward fluid flow through faults can be obstructed at shallower depths, because of the formation of gas hydrates or due to changes in stress regimes in shallow sediments, as both effects can reduce secondary permeability in the system (Liu et al. 2019).

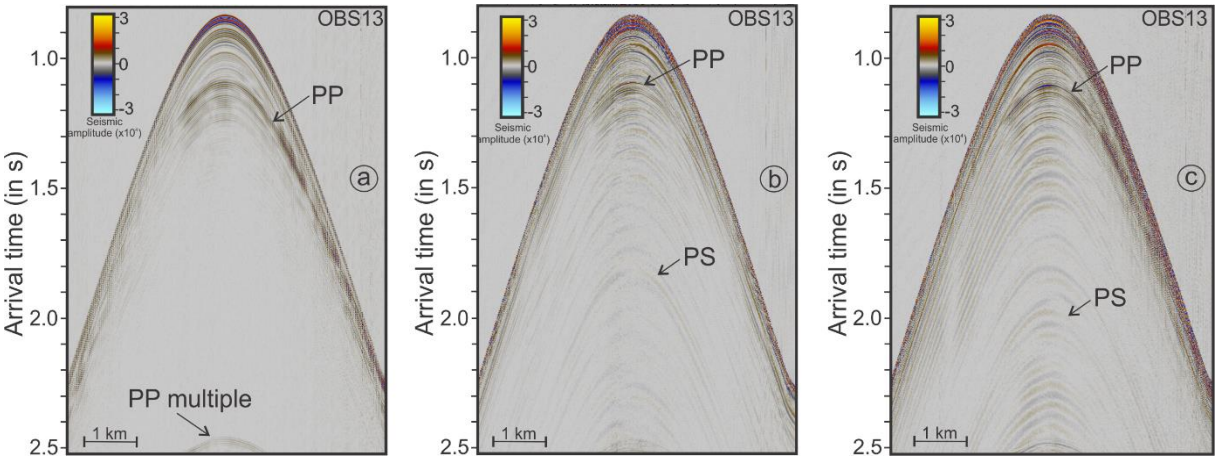

Figure 6.3: Seismic data recorded by vertical (a) and horizontal (b-c) components of OBS13 instrument from shot numbers 9757-10190 (shot locations plotted in green in Figure 1d).

6.3. S-wave in anisotropic media

S-wave splitting depends upon seismic anisotropy which in turn most often depends on subsurface stress distribution (Crampin, 1981; Alford, 1986). The physical mechanism behind S-wave splitting and polarization is still a debatable topic, which creates conflicting interpretation of similar results (Crampin & Peacock, 2008). The presence of aligned fluid-filled micro-cracks/fractures (Crampin, 1987; Crampin & Gao 2008), macroscopic structural features (for example, faults and fractures) oriented in one preferred direction (Pastori et al.,

2019; Zinke & Zoback, 2000), and preferential alignment of minerals (Brocher & Christensen, 1989; Nascimento et al., 2002; Liu et al., 2004; Crampin & Lovell, 1991) are commonly interpreted causes of anisotropy leading to S-wave splitting.

The preferential alignment of minerals cannot cause anisotropy in shallow (<300 m) poorly consolidated sediments at Vestnesa Ridge, as this process becomes dominant in fully consolidated metamorphic rocks (Zinke & Zoback, 2000). In addition, the hypothesis of aligned minerals affecting shear-wave polarization is not a universally accepted, as Crampin and Peacock (2008) give strong evidence in favor of rejecting this hypothesis.

Near-vertical faults and fractures often expressed as vertical fluid migration pathways along Vestnesa Ridge (Plaza-Faverola et al., 2015; Singhroha et al., 2016, 2020) suggests that the orientation of faults and fractures may be an important cause of anisotropy in this setting. Tensional faults and fractures form perpendicular to the minimum horizontal stress direction (Pastori et al., 2019; Zinke & Zoback, 2000; Evans & Brereton, 1990). In shallow sediments, where vertical stress dominates over horizontal stresses, hydro-fractures, created by trapped overpressured fluids, are also typically preferentially oriented perpendicular to the direction of minimum principal stress (Hubbert & Willis 1957).

Crampin and Peacock (2008) argue that stress-aligned fluid-saturated microcracks should be the default interpretation of azimuthally aligned S-wave splitting, and they further argue that other interpretations are either fallacious or have few supporting arguments. Small-scale seismic wave induced stresses interact in a non-linear fashion with effective differential stresses in fluid saturated media, which results in the polarization of fast-S-waves aligned parallel to the maximum principal horizontal stress direction (Zatsepin & Crampin, 1997; Crampin & Zatsepin, 1997, Crampin & Peacock, 2008). It is therefore reasonable to associate S-wave splitting from sub-seabed sediments of Vestnesa Ridge with principal horizontal stresses, with

the polarization of fast S-waves occurring parallel to the maximum horizontal principal stress direction (more arguments provided in supplementary text S1).

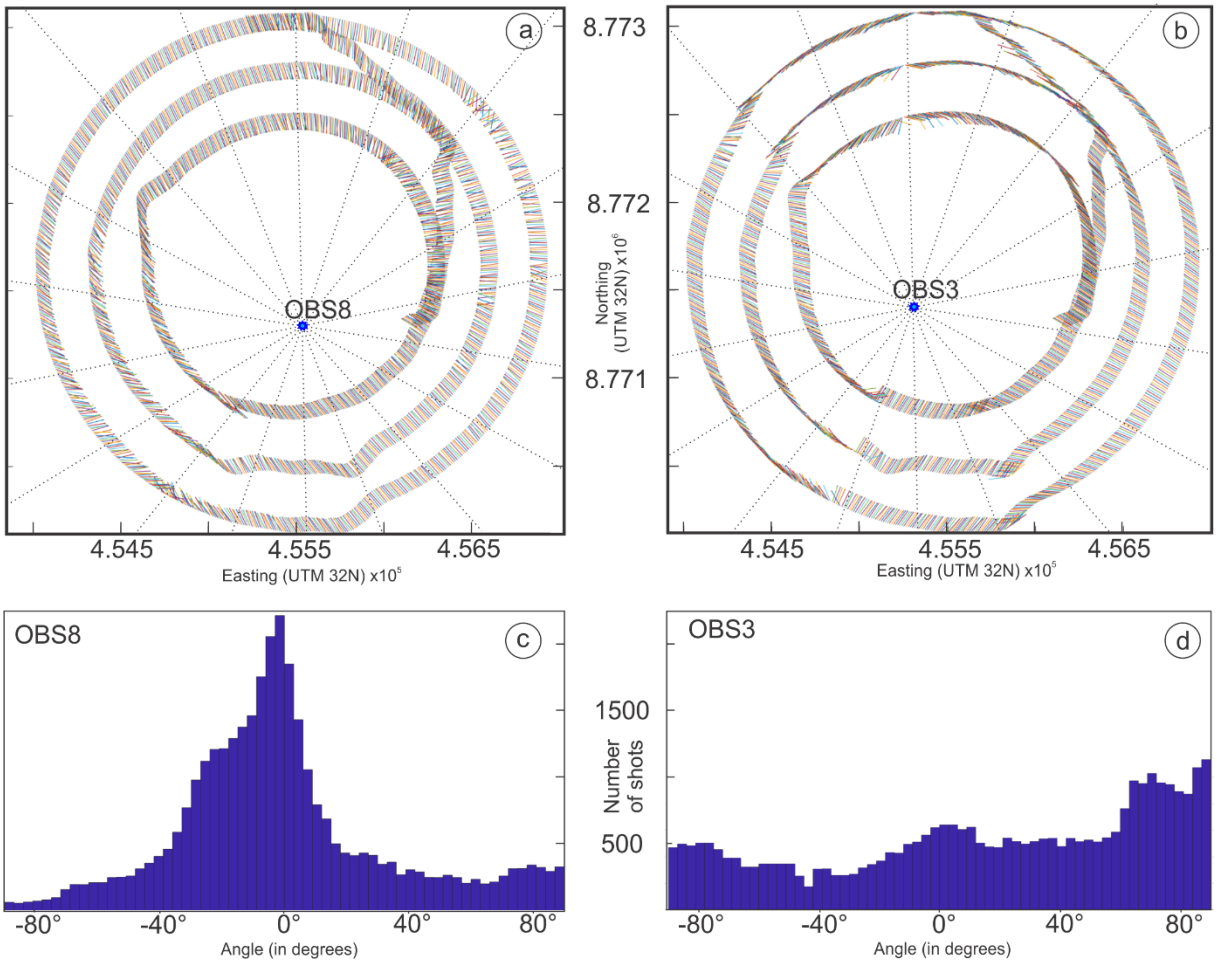

Figure 6.4: Vector fidelity plots for OBS8 (a) and OBS3 (b) show the first S-wave arrival polarization azimuth and OBS locations (blue dots). The center of plotted vectors (a-b) is the position of shot and dotted radial lines from the OBS locations show the radial direction from both OBS8 (a) and OBS3 (b). The histogram plots for OBS8 (c) and OBS3 (d) show the distribution of the difference angle (corrected first S-wave arrival polarization azimuth – radial azimuth; more details in the supplementary Text S2) for different shots.

6.4. Data

During a research expedition (CAGE-2019-1: 29/06/2019-08/07/2019) on-board R/V Helmer Hanssen, we acquired ocean bottom seismic data using an array of 22 ocean bottom seismometers (OBS) around Lunde Pockmark on the eastern segment of Vestnesa Ridge, W-

Svalbard Margin (Figure 1). The OBS instruments were equipped with a three-component seismometer and a hydrophone to record the seismic wavefield.

The OBS distribution and survey configuration were intended to maximize the chances of studying the anisotropy in and around the pockmark (Figure 1c-d). OBS stations were initially planned as a dense grid with 250-350 m spacing between stations covering an area close to and within Lunde Pockmark. However, it was not possible to deploy the OBS equipment with a high spatial precision on the seafloor, due to the failure of an USBL (ultra-short baseline) release system. Consequently, the OBSs were freely dropped in the water, and they drifted sideways as they sank through the water column, landing on the seafloor at locations different to the planned positions (Figure 1c-d). We used the least-squares inversion of direct-arrival travel-times to precisely relocate the instruments. A large number (>33000) of shots from different directions constrained OBS positions, with an expected error in OBS locations of less than 1 m (Figure 1c-d; Table S1). The position of OBSs with respect to the seafloor pockmark was considered suitable for the analyses of S-waves despite the divergence from the planned positions.

A total of 50 seismic profiles (i.e., air gun trajectory) were shot around these stations (Figure 1d). In addition, we recorded several shots along circular trajectories (Figure 1d). These inlines, crosslines and circular trajectories ensured a good azimuthal coverage (Figure 1d). Weather conditions were good (<1 m high waves) throughout the experiment. The seismic signal was generated using a mini generator-injector (GI) air gun (Sercel) configured as 30/30 in^3. The air gun generated signal with frequencies up to 300 Hz at the shot interval of 5 s. OBS data were recorded at a sampling rate of 0.5 ms (OBS1-20) and 0.4 ms (OBS21-22). Data processing after relocation of the instruments included band pass filtering using frequency ranges between 5-100 Hz, depending on the signal to noise ratio characteristic of each instrument. Low frequency

components of the signal were preserved, since a significant portion of the converted shear energy appear in the low frequency range (<20 Hz).

Table 6.1: Analysis of recorded dataset from different OBS stations.

Station	vector fidelity	PS S/N ratio	Seismometer tilt	Overall quality
OBS1	Bad	Bad	No	Bad
OBS2	Average-Bad	Good	No	Medium
OBS3	Bad	Bad-Average	No	Bad
OBS4	Average-Bad	Good	No-(very small)	Medium
OBS5	Average-Bad	Bad	No-(very small)	Bad
OBS6	Good	Good	Medium	Medium-Good
OBS7	Average-Good	Good	no	Medium-Good
OBS8	Very good	Good	no	Very good
OBS9	Good	Good	yes	Medium-Good
OBS10	Bad	Good	Medium	Bad
OBS11	Good-very good	Good	yes	Medium-Good
OBS12	Average-Good	Good	yes	Medium
OBS13	Good	Good	no	Good
OBS14	Very good	Average	yes	Medium
OBS15	Good	Good	no	Good
OBS16	Average-Bad	Good	no	Medium
OBS17	Good	Average-Good	yes	Medium-Good
OBS18		Bad PP and PS records		Bad
OBS19		Bad PS records		Bad
OBS20		Bad PS records		Bad
OBS21		Bad PS records		Bad
OBS22	Average	Good	No	Medium-Good

Data quality control (QC)

Down-going P-wave energy is reflected into upcoming P (PP)-wave and converted S (PS)-wave. PS-waves are recorded in horizontal seismometer components and are used in our S-wave analysis. We analyzed the quality of recorded S-wave data using three parameters/approaches: i) signal/noise (S/N) ratio, ii) seismometer tilt and iii) vector fidelity analysis (Table 1). Any tilt from the vertical axis due to the placement of the seismometer will lead to a distribution of S- and P-wave energies in all three components of the seismometer. The S/N ratio decreases with increase in the noise, and the S-wave energy increases in the

vertical component of the seismometer with increase in the seismometer tilt. The S/N ratio of S-waves in horizontal components and the seismometer tilt can be visually inspected by looking at all three components of the recorded OBS dataset (Table 1 and Figure 3). The absence of good strength of S-wave energy in horizontal components is primarily due to the poor coupling between sediments and the seismometer. A poor coupling can occur due to bad placement of the seismometer on the seafloor. An ideally placed seismometer with no tilt will record S-and P-wave energies in horizontal and vertical components of the seismometer, respectively (Figure 3). By visual inspection we classify the OBS datasets as good/medium/bad based on the S/N ratio and seismometer tilt (Table 1).

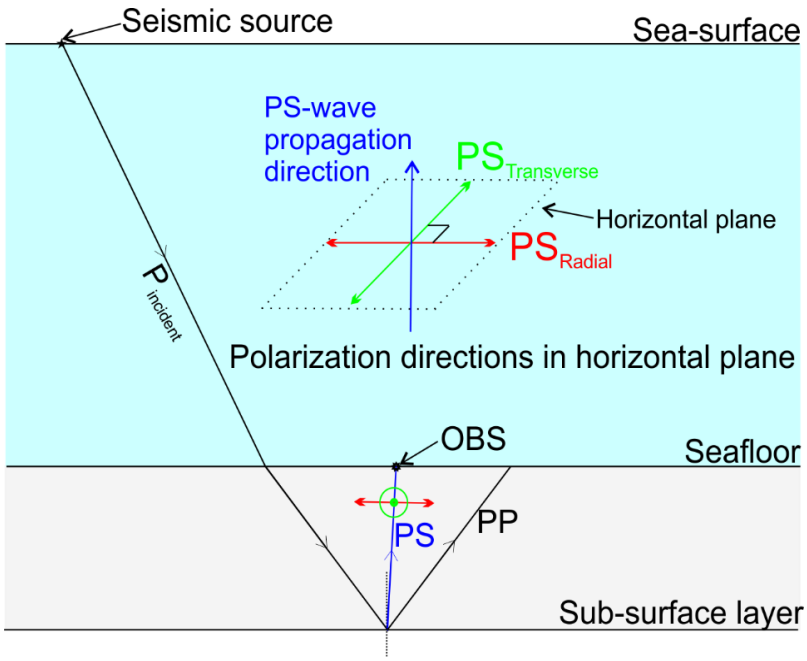

Figure 6.5: Schematic of the radial (shown using the red color) and transverse (shown using the green color) polarization directions for a near-vertically reflected converted PS-wave (shown using the blue color).

Vector fidelity analysis

The vector fidelity analysis is carried out to ensure that the orientation of particle motion in recorded data matches with the orientation of the arriving wavefield (e.g., Exley et al., 2010; Figure 4 and S1-8; Text S2). A bad vector fidelity can be primarily due to the bad quality of sensors inside a seismometer (e.g., differences in the sensitivity of horizontal components),

instrumentation (e.g., electronics) related noises, and roughness of the surface on which a seismometer is placed (Exley et al., 2010).

We analyze the vector fidelity of data recorded in the different datasets using the particle motion of first S-wave arrivals from different shots (Figure 4). The consistent median difference observed in the particle motion and the shot-receiver directions is used to derive the orientations of the two horizontal components. After correcting for the horizontal-component orientations, the deviations observed in different shots between particle motion and shot-receiver directions are used to study the vector fidelity of the seismometer (Figure 4). In a seismometer with a good vector fidelity, the orientation of particle motion inferred from the first arrivals will roughly match the orientation between source and receiver (Figure 4a, c). On the contrary, for data sets with a bad vector fidelity, the particle motion direction cannot be related with sufficient confidence to the direction of the arriving wavefield (Figure 4b, d; more details on vector fidelity analysis provided in supplementary text S2).

This QC process ensures that the particle motion analysis using S-waves converted at greater depths is reliable. Based on the vector fidelity analysis results, we classify different OBS stations as good/medium/bad (Table 1).

Using the three approaches discussed above, we qualitatively classify data from all OBS stations (Table 1) and select nine OBS stations for further analysis, which satisfy all three conditions as either medium or good. Out of these nine stations, two stations (OBS13 and OBS15) can be classified as good stations and one station (OBS8) as a very good station, with a good/very good quality data assessment from all three approaches used for classification (Table 1).

6.5. Methods

When an incoming P-wave encounters a seismic reflector, a part of its energy gets reflected in the form of P-wave (PP) and another part gets reflected as S-wave (referred as converted/PS-wave) (Figure 5). The polarization of this PS-wave in an isotropic medium is in the radial direction (Figure 5). The radial direction is the direction from which the incident P-wave arrives to the receiver, and perpendicular to this is the transverse direction (Figure 5). The distribution of PS energy in radial and transverse components depends on the anisotropy in a medium (Haacke & Westbrook, 2006; Haacke et al., 2009; Exley et al., 2010; Robinson et al., 2022). The PS-wave energy splits along fast and slow S-wave polarization directions in an anisotropic medium and hence the transverse direction also receives energy (Haacke & Westbrook, 2006; Exley et al., 2010). When the radial direction (the direction of arriving P-wave energy) matches with a plane of symmetry in an anisotropic medium, the amount of energy in the transverse direction is smaller compared to other directions (Crampin, 1981). Hence, by looking at the PS-energy in the transverse component, we can reveal the splitting of energy in fast and slow S-wave components and can also identify planes of symmetry in an anisotropic medium.

We assume that the geological system we are investigating (i.e., characterized by near-vertical faults and fractures) can be best studied by assuming horizontal transverse isotropic (HTI) medium (i.e., a medium with vertical faults and fractures predominantly oriented along one orientation). The planes along and perpendicular to vertical faults and fractures are symmetric planes in a HTI medium. If the radial direction matches with one of the symmetry planes of a HTI medium, the energy in PS transverse component is less compared to other directions (Schutt et al., 1998; Pastori et al., 2019). This happens because the planes of HTI symmetry also match with fast and slow S-wave polarization directions, and S-wave splitting is minimal when radial direction matches with fast or slow S-wave polarization direction (Crampin, 1981). Hence, a relative decrease in energy along certain azimuths in the transverse direction indicates

axis of HTI symmetry, fast or slow S-wave polarization direction, and direction parallel or perpendicular to predominant fault- and fracture-orientation (Li, 1998; Robinson et al., 2022). The fast-polarization direction is expected to be parallel to the maximum horizontal stress (Shmax) direction (Crampin & Peacock, 2008; Pastori et al., 2019).

The analysis of S-wave splitting in an anisotropic medium with HTI symmetry can be best performed by transforming the data into an alternative radial-transverse coordinate system (Haacke & Westbrook, 2006; Exley et al., 2010). The radial-transverse rotation of data can be achieved in two ways: i) reorienting data by maximizing the first S-wave arrival energy in the radial component of each shot, or ii) finding an optimum solution (using the entire dataset) for the orientation of horizontal components of a seismometer from the particle motion of first S-wave arrivals, and then using these orientations to align energy parallel to the arriving wavefield (radial) and perpendicular to the arriving wavefield (transverse) directions (Figure 5). Considering that a seismometer gets placed in the sediment at the beginning of the survey, the directions of horizontal components are fixed throughout the survey. Hence, we use the second approach and perform the radial-transverse rotation of data using estimates of orientations of horizontal components and shot-receiver directions. This approach does not always ensure maximization and minimization of the first S-wave arrival energy in radial and transverse components, respectively. However, it provides a better rotation of data from greater depths, as first S-wave arrivals from a single shot can be influenced by a local very-shallow depth anisotropy and may not be an optimum criterion for the rotation of the entire data from that shot.

The lack of energy in certain azimuths in a transverse component, hereafter referred to as energy nulls, indicates the axes/directions of symmetry planes in an anisotropic HTI medium (Figure 6) (i.e., based on the HTI assumption). In a homogeneous anisotropic medium, peaks and troughs of energy occur twice (i.e., 2 energy minima with 180° azimuth spacing) in the radial

component and four times (i.e., 4 energy nulls with 90° azimuth spacing) in the transverse component (Exley et al., 2010). In a HTI medium, one of the energy null symmetry axes in the transverse component corresponds to the fast-polarization direction, whereas the other symmetry axis (i.e., perpendicular to the first axis) corresponds to the slow-polarization direction (Robinson et al., 2022).

Shot selection, binning and stacking

The entire survey consists of 33774 shots. We sort recorded shots using their azimuth and offset for each OBS station. Shots are grouped in 360 azimuths (with each shot grouped to the nearest azimuth). For example, the azimuth of 1° contains all shots with azimuths lying between 0.5°-1.5°. Next, we also sort the common azimuth in relation to offset, with offsets grouped in 250 m long radial bins. Then we combine shots from azimuth and offset groups in their corresponding bins. For example, all shots from azimuths of 0.5°-1.5° and offsets 750-1000 m are put together in one bin. After applying moveout correction (using velocity analyses from Singhroha et al., 2019) and rotating the data to the radial-transverse domain, the shots in each bin are stacked together.

We have stacked data to 2.4 s arrival-time to not include P-wave multiple reflections (Figure 3), which would negatively affect the S-wave analysis. This is especially important since we aim to find azimuths where seismic energy is low, and the presence of noise will degrade the overall quality of contrast between azimuths with low and high energy in the transverse component section. The primary PP signal will also contaminate the data in the 0.8-1.1 s arrival-time interval. We expect a good separation of low and high energy azimuths within the 1.1-2.4 s arrival-time interval, where there is no primary or multiple PP energy (Figure 3).

Energy conversion from P-wave to S-wave at a seismic reflector (Figure 5) is a function of the incident angle, and by dividing data in offset groups of 250 m, we take the utmost care to avoid

a biased interpretation due to differences in incident angles. However, we find no significant differences in amplitudes, neither in the radial nor the transverse component for 750-1000 m, 1000-1250 m and 1250-1500 m offset groups. Here, we present stacked results with 750-1500 m offset to ensure a complete azimuthal coverage and a high signal to noise ratio. The offset range (750-1500 m) is optimal in terms of improving the overall detectability of amplitude nulls, while ensuring the effect of angular dependence of PP-PS energy conversion remains insignificant.

6.6. Results

The occurrence of S-wave splitting is evident in different OBS stations (Figure 6-7). In most OBS stations, there are visible variations in the amplitude with azimuth in the transverse component (Figure 6-7). All OBSs commonly show energy along all azimuths in the radial and transverse sections within the 0.8-1.1 s arrival-time interval. Barring a few exceptions (Figure 6-8): in OBS6, OBS9 and OBS11, we see azimuths with a low energy (e.g., azimuths of: 0°-40°, 180°-220° in OBS6 radial, 115°-125° in OBS9 transverse, 350°-70° in OBS11 radial and 310°-350° in OBS11 transverse components), although most of them are associated with polarity changes (Figure 6a-b, Figure 6g-h and Figure 7a-b). Energy anomalies in the radial and transverse sections have clear separation in OBS6, OBS8 and OBS9 compared to OBS7 or OBS13 (Figure 6). The vector fidelity analysis shows that OBS6, OBS8 and OBS9 have better quality than for example OBS7. As expected, stations with the high-quality vector fidelity, separate transverse and radial energies better and amplitude nulls are sharper at these sites.

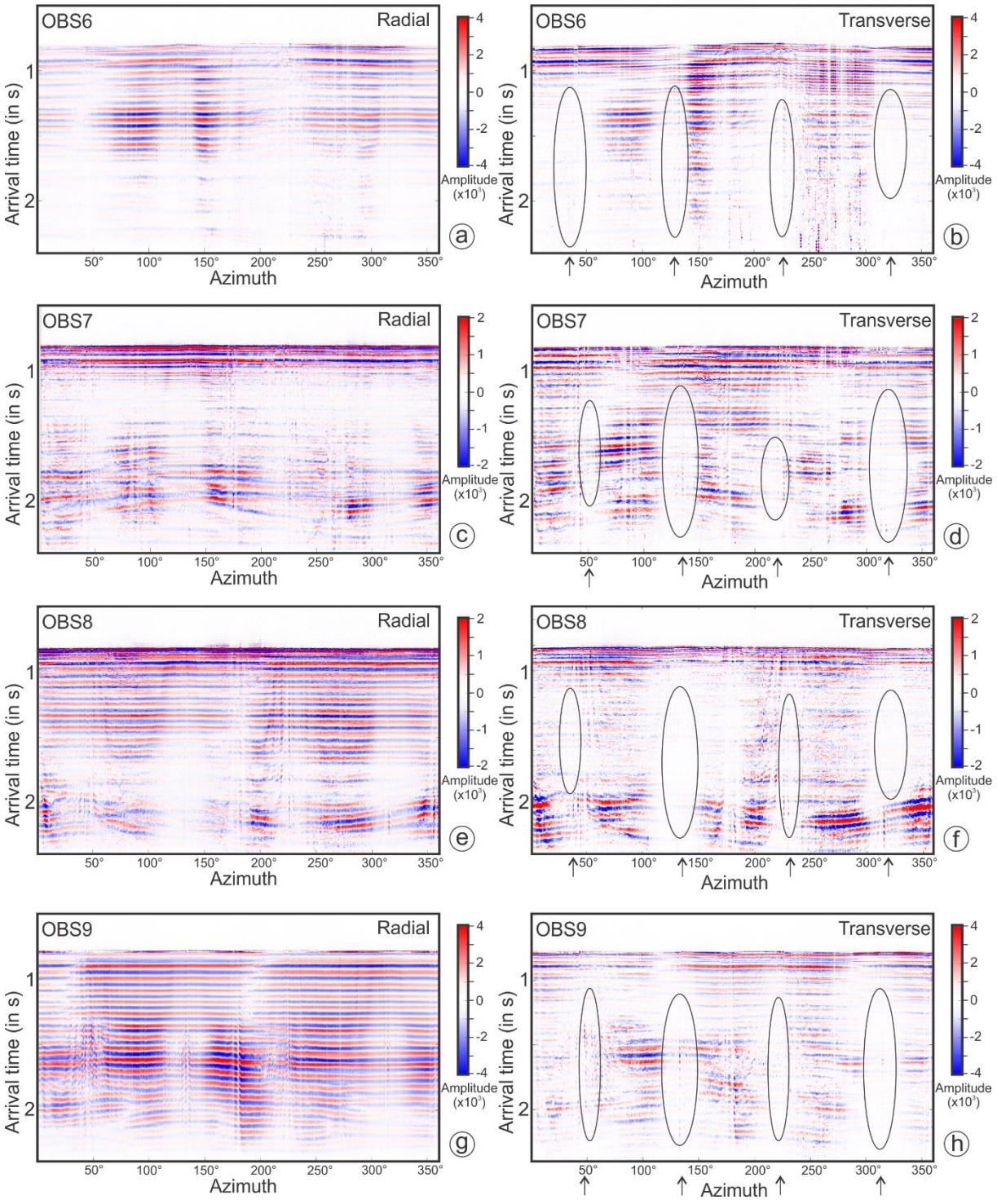

Figure 6.6: Radial and transverse components of recorded S-waves for OBS6-9. Black ellipsoids show regions of low energy in the transverse components from S-wave splitting.

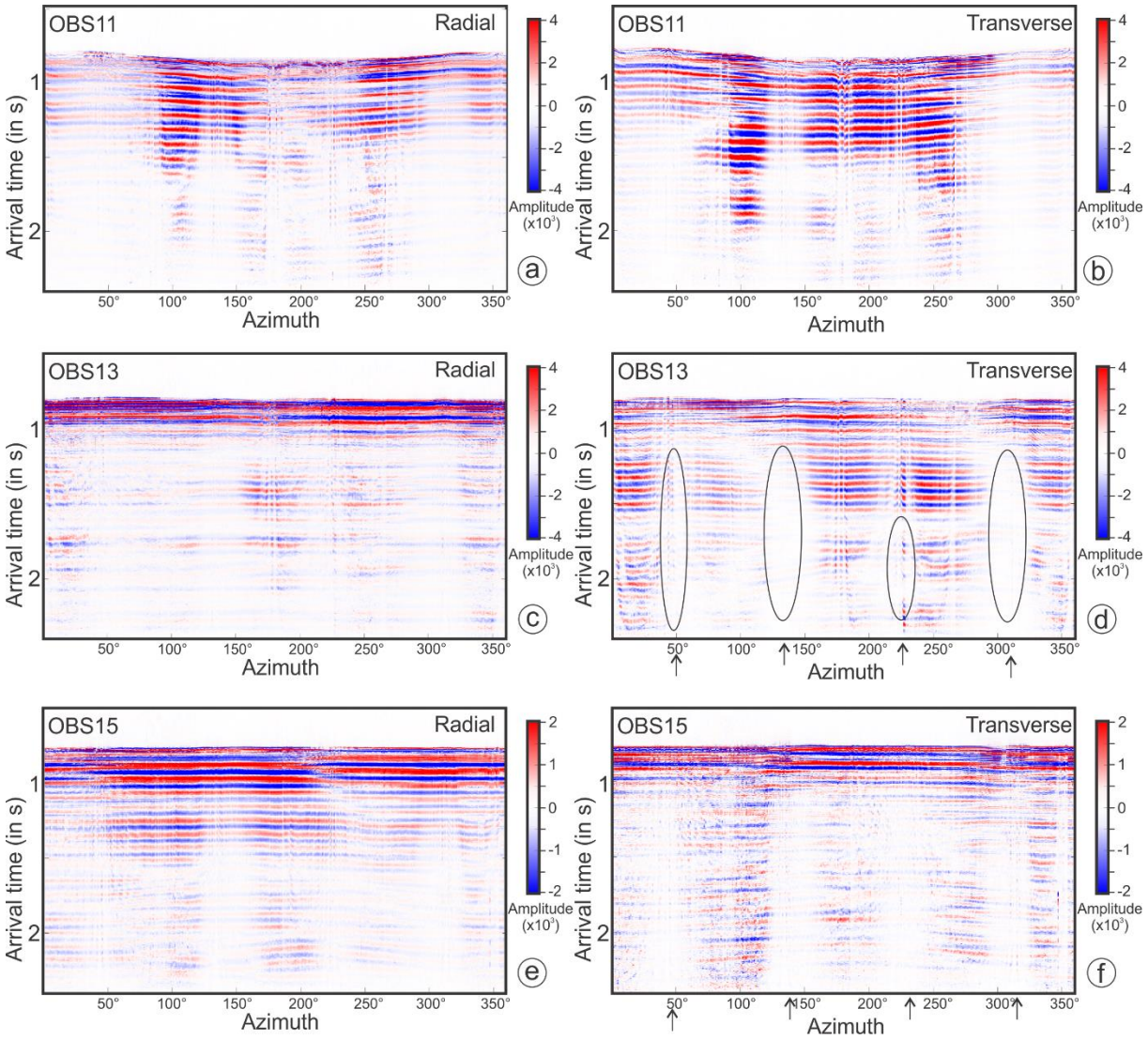

Figure 6.7: Radial and transverse components of recorded S-waves for OBS11, OBS13, OBS15. Black ellipsoids show regions of low energy in the transverse component from S-wave splitting.

OBS6 is to the southwest of Lunde Pockmark (Figure 9a). In OBS6, considerable low energy in the transverse direction occurs in the 1.1-2.4 s arrival-time interval, particularly at azimuths of: 0°-50°, 125°-135°, 220°-230° and 305°-325° (Figure 6b). This represents the amplitude null symmetry (90°-separated four amplitude nulls in a full 360° azimuth) centered at 40°-130°-220°-310° azimuths (Figure 6b).

OBS7 is on the western rim of Lunde Pockmark (Figure 9a). In OBS7, azimuths of 45°-55°, 135°-145°, 215°-225° and 305-320° have relatively low energy in the 1.3-2.4 s arrival-time

interval in the transverse component (Figure 6d). The azimuth ranges are relatively narrow compared to OBS6 (Figure 6b and 6d). Additionally, in the 1.0-1.3 s arrival-time interval, azimuths of 60°-80° and 260°-280° have low energy (Figure 6d). The amplitude null symmetry for the transverse component is along 50°-140°-230°-320° azimuths (although 230° is slightly outside the 215°-225° range) (Figure 6d).

OBS8 is ~100 m away from the southern rim of Lunde Pockmark (Figure 9a). In OBS8, azimuths of 30°-50°, 110°-145°, 175°-185°, 220°-230° and 310°-340° show broader and very distinctive regions of considerable low seismic energy in the transverse component after 1.1 s arrival-time (Figure 6f). The amplitude null symmetry in the transverse component occurs along 45°-135°-225°-315° azimuths (Figure 6f).

OBS9 is on the northwestern rim of Lunde Pockmark (Figure 9a). In OBS9, azimuths of 40°-50°, 120°-145°, 210°-230° and 300°-330° show significantly lower seismic energy in the transverse component (Figure 6h). Azimuth ranges with low energy are broader in the 1.1-1.4 s and 1.7-2.4 s arrival-time intervals compared to the 1.4-1.7 s arrival-time interval (Figure 6h). This approximately represents amplitude null symmetry in the transverse component aligned along 50°-140°-230°-320° azimuths (Figure 6h).

OBS11 is on the southern rim of Lunde Pockmark (Figure 9a). The transverse component of OBS11 does not show energy after 2.0 s arrival-time (Figure 7b). Within the 1.0-1.4 s arrival-time interval, there is low energy in 300°-360° azimuths (Figure 7b). In the 1.4-2.0 s arrival-time interval, low energy in the transverse component occurs along 290°-60°, 120°-150° and 175°-180° azimuths (Figure 7b). There is no amplitude null symmetry in the transverse component at this site (Figure 7b).

OBS13 is ~250 m away from the northern rim of Lunde Pockmark (Figure 9a). In the transverse component of OBS13, azimuths with low energy in the 1.1-2.4 s arrival-time interval are: 40°-

55°, 125°-155°, 200°-225° (in the 1.5-2.4 s arrival-time interval) and 300°-325° (Figure 7d). The amplitude null symmetry occurs along 50°-140°-230°-320° azimuths (Figure 7d).

OBS15 is on the northeastern rim of Lunde Pockmark (Figure 9a). In OBS15, there are some zones of relatively low energy in the transverse component, but they are not as sharply defined as zones observed in most of the other OBS stations (Figure 7f). Azimuths of 125°-150°, 220-245°, 200°-315°, 345°-355° show relatively low energy (Figure 7f), however, there is some energy which appears in-between, and the azimuthal nulls are not distinct (Figure 7f).

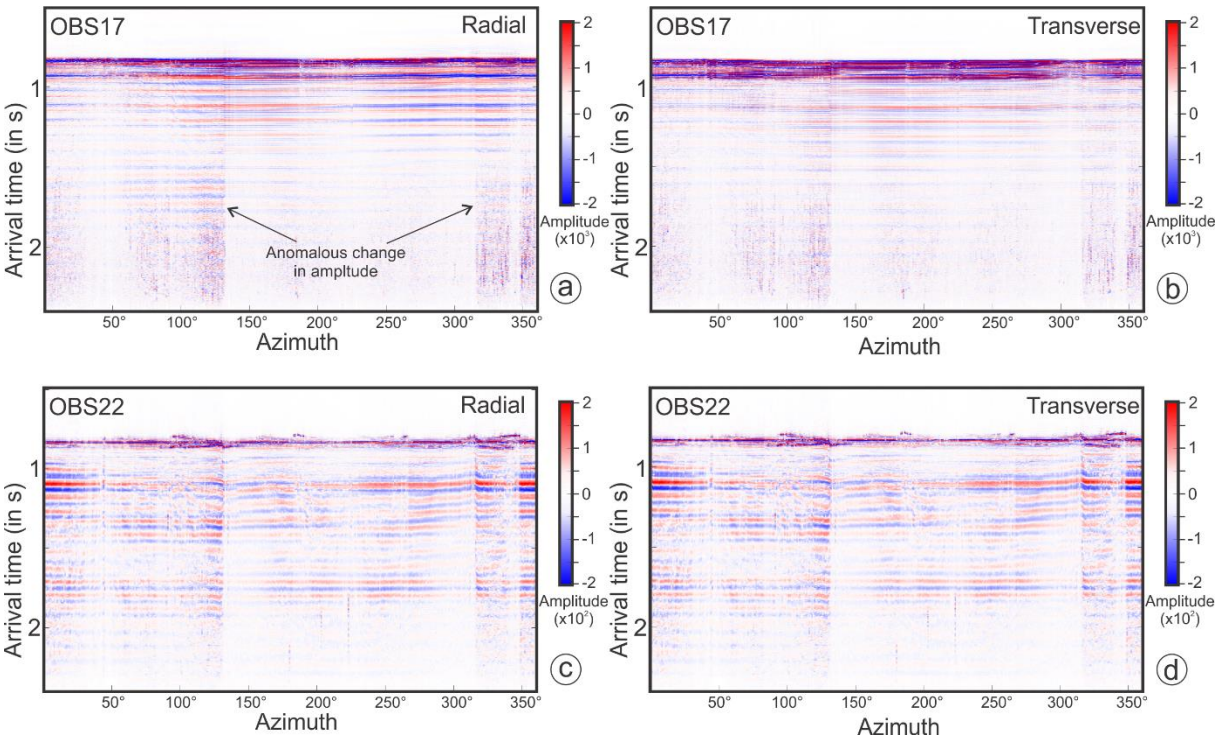

Figure 6.8: Radial and transverse components of recorded S-waves for OBS 17 and OBS22.

The locations of OBS17 and OBS22 are separated only by 15 m, and their seafloor positions lie northeast of Lunde Pockmark (Figure 1c-d and 9d). Transverse components of both OBS show an absence of amplitude nulls (Figure 8b and 8d). However, in both OBS, we observe a sharp change in amplitude strengths at azimuths of 133° and 314° across the entire arrival-time window, in both radial as well as in the transverse component (Figure 8).

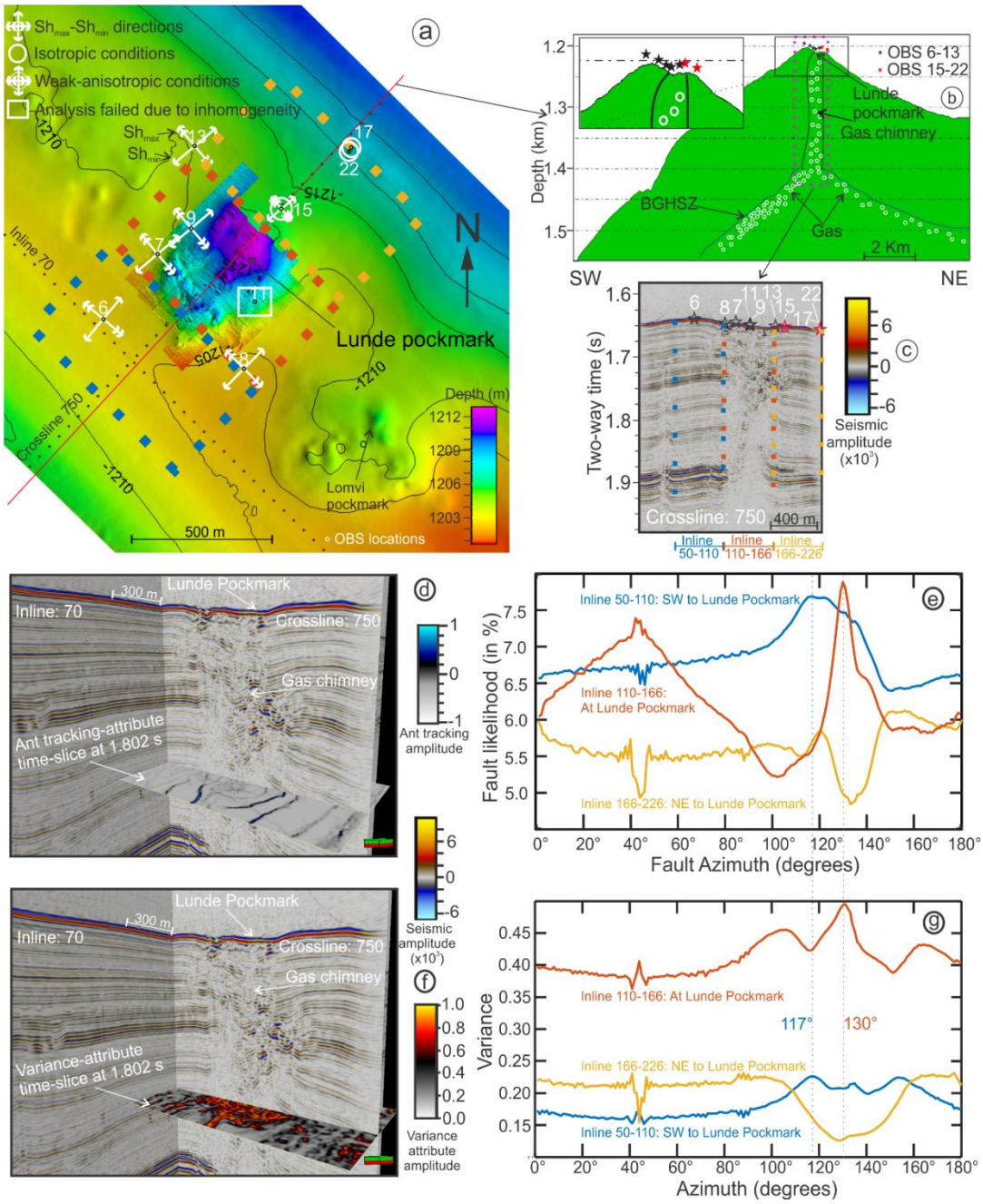

Figure 6.9: a) Maximum (Sh_{max}) and minimum (Sh_{min}) horizontal stress orientations plotted over the seafloor map from 3D seismic and high-resolution bathymetry. b) Conceptual diagram of a gas chimney, free gas flow and the base of gas hydrate stability zone (BGHSZ) laid over the seafloor path-profile along the red line (partly plotted in (8a) and full length plotted as red line in Figure 1b). c) Seismic section along crossline 750 illustrating gas chimney features and OBS locations with respect to gas chimney. d) Inline 70 and crossline 750 plotted along with ant tracking-attribute time-slice. e) Likelihood of occurrence of fault in different orientations (10° fault azimuth corresponds to fault strike orientation of 10°-190°) based on the fault extraction method using ant-tracking in the areas shown by colored rectangles. Blue, red and yellow rectangles have data within crosslines: 700-800 and inlines: 50-110, 110-166 and 166-226, respectively. f) Inline 70 and crossline 750 plotted along with variance attribute time-slice. g) Mean variance amplitude in different orientations (datasets shown with colored rectangles in Figure 9a).

The ratio of radial and transverse energies indicates the partitioning of PS-wave energy in the radial and transverse components (Figure 10-11). The energy ratio is calculated for the 1.1-2.4 s arrival-time interval. The energy ratio peaks with ~90° azimuth separation in the azimuth ranges of ~ (40°-50°) - (130°-140°) - (220°-230°) - (310°-320°) (Figure 10). We do not observe the energy ratio peaks with ~90° azimuth separation for OBS11, OBS17 and OBS22 (Figure 11).

We integrate results from shear-wave analysis with high-resolution 3D seismic data (Plaza-Faverola et al., 2015). Seismic attribute analysis ('variance' and 'ant-tracking') of this data allows us to statistically measure predominant fault and fracture orientations in the subsurface around and within the Lunde pockmark. Details on the methodology of this approach are included in Appendix A.

In the area southwest of Lunde Pockmark (shown by the blue rectangle in Figure 9a), fault analysis, using the ant tracking attribute, suggests a higher (>7%) fault likelihood along azimuths of 100°-140° with the highest (7.7%) fault likelihood along azimuth of 117° (or fault strike: 117°-297°) compared to ~6.4-6.8% fault likelihood observed in other azimuths (Figure 9e). In our fault analysis, a fault along azimuth of X° refers to a fault of fault strike X°-(X°+180°). The variance attribute analysis suggests relatively higher (>0.20) variance along azimuths of 105°-165° with highest (0.2262) variance observed along azimuth of 117° compared to ~0.15-0.17 variance observed along other azimuths (Figure 9g). In the area of Lunde Pockmark and active vent sites (shown by the red rectangle in Figure 9a), fault analysis, using the ant tracking approach, suggests the highest (7.9%) fault likelihood along azimuth of 130° (or fault strike: 130°-310°) (Figure 9e). Another peak of 7.4% fault likelihood occurs along fault azimuth of 42° (or fault strike: 42°-222°) (Figure 9e). Higher (>0.45) variance is observed along azimuths of 125°-135° with highest variance (0.4955) observed along azimuth of 131° compared to mostly ~0.36-0.44 variance observed in other azimuths (Figure 9g). In the area

northeast of Lunde Pockmark (shown by the yellow rectangle in Figure 9a), analysis using the ant tracking attribute, shows a decreased likelihood of fault occurrence along azimuths of 44° (or fault strike: 44°-224°) (4.8%) and 133° (or fault strike: 133°-313°) (4.9%) compared to fault likelihoods of 5.5-6% in other azimuths (Figure 9e). Low variance (<0.2) is observed along azimuths of 43°-46° and 110°-155° with lowest (0.1259) variance observed along 128° compared to ~0.21-0.22 variance observed in other azimuths (Figure 9g).

6.7. Uncertainties and limitations

Before discussing the implications of the observed PS-wave energy distribution for understanding the fluid migration system and associated stress field at Lunde we discuss data uncertainties and the limitations of the approach implemented.

S-wave polarization changes with depth

One major assumption in our analyses is that fast and slow S-wave polarization directions does not change with depth. Amplitude null symmetries represent summation of effects of fast and slow S-wave polarization directions of different anisotropic layers through which S-wave travels (Robinson et al., 2022). Interpretation of fast and slow S-wave polarizations from amplitude null symmetries requires a layer-stripping approach, especially at greater depths (>150-200 m below the seafloor (bsf)), because of changes in S-wave polarization directions with depth (Haacke et al., 2009; Robinson et al., 2022; Slack et al. 1992). However, in shallow sediments (<150 m bsf), particularly in cases with no other visible symmetries, amplitude null symmetry directions correspond to fast and slow S-wave directions (Robinson et al., 2022; Crampin, 1993a,b; Slack et al. 1992). Since we primarily study shallow sediments and we do not see changes in amplitude null symmetry with depth, we avoid the application of relatively complicated layer-stripping approach. Because most amplitude null symmetries are

unambiguous, and we analyze data only up to 2.4 s (~220-250 m bsf, depth converted considering S-wave velocity model from Singhroha et al., 2019), the azimuths of amplitude null symmetry correspond to the planes of symmetry in the anisotropic medium (Crampin, 1993a,b; Robinson et al., 2022; Pastori et al., 2019).

Noise from PP arrivals

The second assumption in our analyses is that the interference of PP signal is insignificant. Such an assumption here allows us to interpret the absence of amplitude nulls between the arrival-time 0.8-1.1 s (~0-20 m bsf) as the absence of the planes of symmetry in the anisotropic shallow sub-surface and the potential lack of horizontal stress differences in sediments near the seafloor (Figure 6-8). Nevertheless, the upper 20 m in the sedimentary column is a low confidence interval and any interpretation should consider potential interference with PP energy.

Inhomogeneity

The third and last major assumption is that the stratum where the PS-wave energy is propagating is homogeneous. This assumption allows us to relate the amplitude nulls to symmetry planes, and therefore to slow and fast energy travelling directions. The presence of vertical cracks in a medium makes it homogenous and anisotropic, whereas the presence of inhomogeneity (e.g., the presence of randomly distributed methane-derived authigenic carbonates, gas hydrates or free gas in a gas chimney) can create amplitude contrasts due to differences in reflectivity and seismic attenuation. In OBS data, since the point of reflection varies with azimuth and offset, the presence of symmetries will not occur at regular 180°/90° intervals in an inhomogeneous medium. Our case study is not an ideal homogeneous medium (i.e., we expect inhomogeneity at small-scales (<10 m), especially at OBS stations which lie within the pockmark, due to changes in the sediment and pore-fill properties (Figure 1-2)) and this is considered when discussing energy nulls in radial and transverse components at different OBS stations.

The seafloor position of OBS11 lies 30 m away from a pit (at azimuth of 320° from OBS11; marked as pit1 in Figure 12a and 10c) and 70 m away from another pit (at azimuth of 10° from OBS11; marked as pit2 in Figure 12a-b) within Lunde Pockmark. We see a significant decrease in S-wave energies arriving from azimuths of 320° and 10° (Figure 7a-b), however, we do not see 180° symmetry in amplitude nulls. The overall energy in azimuths of 270°-70° is significantly lower than the energy in azimuths of 70°-270° (Figure 7a-b). The rest of Lunde Pockmark and the gas chimney below, also lies along azimuths of 270°-70° from OBS11 site (Figure 12). The observed anomalies in OBS 11 radial and transverse components are most likely due to inhomogeneities created by pits, carbonates, or a free gas, and the effect of differences in energy with azimuth are possibly related to energy scattering or seismic attenuation related issues (Figure 1c). The pits within the pockmark often have uneven structures which can scatter arriving seismic energy (Panieri et al., 2017; Figure 12a). The occurrence of pits on the seafloor and strong-reflections around 1.70-1.75 s two-way travel time, indicates the presence of carbonates with high-reflectivity (which potentially can scatter most of the arriving energy) or free gas with high-attenuation (Figure 12b-c; Bünz et al., 2012; Singhroha et al., 2016; Himmler et al., 2019). The vertical anomalous changes in S-wave energy, in OBS17 and OBS22, also appear to be the result of inhomogeneity (Figure 8). Orientations of azimuths corresponding to this anomaly are aligned parallel to the ridge crest. On other OBS sites near Lunde Pockmark (OBS7, OBS9, OBS 15), we observe 180° symmetry in amplitude nulls, suggesting that inhomogeneity due to the pockmark and gas chimneys plays an insignificant role in our observed results.

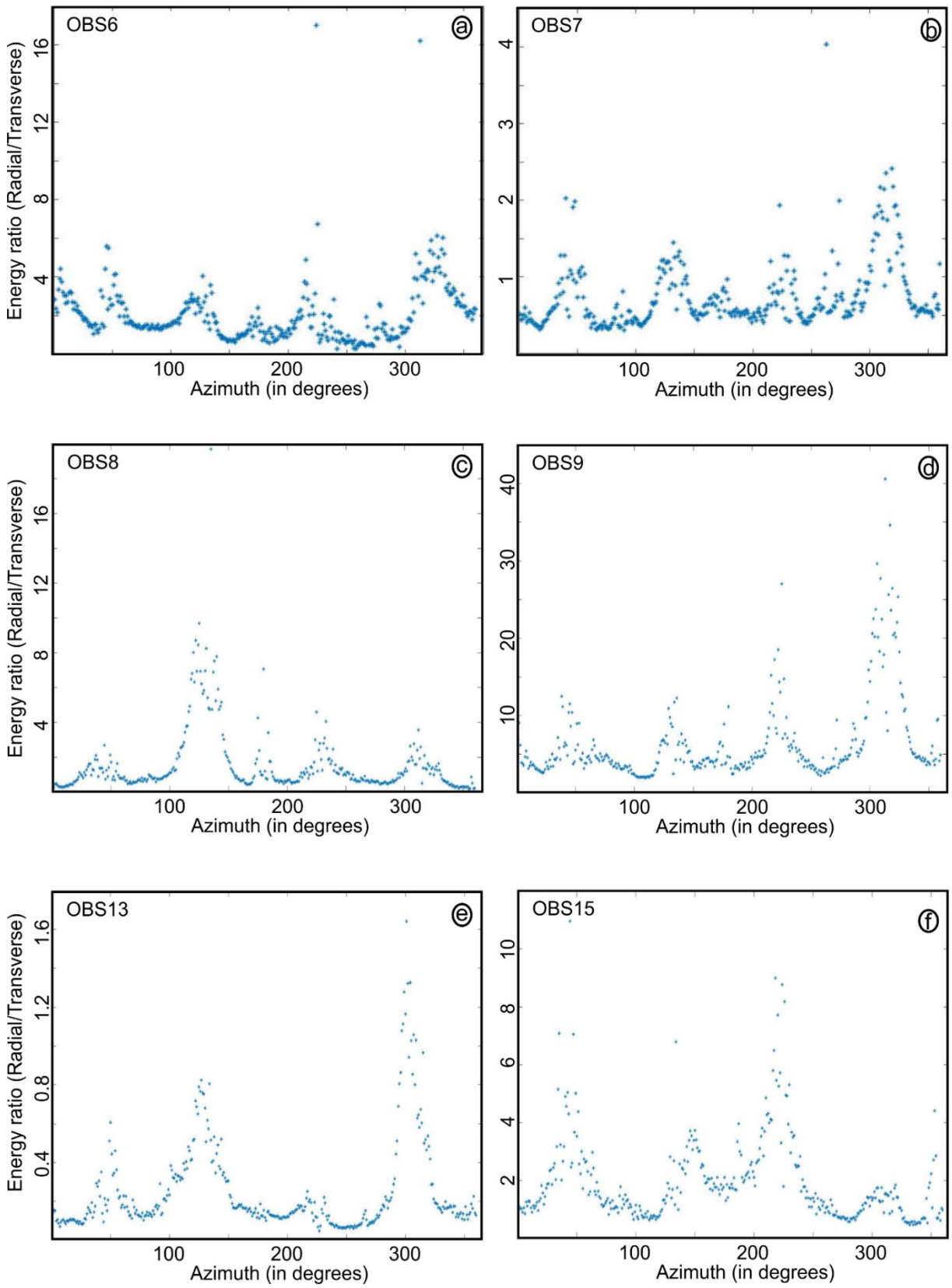

Figure 6.10: The ratio of radial and transverse energies in the 1.1-2.4 s arrival time interval.

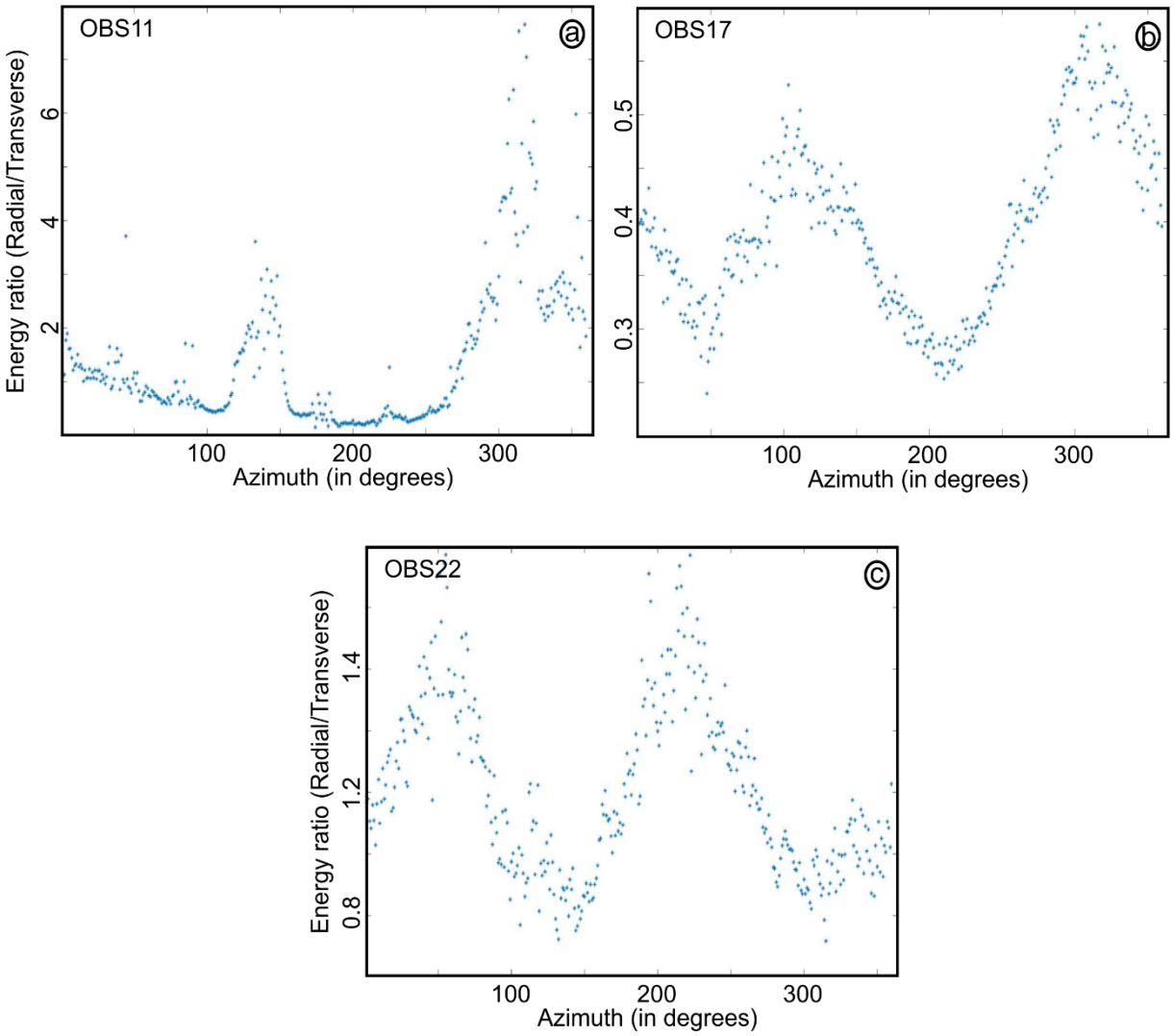

Figure 6.11: The ratio of radial and transverse energies in the 1.1-2.4 s arrival time interval.

6.8. Discussions

Keeping in mind that some of the PS-wave energy distribution trends in the transverse and radial components may reflect amplitude attenuations due to chimney related inhomogeneities and may be mixed with PP energy arrivals, we analyze the potential relationship between amplitude null symmetries, anisotropy in sub-seabed stress fields and fracture orientations.

First, the occurrence of energy in the transverse direction per se (Figure 6-8) confirms the existence of sub-surface anisotropy. In addition, the presence of amplitude null symmetry in the transverse direction (Figure 6-7 and 9) can be correlated to the symmetry axis in the

anisotropic shallow sediments below and southwest of Lunde Pockmark. Assuming a horizontal symmetry axis (HTI), the observed azimuths of amplitude null symmetries in the transverse component can be correlated with directions parallel and perpendicular to the predominant fault/fracture strike direction (Li, 1998).

In OBS6-9 and OBS13, we see consistency in the azimuths of amplitude null symmetries in the 1.1-2.4 s arrival-time interval (~20-250 m bsf) (Figure 6-7). Amplitude null symmetries vary within the azimuth ranges of (40°-50°) - (130°-140°) - (220°-230°) - (310°-320°) (Figure 6-7). We observe a change in the S-wave amplitude patterns across the Vestnesa Ridge crest from the southwestern side (OBS6-9) to the northeastern side (OBS15, OBS17 and OBS22) of Lunde Pockmark (Figure 1, 6-9). There are no distinguishable symmetry planes at OBS17 and OBS22 sites (Figure 8). Even OBS15, close to the ridge crest, shows a significantly different strength of amplitude nulls compared to OBS6-9 (Figure 6 and 7f). We interpret these significant differences in amplitude strengths as an indication of changes in the anisotropic conditions on the Vestnesa Ridge crest and across Lunde Pockmark. Southwest of Lunde Pockmark, the orientation of faults and fractures are dominantly NW-SE, presumably creating symmetry planes in the anisotropic medium and explaining the observed amplitude null symmetry (Figure 6, 9e and 9g). However, across the ridge crest (northeast of Lunde Pockmark), faults and fractures do not show a dominant orientation and the amplitude null symmetry planes are therefore not expected (Figure 8, 9e and 9g). Overall, the structural attribute analysis suggests that the likelihood of fracturing northeast of Lunde Pockmark is lower for all the azimuths in comparison to the predictions for the southwestern region (Figure 9). Therefore, the strata towards the northeast of Lunde Pockmark are characterized by the absence of amplitude nulls and by a low likelihood of fracturing (Figure 8-9; example, OBS17 and OBS22)

The structural attribute analysis suggests 117°-297° as a dominant fault strike orientation in the area (shown by the blue rectangle in Figure 9a) southwest of Lunde Pockmark (Figure 9e and

9g). This dominant fault orientation rotates clockwise by 13° to 130°-310° at Lunde Pockmark (area shown by the red rectangle in Figure 9a; Figure 9e and 9g). As we go across Vestnesa Ridge from southwest to northeast (from OBS6 to OBS8 to OBS7) (Figure 9c), amplitude null symmetries also change from 40°-130°-220°-310° (in OBS6) to 45°-135°-225°-315° (OBS8) to 50°-140°-230°-320° (in OBS7) (Figure 9a). Interestingly, this 10° clockwise rotation in the symmetry axis estimated from shear-wave analysis is very close to the 13° clockwise rotation for the dominant fault orientation (Figure 9a). This suggests a close link between preferred fault orientation and inferred symmetry axes.

Stress fields are the most important factor governing the orientation of fractures and faults, with their predominant orientation perpendicular to the minimum principal horizontal stress (Hubbert & Willis 1957; Evans & Brereton, 1990). The data reveal a preferential orientation of faults along an azimuth of 130° (i.e., 130°-310° fault strike; NW-SE) (Figure 9e and 9g) in the areas where the symmetry axis exists in the anisotropic sub-surface (i.e., in the blue and red rectangular areas as shown in Figure 9a). This observation in conjunction with the NE-SW and NW-SE distribution of amplitude null symmetries (i.e., (40°-50°) - (130°-140°) - (220°-230°) - (310°-320°)) suggests that the minimum principal horizontal stress is oriented along NE-SW (i.e., (40°-50°) - (220°-230°)) whereas the maximum principal horizontal stress is oriented along NW-SE (i.e., (130°-140°) - (310°-320°)).

Assuming that hydrofracturing develops documented faults and fractures, southwest of Lunde Pockmark (i.e., the area within the blue rectangle in Figure 9a), our study suggests that there is a ~14-20% higher probability of fault orientation following stress conditions (7.7% fault likelihood along stress directions as opposed to ~6.4-6.8% of fault likelihood in other directions (Figure 9e)). In the area containing Lunde Pockmark (i.e., the area within the red rectangle in Figure 9a), there is a ~32% higher probability of fault orientation following stress conditions (7.9% fault likelihood along stress directions as opposed to ~6.0% of fault likelihood in other

directions) (Figure 9e). In the area northeast of Lunde Pockmark (shown by the yellow rectangle in Figure 9a), stresses do not favor formation of any preferential fault orientation potentially due to undetectable differences in maximum and minimum horizontal stresses. The absence of predominant fault orientation in the structural attribute analysis and the absence of the occurrence of symmetry axis in the area support our interpretation.

The gas leakage distribution within the pockmark coincides with inferred changes in the subsurface anisotropic conditions (Figure 9). We speculate that leakage points may relieve pressure and form zones where the sub-seabed stress field is locally modified (i.e., explaining the contrasting fracturing and faulting patterns to the northeast and southwest of Lunde Pockmark; Figure 9). Ultimately, the relationship between stresses, faulting and leakage may be the other way around; potential changes in the differential stress conditions generated by regional processes (e.g., glacial isostasy, mid-ocean ridge spreading, differential compaction; Lindholm et al., 2000; Fejerskov & Lindholm, 2000; Olesen et al., 2013, Vachon et al., 2022) may trigger leakage at this location by modifying the permeability of already in place faults and fractures.

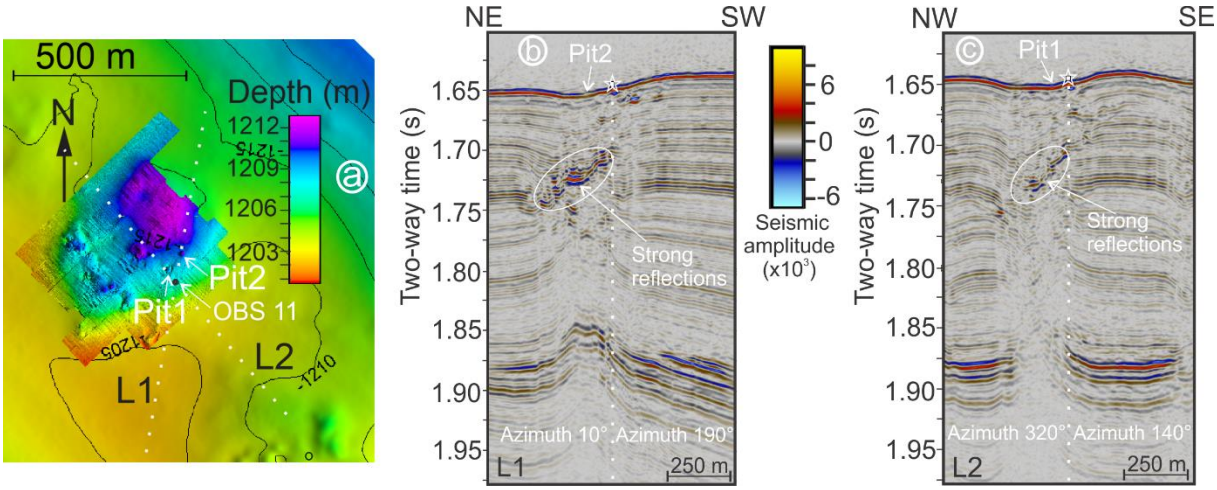

Figure 6.12: a) High-resolution bathymetry map showing the locations of pits, OBS11, L1-2 lines. b) L1 line shows seismic section along Azimuths of 10° and 190° from OBS11. c) L2 line shows seismic section along Azimuths of 320° and 140° from OBS11. White ellipsoids show high reflections observed along azimuths of 10° and 320° in L1 and L2, respectively.

The fracture/crack-induced permeability is important, considering hemipelagic sediments with low primary permeability in the region (Eiken and Hinz, 1993; Vogt et al., 1994). Vertically connected fractures increase permeability of a medium, promote leakage, and create anisotropy as inferred from the results we document here. In shallow sediments with a typical normal-faulting regime, fracture and crack planes oriented perpendicular to maximum stress can be closed due to stress (Nur & Simmons, 1969). Previous studies document that some faults and fractures are permeable to fluid flow whereas other faults and fractures are closed to fluid flow in the region (Singhroha et al., 2015, 2019, 2020; Plaza-Faverola et al., 2015, 2019). The relative decrease in faults detected along azimuths of 43°-47° in the area southwest of Lunde Pockmark (shown by the blue rectangle in Figure 9a) could be due to the presence of closed faults oriented perpendicular to the present day maximum horizontal stress (blue curve in Figure 9e). There is a relatively high occurrence of fractures and faults, (>7% fault likelihood in azimuths of 33°-51° as shown by the red curve in Figure 9e) in the direction perpendicular to the maximum horizontal stress, in the active seep area (shown by the red rectangle in Figure 9a). In the direction perpendicular to the maximum horizontal stress, fault likelihood decreases in the area without observed gas leakage (shown by the blue rectangle in Figure 9a), whereas it increases in the area with the observed gas leakage (shown by the red rectangle in Figure 9a). This finding suggests that faults are open due to a high gas pressure in the system.

With the available data, we are not able to resolve potential sources of local stress fields. However, a similar OBS study conducted ~40-45 km south from Lunde Pockmark (north of the Knipovich Ridge and Molly Transform Fault intersection; Figure 1a-b) concludes that gravitational forcing may be dominating the stress regime within the upper 100 m (Haacke & Westbrook, 2006; Haacke et al., 2009). They document a transition in the orientation of maximum and minimum horizontal stresses at ca. 200 m and argue that regional tectonic stress may be overcoming the effect of gravitational stress at these depths (Haacke & Westbrook,

2006; Haacke et al., 2009). Our approach on Vestnesa Ridge only allows us to infer stress orientations within the upper 200 m. In line with the study by Haacke and Westbrook (2006) we think it is likely that the inferred orientations of minimum and maximum principal stresses on Vestnesa Ridge reflect the effect of gravitational stress acting beneath the sub-surface given that the Vestnesa Ridge crest is NW-SE oriented and has a southwest-dipping slope at its steepest flank (i.e., its southern flank) (Figure 1a-b and 9a-b). The inferred sub-seabed minimum and maximum stress orientations based on amplitude null symmetries are consistent with the Vestnesa Ridge geometry.

6.9. Conclusions

We analyze active-source PS-wave energy recorded by ocean-bottom seismic recorders (OBSs) from a seabed pockmark on Vestnesa Ridge offshore west-Svalbard. We document amplitude null symmetries in the transverse component from different OBS stations and interpret them as an evidence of anisotropy. Simultaneously, we analyze the likelihood of forming faults and fractures at specific azimuths via implementation of structural attributes on high-resolution 3D P-cable seismic data.

The combined interpretation from both analyses suggest the presence of a minimum horizontal stress exerted along the ~45°-225° (NE-SW) direction and a maximum horizontal stress exerted along the ~135°-315° (NW-SE) direction within the upper 100 m of sedimentary column. A change in the fracture pattern together with a lack of amplitude nulls symmetries to the northeast of the investigated pockmark indicate a drastic change in the local stress regime coinciding with the zone where seepage is concentrated at present day. The change in the differential stress across the seep site could have triggered seepage or conversely, the occurrence of seepage could be responsible for the observed stress differences inside and outside the pockmark region. The

change in stresses across the seep site establish a correlation between the occurrence of seepage and the stress regime in shallow sediments in this region which favors (~32% higher probability) the occurrence of faults perpendicular to the minimum horizontal stress.

The sources of sub-seabed stress cannot be resolved with the implemented approach. However, a close correlation of inferred principal stress orientations with the geometry of the Vestnesa Ridge suggest a dominance by gravitational forcing in line with similar OBS studies farther south on the same contourite system. Future analyses of the propagation of PS-wave energy from deeper layers may help to identify vertical changes in the stress field orientation potentially indicating the effect of glacio-tectonics on sedimentary deformation and seepage evolution in this deep marine Arctic setting.

Acknowledgement

This work is part of the SEAMSTRESS project, and it is supported by grants from the Tromsø Research Foundation (project nr. A31680) and the Research Council of Norway (project nr. 287865). The work is also supported by the Research Council of Norway through its Centers of Excellence funding scheme grant nr. 223259 (Centre for Arctic Gas Hydrate, Environment and Climate—CAGE). OBS data was acquired on board R/V Helmer Hanssen, and we are thankful to the ship and scientific crew for data acquisition. The OBS experiment with 22 instruments was possible thanks to stablished collaborations with Christian Berndt and Jörg Bialas from Geomar, Kiel, Germany. We thank editors and reviewer for constructive feedback and insightful comments. We also thank Schlumberger for Petrel Software and support.

The data are stored at UiT open research data repository and can be accessed using the weblink (https://dataverse.no/privateurl.xhtml?token=120bac3e-71f1-42d5-a227-0cdebb40f7bc).

Appendix

Fault analysis

We use structural seismic attributes (i.e., Petrel's variance and ant tracking attributes) derived from high-resolution 3D seismic data (Plaza-Faverola et al., 2015) to study fault orientations in our study area. The seismic variance attribute measures the difference in the shape of waveforms of adjacent traces, over a given lateral and vertical window (Van Bemmel & Pepper, 2000). This attribute detects discontinuities, faults, and changes in lithology. The ant tracking method, an even more powerful automatic tool, by using an analogue of swarm intelligence inspired by the behavior of ants, detects faults in the seismic data with a very high level of accuracy (Pedersen et al., 2002). We use these two methods to estimate the likelihood of the occurrence of faults in different orientations (details on parameters used for attribute analysis

available in the supplementary text S3). In order to do this, we employ a statistical measure to identify predominant fault and fracture directions (Figure A1). Fault analysis is performed on three subsets of data within the 3D seismic data, published and interpreted in Plaza-Faverola et al., 2015 (blue, red and yellow rectangles (shown in Figure 9a)). The area bounded by the blue rectangle covers the undeformed strata to the southwest of Lunde Pockmark and has data within inlines: 50-110 and crosslines: 700-800. The area bounded by the red rectangle contains Lunde Pockmark and active venting sites and has data within inlines: 110-166 and crosslines: 700-800. The area bounded by the yellow rectangle comprises undeformed strata to the northeast of Lunde Pockmark and has data within inlines: 166-226 and crosslines: 700-800.

After estimating variance and ant tracking attributes, we normalize values in the attribute volume by assigning the maximum value to one and minimum value to zero. We calculate the mean of attribute values along different azimuths in subsets of the data, e.g., for data bounded by inlines: 50-110 and crosslines: 700-800, we calculate the mean attribute value along all azimuths from a reference CDP bin corresponding to inline 80 and crossline 750 (Figure A1), i.e., if 20 CDP bins occur along a certain azimuth, we calculate the mean value of the normalized attribute values, corresponding to traces from 20 CDP bins.

$$M(A(X), y) = \frac{\sum_{t=t1}^{t2} \sum_{b=1}^{N} NAV_X(t, b)}{N \; X \; NT}$$

Where, $M(A(X), y)$ is the mean attribute value along azimuth of X° ($A(X)$) from a reference bin y. $NAV_X(t, bin)$ is the normalized attribute value at time t in a bin b, where bin b has an azimuth of X° or (X°+180°) from the reference bin. N is the total number of bins that have azimuth of X° or (X°+180°) from the reference bin and NT is the total number of samples between t1 (seafloor) and t2 (BSR).

We repeat the same procedure while shifting the reference CDP bins to other places (e.g., shifting the reference CDP bin to inline 81 and crossline 750) and estimating mean attribute

values there (Figure A1). Subsequently, we derive fault likelihood as a mean value taken from all reference bins (e.g., if 0.01, 0.02 and 0.06 are mean ant tracking attribute values along azimuth of 30° from three different reference bins, fault likelihood along azimuth of 30° is 0.03 or 3%).

$$Fault\ likelihood\ (X)(in\ \%) = \left(\frac{\sum_{y=1}^{K} M(A(X), y)}{K}\right) x100$$

Where, *fault likelihood (X) (in %)* is the likelihood of fault occurrence within a fault strike azimuth of X° (or fault strike orientation of X° - (X°+180°)). K is the total number of reference bins.

The averaging ensures that we statistically capture fault orientations even with very small variations in likelihood. Azimuths with 180° spacing are considered the same for the purpose of fault analysis in this study (e.g., fault strikes of 10° and 190° have the same fault strike orientation (10°-190°) and are together referred to as a fault with 10° azimuth (or fault azimuth of 10°) in this study).

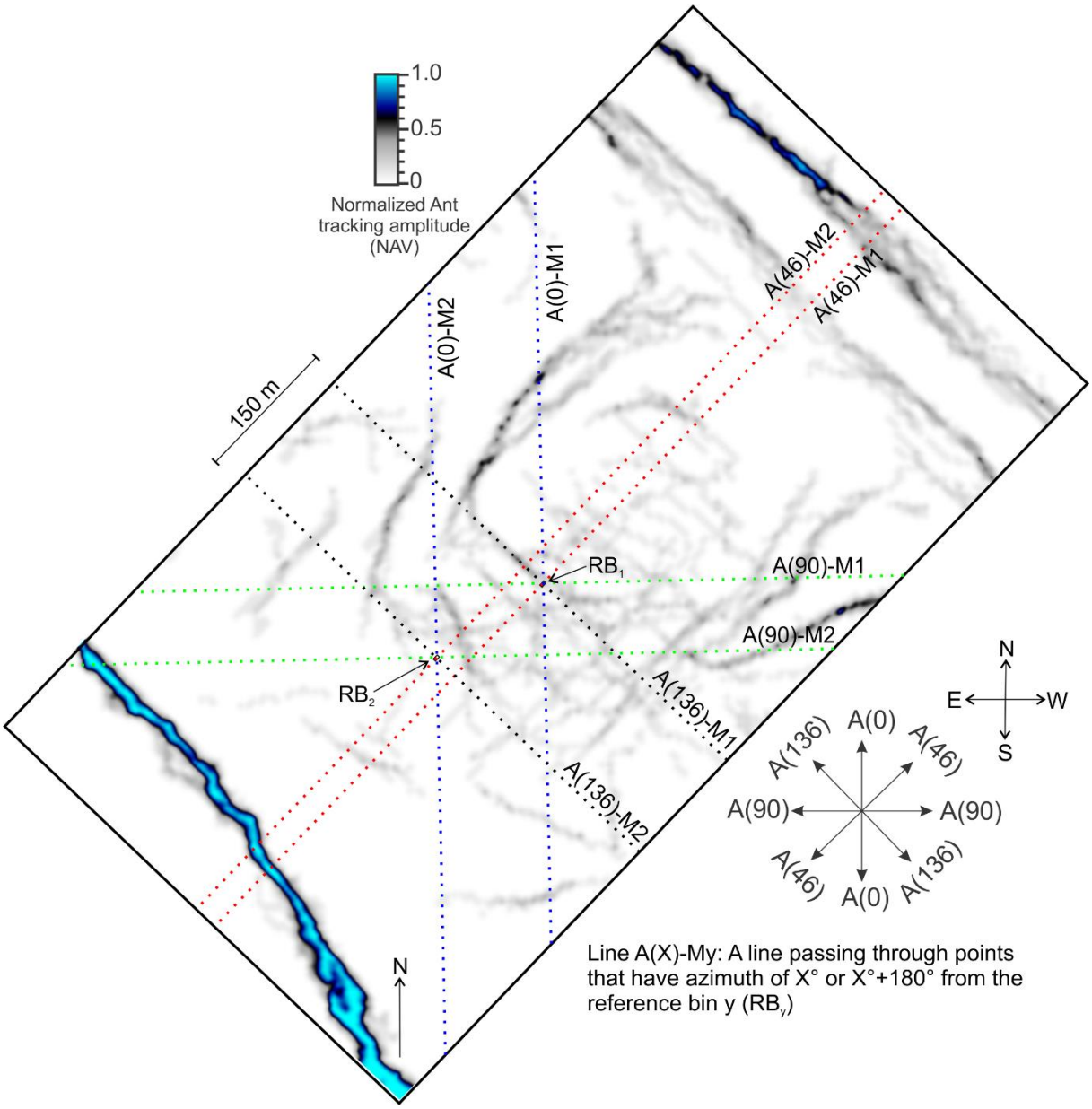

Figure 6.A10.13: Ant tracking-attribute time-slice at 1.692 s two-way time. A(X) represents azimuth of X° from a given point or reference bin. A(X) and A(X+180) are considered as A(X) for the purpose of fault analysis. Blue lines, red lines, green lines and black lines show data points in the attribute time-slice along azimuths of 0°, 46°, 90° and 136°, respectively from two different reference bins. M(A(X), y) in equations in Appendix A represents mean of all normalized attribute values (NAV) along a A(X)-My line. The A(X)-My line has azimuth of X° from a reference bin y (RB_y) (e.g., value of A(46)-M1 will be mean of all values along the red line passing through RB_1 (the red line lies along azimuth of 46° from RB1)).

References

Alford, R. M. (1986). Shear data in the presence of azimuthal anisotropy. 56th Ann. Int. SEG Meeting, Houston, Dilley, Texas, Expanded Abstracts, 476-479.

Amundsen, I. M. H., Blinova, M., Hjelstuen, B. O., Mjelde, R., & Haflidason, H. (2011). The Cenozoic western Svalbard margin: sediment geometry and sedimentary processes in an area of ultraslow oceanic spreading. Marine Geophysical Research, 32(4), 441-453. Doi:10.1007/s11001-011-9127-z

Biot, M. A. (1941). General theory of three-dimensional consolidation. J. appl. Phys., 12, 155-164.

Biot, M. A. (1956a). Theory of propagation of elastic waves in a fluid saturated porous solid. I. Low-frequency range. J. acoust. Soc. Am., 28, 168-178.

Biot, M. A. (1956b). Theory of propagation in a fluid saturated porous solid. 11. Higher-frequency range. J. acoust. Soc. Am., 28, 179-191.

Boggess, R., & Robertson, P. (2011). CPT for Soft Sediments and Deepwater Investigations. Paper presented at the Offshore Technology Conference. https://doi.org/10.4043/21244-MS

Brocher, T. M., & Christensen, N. I. (1989). Seismic anisotropy due to preferred mineral orientation observed in shallow crustal rocks in southern Alaska. Geology, 18, 737–740.

Bünz, S., Mienert, J., & Berndt, C. (2003). Geological controls on the Storegga gas-hydrate system of the mid-Norwegian continental margin. Earth and Planetary Science Letters, 209(3-4), 291-307. Doi: 10.1016/S0012-821X(03)00097-9.

Bünz, S., Polyanov, S., Vadakkepuliyambatta, S., Consolaro, C., & Mienert, J. (2012). Active gas venting through hydrate-bearing sediments on the Vestnesa Ridge, offshore W-Svalbard. Marine Geology, 332-334, 189-197. Doi: 10.1016/j.margeo.2012.09.012

Cartwright, J., Huuse, M. & Aplin, A. (2007). Seal bypass systems. AAPG bulletin, 91, 1141-1166. Doi: 10.1306/04090705181.

Cartwright, J., & Santamarina, C. (2015). Seismic characteristics of fluid escape pipes in sedimentary basins: Implications for pipe genesis, Marine and Petroleum Geology, 65, 126-140. Doi: 10.1016/j.marpetgeo.2015.03.023.

Cole, D., Stewart, S.A. & Cartwright, J.A. (2000). Giant irregular pockmark craters in the Palaeogene of the Outer Moray Firth Basin, UK North Sea. Marine and Petroleum Geology, 17, 563-577. Doi: 10.1016/S0264-8172(00)00013-1.

Crampin, S. (1981). A review of wave motion in anisotropic and cracked elastic-media. Wave Motion, 3(4), 343-391. Doi: https://doi.org/10.1016/0165-2125(81)90026-3

Crampin, S., (1984). Anisotropy in exploration seismics. First Break, 2 (3), 19-21.

Crampin, S. (1985). Evaluation of anisotropy by shear-wave splitting. Geophysics, 50(1), 142-152. Doi:10.1190/1.1441824

Crampin S., (1987). Geological and industrial implications of extensive-dilatancy anisotropy. Nature, 328, 491–496.

Crampin S., (1993a). A review of the effects of crack geometry on wave propagation through aligned cracks. Canadian Journal of Exploration Geophysics. VOL. 29 (1), 03-17.

Crampin S., (1993b). Arguments for EDA. Canadian Journal of Exploration Geophysics, 29, 18-30

Crampin, S., Zatsepin, S.V., Slater, C. & Brodov, L., (1996). Abnormal shear-wave polarizations as indicators of high pressures and over pressures. 58th Conf. EAGE, Amsterdam, Extended Abstracts, 1, X038.

Crampin, S., & Zatsepin, S. V. (1997). Modelling the compliance of crustal rock—II. Response to temporal changes before earthquakes. Geophysical Journal International, 129 (3), 495–506. Doi: 10.1111/j.1365-246X.1997.tb04489.x

Crampin, S., & Gao, Y. (2008). A review of the New Geophysics: a new understanding of pre-fracturing deformation in the crack-critical crust with implications for hydrocarbon production. Petrol. Sci., 5, 1–12.

Crampin, S., & Peacock, S. (2008). A review of the current understanding of seismic shear-wave splitting in the Earth's crust and common fallacies in interpretation. Wave Motion, 45(6), 675-722. Doi:10.1016/j.wavemoti.2008.01.003

Crampin, S., & Lovell, J. H. (1991). A decade of shear-wave splitting in the Earth's crust: What does it mean? What use can we make of it? and what should we do next? Geophysical Journal International, 1(107), 387–407.

Crampin, S., Volti, T., & Jackson, P. (2000). Developing a stress-monitoring site (SMS) near Húsavík for stress-forecasting the times and magnitudes of future large earthquakes. In B. Thorkelsson, & M. Yeroyanni (Eds.), Destructive Earthquakes: Understanding CrustalProcesses Leading to Destructive Earthquakes, Proc. 2nd EU-Japan Workshop on Seismic Risk, Europ. Comm., Res. Dir. Gen., (pp. 136–149).

Crane, K., Doss, H., Vogt, P., Sundvor, E., Cherkashov, G., Poroshina, I., & Joseph, D. (2001). The role of the Spitsbergen shear zone in determining morphology, segmentation and evolution of the Knipovich Ridge. Mar. Geophys. Res., 22, 153–205.

Daigle, H., Bangs, N. L., & Dugan, B. (2011). Transient hydraulic fracturing and gas release in methane hydrate settings: A case study from southern Hydrate Ridge. Geochemistry, Geophysics, Geosystems, 12, Q12022.

Demenitskaya, R. M., & Karasik, A. M. (1969). The active rift system of the Arctic Ocean. Tectonophysics 8(4-6): 345-351.

Domel, P., Singhroha, S., Plaza-Faverola, A., Schlindwein, V., Ramachandran, H., & Bünz, S. (2022). Origin and Periodic Behavior of Short Duration Signals Recorded by Seismometers at Vestnesa Ridge, an Active Seepage Site on the West-Svalbard Continental Margin. Frontiers in Earth Science, 10. Doi:10.3389/feart.2022.831526

Ehlers, B. & Jokat, W. (2009). Subsidence and crustal roughness of ultra-slow spreading ridges in the northern North Atlantic and the Arctic Ocean. Geophysical Journal International, 177, 451–462. Doi: 10.1111/j.1365-246X.2009.04078.x

Eiken, O., & Hinz, K. (1993). Contourites in the Fram Strait. Sed. Geol., 82, 1–4.

Eldholm, O., Faleide, J. I., & Myhre A. M. (1987). Continent-ocean transition at the western Barents Sea/Svalbard continental margin. Geology, 15(12): 1118-1122.

Evans C.J. & Brereton N.R. (1990). In situ crustal stress in the United Kingdom from borehole breakouts. Geol. Soc., Lond., Spec. Publ., 48, 327–338.

Evans, R., Beamish, D., Crampin, S. & Uqer, S. B. (1987). The Turkish Dilatancy Project (TDP3): multidisciplinary studies of a potential earthquake source region. Geophys. J. R. astr. SOC., 91, 265-286 & 287-330.

Exley, R. J. K., Westbrook, G. K., Haacke, R. R., & Peacock, S. (2010). Detection of seismic anisotropy using ocean bottom seismometers: a case study from the northern headwall of the Storegga Slide. Geophysical Journal International, 183(1), 188-210. Doi:10.1111/j.1365-246X.2010.04730.x

Fejerskov, M. & Lindholm, C. (2000). Crustal stress in and around Norway: an evaluation of stress-generating mechanisms. Geol. Soc. Spec. Publ., 167, 451–467, 2000.

Forsberg, C.F., Solheim, A., Elverhøi, A., Jansen, E., Channell, J. E. T., & Andersen, E.S. (1999). 17. The depositional environment of the western Svalbard margin during the late Pliocene and the Pleistocene: Sedimentary facies changes at Site 986. Proceedings of the Ocean Drilling Program: Scientific Results 162:233-246. Doi:10.2973/odp.proc.sr.162.032.1999

Gay, A., Lopez, M., Berndt, C., & Séranne, M. (2007). Geological controls on focused fluid flow associated with seafloor seeps in the Lower Congo Basin. Marine Geology, 244, 68-92. Doi: 10.1016/j.margeo.2007.06.003.

Haacke, R.R., & Westbrook, G.K. (2006). A fast, robust method for detecting and characterizing azimuthal anisotropy with marine PS converted waves, and its application to the west Svalbard continental slope. Geophys. J. Int., 167, 1402–1412.

Haacke, R.R., Westbrook, G.K., & Peacock, S. (2009). Layer stripping of shear-wave splitting in marine PS waves. Geophysical Journal International, 176: 782-804. Doi: 10.1111/j.1365-246X.2008.04060.x

Hansen, B., & Østerhus, S. (2000). North Atlantic–Nordic Seas exchanges. Progress in Oceanography, 45(2), 109-208. Doi:10.1016/S0079-6611(99)00052-X

Harland, W.B., Cutbill, J.L., Friend, P.F., Gobbett, D.J., Holliday, D.W. Maton, P.I., Parker, J.R., & Wallis, R.H. (1974). The Billefjorden fault zone, Spitsbergen: The long history of a major tectonic lineament. Norsk Polarinstitutt, Oslo, No. 161.

Himmler, T., Sahy, D., Martma, T., Bohrmann, G., Plaza-Faverola, A., Bünz, S., . . . Lepland, A. (2019). A 160,000-year-old history of tectonically controlled methane seepage in the Arctic. Science Advances, 5(8), eaaw1450. Doi:10.1126/sciadv.aaw1450

Hong, W.-L., Sauer, S., Panieri, G., Ambrose Jr., W. G., James, R. H., Plaza-Faverola, A., & Schneider, A. (2016). Removal of methane through hydrological, microbial, and geochemical processes in the shallow sediments of pockmarks along eastern Vestnesa Ridge (Svalbard). Limnology and Oceanography, 61(S1), S324-S343. Doi: 10.1002/lno.10299

Hong, W. L., Pape, T., Schmidt, C., Yao, H., Wallmann, K., Plaza-Faverola, A., . . . Bohrmann, G. (2021). Interactions between deep formation fluid and gas hydrate dynamics inferred from pore fluid geochemistry at active pockmarks of the Vestnesa Ridge, west Svalbard margin. Marine and Petroleum Geology, 127, 104957. Doi: 10.1016/j.marpetgeo.2021.104957

Hovland, M., & Sommerville, J. H. (1985). Characteristics of two natural gas seepages in the North Sea. Marine and Petroleum Geology, 2(4), 319-326. Doi: 10.1016/0264-8172(85)90027-3

Hovland, M., Svensen, H., Forsberg, C. F., Johansen, H., Fichler, C., Fosså, J. H., et al. (2005). Complex pockmarks with carbonate-ridges off mid-Norway: Products of sediment degassing. Marine Geology, 218(1-4), 191–206. Doi: 10.1016/j.margeo.2005.04.005

Howe, J. A., Shimmield, T. M., Harland, R., & Eyles, N. (2008). Late Quaternary contourites and glaciomarine sedimentation in the Fram Strait. Sedimentology, 55(1), 179-200. Doi:10.1111/j.1365-3091.2007.00897.x

Hubbert, M.K., & Willis, D.G. (1957). Mechanics of Hydraulic Fracturing. Transactions of Society of Petroleum Engineers of AIME, 210, 153-163.

Hudson, J. A. (1981). Wave speeds and attenuation of elastic-waves in material containing cracks. Geophysical Journal of the Royal Astronomical Society, 64(1), 133–150

Jakobsson, M., Backman, J., Rudels, B., Nycander, J., Frank, M., Mayer, L., Jokat, W., Sangiorgi, F., O'Regan, M., & Brinkhuis, H. (2007). The early Miocene onset of a ventilated circulation regime in the Arctic Ocean. Nature 447, 986-990.

Johnson, G. L., Southall, J. R., Young, P. W., & Vogt, P. R. (1972). Origin and structure of the Iceland Plateau and Kolbeinsey Ridge. Journal of Geophysical Research, 77(29), 5688-5696. Doi:10.1029/JB077i029p05688

Johnson, J.E., Mienert, J., Plaza-Faverola, A., Vadakkepuliyambatta, S., Knies, J., Bünz, S., Andreassen, K., & Ferré, B. (2015). Abiotic methane from ultraslow-spreading ridges can charge Arctic gas hydrates. Geology, G36440. 36441.

Karstens, J. & Berndt, C. (2015). Seismic chimneys in the Southern Viking Graben – Implications for palaeo fluid migration and overpressure evolution. Earth and Planetary Science Letters, 412, 88-100. Doi: 10.1016/j.epsl.2014.12.017.

Ketzer, M., Praeg, D., Rodrigues, L. F., Augustin, A., Pivel, M. A. G., Rahmati-Abkenar, M., . . . Cupertino, J. A. (2020). Gas hydrate dissociation linked to contemporary ocean warming in the southern hemisphere. Nature Communications, 11(1), 3788. Doi:10.1038/s41467-020-17289-z

Kovacs, L. C., & Vogt, P. R. (1982). Depth-to-magnetic source analysis of the Arctic Ocean region. Tectonophysics, 89(1), 255-294. Doi:10.1016/0040-1951(82)90041-5

Leary, P. C., Li, Y. G., & Aki, K. (1987). Observation and modelling of fault-zone fracture seismic anisotropy — I. P, SV and SH travel times. Geophysical Journal International, 91(2), 461-484. doi:10.1111/j.1365-246X.1987.tb05239.x

Li, X.Y. (1997). Fractured reservoir delineation using multicomponent seismic data. Geophysical Prospecting 45, 39-64

Li, X.-Y. (1998). Processing PP and PS waves in multicomponent sea-floor data for azimuthal anisotropy: theory and overview. Proceeding of the Eighth International Workshop on seismic Anisotropy (Revue De L'institut francia du petrole), 53, 607-620

Lindholm, C. D., Bungum, H., Hicks, E., and Villagran, M. (2000). Crustal stress and tectonics in Norwegian regions determined from earthquake focal mechanisms, Geol. Soc. Spec. Pub., 167, 429–439.

Liu, Y., Teng, T.-L., & Ben-Zion, Y. (2004). Systematic analysis of shear-wave splitting in the aftershock zone of the 1999 Chi–Chi, Taiwan, Earthquake: shallow crustal anisotropy and lack of precursory changes. Bull. Seismol. Soc. Am. 94, 2330–2347.

Liu, X., & Flemings, P. B. (2007). Dynamic multiphase flow model of hydrate formation in marine sediments. Journal of Geophysical Research, 112, B03101, Doi: 10.1029/2005JB004227.

Liu, J., Haeckel, M., Rutqvist, J., Wang, S., & Yan, W. (2019). The mechanism of methane gas migration through the gas hydrate stability zone: Insights from numerical simulations. Journal of Geophysical Research: Solid Earth, 124, 4399–4427. Doi: 10.1029/2019JB017417

Lunne, T., Robertson, P.K., & Powell, J.J.M. (1997). Cone penetration testing in geotechnical practice. Blackie Academic, EF Spon/Routledge Publ., New York, 1997, 312 pp.

Løseth, H., Wensaas, L., Arntsen, B., Hanken, N.-M., Basire, C., & Graue, K. (2011). 1000 m long gas blow-out pipes, Marine and Petroleum Geology, 28, 1047-1060. Doi: 10.1016/j.marpetgeo.2010.10.001.

Madrussani, G., Rossi, G., & Camerlenghi, A. (2010). Gas hydrates, free gas distribution and fault pattern on the west Svalbard continental margin. Geophysical Journal International, 180(2), 666-684. Doi:10.1111/j.1365-246X.2009.04425.x

Moss, J. L., & Cartwright, J. (2010a). 3D seismic expression of km-scale fluid escape pipes from offshore Namibia. Basin Research, 22(4), 481-501. Doi: 10.1111/j.1365-2117.2010.00461.x.

Moss, J. L., & Cartwright, J. (2010b). The spatial and temporal distribution of pipe formation, offshore Namibia. Marine and Petroleum Geology, 27(6), 1216-1234. Doi: 10.1016/j.marpetgeo.2009.12.013.

Mueller M.C. (1992). Using shear waves to predict lateral variability in vertical fracture intensity. The Leading Edge 11(2), 29-35.

Myhre, A. M., & Eldholm, O. (1988). The Western Svalbard Margin (74°-80°N). Marine and Petroleum Geology 5, 134-156.

Nascimento, A.F. do, R.G. Pearce, M.K. Takeya (2002). Local shear wave observations in João Câmara, northeast Brazil. J. Geophys. Res. 107, 2232, Doi:10.1029/2001JB000560.

Nunns, A. G., & Peacock, J. H. (1983). Correlation, identification and inversion of magnetic anomalies in the Norway Basin. Earth Evol. Sci., 2, 130-138.

Nunns, A. G., (1983). Plate tectonic evolution of the Greenland-Scotland Ridge and surrounding regions, in Structure and Development of the Greenland-Scotland Ridge, New Methods and Concepts, edited by Bott et al., pp. 11-30, Plenum, New York.

Nur, A., & Simmons, G. (1969). Stress-induced velocity anisotropy in rock: an experimental study, J. geophys. Res., 74, 6667-6674

Olesen, O., Bungum, H., Dehls, J., Lindholm, C., Pascal, C., & Roberts, D. (2013). Neotectonics, seismicity and contemporary stress field in Norway–mechanisms and implications, Quaternary Geology of Norway, in: Geological Survey of Norway Special Publication, 13, 145–174.

Ottesen, D., Dowdeswell, J.A., & Rise, L. (2005). Submarine landforms and the reconstruction of fast-flowing ice streams within a large quaternary ice sheet: the 2500-km-long Norwegian-Svalbard margin (57 degrees-80 degrees N). Geological Society of America Bulletin 117, 1033–1050.

Overpeck, J., Hughen, K., Hardy, D., Bradley, R., Case, R., Douglas, M., . . . Zielinski, G. (1997). Arctic Environmental Change of the Last Four Centuries. Science, 278(5341), 1251-1256. Doi: 10.1126/science.278.5341.1251

Panieri, G., Bünz, S., Fornari, D. J., Escartin, J., Serov, P., Jansson, P., . . . Gracias, N. (2017). An integrated view of the methane system in the pockmarks at Vestnesa Ridge, 79°N. Marine Geology, 390, 282-300. Doi: 10.1016/j.margeo.2017.06.006

Pastori, M., Baccheschi, P., & Margheriti, L. (2019). Shear wave splitting evidence and relations with stress field and major faults from the "Amatrice-Visso-Norcia Seismic Sequence". Tectonics, 38. Doi: 10.1029/2018TC005478

Pedersen, S. I., Randen, T., Sonneland, L., & Steen, O. (2002). Automatic 3D Fault Interpretation by Artificial Ants. 64th Meeting, EAEG Expanded Abstracts, G037.

Petersen, C. J., Bünz, S., Hustoft, S., Mienert, J., & Klaeschen, D. (2010). High-resolution P-Cable 3D seismic imaging of gas chimney structures in gas hydrated sediments of an Arctic sediment drift. Marine and Petroleum Geology, 27(9), 1981-1994. Doi: 10.1016/j.marpetgeo.2010.06.006

Phrampus, B. J., & Hornbach. M. J. (2012). Recent changes to the Gulf Stream causing widespread gas hydrate destabilization. Nature, 490, 527–530.

Plaza-Faverola, A., Bünz, S., Johnson, J. E., Chand, S., Knies, J., Mienert, J., & Franek, P. (2015). Role of tectonic stress in seepage evolution along the gas hydrate-charged Vestnesa Ridge, Fram Strait. Geophysical Research Letters, 42(3), 733-742. Doi: 10.1002/2014GL062474

Plaza-Faverola, A., & Keiding, M. (2019). Correlation between tectonic stress regimes and methane seepage on the western Svalbard margin. Solid Earth, 10(1), 79-94. Doi:10.5194/se-10-79-2019

Plaza-Faverola, A., Vadakkepuliyambatta, S., Hong, W. L., Mienert, J., Bünz, S., Chand, S., & Greinert, J. (2017). Bottom-simulating reflector dynamics at Arctic thermogenic gas provinces: An example from Vestnesa Ridge, offshore west Svalbard. Journal of Geophysical Research: Solid Earth, 122(6), 4089-4105. Doi: 10.1002/2016JB013761

Portnov, A., Vadakkepuliyambatta, S., Mienert, J., & Hubbard, A. (2016). Ice-sheet-driven methane storage and release in the Arctic. Nature Communications, 7, 10314. Doi: 10.1038/ncomms10314

Rai, C.S. & Hanson, K.E. (1988). Shear-wave velocity anisotropy in sedimentary rocks: a laboratory study, Geophysics, 23, 800-806.

Ramachandran, H., Plaza-Faverola, A., & Daigle, H. (2022). Impact of Gas Saturation and Gas Column Height at the Base of the Gas Hydrate Stability Zone on Fracturing and Seepage at Vestnesa Ridge, West-Svalbard Margin. Energies, 15(9), 3156.

Robinson, A., Bayrakci, G., Macdonald, C., Minshull, T., Bull, J., Chapman, M., Henstock, T. & Callow, B. (2022). Constraints on fluid flow pathways from shear-wave splitting in and around an active fluid-escape structure: Scanner Pockmark, North Sea. Geophysical Journal International, 231 (2), 1164-1195. Doi: 10.1093/gji/ggac197.

Ruppel, C. D., & Kessler, J. D. (2017). The interaction of climate change and methane hydrates. Reviews of Geophysics, 55(1), 126-168. Doi: 10.1002/2016RG000534

Rutqvist, J. (2015). Fractured rock stress-permeability relationships from in situ data and effects of temperature and chemical-mechanical couplings. Geofluids, 15(1-2), 48-66. Doi: 10.1111/gfl.12089

Sayers, C.M. & van Munster, J.G. (1991). Microcrack-induced seismic anisotropy of sedimentary rocks, J. geophys. Res., 96, 16 529-16 533.

Sayers, C.M. (1988). Stress-induced ultrasonic wave velocity anisotropy in fractured rock. Ultrasonics, 26, 311-317.

Schoenberg, M., & Douma, J. (1988). Elastic wave propagation in media with parallel fractures and aligned cracks. Geophysical Prospecting, 36(6), 571–590.

Schutt, D., Humphreys, E. D., & Dueker, K. (1998). Anisotropy of the yellowstone hot spot wake, Eastern Snake River Plain, Idaho. Pure and Applied Geophysics,151, 443–462.

Siegesmund, S., Kern, H., & Vollbrecht, A. (1991). The effect of oriented microcracks on seismic velocities in an ultramylonite. Tectonophysics, 186, 241-251.

Singhroha, S., Bünz, S., Plaza-Faverola, A., & Chand, S. (2016). Gas hydrate and free gas detection using seismic quality factor estimates from high-resolution P-cable 3D seismic data. Interpretation, 4(1), SA39–SA54. Doi: 10.1190/INT-2015-0023.1

Singhroha, S., Chand, S., & Bünz, S. (2019). Constraints on gas hydrate distribution and morphology in Vestnesa Ridge,W-Svalbard margin using multicomponent ocean-bottom seismic data. Journal of Geophysical Research: Solid Earth, 124, 4343–4364. Doi:10.1029/2018JB016574

Singhroha, S., Bünz, S., Plaza-Faverola, A., & Chand, S. (2020). Detection of gas hydrates in faults using azimuthal seismic velocity analysis, Vestnesa Ridge, W-Svalbard Margin. Journal of Geophysical Research: Solid Earth, 125, e2019JB017949. Doi: 10.1029/2019JB017949

Slack, R., Ebrom, D., McDonald, J.A. & Tatham, R.A. (1992). Shear-wave birefringence in the presence of two azimuthally anisotropic layers with difference symmetry axes, SEG Expanded Abstracts, 11, 1359.

Smith, A. J., Mienert, J., Bünz, S., & Greinert, J. (2014). Thermogenic methane injection via bubble transport into the upper Arctic Ocean from the hydrate-charged Vestnesa Ridge, Svalbard. Geochemistry, Geophysics, Geosystems, 15, 1945–1959, Doi: 10.1002/2013GC005179.

Steel, R., Gjelberg, J., Helland-Hansen, W., Kleinspehn, K., Nøttvedt, A., & RyeLarsen, M. (1985). The Tertiary strike-slip basins and orogene belt of Spitsbergen. In: Biddle, K., & Cristie-Blick, N. (eds.), Strike-slip Deformation, Basin Formation, and Sedimentation, Soc. Econ. Paleontol. Mineral., Spec. Publ. 37, 339-359.

Stein, R., Niessen, F., Schoster, F., Bahr, B., Gebhardt, C., Kukina, N., Lensch, N., Nam, S., Noffke, H., Penshorn, D., Puhr, A., Saraswat, R., Scha¨ fer, Chr., Schnieder, J., Thiede, J., Winkleman, D., & Yanina, Y. (2005). Marine geology. In: Scientific Cruise Report of the Arctic Expedition ARK-XX/3 of RV Polarstern in 2004: Fram Strait, Yermak Plateau and East Greenland Continental Margin (ed. R. Stein). Ber. Polarfors., 517, 41–95.

Sultan, N., Bohrmann, G., Ruffine, L., Pape, T., Riboulot, V., Colliat, J.-L., . . . Wei, J. (2014). Pockmark formation and evolution in deep water Nigeria: Rapid hydrate growth versus slow hydrate dissolution. Journal of Geophysical Research: Solid Earth, 119(4), 2679-2694. Doi:10.1002/2013JB010546

Sultan, N., Marsset, B., Ker, S., Marsset, T., Voisset, M., Vernant, A. M., . . . Drapeau, D. (2010). Hydrate dissolution as a potential mechanism for pockmark formation in the Niger delta. Journal of Geophysical Research: Solid Earth, 115(B8). Doi:10.1029/2010JB007453

Talwani, M., & Eldholm, O. (1977). Evolution of the Norwegian-Greenland Sea. Geological Society of America Bulletin 88(7), 969-999.

Vachon, R., Schmidt, P., Lund, B., Plaza-Faverola, A., Patton, H., & Hubbard, A. (2022). Glacially induced stress across the Arctic from the Eemian interglacial to the present—Implications for faulting and methane seepage. Journal of Geophysical Research: Solid Earth, 127, e2022JB024272. Doi: 10.1029/2022JB024272

Van Bemmel, P. & Pepper, R. (2000). Seismic Signal Processing Method and Apparatus for Generating a Cube of Variance Values. United States Patent 615155.

Vanneste, M., Guidard, S., & Mienert, J. (2005). Bottom-simulating reflections and geothermal gradients across the western Svalbard margin. Terra Nova, 17(6), 510-516. Doi:10.1111/j.1365-3121.2005.00643.x

von Appen, W.-J., Schauer, U., Somavilla, R., Bauerfeind, E., & Beszczynska-Möller, A. (2015). Exchange of warming deep waters across Fram Strait. Deep Sea Research Part I: Oceanographic Research Papers, 103, 86-100. doi: 10.1016/j.dsr.2015.06.003

Vogt, P. R., Crane, K., Sundvor, E., Max, M. D., & Pfirman, S. L. (1994). Methane-generated (?) pockmarks on young, thickly sedimented oceaniccrust in the Arctic: Vestnesa ridge, Fram strait. Geology, 22(3), 255–258.

Vogt, P. R. (1986). Geophysical and geochemical signatures and plate tectonics, in The Nordic Seas, edited by B. G. Hurdle, SpringerVerlag, New York.

Vogt, P. R., Kovacs, L. C., Bernero, C., & Srivastava, S. P. (1982). Asymmetric geophysical signatures in the Greenland-Norwegian and Southern Labrador Seas and the Eurasia Basin. Tectonophysics, 89(1), 95-160. Doi:10.1016/0040-1951(82)90036-1

Waghorn, K. A., Bünz, S., Plaza-Faverola, A., & Johnson, J. E. (2018). 3-D Seismic Investigation of a Gas Hydrate and Fluid Flow System on an Active Mid-Ocean Ridge; Svyatogor Ridge, Fram Strait. Geochemistry, Geophysics, Geosystems, 19(8), 2325-2341. Doi:10.1029/2018gc007482

Westbrook, G. K., Thatcher, K. E., Rohling, E. J., Piotrowski, A. M., Pälike, H., Osborne, A. H., . . . Aquilina, A. (2009). Escape of methane gas from the seabed along the West Spitsbergen continental margin. Geophysical Research Letters, 36(15). doi:10.1029/2009gl039191

Willis, H.A., Rethford, G.L. & Bielandski, E. (1986). Azimuthal anisotropy: occurrence and effect on shear-wave data quality. 56th Ann. lnt. SEG Meeting, Houston, Expanded Abstracts. 479-481.

Zinke, J. C., & Zoback, M. D. (2000). Structure-related and stress-induced shear-wave velocity anisotropy: observations from microearth-quakes near the Calaveras fault in central California. Bulletin of the Seismological Society of America, 90(5), 1305–1312. Doi: 10.1785/0119990099

Zatsepin, S. V., & Crampin, S. (1997). Modelling the compliance of crustal rock—I. Response of shear-wave splitting to differential stress. Geophysical Journal International,129, 477–494.

Zheng, J., Zheng, L., Liu, H.-H., & Ju, Y. (2015). Relationships between permeability, porosity and effective stress for low-permeability sedimentary rock. International Journal of Rock Mechanics and Mining Sciences, 78, 304-318. Doi: 10.1016/j.ijrmms.2015.04.025

7. Focused methane migration formed pipe structures in permeable sandstones: Insights from uncrewed aerial vehicle-based digital outcrop analysis in Varna, Bulgaria

Christoph Böttner[1], Ben J. Callow[2], Bettina Schramm[1], Felix Gross[3], Jacob Geersen[1], Mark Schmidt[1], Atanas Vasilev[4], Petar Petsinski[4], Christian Berndt[1]

[1]*GEOMAR Helmholtz-Centre for Ocean Research Kiel, Kiel, Germany*

[2]*Ocean and Earth Science, University of Southampton, Southampton, UK*

[3]*Center for Ocean and Society, University of Kiel, Kiel, Germany*

[4]*Institute of Oceanology – Bulgarian Academy of Sciences, Varna, Bulgaria*

Abstract

Focused fluid flow shapes the evolution of marine sedimentary basins by transferring fluids and pressure across geological formations. Vertical fluid conduits may form where localized overpressure breaches a cap rock (permeability barrier) and thereby transports overpressured fluids towards shallower reservoirs or the surface. Field outcrops of an Eocene fluid flow system at Pobiti Kamani and Beloslav Quarry (ca 15 km west of Varna, Bulgaria) reveal large carbonatecemented conduits, which formed in highly permeable, unconsolidated, marine sands of the northern Tethys Margin. An uncrewed aerial vehicle with an RGB sensor camera produces ortho-rectified image mosaics, digital elevation models and point clouds of the two kilometre-scale outcrop areas. Based on these data, geological field observations and petrological analysis of rock/core samples, fractures and vertical fluid conduits were mapped and analyzed with centimetre accuracy. The results show that both outcrops comprise several hundred carbonate-cemented fluid conduits (pipes), oriented perpendicular to bedding, and at least seven bedding-parallel calcite cemented interbeds which differ from the hosting sand formation only by their increased amount of cementation. The observations show that carbonate precipitation likely initiated around areas of focused fluid flow, where methane entered the formation from the underlying fractured subsurface. These first carbonates formed the outer walls of the pipes and continued to grow inward, leading to self-sustaining and self-reinforcing focused fluid flow. The results, supported by literature-based carbon and oxygen isotope analyses of the carbonates, indicate that ambient seawater and advected fresh/brackish water were involved in the carbonate precipitation by microbial methane oxidation. Similar structures

may also form in modern settings where focused fluid flow advects fluids into overlying sand-dominated formations, which has wide implications for the understanding of how focusing of fluids works in sedimentary basins with broad consequences for the migration of water, oil and gas.

Keywords: Flow processes, fluid flow, fluid–rock-interaction, freshened groundwater system, Pobiti Kamani, SfM, Tethys Margin.

7.1. Introduction

Fluids play an important role in the evolution of marine sedimentary basins. Fluid abundance and composition are primarily governed by flow along permeable beds or focused flow across geological formations (Whitaker, 1986; Berndt, 2005). Seismic data have revealed focused fluid flow conduits in various geological settings around the world, manifesting themselves in a wide range of seismic anomalies (Cartwright, 2007; Løseth et al., 2009; Andresen, 2012; Karstens & Berndt, 2015). Seismic imaging is an effective way to investigate fluid flow systems because acoustic impedance and seismic wave attenuation are highly sensitive to pore space filling (White, 1975). This sensitivity allows the imaging and interpretation of basin-scale fluid flow systems, subsurface geometries, fluid accumulations and permeability barriers (Berndt, 2005; Cartwright, 2007). However, there is an observational gap between seismic data (several metre-scale) and geological field mapping (millimetre-scale to centimetre-scale) of natural fluid flow systems.

Field observations and geological sampling from exhumed ancient fluid flow systems can constrain their internal architecture, the diagenetic interaction of fluids with the bedrock and physical properties of flow processes (De Boever et al., 2006a; Huuse et al., 2010; Capozzi et al., 2015; Nelson et al., 2017). The comparison of field observations from ancient fluid flow systems with seismic data from modern marine sedimentary systems can narrow the interpretation gap between seismic and sub-seismic scales, for example, below 4 m vertical resolution of highresolution three-dimensional P-cable seismic data (Planke & Berndt, 2007).

Uncrewed aerial vehicles (UAVs) equipped with high-resolution optical RGB sensor cameras represent a cost-effective and efficient way to map complex geological patterns in 3D providing kilometre-scale maps of fluid flow features in terrestrial outcrops with centimetre-resolution (e.g. Bemis et al., 2014). This yields valuable information on the spatial distribution patterns and internal architecture. Combination with field observations and rock sampling provides a

further insight into the interaction between fluid flow and the bedrock and hydraulic properties, especially permeability (Bisdom et al., 2017).

Pobiti Kamani, located 20 km north-west of Varna, Bulgaria, hosts several hundred ancient

carbonate-cemented tubular concretions (hereafter referred to as 'pipes') which are up to 10 m high (De Boever et al., 2006a,b). The cemented pipes are the largest exposed hydrocarbonderived carbonate conduits known globally and are well-exposed in the unconsolidated sands and lithified sandstones of the Dikilitash Formation (Sinclair et al., 1998; De Boever et al., 2006a; Capozzi et al., 2015). At Beloslav Quarry, an old sand extraction quarry near the Village of Beloslav, the pipes crop out along a ca 40 m high cliff which provides the opportunity to map their spatial distribution and vertical extent (De Boever et al., 2009a).

Focused fluid flow in marine settings, which is primarily dependent on the hydraulic parameters of the hosting sediments, is predominantly observed through faults and fracture networks in low permeability silty to muddy sediments or lithified rocks (e.g. Judd & Hovland, 2007; B¨ottner et al., 2019). It is far less clear how fluids can stay focused in permeable sand because the high permeability should allow fluids to disperse. Nevertheless, the hydrocarbon-derived carbonate conduits unequivocally document focused fluid flow in the unconsolidated sand of the Dikilitash Formation in the study area (De Boever et al., 2006a,b). Similar but much smaller pipe structures also exist in the Kattegat, Denmark or on the Montenegrin margin, Adriatic Sea (Jørgensen, 1992; Angeletti et al., 2015).

The aim of this study is to analyze the pipeforming processes within sand formations using the two outcrops at Beloslav Quarry and Pobiti Kamani. The objectives are to first evaluate the structural control on seep location and determine the influence of regional and local tectonic deformation on pipe location. Second, the involved fluids and key pre-conditions for focused fluid flow and subsequent formation of pipes in sand formations are identified and characterized. This includes constraining the temporal evolution of such pipe formation during the Eocene; and, third, the geological setting in which such pipes may form is assessed.

7.2. Geological setting

The Pobiti Kamani natural park covers an area of about 253 ha within the Varna depression, along the eastern side of the Alpine Balkanides. It forms a section of the Moesian Platform, a tectonic unit that extends from northern Bulgaria to southern Romania (Bergerat et al., 1998; Georgiev et al., 2001). The Moesian Platform was likely part of a block-faulted Triassic to

Oligocene siliciclastic shelf and carbonate succession along the northern Tethys margin (Sinclair et al., 1998). Several hundreds of calcite-cemented tubular concretions (hereafter referred to as pipes) (Figure 7.1; Botz et al., 1993; De Boever et al., 2006a, 2006b, 2009a, 2009b, 2011a, 2011b) are hosted in the Dikilitash Formation. This formation comprises alternating sequences of unconsolidated silt to sand sediments with interbeds of calcite-cemented sandstones (Figure 7.1). The Dikilitash Formation is ~ 40 m thick and was deposited in the Early Eocene in a mid to outer ramp depositional system at water depths around 100 m (De Boever et al., 2006a, 2009a, 2009b).

The pipes are 0.5-3 m in diameter and up to 10 m high. Groups of pipes have been documented at several locations dispersed over an area of 70 km², including the Central, Strashimirovo, Beloslav quarry, Banovo and Teterlik groups (Figure 7.1; De Boever et al., 2009a, 2009b, 2011a, 2011b). These groups align along Palaeogene NNE-SSW trending transtensional faults that have up to 80 m vertical displacement (Bergerat et al., 1998; De Boever et al., 2009b). The colocation of the groups with the Palaeogene faults suggests a structural control on the location of the pipes (De Boever et al., 2009b).

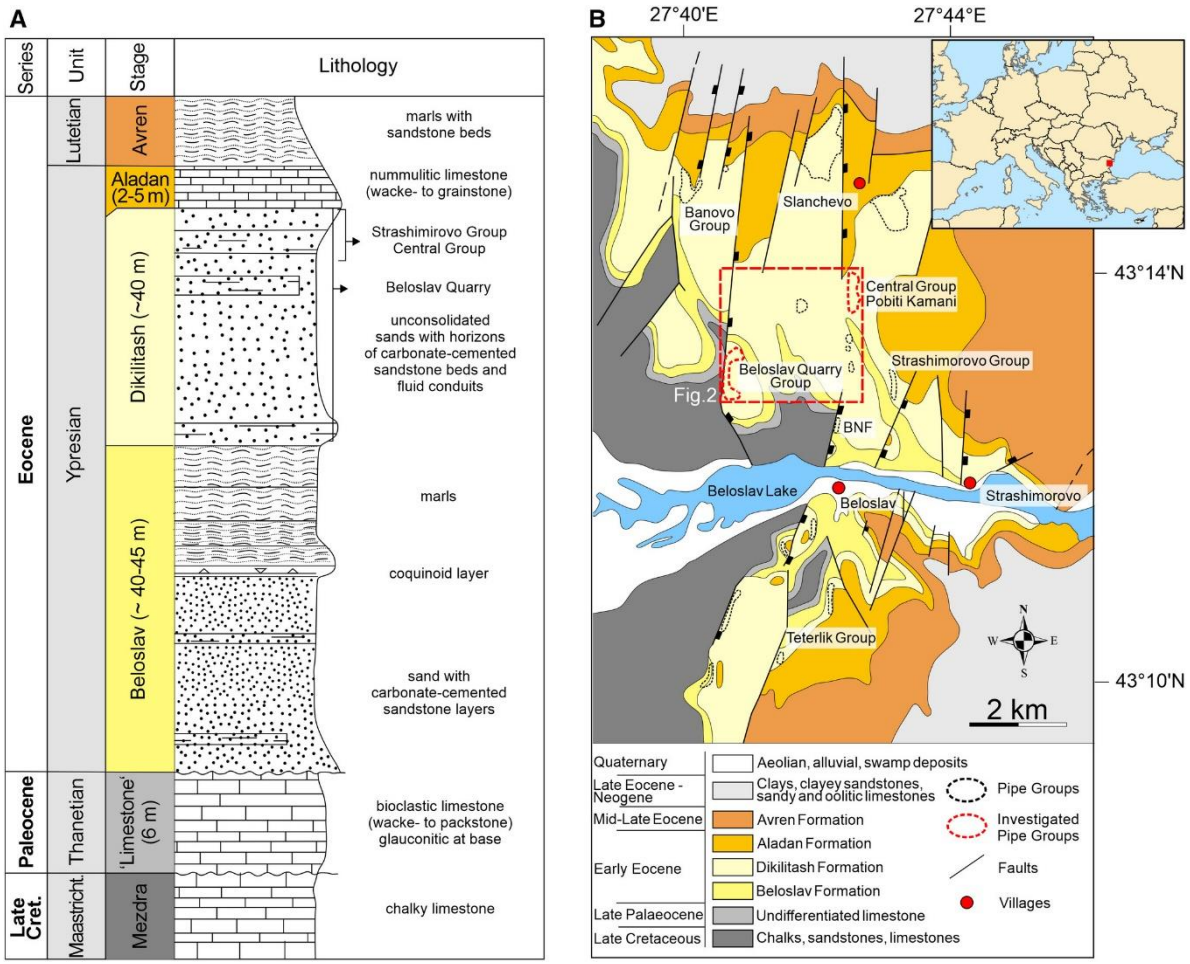

Figure 7.1: (A) Stratigraphic column with the main lithologies (with highlighted formations in which the pipes appear) and (B) simplified geological setting of the survey area. Investigated pipe groups are highlighted with red dotted lines. BNF = Beloslav North fault (modified after De Boever et al., 2009b). The small inset shows a red square with the location of the simplified geological map. The red dashed box shows the location of Figure 7.2.

Geochemical analyses of the calcite-cemented tubular concretions show that they formed from ascending methane-rich fluids resulting in low-Mg carbonate precipitation (Botz et al., 1993; De Boever et al., 2006a, 2006b, 2009a, 2009b). Stable carbon isotope composition of carbonates of about -43 to -45 ‰ V-PDB (Botz et al., 1993; De Boever et al., 2006a) and heavily depleted $\delta^{13}C$ isotope ratios of archaeal biomarker ($\delta^{13}C$ -123‰ to -81‰ V-PDB, De Boever et al., 2009a) indicate that the exposed pipes and calcite cemented interbeds likely formed because of microbially mediated anaerobic oxidization of methane at or below the seafloor. The corresponding fluids likely migrated along the transtensional faults into the Dikilitash Formation (De Boever et al., 2009b). Based on oxygen isotope ratios of carbonates the environmental conditions during formation were correlated with Lower Eocene marine environment (age ~50 Ma; De Boever et al., 2006a). There are two distinct groups of pipes with

differing $\delta^{13}C$ and $\delta^{18}O$ isotope ratios. Group 1 carbonates ($\delta^{13}C$ ~ -45 to -35‰ V-PDB & $\delta^{18}O$ ±1‰ V-PDB) likely formed because of fluids from below that included biogenic methane and ancient sea (salt) water. Group 2 carbonates ($\delta^{13}C$ <-25‰ V-PDB & $\delta^{18}O$ <-6.5‰ V-PDB) are characterised by alteration of the isotope ratios likely due to mixing of ascending methane with marine DIC ($\delta^{13}C$ ~ 0‰) and/or δ^{13}-enriched CO_2 and recrystallisation because of percolating Cenozoic meteoric water (De Boever et al., 2009a). These distinct groups appear in alternating concentric bands from the centre of the carbonate conduits (De Boever et al., 2006a).

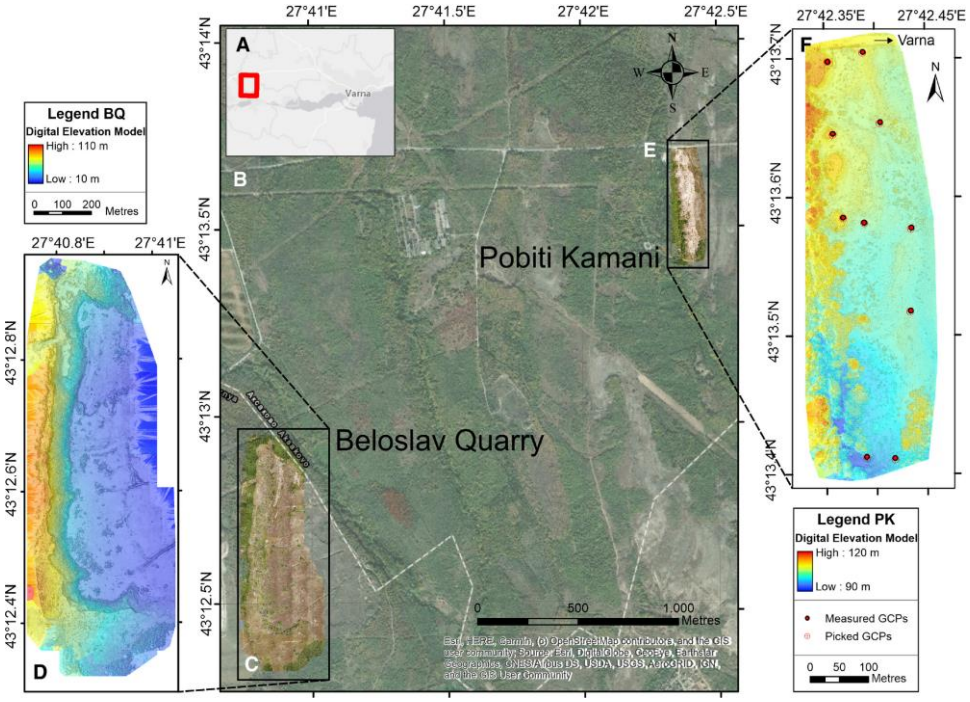

Figure 7.2: Overview map of the survey areas located 20 km west of Varna, Bulgaria. (A) Regional map showing the location of the investigated areas in a red box. (B) Local map of the two investigated outcrops of Pobiti Kamani and the Beloslav Quarry (white boxes). Black lines indicate the approximate location of normal faults in the area (modified from De Boever et al., 2006a). (C) Ortho-rectified image mosaic of Beloslav Quarry and (D) corresponding SfM-derived digital elevation model (DEM). (E) Ortho-rectified image mosaic of Pobiti Kamani and (F) corresponding DEM. Red dots indicate measured ground control points (GCPs) and red crosses the picked GCPs.

7.3. Methods

An uncrewed aerial vehicle (UAV, DJI Inspire 2), equipped with a 20.8 MP Zenmuse X5S (RGB channels) camera and a DJI MFT 15mm/1.7 ASPH lens, was used to acquire images of the Pobiti Kamani area and Beloslav Quarry (Figure 7.2). The images were stored in jpg format. The flight surveys were designed with DJI GroundStationPro, and the surveys were subsequently flown automatically by the UAV. This procedure results in a very regular flight

pattern and good overlap of neighbouring images (Overlap: Front 90%, Sides 60%; Shot interval: 2 s; Speed: 2.6 m/s). For the Beloslav Quarry, manually-controlled surveys were conducted to achieve better coverage of the cliff, which represents the 80 m-high surface expression of a transtensional fault. The average flight time was ~25 minutes with rolling shutter set to 2-3 s resulting in a data set of more than 4500 images (~42 GB) for the 200 by 600 m wide Pobiti Kamani area and more than 2000 images (~25 GB) for the 400 by 1200 m-wide area of Beloslav Quarry.

The commercial software Pix4D™ was used to calculate the digital elevation model (DEM), a point cloud, and an ortho-rectified mosaic (RGB) by the structure from motion (SfM) approach. For the Pobiti Kamani area, the resolution of the derived ortho-rectified mosaic, point cloud and DEM resolution is ~1 cm per pixel. Ten ground control points were used to adjust the geo-referencing of the results. Real-time kinematic (RTK) service was not available during the acquisition campaign, resulting in a minimum accuracy of the location of the overall model of 1.3 m ± 0.6 m. The Beloslav Quarry area is hard to access because of the high relief and thus ground control points could not be established, resulting in a location accuracy of ~ 2 m. The resolution of the Beloslav Quarry model is ~2 cm per pixel.

Surface fractures and pipes were manually picked in the ortho-rectified mosaic to analyse the spatial distribution of the pipe structures and fractures. The manual picking of in-situ pipes was validated with outcrop observations, ensuring the omission of eroded pipes which are not in situ. Multiple ESRI ArcGIS (version 10.6) geoprocessing tools delineate the outlines of the pipes. In the first step, the inverse of the DEM was calculated and all depressions filled. Subsequently a differential grid was calculated by subtracting the original DEM from the filled DEM and classified all regions that had changed by more than 0.1 m. After automatically drawing outlines around the classified areas, all generated polygons that did not include one of the manually-picked pipe structures were removed. This step was necessary to remove trees and houses, which were also picked and outlined by the workflow. In a final step, all polygons were manually inspected and some were edited due to their proximity to trees or eroded pipe fragments which resulted in enlarged polygons. During the analysis of the spatial distribution of pipes, the pattern analyses tool ‘z-score’ was used. The z-score is the standard deviation that a given population distribution deviates from a normal distribution. It provides a measure of clustering. A z-score below –2.58 indicates the presence of clustering, with a below 1 % likelihood that the clustering is statistically random.

UAV-based photogrammetric SfM allows rapid mapping of pipes and tectonic deformation structures over large areas (tens of square kilometres). However, ground-based geologic mapping and sampling is necessary to analyse the composition, texture and geometry of the pipes, to understand further the relationship between the pipes with the surrounding host sediment and the sub-horizontal interbeds. Field samples were collected with a hand-held drill with a 32 mm diamond drill bit to compare the composition and texture of the pipes with the surrounding host rock and the carbonate beds. Samples were collected along vertical and horizontal transects across single well-exposed pipes to a maximum depth of 25 mm into the carbonates and documented the sample orientation. Thin sections (30 μm thickness) were prepared and mounted onto glass slides, for petrological analysis and scanning electron microscopy (SEM). The samples were impregnated with blue epoxy resin, highlighting the pore space. A total of 18 thin sections were prepared and analysed using a polarising microscope. SEM imaging was conducted with a Carl Zeiss Leo 1450 VP SEM with an energy dispersive spectrometer (EDX). The samples were carbon coated and imaged at a spatial resolution of 700 nm. From the SEM image data, the contrast between mineral phases are determined by their relative X-ray attenuations (Ketcham and Carlson, 2001). There was a significant image contrast between each mineral phase, allowing the calculation of each phase, accurate to the nearest percent. SEM-EDX analysis verified the elemental composition of each phase. Using the method approach described in Callow et al. (2020), image processing of the SEM images was done using ImageJ software to obtain calculations of porosity, mineral area fractions, as well as grain and pore size distributions.

7.4. Results

7.4.1. Mapping and analyses of spatial distribution

7.4.1.1. Pobiti Kamani

The data set comprises 672 individual pipes, 42 individual calcite-cemented interbed exposures covering at least 945 m² and 1016 individual fractures with a total length of 1471 m and a mean length of ~ 1.45 m (Figure 7.3). These fractures are predominantly oriented in a NNE-SSW strike direction with a ~90° dip, which is validated with field measurements (Figure 7.3A). The pipes in Pobiti Kamani are highly clustered (Average nearest neighbour, z-score: -13.33) with an average distance between nearest pipes of 3.58 ± 3.38 m (Maximum 43.16 m; Figure 7.3B). The pipe distribution is densely spaced with a maximum of 1 pipe per 14.3 m² (Mean: 1 pipe per 36.7 m²). There is no predominant pipe cluster strike direction nor can a direct relationship

be discerned between fracture geometries and pipe location (Figure 7.3A. vs B, Figure 7.3D) as suggested by De Boever et al. (2009b).

Geomatric parameter	Area [m^2]	Perimeter [m]	Maximun height [m]	Minimum width [m]	Maximum width [m]	Area/ Perimeter [m]	Eccentricity	Volume [m3]	Nearest Neighbour [m]
Minimum	0.05	0.76	0.00	0.24	0.24	0.06	1.00	0.00	0.58
Mean	1.03	3.49	1.08	0.96	1.24	0.26	1.32	1.58	3.58
Maximum	2.56	13.53	5.83	2.95	4.20	0.66	2.63	24.75	43.16

Table 1: Geometric parameters from high-resolution digital elevation model (DEM) and polygons of pipes within Pobiti Kamani include area, perimeter, maximum height, minimum and maximum width, and derived parameters such as the ratio between area and perimeter, the eccentricity, and volume as well as spatial information on the distance to their nearest neighbour.

For Pobiti Kamani, approximately one fifth of pipes in the Pobiti Kamani show predominantly solidified inner cores (~22%). The majority of pipes (~78%) have unlithified inner cores (Figure 7.3E). The outlines of the pipes allow assessing geometric parameters from the high-resolution DEM. The average, maximum and minimum values are summarised in Table 1. The horizontal eccentricity and area versus perimeter parameters indicate less complex, subrounded circular features.

The data analyses of the pipes are limited by the extent of the surveyed area. There are more pipes to the North and to the South, which are not part of the orthomosaic map. The DEM suggests that the pipes occur in the hangingwall side of the NNE-SSW striking Paleogene transtensional faults. However, the fault contact that would constrain the pipe location towards the West is not visible in the orthomosaic or DEM maps.

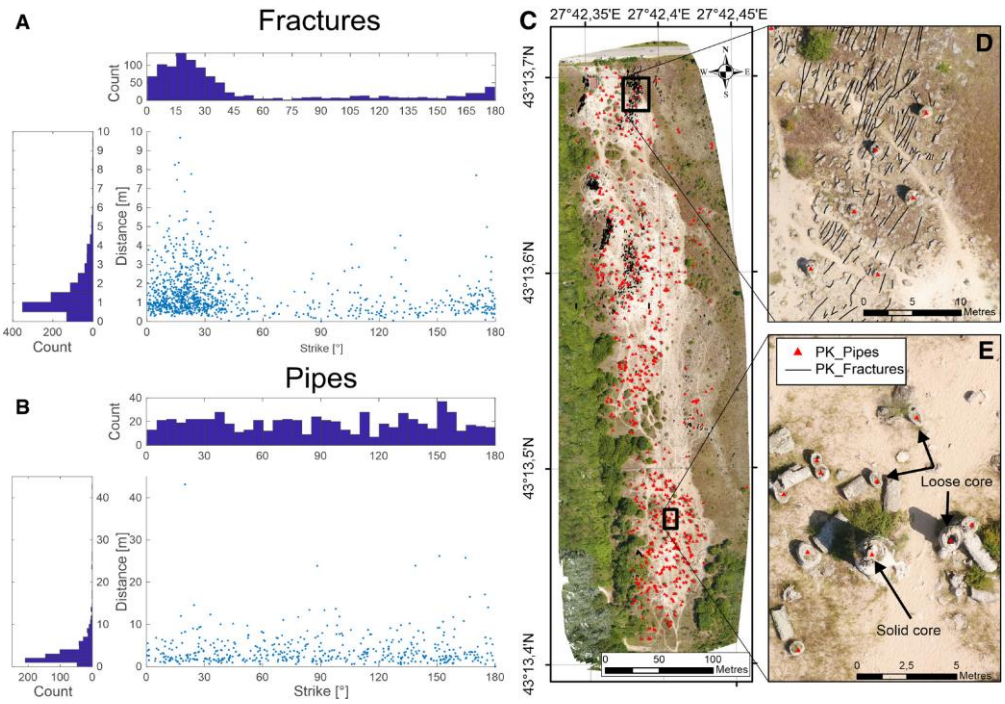

Figure 7.3: Uncrewed aerial vehicle (UAV)-based orthomosaic map from Pobiti Kamani. (A) Scatterplot for fractures of their strike direction against measured length and corresponding histograms showing the frequency of both per unit. (B) Scatterplot for pipes and their nearest neighbour direction against nearest neighbour distance and corresponding histograms showing the frequency of both per unit. (C) UAV-based ortho-rectified image of Pobiti Kamani with manually picked pipes and fractures. Black boxes show the location of (D) and (E); red triangles show pipe location and black lines indicate fractures. (D) The pipe location with respect to the fractures and (E) the location of pipe with respect to each other and the appearance of single pipes (loose inner core and solid inner core). PK = Pobiti Kamani.

7.4.1.2. Beloslav Quarry

The 3D point cloud was used in combination with the original RGB-images to manually pick the pipes on different elevation levels. The point cloud shows that the pipes are separated by at least seven distinct interbeds, separating the pipes into tiers (colour coded triangles between I1-I7, see Figure 7.4B). These interbeds show sub-horizontal bedding with slight dip of less than 10° in south-eastern direction (Figure 7.4B) and consists of calcite-cemented sandstones that separate the beds of unconsolidated silt to sand sediments which host the pipes.

The data set comprises 1066 individual pipes and large carbonate interbed exposures covering more than 1600 m², but the coarser resolution of this data set and denser vegetation prohibit digital analyses of fractures. Spatial analyses of the pipes show that they are highly clustered (Average nearest neighbour, z-score: -37.84) and have a neighbouring distance of 2.24 m ± 3.38

m (Max. 55.47 m, Min. 0.04 m). The pipes are densely spaced with an average of 1 pipe per 13.6 m² (Max. 1 pipe per 4.6 m²). There is no preferred pipe cluster orientation observed from the data.

7.4.2. Field observations

Field observations within the Beloslav Quarry are used to characterise the geometry of the carbonate pipes and their relation to the surrounding host strata. Carbonate pipes of meter-scale diameter (Figure 7.5A) protrude from a light grey sand bed. The lack of bedding in the host sediment intervals is evidence for significant bioturbation or sediment reworking. The carbonate pipes are orientated sub-vertically and perpendicular to the carbonate horizons (Figure 7.5B-C). The pipes are meter-scale in width and appear to occur in discrete clusters (Figure 7.5D). There is no evidence that the spatial distribution of the individual clusters follows any regular pattern and the distance between individual pipes (~2-4 m) fits the results from the orthomosaic analyses. Many carbonate pipes bifurcate upwards (Figure 7.4E) confirming interpretations based on the UAV raw imagery. However, the convergence of pipes also occurs in some places (two pipes merging into one; see Figure 7.5). More complex geometries where pipes appear intertwined are also observed.

All pipes show a more globular or bulbous outer surface towards their top (Figure 7.5F), which often correlates with overlying calcite cemented interbeds. The interbeds dip down slightly towards the pipes, highlighting a direct relationship between the pipes and calcite cemented interbeds (Figure 7.5G). There appear to be two main calcite cemented interbeds of meter-scale thickness, comprising an upper (Figure 7.5G) and lower interbed (Figure 7.5H). Furthermore, the base of the calcite cemented interbeds display a branching network of burrows, similar in morphology to the interpreted vertical burrows on the outer margin of the pipes (Figure 7.5-L).

The colour of the host sand bed is the same as that of unweathered pipes (Figure 7.5I). The outer boundary between the carbonate pipe and the surrounding host rock is sharp in weathered examples, but slightly more diffuse in unweathered examples (Figure 7.5I-K). The host sediment is composed of poorly consolidated, quartz sand with minor micritic cement (Figure 7.5I). The overall bed is heavily bioturbated, with an abundance of shell fragments and Nummulites, ranging from 0.5-25 mm in diameter, providing evidence for an outer ramp depositional environment (Figure 7.5M).

To ground-truth the orthomosaic map and DEM, fracture distribution, orientation, and dip was measured in the field. For Pobiti Kamani, 36 fractures are measured which strike in NNE/SSW direction and dip steeply to the east, matching the NNE/SSW trend of the 1016 fracture orientations measured from the orthomosaic map (Figure 7.7A). The observed fractures cross-cut the carbonate pipes, suggesting that the fractures post-date the pipes. From geological field data at Beloslav Quarry, the carbonate pipes display sub-vertical carbonate veining within open fractures (Figure 7.7B-C). The veins are linear in shape, displaying no degree of sinuosity and no evidence of veins branching. The veins are commonly secondarily infilled with carbonate into previously open fractures. The veins appear to display a predominant N/S orientation. Within a (lower) carbonate bed, S-shearing is observed (Figure 7.7D). Overall, there appears to be no clear diagenetic link between the fractures that cross-cut the pipes and formation of the pipes within the Dikilitash Formation.

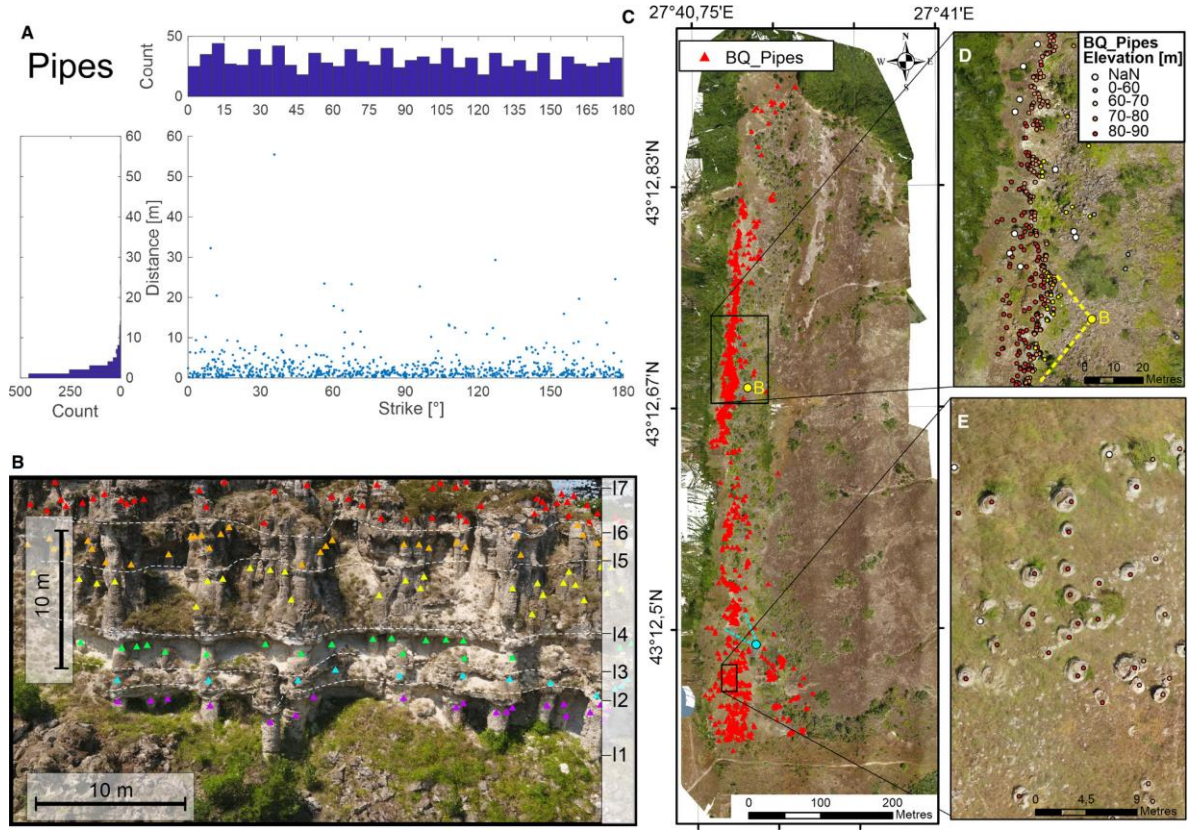

Figure 7.4: Uncrewed aerial vehicle (UAV)-based photogrammetric results from Beloslav Quarry. (A) Scatterplot for pipes and their nearest neighbour direction against nearest neighbour distance and corresponding histograms showing the frequency of both per unit. (B) Point cloud image of one prominent cliff showing six tiers of pipes (coloured triangles) corresponding to the intervals between the seven carbonate cemented interbeds (I1 to I7). See (D) for location. (C) UAV-based ortho-rectified image of Beloslav Quarry (BQ) with manually picked pipes and fractures. Black boxes show the location

of (D) and (E), red triangles show pipe location, turquoise circle shows the location of Figure 7.5. (D) Pipes picked in the point cloud separated by their elevation. Yellow dot marks the viewing location of (B). (E) Close-up of the densely-spaced pipes in the southern part of the outcrop.

7.4.3. SEM analyses

Light microscopy and SEM imaging show that the host sediment and pipes have identical composition, differing only by the amount of carbonate cementation (low-Mg calcite cement, Figure 7.6). The host sediment and pipes are composed of quartz grains (92 %), with minor plagioclase feldspar (8 %) and opaque minerals (0.1%). The grains are well-sorted and subangular, ranging from 100-140 μm diameter. The host sediment has a very high porosity of 44.3 %, reducing to 6.7 % in the pipe, with precipitated low-Mg calcite cement occupying greater than 85 % of the total pore volume. Using the known calculated porosity and average pore diameter (100 μm) values, the permeability of the uncemented sediments (k_u) is estimated using the Kozeny-Carman equation:

$$k_u = \left(\frac{1}{180}\right)\left(\frac{{n_o}^3}{(1-n_o)^2}\right) d^2 \quad (1)$$

Where n_0 is total porosity and d is average pore diameter. While for cemented samples, the permeability (k_c) is given by

$$k_c = k_u \left(\frac{\varepsilon}{\varepsilon_0}\right)^3 \left(\frac{1-\varepsilon_0}{1-\varepsilon}\right)^2 \quad (2)$$

Where ε is the total porosity of cemented sediments (new porosity), and ε_0 is the total porosity of the uncemented sediments (initial porosity). With increased calcite precipitation inside the pipes the permeability reduces by three orders of magnitude to 1.9 x10^{-14} m^2 (0.02 Darcy) relative to the surrounding host sediment of 1.5 x10^{-11} m^2 (15 Darcy). This equation is based on the reduction of porosity relative to the uncemented sample, which is commonly used to estimate the effect of cementation on permeability (Philips & Wilson, 1991; Lichtner, 1996). The precipitation of calcite cement occurs progressively (Figure 7.6A-C). Pre-existing grain surfaces commonly act as a substrate for the aggregation of calcite cement grains, though mineral precipitation independent of grain surfaces is also observed (Figure 7.6A-C).

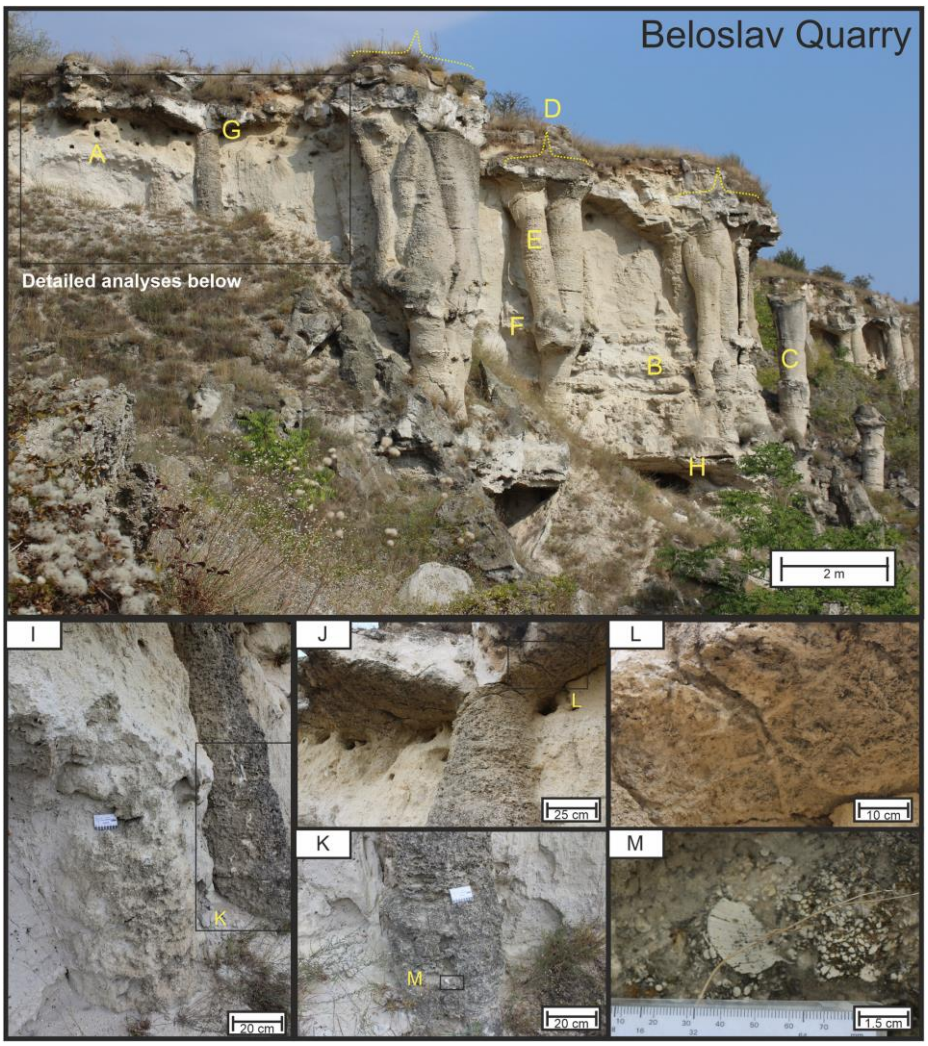

Figure 7.5: Vantage point looking NNW within the Beloslav Quarry, providing an understanding of carbonate pipe geometry, and the relationship of the pipes with the surrounding sandy host rock, and the upper and lower carbonate horizontal interbeds. The letters (A) to (H) correspond to the main field observations described above. Detailed analyses indicated by black box. (I) Two carbonate pipes observed, one less weathered (in the foreground) and one more weathered (the dark grey coloured pipe). (J) The interface between the top of the carbonate pipe and the upper carbonate bed. The carbonate pipe emanates into the upper carbonate bed, despite the false appearance of a sharp contact due to a sub-horizontal fracture and white staining of the upper carbonate bed. (K) Another view of the carbonate pipe, appearing to have intruded vertically upward through the poorly consolidated sand host rock. (L) Horizontal branching burrow network at the base of the upper carbonate bed. (M) An abundance of shells and shell fragments 0.5 to 25 mm in size within the carbonate pipe, highlighting the similarity in composition between the pipe and the surrounding sandstone host rock.

7.5. Discussion

7.5.1. Distribution of pipes

Pipe distribution and spacing can provide an insight into the possible relationship between tectonic stress and pipe formation. Orthomosaic image analysis reveals comparable pipe diameters and spacings at Pobiti Kamani (3.58 m ± 3.38) and Beloslav Quarry (2.24 m ± 3.38 m), indicating that the controlling mechanisms for pipe formation are the same for both study areas. In both areas, the pipes are located along the N-S trending transtensional faults, within the Dikilitash Formation sediments. The pipes are situated on the eastern side hanging wall of the transtensional faults, that indicates a regional tectonic control on pipe location and genesis (Figure 7.3). When observed on a localised scale, individual groups of pipes in both study areas are highly clustered (z-scores below -13). However, the orthomosaic maps and DEM reveal no apparent preferential orientation of the pipe clusters (nearest neighbour; Figure 7.3). The findings oppose a localised structural control of pipe formation along pre-existing faults or fractures within the Dikilitash Formation, as suggested by De Boever et al. (2009b). Regionally-developed fractures with an orientation of NNE-SSW are observed across the study areas (Figure 7.3). The fractures cross-cut the pipes, and therefore post-date the pipes. Therefore, regional-scale tectonic deformation is interpreted as the controlling factor for the presence of pipes proximal to transtensional faults, however the pipes are unlikely to have formed along pre-existing planes of weakness within the Dikilitash Formation.

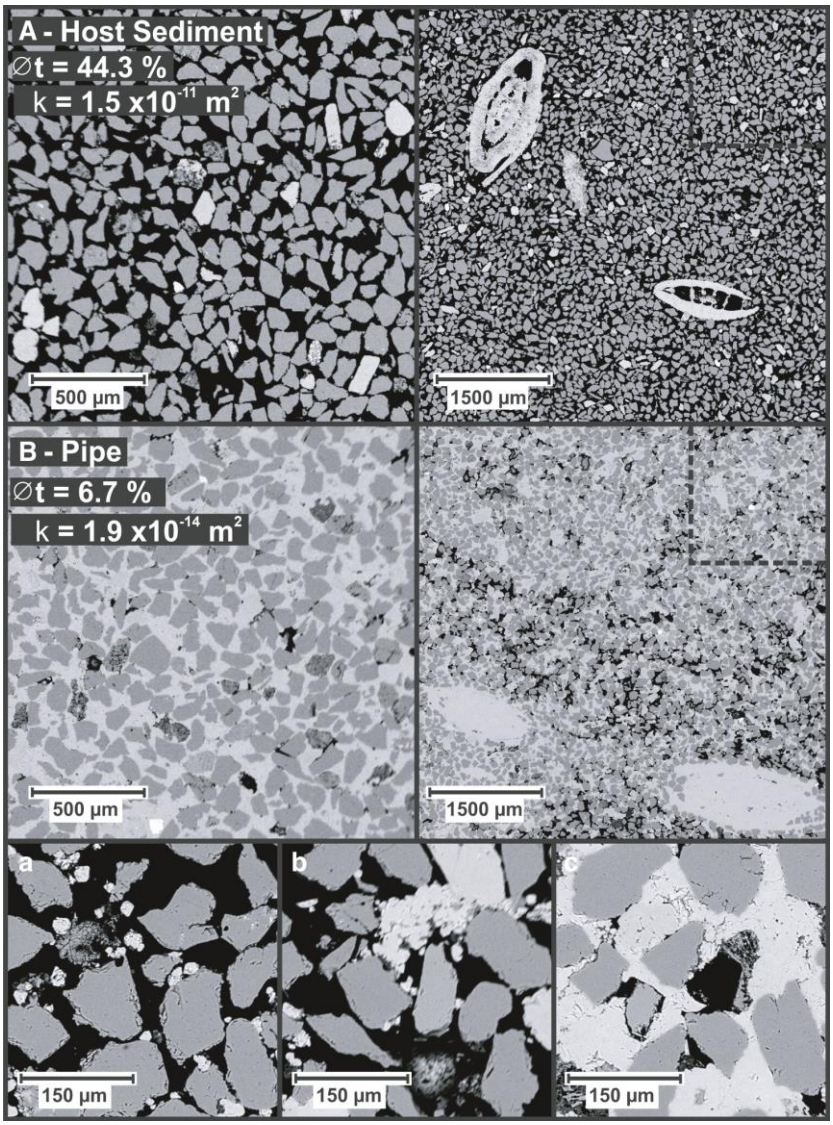

Figure 7.6: Scanning electron microscopy (SEM) images displaying the textural similarity of the uncemented host sediment and the carbonate cemented pipes at Beloslav Quarry. (A) Well-sorted, poorly consolidated quartz sediment (100 to 140 µm grain size) with high porosity (Øt) and estimated permeability (k) of 44.3% and 1.5 × 10−11 m2 (15 darcy), respectively. Nummulite bioclasts are present in both samples. (B) Carbonate cement precipitation, occupying greater than 85% of the total pore volume, reducing permeability by three orders of magnitude (0.02 darcy). ('a' to 'c') shows the progressive cementation process of granular calcite within the intergranular pores.

7.5.2. Pipe formation

Subaerial outcrop exposures of pipes provide an improved understanding of the conditions at the time of pipe formation. The host sediment of the Dikilitash Formation was deposited in a mid- to outer ramp environment, evidenced by the lack of sediment bedding laminations, as well as the presence and clustering of nummulite fossils. This type of depositional environment lays above the storm wave base and is prone to the frequent reworking of sediments (Sinclair

et al., 1998). Therefore, the large height and the well-preserved status of the pipes (Figure 7.5) argue against a formation within the water column, as bottom currents in the mid- to outer ramp environment would likely have resulted in erosion and low preservation potential. The subsurface formation of the pipes is further supported by SEM imaging, showing the pipes and host sediment have an identical grain composition and texture. The only difference between the pipes and surrounding sediment is the presence of low-Mg calcite that is observed to infill above 80% of the sediment pores, that causes reductions in porosity and permeability by up to 40% and three orders of magnitude, respectively. Therefore, the analysis demonstrates that pipe-forming methane-derived authigenic carbonates (MDAC) likely precipitated within the unconsolidated sand of the Dikilitash Formation below the seafloor. Previous work by De Boever et al. (2009a) further showed that the MDACs precipitated due to the microbially mediated anaerobic oxidisation of methane (AOM).

Calcite cemented interbeds also observed in the study area reveals further information about the active history of the methane-seep system. The presence of burrow (trace) fossils on the base of the interbeds provides key evidence to interpret that the horizons formed on the seabed, and hence represent the paleo-seafloor. Additional field observations at Beloslav Quarry showed that the upper sections of pipes thicken and emanate into the overlying calcite cemented interbeds, showing a direct relationship between pipes and the interbeds (Figure 7.5). Orthomosaic image mapping identified at least seven calcite cemented bedding-parallel interbeds separating the vertically stacked tiers of pipes (Figure 7.4, Figure 7.5). If each of these interbeds represents a paleo-seafloor, it can be deduced that there was at least seven phases of methane emission from the methane seep-system, and hence at least seven phases of pipe formation during the Early Eocene.

The assessment of pipe morphology and the physical properties of the host sediment may permit a further understanding of the nature of fluid flow that led to pipe formation. The high permeability (1.5×10^{-11} m^2) unconsolidated sand of the Dikilitash Formation should permit the advective flow of fluids. DEM and orthomosaic image mapping reveal that the pipes have a cylindrical (tube-like) geometry, displaying a large height to diameter ratio and low eccentricity. Further, the pipes also have a sub-vertical orientation, and are oriented perpendicular to bedding. The pipe morphology observations, correlated with the physical property measurements calculated from the SEM image analysis, further support advective flow, whereby mechanical dispersion is minimal. The SEM image analysis reveals that the sediment matrix has not been displaced by the fluids, which supports the interpretation of

capillary-dominant flow, rather than fracture-dominant flow (Fauria & Rempel, 2011). Further, it is suggested that the pipes formed due to the focused, buoyancy-driven ascent of fluids (De Boever et al., 2006a; De Boever et al., 2009a). The sub-vertical ascent of fluids may also have been overpressure-driven. However, high overpressures that would result in high flow velocities and turbulent flow are not supported by any observations, i.e. erosive fluidisation (sediment remobilization; Lowe, 1975). The propagation of pressure waves or viscous flow of rising gas bubbles into the Dikilitash Formation may explain the formation of tube-shaped zones of vertical fluid flow (Boudreau et al., 2005; Räss et al., 2018).

Field observations show that the pipes have an outer layer of carbonates with a moderately diffuse boundary to unconsolidated sand in the interior (Figure 7.5). Further quantified using the orthomosaic map, the pipes display predominantly unlithified cores (78%), and less commonly lithified inner cores (22%). Supported by the field observations, it is interpreted that carbonate precipitated on the outside of bubble streams at the interface of ascending fluids to ambient brackish or sea water, and likely resulted in a self-sustaining, positive feedback of focused fluid flow towards pipe centres (Clari et al., 2004). Where methane flux rates were higher, the focused flow of methane likely prevented carbonate precipitation in the pipe centres (Luff & Wallmann, 2003). The observed large fraction of unlithified cores (78%), as well as the common field observation of bifurcation and merging of pipes, could be further used to interpret that fluid supply to the methane seep system from below was likely diverted rapidly to other migration pathways, that may include other pipes or the regional transtensional fault, which would be in accordance with the findings by De Boever et al. (2011b). Supported by the evidence of pipe clustering, it is interpreted that fluid flow was mainly focused along the Palaeogene transtensional faults and surrounding fractures beneath the Dikilitash Formation (e.g. within the Beloslav Formation, Sinclair et al., 1998, Figure 7.1), that provided a source for the methane that entered the Dikilitash Formation at discrete zones.

The pipe formation processes interpreted in the study areas in Varna, Bulgaria, can be directly observed at modern, active seep systems. For example, focused fluid flow in marine sand formations is also documented from the “bubbling reefs” in the Kattegat, offshore Denmark (Jørgensen, 1992). These pipes show ongoing discharge of methane and have formed below the seafloor. Constant erosion because of post-glacial isostatic uplift has exposed these features in 10-12 m water depth. The bubbling reef pipes can only be distinguished from their host sand by the amount of cementation. Some of the pipes are almost 4 m tall and 1.5 m in diameter (Jensen et al., 1992). Carbon-isotope studies of the pipes identified a probable link between the

bubbling gas ($\delta^{13}C_{CH4}$: -63 to -75‰), the carbonates ($\delta^{13}C$: -26 to -63‰), and the methanotrophic bacteria ($\delta^{13}C_{OM}$: -43.4‰) (Judd & Hovland, 2007). It can be suggested that focused fluid flow in sand and sandstone formations is not an exceptional case but also likely in other marine settings at the transition between tectonically faulted low permeable formations and overlying and higher-permeable formations (shale-sand-interface). The focusing of fluids and subsequent formation of vertical conduits in high permeability formations largely depends on the focused advection of methane-rich fluid from below, e.g. through pre-existing faults and fractures (Figure 7.8A), the flux rate and progressive inward growth of carbonates (Figure 7.8B, C, D).

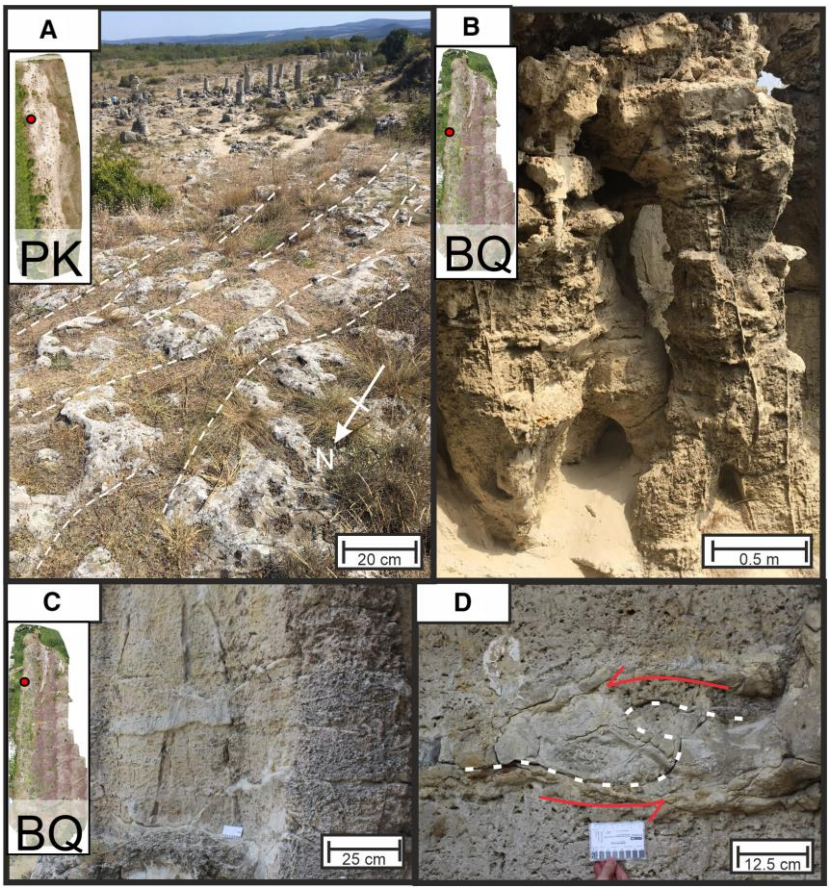

Figure 7.7: (A) North/north-east trending fracture network on a carbonate interbed surface, at higher elevation than the carbonate pipes observed to the East. PK = Pobiti Kamani. Red dot in mini map indicates location of picture within the outcrop. (B) Metre-scale carbonate pipes displaying secondary sub-vertical carbonate veining within fractures. The veins are orientated NNE/SSW. BQ = Beloslav Quarry. Red dot in mini map indicates location of picture within the outcrop. (C) Fractures and carbonate veins observed, cross-cutting both the carbonate pipes and surrounding host rock, with no clear orientation trend. Red dot in mini map indicates location of picture within the outcrop. (D) S-shaped shear fabric within a carbonate horizon, indicating the presence of active north–south shear stress during the formation of this interval. (C) and (D) were taken at the same location.

7.5.3. Geological flow model

There are two alternating carbon and oxygen isotope signatures groups (group 1: $\delta^{13}C$ ~-45 to -35‰ V-PDB & $\delta^{18}O$ ±1‰ V-PDB; group 2: $\delta^{13}C$ <-25‰ V-PDB & $\delta^{18}O$ <-6.5‰ V-PDB; De Boever et al., 2009a), which appear in concentric bands around the centre of the pipes. Depleted $\delta^{18}O$ isotope ratios (<-6.5‰ V-PDB) can indicate carbonate precipitation in freshened, meteoric waters while more enriched values that plot closer to 0 ‰ V-PDB indicate the formation in brackish or sea water (Hays & Grossman, 1991). However, the process of late diagenetic secondary isotope re-equilibration at higher temperatures, which usually decreases the original $^{18}O/^{16}O$-ratio of the carbonates, has to be considered during burial of carbonate deposits (e.g. Fischer et al., 2006). The observed alternating isotope signature groups can only be partly explained by percolating meteoric waters within the Dikilitash Formation (host sand) postdating pipe formation (De Boever et al., 2009a), as this would have only affected the outside of the pipes, assuming progressive precipitation of carbonate towards the centre of the pipe (Figure 7.8), or resulted in a homogenisation of isotopic signature groups. At the same time, the ascend of fluids with elevated temperatures would explain the different groups, but, in accordance with De Boever et al. (2006a), we consider it unlikely that fluids of different temperature ranges (hot/cold) share the same fluid migration system. In addition, this would have resulted in homogenisation of carbon and oxygen isotope ratio groups, which is not observed. In contrast to previous interpretations, it can be suggested that the two signature groups were captured during precipitation and are likely the cause of alternating fluid source characteristics. The alternating concentric rings of carbon and oxygen isotope signatures (De Boever et al., 2006a) thus indicate episodic fresh/brackish water advection that fed the pipe structures from below.

The alternating carbonate isotope ratios in the pipes indicate that fresh water was episodically involved in the precipitation of carbonates (Figure 7.8). Considering the presence and activity of the transtensional faults below the Dikilitash Formation, the fresh water was likely sourced from an aquifer below the Dikilitash Formation (e.g. the Beloslav Formation or deeper; Sinclair et al., 1998), which advected fluids from onshore resulting in episodic submarine groundwater discharge offshore. A similar coupled groundwater-methane discharge system is currently active along the eastern Bulgarian coastal areas documented by ongoing venting of methane (Dimitrov, 2002) and elevated Radon isotope ratios (Moore & Falkner, 1999). In order to create topography-driven groundwater flow far out into the shelf (Hughes et al., 2009; Morrissey et al., 2010; Post et al., 2013), e.g. analogues to the New Jersey Margin (Gustafson et al., 2019), tectonic compression in the onshore realm during the Palaeogene (Sinclair et al., 1998) likely

provided the necessary hydraulic head (Figure 7.8). This topography-driven groundwater flow likely forced episodic submarine groundwater discharge in addition to the methane emissions resulting in the two alternating characteristic isotope groups found in the carbonate pipes (Figure 7.8).

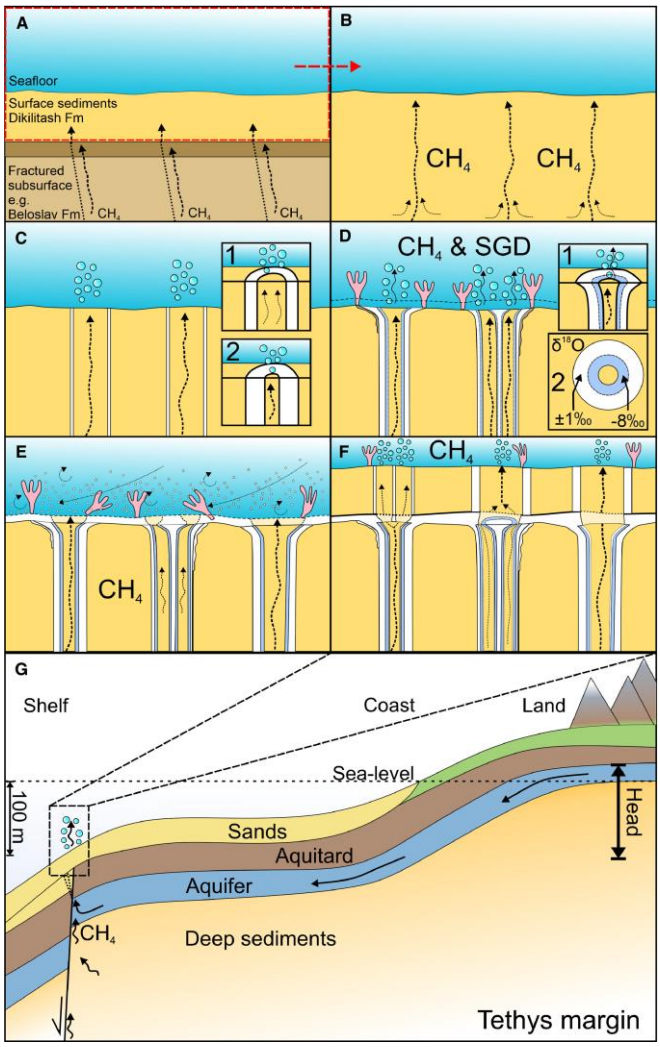

Figure 7.8: Conceptual model showing the carbonate pipe formation through time – (B) to (F) modified after Clari et al., 2004). (A) Methane ascends from below possibly along pre-existing planes of weakness in the subsurface due to transtensional tectonism in the Palaeogene. (B) Buoyancy driven focused upward migration of methane (CH4) through poorly consolidated sandstone of the Dikilitash Formation. (C) Carbonate precipitation on the margins of methane gas seeps, forming the outer walls of the carbonate pipe. Progressive precipitation of carbonate towards the centre of the pipe through time ('1' to '2'). (D) Continued carbonate precipitation, widening at the seabed interface. Cold-seep benthic communities, such as tubeworms, form at the seabed around the methane release site. Benthic organisms may form vertical burrows or roots to allow uptake of hydrogen sulphide from the seep sediments. Episodic submarine groundwater discharge (SGD) leads to depleted oxygen isotope ratios in precipitated carbonates ('1' to '2'). (E) Bottom water currents provide additional sediment into the

system, within an outer-ramp depositional setting. An outer carbonate crust forms at the seabed, interpreted to form from continued methane flux and precipitation of carbonate. (F) The process of pipe formation in the near subsurface repeats, methane continues to flow through preferential pathways created by older pipe structures. (G) Schematic model of coupled methane release and episodic submarine groundwater discharge at the shelf of the Tethys margin.

7.6. Conclusion

The low-Mg calcite-cemented pipes of the Pobiti Kamani and Beloslav Quarry formed below the seafloor within unconsolidated sand of the Dikilitash Formation due to anaerobic microbial oxidation of methane fed by methane-rich fluids that were advected from deeper sources. As the pipes occur within the vicinity of major fault deformation of the unit underlying the Dikilitash Formation has probably focused the fluid flow at certain points. Efficient microbial turnover of methane to carbonate within the shallow marine sediment has maintained the focused flow paths. This explains the large diameters and size of the pipes despite their dense spacing. The calcite cemented interbeds likely represent paleo-seafloors. Thus, there have been at least seven phases of increased carbonate precipitation during phases of sea level changes in the past.

Regional tectonic deformation likely played a key role in controlling the location of the pipe clusters on a regional scale. The pipe clusters tend to form towards the eastern side of major transtensional fault in the sand of the Dikilitash Formation. However, on a local scale, tectonic deformation does not govern the distribution of the pipes within the unconsolidated sand.

The calcite cementation of the conduits show two distinct groups of carbon and oxygen isotopes that appear in concentric bands around the centre of the pipes. These groups likely represent different phases of episodic fluid release with different characters. The isotope systematics suggest that the first group of methane-derived authigenic carbonates formed from biogenic methane and ambient seawater DIC. The second group of MDAC formed during the episodic release of groundwater mixed with methane-rich fluids.

In analogy to the New Jersey Margin (Gustafson et al., 2019), groundwater was likely advected to the mid-to outer ramp shelf setting through an aquifer driven by topographic changes in the onshore realm. Sufficient groundwater heads likely existed because of active deformation and uplift during the Eocene. Focused fluid flow in sand and sandstone formations is not an exception but it is also likely present in current marine settings at the transition between low

and high-permeable formations (e.g. shale-sand-interface) where methane seepage is combined with submarine groundwater discharge.

Acknowledgements

We acknowledge the Integrated School of Ocean Sciences (ISOS) Kiel for funding proposal GRAPA. We also acknowledge funding from the European Union's Horizon 2020 research and innovation programme under grant agreement No. 654462 – STEMM-CCS. We thank Pix4D for providing academic licenses and cloud computing capacities. The rock sample thin sections were prepared by technicians Matthew Beverley-Smith and Daniel Doran in the rock preparation and thin-sectioning laboratories, and analysed using the scanning electron microscope (SEM) facility at the National Oceanography Centre, University of Southampton. Additional thanks to Dipl. Eng. Darinka Sarova, director of "Zlatni Pyassatsi" Nature Park Directorate, for granting access to the protected area "Pobiti Kamani" and support during the scientific fieldwork. Many thanks to Thor Hansteen, Volker Liebetrau and Gero Wetzel for their support with scientific drilling of carbonate rocks prior to the fieldwork and equipment preparation. Atanas Vasilev and Petar Petsisnki received funding within the framework of the Project KP-06-OPR04/7 GEOHydrate (Bulgarian Science Fund). The data that support the findings of this study are available from the corresponding author upon reasonable request.

References

Andresen, K. J. (2012). Fluid flow features in hydrocarbon plumbing systems: What do they tell us about the basin evolution? *Marine Geology*, 332, 89-108. https://doi.org/10.1016/j.margeo.2012.07.006

Angeletti, L., Canese, S., Franchi, F., Montagna, P., Reitner, J., Walliser, E. O., & Taviani, M. (2015). The "chimney forest" of the deep Montenegrin margin, south-eastern Adriatic Sea. *Marine and Petroleum Geology*, *66*, 542-554. https://doi.org/10.1016/j.marpetgeo.2015.04.001

Bemis, S. P., Micklethwaite, S., Turner, D., James, M. R., Akciz, S., Thiele, S. T., & Bangash, H. A. (2014). Ground-based and UAV-based photogrammetry: A multi-scale, high-resolution mapping tool for structural geology and paleoseismology. *Journal of Structural Geology*, *69*, 163-178. https://doi.org/10.1016/j.jsg.2014.10.007

Bergerat, F., Martin, P. & Dimov, D., 1998. The Moesian Platform as a key for understanding the geodynamical evolution of the Carpatho-Balkan alpine system. Mémoires du Muséum national d'histoire naturelle, 177, 129-150.

Berndt, C. (2005). Focused fluid flow in passive continental margins. *Philosophical Transactions of the Royal Society of London A: Mathematical, Physical and Engineering Sciences*, 363(1837), 2855-2871. https://doi.org/10.1098/rsta.2005.1666

Bisdom, K., Nick, H. M., & Bertotti, G. (2017). An integrated workflow for stress and flow modelling using outcrop-derived discrete fracture networks. *Computers & Geosciences*, 103, 21-35. https://doi.org/10.1016/j.cageo.2017.02.019

Böttner, C., Berndt, C., Reinardy, B. T., Geersen, J., Karstens, J., Bull, J. M., ... & Schramm, B. (2019). Pockmarks in the Witch Ground Basin, Central North Sea. *Geochemistry, Geophysics, Geosystems*, *20*(4), 1698-1719. https://doi.org/10.1029/2018GC008068

Botz, R.W., Georgiev, V., Stoffers, P., Khrischev, Kh., Kostadinov, V. (1993) Stable isotope study of carbonate-cemented rocks from the Pobitite Kamani area, north-eastern Bulgaria. Geologische Rundschau 82, 663-666. https://doi.org/10.1007/BF00191493

Boudreau, B. P., Algar, C., Johnson, B. D., Croudace, I., Reed, A., Furukawa, Y., ... & Gardiner, B. S. (2005). Bubble growth and rise in soft sediments. *Geology*, 33(6), 517-520. https://doi.org/10.1130/G21259.1

Callow, B., Falcon-Suarez, I., Marin-Moreno, H., Bull, J. M., & Ahmed, S. (2020). Optimal X-ray micro-CT image based methods for porosity and permeability quantification in heterogeneous sandstones. *Geophysical Journal International*, *223*(2), 1210-1229. https://doi.org/10.1093/gji/ggaa321

Capozzi, R., Negri, A., Reitner, J. & Taviani, M., 2015. Carbonate Conduits linked to Hydrocarbon-enriched Fluid Escape. Marine and Petroleum Geology, 66, 497-500, https://doi.org/.1016/j.marpetgeo.2015.08.025.

Cartwright, J. (2007). The impact of 3D seismic data on the understanding of compaction, fluid flow and diagenesis in sedimentary basins. *Journal of the Geological Society*, 164(5), 881-893. https://doi.org/10.1144/0016-76492006-143

Clari, P., Cavagna, S., Martire, L. & Hunziker, J., 2004. A Miocene Mud Volcano and Its Plumbing System: A Chaotic Complex Revisited (Monferrato, NW Italy). Journal of Sedimentary Research, 74(5), 662-676. https://doi.org/10.1306/022504740662

De Boever, E., Birgel, D., Muchez, P., Peckmann, J., Dimitrov, L., & Swennen, R. (2011a). Fabric and formation of grapestone concretions within an unusual ancient methane seep system (Eocene, Bulgaria). *Terra Nova*, *23*(1), 56-61. https://doi.org/10.1111/j.1365-3121.2010.00984.x

De Boever, E., Birgel, D., Thiel, V., Muchez, P., Peckmann, J., Dimitrov, L., & Swennen, R. (2009a). The formation of giant tubular concretions triggered by anaerobic oxidation of methane as revealed by archaeal molecular fossils (Lower Eocene, Varna, Bulgaria). *Palaeogeography, Palaeoclimatology, Palaeoecology*, *280*(1-2), 23-36. https://doi.org/10.1016/j.palaeo.2009.05.010

De Boever, E., Huysmans, M., Muchez, P., Dimitrov, L., & Swennen, R. (2009b). Controlling factors on the morphology and spatial distribution of methane-related tubular concretions–Case study of an Early Eocene seep system. *Marine and Petroleum Geology*, *26*(8), 1580-1591. https://doi.org/10.1016/j.marpetgeo.2008.11.004

De Boever, E., Muchez, P., Swennen, R., & Dimitrov, L. (2011b). Evolution of deformation and fault-related fluid flow within an ancient methane seep system (Eocene, Varna, Bulgaria). *Geofluids*, *11*(2), 166-183. https://doi.org/10.1111/j.1468-8123.2011.00328.x

De Boever, E., Swennen, R., & Dimitrov, L. (2006a). Lower Eocene carbonate cemented chimneys (Varna, NE Bulgaria): Formation mechanisms and the (a) biological mediation of chimney growth?. *Sedimentary Geology*, *185*(3-4), 159-173. https://doi.org/10.1016/j.sedgeo.2005.12.010

De Boever, E., Swennen, R., & Dimitrov, L. (2006b). Lower Eocene carbonate-cemented “chimney” structures (Varna, Bulgaria)—control of seepage rates on their formation and stable isotopic signature. *Journal of Geochemical Exploration*, *89*(1-3), 78-82. https://doi.org/10.1016/j.gexplo.2005.11.028

Dimitrov, L. (2002). Contribution to atmospheric methane by natural seepages on the Bulgarian continental shelf. *Continental Shelf Research*, *22*(16), 2429-2442. https://doi.org/10.1016/S0278-4343(02)00055-9

Fauria, K. E. & Rempel, A. W., 2011. Gas invasion into water-saturated, unconsolidated porous media: Implications for gas hydrate reservoirs. *Earth and Planetary Science Letters*, 312(1-2), 188-193. https://doi.org/10.1016/j.epsl.2011.09.042

Fischer, M., Botz, R., Schmidt, M., Rockenbauch, K., Garbe-Schönberg, D., Glodny, J., ... & Littke, R. (2006). Origins of CO2 in permian carbonate reservoir rocks (Zechstein, Ca2) of the NW-German Basin (Lower Saxony). *Chemical Geology*, *227*(3-4), 184-213. https://doi.org/10.1016/j.chemgeo.2005.09.014

Georgiev, G., Dabovski, C. & Stanisheva-Vassileva, G., 2001. East Srednogorie-Balkan rift zone. Mémoires du Muséum national d'histoire naturelle, 186, 259-293.

Gustafson, C., Key, K., & Evans, R. L. (2019). Aquifer systems extending far offshore on the U.S. Atlantic margin. *Scientific Reports*, 1–10. http://doi.org/10.1038/s41598-019-44611-7.

Hays, P.D. & Grossman, E.L., 1991. Oxygen isotopes in meteoric calcite cements as indicators of continental paleoclimate. Geology, 19(5), 441-444, https://doi.org/10.1130/0091-7613(1991)019%3C0441:OIIMCC%3E2.3.CO;2

Hughes, J. D., Vacher, H. L., & Sanford, W. E. (2009). Temporal response of hydraulic head, temperature, and chloride concentrations to sea-level changes, Floridan aquifer system, USA. *Hydrogeology journal*, *17*(4), 793-815.

Huuse, M., Jackson, C. A. L., Van Rensbergen, P., Davies, R. J., Flemings, P. B., & Dixon, R. J. (2010). Subsurface sediment remobilization and fluid flow in sedimentary basins: an overview. *Basin Research*, *22*(4), 342-360. https://doi.org/10.1111/j.1365-2117.2010.00488.x

Jensen, P., Aagaard, I., Burke Jr, R. A., Dando, P. R., Jorgensen, N. O., Kuijpers, A., ... & Schmaljohann, R. (1992). 'Bubbling reefs' in the Kattegat: submarine landscapes of carbonate-cemented rocks support a diverse ecosystem at methane seeps. *Marine Ecology Progress Series*, *83*, 102-112.

Jørgensen, N. O. (1992). Methane-derived carbonate cementation of marine sediments from the Kattegat, Denmark: geochemical and geological evidence. *Marine Geology*, *103*(1-3), 1-13. https://doi.org/10.1016/0025-3227(92)90006-4

Judd, A., & Hovland, M. (2007). *Seabed fluid flow: the impact on geology, biology and the marine environment*. Cambridge University Press.

Karstens, J., & Berndt, C. (2015). Seismic chimneys in the Southern Viking Graben–Implications for palaeo fluid migration and overpressure evolution. *Earth and Planetary Science Letters*, 412, 88-100. https://doi.org/10.1016/j.epsl.2014.12.017

Ketcham, R. A., and W. D. Carlson (2001), Acquisition, optimization and interpretation of X-ray computed tomographic imagery: applications to the geosciences, Computers & Geosciences, 27, 381-400. http://dx.doi.org/10.1016/S0098-3004(00)00116-3.

Lichtner, P. C. (1996). Continuum formulation of multicomponent-multiphase reactive transport. *Reviews in mineralogy*, 34, 1-82.

Lowe, D. R. (1975). Water escape structures in coarse-grained sediments. *Sedimentology*, *22*(2), 157-204. https://doi.org/10.1111/j.1365-3091.1975.tb00290.x

Luff, R., & Wallmann, K. (2003). Fluid flow, methane fluxes, carbonate precipitation and biogeochemical turnover in gas hydrate-bearing sediments at Hydrate Ridge, Cascadia Margin: numerical modeling and mass balances. *Geochimica et Cosmochimica Acta*, *67*(18), 3403-3421. https://doi.org/10.1016/S0016-7037(03)00127-3

Moore, W. S., & Falkner, K. K. (1999). Cycling of radium and barium in the Black Sea. *Journal of environmental radioactivity*, *43*(2), 247-254. https://doi.org/10.1016/S0265-931X(98)00095-2

Morrissey, S. K., Clark, J. F., Bennett, M., Richardson, E., & Stute, M. (2010). Groundwater reorganization in the Floridan aquifer following Holocene sea-level rise. *Nature Geoscience*, *3*(10), 683. https://doi.org/10.1038/ngeo956

Nelson, C.S., Nyman, S.L., Campbell, K.A. & Rowland, J.R., 2017. Influence of faulting on the distribution and development of cold seep-related dolomitic conduit concretions at East Cape, New Zealand. New Zealand Journal of Geology and Geophysics, 60(4), 478-496, doi: 10.1080/00288306.2017.1372489. https://doi.org/10.1080/00288306.2017.1372489

Planke, S., & Berndt, C. (2007). U.S. Patent No. 7,221,620. Washington, *DC: U.S. Patent and Trademark Office*.

Post, V. E., Groen, J., Kooi, H., Person, M., Ge, S., & Edmunds, W. M. (2013). Offshore fresh groundwater reserves as a global phenomenon. *Nature*, *504*(7478), 71-78. https://doi.org/10.1038/nature12858

Räss, L., Simon, N. S., & Podladchikov, Y. Y. (2018). Spontaneous formation of fluid escape pipes from subsurface reservoirs. *Scientific reports*, *8*(1), 11116. https://doi.org/10.1038/s41598-018-29485-5

Sinclair, H. D., Juranov, S.G., Georgiev, G., Byrne, P., & Mountney, N.P., 1998. The Balkan thrust wedge and foreland basin of eastern Bulgaria: Structural and stratigraphic development. Memoirs-American Association Of Petroleum Geologists, 68, 91-114.

Whitaker, S. (1986). Flow in porous media I: A theoretical derivation of Darcy's law. *Transport in porous media*, *1*(1), 3-25. https://doi.org/10.1007/BF01036523

White, J. E. (1975). Computed seismic speeds and attenuation in rocks with partial gas saturation. *Geophysics*, 40(2), 224-232. https://doi.org/10.1190/1.1440520

8. Discussion, Conclusion and Outlook

8.1. Ocean bottom seismic characterisation of fluid flow conduits below pockmarks in marine basins

Pore fluid expulsion occurs in various forms such as sand intrusions, mud volcanos, or fluid escape pipes and chimneys in sedimentary basins all over the world (Bernd, 2005; Cartwright, 2007; Cartwright and Santamarina, 2015). Fluid escape pipes or chimneys are defined as columnar vertical to sub-vertical zones with reduced seismic amplitude (Cartwright et al., 2007; Løseth et al., 2011; Andresen 2012; Karstens and Berndt. 2015). They have a three-dimensional, columnar geometry and the upper termination of pipes and chimneys often coincide with pockmarks or paleo-pockmarks (Cartwright and Santamarina, 2015).

These vertical fluid escape structures are important to understand for a variety of reasons. Pipes or chimneys often have vertical dimensions of hundreds of metres and they likely represent important pathways for vertical fluid flow and secondary hydrocarbon migration in sedimentary basins (Berndt, 2005; Cartwright et al., 2007). They may act as venting routes for overpressured source layers at greater depth (Davies, 2003), as pathways for supply of methane to hydrate stability zones, or allow methane to even cross the stability zone and vent at the seafloor (Berndt, 2005; Davies and Clarke, 2010; Hustoft et al., 2010).

Most of the available knowledge of pipes and chimneys has been inferred from high resolution marine seismic studies (Cartwright and Santamarina, 2015). In multi-channel seismic data, pipes and chimneys manifest as vertical to sub-vertical zones of disrupted reflections across an otherwise well layered host succession. The vertical orientation of pipes or chimneys have only minor lateral offsets and inclination (Løseth et al., 2011). The dimensions of pipes and chimneys vary in wide ranges with heights between 200-500 m, but some reach up to 2000 m in height (Moss and Cartwight, 2010a, b). The diameter of fluid flow conduits typically range from a few tens of metres to over 500 m (Hansen at al., 2005; Rensbergen et al., 2007). Indeed, the detection of shorter and smaller pipes and chimney structures is limited by the vertical resolution of the interpreted data and could be under-presented in seismic studies.

Often, the actual depth (or root zone) of a fluid flow conduit is difficult to identify, but the definition of these root zones is a key parameter for interpretation, because they link the source region of the fluid to the formation of the fluid flow conduit. However, studies where the root zones can be identified are rare (Cartwright and Santamarina, 2015). The reason for this lack

of root zone imaging is the decreasing imaging accuracy of seismic data with increasing depth. In addition, the upwelling gas in the fluid flow conduits can reduce the resolution of seismic imaging, so the root zone cannot be identified.

There are only a few reliable data examples where the internal structure of pipes and chimneys is imaged (Hansen et al., 2005; Moss and Cartwright, 2010a). In order to image these fluid flow conduits, they must be very large or very shallow, otherwise the pipe/chimney diameter is in the order of the spatial resolution limit (Brown, 2011). The diameter has to be several times the spatial resolution, otherwise significant seismic imaging artefacts like consistent upward convexity in internal reflection geometry can mimic true deformational structures (Løseth et al., 2011).

Most study areas of pipe and chimney structures are located in sedimentary basins, with a majority of them on passive continental margins but some structures also occur in active margins, intra-continental post-rift sag and backarc basins (Cartwright and Santamarina, 2015). In most cases, fluid escape structures are found in layered, mostly clay-dominated marine sediment basins, typically of Neogene age and in the upper kilometre of the sediment column (Cartwright and Santamarina, 2015). But many pipes and chimneys have been also reported in the context of hydrate bearing sediments (Cartwright and Santamarina, 2015).

The dating of the formation of pipes and chimneys is difficult and their growth histories may be complex. However, some indicators for the dating of the formations are:

1) Pockmarks at the seafloor suggest a relatively recent pipe formation (Løseth et al., 2001; Hustoft et al., 2010).
2) Pipes growth can be episodically, indicated by stacked pockmarks within a single fluid flow structure (Andresen and Huuse, 2011).
3) Mound development at the upper terminus potentially constrains the later stages of the fluid flow history, because it contributes materials at the top of the pipe (Hustoft et al., 2010).

Five mechanisms have been suggested to explain pipe genesis (Cartwright and Santamarina, 2015):

1) Hydraulic fracturing is the most frequently proposed mechanism to explain the formation of pipes and chimneys (Cartwright et al., 2007; Hustoft et al., 2007; Moss and Cartwright, 2010; Løseth et al., 2011). Thereby, overpressure occurs in the root zone

and induces hydraulic fracturing in the overburden and a network of hydraulic fractures propagates upwards to the surface to normalize the stress.

2) Pressure dependent fluid expansion (e.g., gas exsolution or steam expansion) increases the efficiency of fluidization. This erosive fluidization is also observed in multiphase magmatic eruptions, diatremal structures and kimberlites (Woolsey et al., 1975; McCallum, 1985), and is considered responsible for the development of pockmarks (Judd & Hovland, 2009).
3) Capillary invasion is a potential mechanism for pipe formation if the root zone generates free phase gas (Liu and Flemings, 2007). The gas is trapped at a capillary seal and accumulated up to a critical thickness until the buoyancy at the top of the seal forces the gas through the pore throats at which point it forms an upward migrating gas column.
4) Localised subsurface volume loss causes a pipe-shaped collapse geometry in the overburden with the size of known pipes and chimney structures (Whittaker and Reddish, 1989).
5) Compacting basin sustains upwards fluid flow, but the flow is not necessarily uniform. Localized flow, due to sediments with a broad grain size distribution or depositional sequence consist of successive fine-to-coarse grained layers, may be preserved during the sedimentation process. This syn-sedimentary flow localisation can form pipe and chimney structures (Cartwright and Santamarina, 2015).

It is unlikely that just a single mechanism leads to pipe and chimney formation. Rather a combination of these mechanisms is likely to occur in particular context (Cartwright and Santamarina, 2015).

The seismic interpretation of fluid flow structures, especially when they are vertically orientated, can be ambiguous (Kristensen and Huuse, 2012; Karstens and Berndt, 2015). Conventional reflection seismic surveys have significant shortcomings in imaging the internal structure of focused fluid conduits, and in differentiating between real geological structures and imaging artefacts (Karstens and Berndt, 2015; Böttner et al., 2019). Effects like blanking beneath gas accumulations, migration artefacts due to insufficiently resolved lateral velocity variations at shallow depth, or bad seismic traces often lead to misinterpretation of certain features as seismic pipes or chimneys (Karstens & Berndt, 2015). In contrast, seismic velocity models, for example derived from ocean bottom seismometer experiments, can provide valuable information about the internal structure of focused fluid conduits. They can provide

information on the type of pore fill, e.g. gas and aqueous fluids, and qualitative information on porosity as it correlates with seismic velocity.

In the following, I compare three wide-angle seismic studies that have used similar experiment designs to investigate fluid flow structures, and show the diversity of pipes and chimneys (Figure 8.1). Schramm et al. (2021) present a three-dimensional seismic P-wave velocity model of an active fluid conduit beneath the Scanner Pockmark in the Central North Sea (Chapter 4), Plaza-Faverola et al. (2010) show 3D P-wave velocities inside a chimney in the Nyegga pockmark field offshore Norway, and Schramm et al. (submitted) study P-wave velocities under the Lunde Pockmark at the Vestnesa Ridge, Svalbard (Chapter 5).

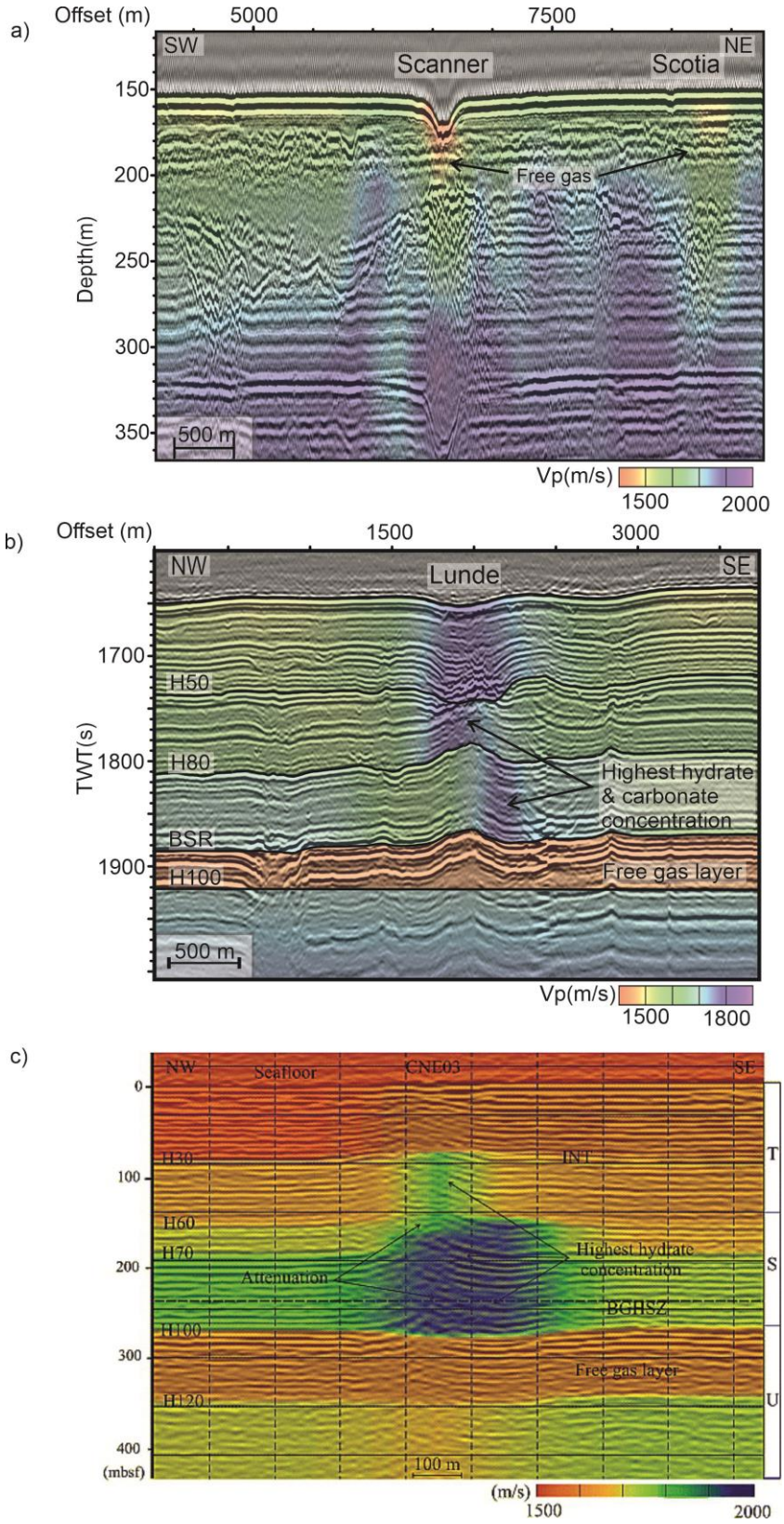

Figure 8.1: Seismic reflection section on which the Vp model has been overlaid of the a) Scanner Pockmark, b) Lunde Pockmark and c) CNE03 Pockmark (Plaza-Faverola et al. (2010). Each section shows a clear seismic velocity anomaly below the pockmark.

All three structures are located beneath a pockmark, which are comparable in size and depth (Scanner Pockmark ~150 m wide, ~250 m long, and ~15 m deep; CNE03 Pockmark ~200 m in diameter and ~10 m deep; Lunde Pockmark ~500 m in diameter and ~15 m deep).

The Scanner Pockmark is located within the Witch Ground Graben, which developed from the Triassic to the early Cretaceous as part of the North Sea Basin failed rift system (Judd et al., 1994). The chimney below CNE03 Pockmark is one of the fluid-outflow structures associated with the Nyeggy pockmark field, an area north of the Storegga slide in the mid-Norwegian margin, and lies above the Helland Hansen arch, which separates the two Cretaceous basins Vøring and Møre, (Brekke, 2000; Plaza-Faverola et al., 2010). The Lunde Pockmark is located in the Vestnesa Ridge, a large sediment drift on the western Svalbard continental margin (Eiken & Hinz, 1993). The sedimentary deposits mostly consist of turbiditic, glaciomarine and hemipelagic sediments (Howe et al., 2008) and the ridge is growing due to bottom-current controlled sediment dynamics (Eiken and Hinz, 1993).

The results of the three seismic P-wave velocity tomographies indicate a diverse range of the physical properties of fluid flow structures. The pipe structure beneath the Scanner Pockmark can be characterized by both positive and negative seismic P-wave velocity anomalies at different depths (Figure 4.4). The low velocity anomaly in the upper part of the pipe corroborates the presence of free gas, probably hosted in a network of open fractures (Chapter 4). Although the nature of the deeper part of the pipe structure beneath the Scanner Pockmark is less clear, the positive seismic velocity anomaly may be the result of calcite precipitation or an overprinting of the original sediment texture by fluid migration.

The nature of the chimney beneath CNE03 is quite different compared to the pipe beneath Scanner Pockmark (Figure 8.1). The upper interfaces down to ~250 mbsf dome upwards beneath the CNE03 Pockmark (Plaza-Faverola et al., 2010). The core of the CNE03 chimney is built by a zone of a high P-wave velocity anomaly, which is about 500 m in diameter (~150 – 270 mbsf) and 200 m in diameter near the seabed and is restricted to the gas hydrate stability zone (Figure 7 in Plaza-Faverola et al., 2010). The P-wave velocity inside the chimney is up to 300 m/s higher than the velocities in the surrounding area. Based on the depth of the high velocity anomaly and the absence of a high velocity anomaly beneath the base of the methane-hydrate stability field, it is more likely that gas hydrate accumulation caused the high velocity anomaly and not carbonate cementation within fractures, which is for example observed at the vent complex at Heidrun, in the Norwegian Sea (Garten et al., 2008). The base of the high velocity anomaly (~270 mbsf) lies on top of a low permeability unit above what is inferred to

be a high porosity unit containing free gas (Plaza-Faverola et al., 2010). Beneath ~270 mbsf, the boundaries exhibit no doming, which implies that the process of doming of the chimney occurs within the gas hydrate stability zone (GHSZ), or at its immediate base (Plaza-Faverola et al., 2010). Plaza-Faverola et al. (2010) cannot determine if there is any free gas in the chimney at present, due to seismic blanking and scattering in combination with structural disturbance and high P-wave velocities. If there is free gas in the chimney, the volume is likely very small and the gas' effect on seismic P-wave velocity would be largely masked by the strong influence of the present hydrates.

The chimney below the Lunde pockmark increases the seismic velocities up to 14 % higher than the surrounding background velocities, probably due to the presence of gas hydrates and buried authigenic carbonate concretions (Chapter 5). The seismic velocity increases radially towards the centre of the chimney. This positive velocity anomaly is visible up to the BSR, which is located approximately 200 mbsf (Hustoft et al., 2009, Chapter 5). In many studies, upwelling gas has been documented at the Lunde Pockmark (Panieri et al., 2017; Hong et al., 2021). However, gas hydrates and carbonate cementations overprint the velocity effect of ascending gas resulting in a positive seismic velocity anomaly. Due to the authigenic carbonate buried within the chimney under Lunde Pockmark, the system is self-sealing (carbonates precipitate and close the cracks), and later reactivated when the flow of fluids is redirected to open cracks (Himmler et al., 2019; Hong et al., 2021; Chapter 5). The tomographic inversion results show a movement of the seismic Vp anomaly in northeast direction towards the periphery of the chimney, confirming Hong et al. (2021) and may be an evidence of fluid redirection.

The formation of all three fluid flow conduits is not fully understood, yet. The pipe beneath the Scanner Pockmark is separated in two parts. The upper part up to a depth of about 260 mbsf suggests that the fluid flow is active and that gas seeps at the seafloor originate from an accumulation of biogenic methane at the base of glacial sediments (Böttner, 2019; Chapter 4). The increased velocities in the deeper part of the pipe are caused by calcite cements in the fracture network. This process has been observed in boreholes, e.g. at the Heidrun complex (Garten et al., 2008) or in onshore outcrops of the Ravnefjeld Formation, East Greenland (Nielsen and Hanken, 2002). It is also possible that the pipe provides a pathway for methane to escape from the sediments, thus increasing the average P-wave velocity. In both cases, this would suggest that a fracture network in the pipe structure is not open at present. How long the

deeper part of the pipe structure was active and whether it's possible that the fracture network opens and closes episodically has not yet been conclusively determined.

Plaza-Faverola et al. (2010) present two possible scenarios for the formation of the chimney below the pockmark CNE03. The first one is a long-period formation scenario: the chimney grew over a long period of time with a minimum formation period of about 350,000 years. During this time, carbonates formed, which increase the seismic P-wave velocities. However, these carbonates would extend beneath the present GHSZ, but there is no evidence for seismic P-wave anomalies beneath the chimney below the present-day GHSZ (Plaza-Faverola et al., 2010). Furthermore, we would expect paleo-seepage features like onlap of reflectors against paleo-seabed mounds created during active periods. The absence of these features makes it unlikely that the chimney is 350 ka or older. However, on the basis of the available data, Plaza-Faverola et al. (2010) cannot exclude the possibility of short active periods, creating very thin carbonate deposits since 350 ka, the age of the present-day base of the GHSZ. The second scenario is a short-period formation scenario, where gas migrates vertically through polygonal faults and fractures from deep reservoirs. At a shallow level, the gas passes through the more-permeable-porous unit and migrates to the base of the GHSZ where it remains within permeable units, until it gets a sufficient pressure to propagate into fractures (Plaza-Faverola et al., 2010). With a critical overpressure, the gas migrates into the GHSZ by creating fractures and forming hydrate veins. Carbonates form above the chimney at the seafloor and in immediate sediments (Plaza-Faverola et al., 2010).

The Lunde Pockmark is located on the relatively young Vestnesa Ridge and directly at the seafloor. This suggests a relatively recent pipe formation (Hustoft et al., 2010). Measurements of the water column show a leakage of gases, mostly methane. This activity is another indication of the rather young age of the chimney. Carbonate cementations have been detected in wells drilled in the Lunde Pockmark (Himmler et al., 2019). The uprising fluids caused cementation processes, which resulted in a repeated displacement of the chimney.

The three presented studies show the diversity of fluid flow conduits. The Scanner Pockmark area is outside the gas hydrate stability zone, one reason why this pipe structure is different from the other two chimneys.

However, for the distinct comparison of the three studies, it should be noted, that the experiments have been performed slightly different. Plaza-Faverola et al. (2010) and Schramm et al. (submitted) used shot lines including circles, while Schramm et al. (2021) worked with a

parallel shot grid, only. The circular shots provide a denser coverage from all azimuths, which results in a higher spatial resolution. Therefore, the models by Plaza-Faverola et al. (2010) and Schramm et al. (submitted) likely provide a more realistic image of the 3D internal structure of the chimney, while Schramm et al. (2021) have a better resolution over the area with additional OBSs on a reference site.

With the available seismic P-wave tomographies it is not possible to directly derive the hydraulic permeability of pipe and chimney structures. The fact that the evaluation of OBS data was severely hampered by seafloor multiples, a surface ghost, and the dimming of reflectors due to gas suggests that future geophysical investigations of pipe structures should also involve detailed tomographic inversion of sea surface-towed 3D seismic data with long-offset streamers. This may avoid the multiple and ghost problems by making use of deeper reflections to generate velocity fields with higher resolution. Also, tomographic inversion of P-to-S converted wave arrivals may provide further insights as it would not be affected by the dimming effect of free gas. Additionally, P-to-S wave inversions would provide information on the shear strength of the rocks inside the pipe structure which may reveal further indications for fracturing. In any case, a thorough assessment of fluid flow conduits' permeability requires drilling campaigns in addition to all geophysical campaigns.

8.2. Conclusion

Focused fluid flow in marine basins is a crucial component in different research fields because (1) it is a key process linking the geosphere with the biosphere, (2) it changes the sedimentary records and influences, for example, CO_2 sequestration, and (3) it transports large amounts of carbon from the subsurface to the atmosphere. Fluid flow varies in time and space and in my thesis, I highlight the importance of seismic imaging to analyse and understand the different evolution processes, flow mechanisms, and resulting conduit geometries of fluid flow structures. The comparison of three initially similar fluid flow conduits using OBS data demonstrates the complexity and variability of pipes and chimney structures (Chapter 8.1). Generally, multichannel seismic experiments are unsuited to image vertical structures, where lateral and vertical seismic velocity anomalies are present. Seismic tomography however, minimises this problem and is therefore a crucial method to provide a thorough image of the internal structure of pipes and chimneys with less potential artefacts, as I have shown in my study on Scanner Pockmark (Chapter 4).

The study on Scanner Pockmark (Chapter 4) highlights the complexity in evaluating focused fluid conduits and the necessity of their detailed assessment when selecting CO_2 storage sites, especially in an area with many pockmarks and fluid migration pathways (Chapter 3; Aim 4). The low seismic velocities in the upper part of the pipe corroborate the presence of free gas, which is likely distributed in a network of open fractures in the upper part of the pipe structure. The deeper part of the pipe shows a positive seismic velocity anomaly, which may be the result of calcite precipitation or an overprinting of the original sediment texture of fluid migration (Aims 1, 2, 3). This strongly suggests different physical properties at different depths along the pipe structure, likely caused by different hydraulic properties of the pipe compared to the surrounding sediments that have not been affected by fluid migration.

The comparison with the study on the seismic characterisation of the chimney below the Lunde Pockmark (Chapter 5) emphasizes how diverse the results of seismic velocity modelling of active fluid migration pathways in marine basins can be. Measurements of the water column show a leakage of gas. Nevertheless the seismic anomaly beneath the Lunde Pockmark is positive, which means that seismic P-wave velocities increase. Gas hydrates and carbon cementations overprint the effect of upcoming gas and the chimney can act as a fluid pathway through the gas hydrate stability zone (Aims 2, 3).

The analysis of the OBS data using converted S-waves shows the occurrence of subsurface anisotropy in shallow sediments around the Lunde Pockmark, with different anisotropic behaviour observed across the pockmark (Chapter 6). We investigate differences in symmetry plane directions in anisotropic media using null energy symmetries in transverse components. We conclude minimum (NE-SW) and maximum (SE-NW) horizontal stress directions and our analysis indicates a potential correlation between hydrofractures and horizontal stresses.

In the Pobiti Kamani area and the Beloslav Quarry (Bulgaria) hundreds of carbonate pipes, which formed below the seafloor, are well exposed nowadays and can be studied onshore (Chapter 7). These vertical conduits may have formed in high-permeable sediments when underlying low-permeable sedimentary units have been faulted or fractured. The resulting flux rates were high enough to result in extensive precipitation of carbonates at the margins of the seep. Geochemical and geological data indicate that the methane seepage was likely coupled with an intermitting submarine groundwater discharge. Chapter 3 emphasises that venting is restricted in time.

Overall, my results imply a diverse range of the internal structures of fluid flow conduits (Aim 1). The three investigated sites (Schramm et al., 2021; Schramm et al., submitted; and Plaza-Faverola et al., 2010) show a similar evolution and yielded comparably large pockmarks at the seafloor. Therefore, we would have expected them to have comparable seismic properties. Nevertheless, this thorough analysis of the 3D P-wave velocity of all three structures demonstrates that they are fundamentally different in their geophysical and hydraulic characteristics depending on depth and the geological setting.

Although P-wave velocity tomography is a sensitive method to determine the distribution of free gas, gas hydrates and carbonate cementations, smearing effects and uncertainties impede a precise distinction between, for example, gas hydrates and carbonate cementations (Aim 2, 3). Therefore, resolution and error analysis such as checkerboard- or characteristic tests are required to interpret the results of seismic velocity modelling. Nevertheless, tomographic models deliver information about the nature and volume of the fluid flow conduits, flux type, origin of the upcoming fluid and -in some cases- the formation of the focussed fluid flow. Therefore, seismic P-wave velocity tomography is a powerful tool to exclude pipes and chimneys as artefacts, in contrast to MCS data.

The credible discrimination of potential artefacts from actual fluid flow structures is crucial for the large-scale implementation of the geological storage of CO_2 in sedimentary basins in order to prevent leakage of stored material. Therefore, I suggest that a detailed, multi-method assessment of specific fluid conduits needs to be an essential part of CO_2 storage site selection. A combination of seismic P-wave modelling with hydroacoustic and geochemical data significantly enhances the detection of seeping gas (e.g. methane) and constrains the root of the seepage. With seismic P-wave velocity modelling alone, it is not possible to directly derive the hydraulic permeability of pipes and chimneys. The combination of the proposed multi-scale, multi-disciplinary experimental approach is required for complete characterisation of fluid escape structures.

In conclusion, OBS experiments above fluid flow conduits should be part of any offshore CCS site selection to investigate their potential to function as pathways for CO_2 and to ensure the integrity of the reservoir for CO_2 sequestration (Aim 4).

8.3. Recommendation and Outlook

My thesis shows the diverse range of the internal structures of fluid flow conduits (Chapter 4, 5). The thesis highlights that the nature and internal structure of fluid flow conduits are poorly

understood and their hydraulic properties, especially their permeability, need to be further studied (Chapter 4, 5, 6). The permeability is critical for the safety of CO_2 storage formations. All credible climate change scenario models show that CCS will be essential to meet the internationally agreed targets of the UNFCCC Paris Agreement in 2015. The ubiquity of pipe structures requires their detailed understanding to incorporate them into CCS site selection and assess the risk of a potential CO_2 storage site. The STEMM-CCS project significantly improved the understanding of the role of pipes and chimneys in fluid migration through sedimentary basins and will contribute to the further development of more advanced modelling approaches (Chapter 3, 4). Based on the framework of this project in combination with my work, I recommend the following steps:

First, I recommend a detailed seismic assessment of fluid flow conduits as an essential part of CO_2 storage site selection. Thereby it is important that structures are undershot, for example with an OBS experiment or a long-streamer multichannel seismic survey, in order to exclude that it is only a seismic imaging artefact and to identify possible origins of the structure.

Second, I recommend to investigate more formations like the Scanner Pockmark. My thesis shows the wide range of geophysical properties and the diversity of fluid flow conduits. More research on targets like the pipe beneath the Scanner Pockmark could provide comparability and improve the understanding of such structures. However, such research projects should include drilling into the fluid flow conduit with higher recovery rates than the STEMM-CCS project (the maximum drilling depth was 33 mbsf at the reference site, sediment recovery rate ~50%). Direct probing like drilling is only a point information, but in combination with geophysical surveys it facilitates insights into the fluid flow system and the role of pipes and chimneys within this system. These borehole data can be extrapolated when used together with seismic data. In addition, the velocity models can be calibrated with borehole data and thereby extrapolated into the area.

Third, my work and all other results of the STEMM-CCS project as well, show that individual geophysical or geochemical experiment approaches can only determine selected physical properties of a fluid flow conduit and their role in fluid migration (Chapter 3, 4, 5, 6). Only the integration of different methods can fully characterise the whole system. For example, seismic reflection, seismic travel-time tomography, seismic anisotropy, direct sampling and laboratory experiments provide information about the fracture geometry, orientation and subsurface structure. The marine controlled source electromagnetic method (CSEM), seismic travel-time tomography, seismic anisotropy, direct sampling and laboratory experiments supply

information about physical properties such as e.g. the electrical resistivity, P- and S-waver velocity, and porosity. CSEM-, acoustic-, seismic reflection data, direct sampling and seismic anisotropy analysis deliver information about fluid presence, distribution, composition and flux. Thereby, the different experiments each have advantages and disadvantages. Drillings provide only local information, MCS data include artefacts and provide less information about the physical properties of the subsurface, seismic tomography provides many different models and is, like CSEM, especially useful in combination with MCS. Often, the results of these methods are ambiguous (e.g. seismic velocity anomalies can be caused by very different materials) and only the combination can provide more specific results.

Fourth, I propose an addition of the experiment setup. Even with the multi-scale and multi-method setup of the STEMM-CCS project, which includes seismic data, electromagnetic data, drilling and studies of onshore analogies, open questions remain. For example, the evolution of the pipe structure beneath the Scanner Pockmark or its permeability (Chapter 4). I suggest to integrate the time component into the study of the fluid flow conduit. Geophysical experiments should be done repeatedly to validate temporal changes in the migration of the fluids, for a better understanding of the formation and development of fluid flow features. I recommend multiple 3D high-resolution MCS dataset with long streamers. This 4D dataset could show temporal variations and the evolution of fluid flow structures. This experiment can be combined with permanent OBSs or fibre optic cables, which allow a more cost-effective way and repeated seismic surveying. A long-term, passive OBS experiment, with a densely spaced network of OBSs across the pockmark, could provide information about the rise of fluids (continuous or episodic, depending on tides or seasons, etc.). Additionally, I recommend monitoring in the available borehole. Circulation Obviation Retrofit Kit (CORK) is a method that has been used for over 30 years and can provide further insight into the evolution of fluid flow conduits.

Fifth, I recommend the extraction of more information from OBS data. As shown in Chapter 6, S-waves contain geological and geophysical information (e.g. anisotropy, stress regime). In addition, a Full Waveform Inversion (FWI) can estimate the elastic material parameter in the underground. However, FWI needs more computing power, but by using the entire wavefield, smearing effects, such as occurred in Chapter 4 and 5, can be minimized. The OBS tomography model can be used as the initial model for a FWI, which is highly sensitive to the initial model.

Sixth, and last: my work has demonstrated that many open questions and uncertainties remain to the risk assessment of CCS in sedimentary basins due to fluid flow conduits. Additionally, in sedimentary basins around Europe, large offshore areas are likely to be reserved for the

development of wind farms. Even if discussions about a multiple usage of offshore areas are in progress and, for example, exploitation licenses of the German North Sea will probably be soon in 3D, areas below already existing wind farms cannot be explored geophysical, which eliminates them as possible CCS sites. Therefore, I propose an increased focus on the identification of alternative storage locations in other geological settings. Research efforts in Iceland have shown that CO_2 storage in porous basalt provides a potentially permanent storage due to a high hydraulic permeability and a rapid mineralisation of CO_2 (IEAGHG, 2017). The CarbFix project reports that 95% and >60% carbon from injected CO_2 is mineralised within two years (Clark et al., 2020).

Overall, my thesis highlights that interdisciplinary and detailed research of fluid migration pathways through marine sediments is necessary to increase the safety of sub-seabed CO_2 storage sites.

References

Andresen, K. J. (2012). Fluid flow features in hydrocarbon plumbing systems: What do they tell us about the basin evolution?. *Marine Geology*, *332*, 89-108. https://doi.org/10.1016/j.margeo.2012.07.006

Andresen, K.J., Huuse, M., 2011. 'Bulls-eye' pockmarks and polygonal faulting in the Lower Congo Basin: relative timing and implications for fluid expulsion during shallow burial. Mar. Geol. 279, 111e127. https://doi.org/10.1016/j.margeo.2010.10.016

Berndt, C. (2005). Focused fluid flow in passive continental margins. *Philosophical Transactions of the Royal Society A: Mathematical, Physical and Engineering Sciences*, *363*(1837), 2855-2871. https://doi.org/10.1098/rsta.2005.1666

Böttner, C., Berndt, C., Reinardy, B. T., Geersen, J., Karstens, J., Bull, J. M., Callow, B. J., Lichtschlag, A., Schmidt, M., Elger, J., Schramm, B., Haeckel, M. (2019). Pockmarks in the Witch Ground Basin, Central North Sea. *Geochemistry, Geophysics, Geosystems*, *20*(4), 1698-1719. https://doi.org/10.1029/2018GC008068

Brekke, H. (2000). The tectonic evolution of the Norwegian Sea continental margin, with emphasis on the Voring and More basins. *Special Publication-Geological Society of London*, *167*, 327-378.

Brown, A. R. (2011). *Interpretation of three-dimensional seismic data*. Society of Exploration Geophysicists and American Association of Petroleum Geologists.

Cartwright, J., Huuse, M., & Aplin, A. (2007). Seal bypass systems. *AAPG bulletin*, *91*(8), 1141-1166. https://doi.org/10.1306/04090705181

Cartwright, J., & Santamarina, C. (2015). Seismic characteristics of fluid escape pipes in sedimentary basins: implications for pipe genesis. *Marine and Petroleum Geology*, *65*, 126-140. https://doi.org/10.1016/j.marpetgeo.2015.03.023

Clark, D. E., Oelkers, E. H., Gunnarsson, I., Sigfússon, B., Snæbjörnsdóttir, S. Ó., Aradottir, E. S., & Gíslason, S. R. (2020). CarbFix2: CO2 and H2S mineralization during 3.5 years of continuous injection into basaltic rocks at more than 250 C. *Geochimica et Cosmochimica Acta*, *279*, 45-66. https://doi.org/10.1016/j.gca.2020.03.039

Davies, R. J. (2003). Kilometer-scale fluidization structures formed during early burial of a deep-water slope channel on the Niger Delta. *Geology*, *31*(11), 949-952. https://doi.org/10.1130/G19835.1

Davies, R. J., & Clarke, A. L. (2010). Methane recycling between hydrate and critically pressured stratigraphic traps, offshore Mauritania. *Geology*, *38*(11), 963-966. https://doi.org/10.1130/G31058.1

Eiken, O., & Hinz, K. (1993). Contourites in the Fram Strait. *Sedimentary Geology*, *82*(1-4), 15-32. https://doi.org/10.1016/0037-0738(93)90110-Q

Garten, P., Houbiers, M., Planke, S., & Svensen, H. (2008). Vent complex at Heidrun. In *SEG Technical Program Expanded Abstracts 2008* (pp. 809-813). Society of Exploration Geophysicists. https://doi.org/10.1190/1.3063767

Hansen, J. P. V., Cartwright, J. A., Huuse, M., & Clausen, O. R. (2005). 3D seismic expression of fluid migration and mud remobilization on the Gjallar Ridge, offshore mid-Norway. *Basin Research*, *17*(1), 123-139. https://doi.org/10.1111/j.1365-2117.2005.00257.x

Himmler, T., Sahy, D., Martma, T., Bohrmann, G., Plaza-Faverola, A., Bünz, S., Condon, D.J., Knies, J., Lepland, A. (2019). A 160,000-year-old history of tectonically controlled methane seepage in the Arctic. Science advances, 5(8), eaaw1450. https://doi.org/10.1126/sciadv.aaw1450

Hong, W. L., Pape, T., Schmidt, C., Yao, H., Wallmann, K., Plaza-Faverola, A., Rae, J.W.B., Lepland, A., Bünz, S., Bohrmann, G. (2021). Interactions between deep formation fluid and gas hydrate dynamics inferred from pore fluid geochemistry at active pockmarks of the Vestnesa Ridge, west Svalbard

margin. Marine and Petroleum Geology, 127, 104957, https://doi.org/10.1016/j.marpetgeo.2021.104957

Howe, J. A., Shimmield, T. M., Harland, R. E. X., & Eyles, N. (2008). Late Quaternary contourites and glaciomarine sedimentation in the Fram Strait. *Sedimentology*, *55*(1), 179-200. https://doi.org/10.1111/j.1365-3091.2007.00897.x

Hustoft, S., Mienert, J., Bünz, S., & Nouzé, H. (2007). High-resolution 3D-seismic data indicate focussed fluid migration pathways above polygonal fault systems of the mid-Norwegian margin. *Marine Geology*, *245*(1-4), 89-106. https://doi.org/10.1016/j.margeo.2007.07.004

Hustoft, S., Bünz, S., Mienert, J., & Chand, S. (2009). Gas hydrate reservoir and active methane-venting province in sediments on< 20 Ma young oceanic crust in the Fram Strait, offshore NW-Svalbard. *Earth and Planetary Science Letters*, *284*(1-2), 12-24. https://doi.org/10.1016/j.epsl.2009.03.038

Hustoft, S., Bünz, S., & Mienert, J. (2010). Three-dimensional seismic analysis of the morphology and spatial distribution of chimneys beneath the Nyegga pockmark field, offshore mid-Norway. *Basin Research*, *22*(4), 465-480. https://doi.org/10.1111/j.1365-2117.2010.00486.x

IEAGHG. (2017). CCS Deployment in the Context of Regional Developments in Meeting Long-Term Climate Change Objectives.

Judd, E. R. (1994). Gender and power in rural North China. Stanford University Press.

Judd, A., & Hovland, M. (2009). Seabed fluid flow: the impact on geology, biology and the marine environment. Cambridge University Press.

Karstens, J., & Berndt, C. (2015). Seismic chimneys in the Southern Viking Graben–Implications for palaeo fluid migration and overpressure evolution. *Earth and Planetary Science Letters*, *412*, 88-100. https://doi.org/10.1016/j.epsl.2014.12.017

Kristensen, T. B., & Huuse, M. (2012). Multistage erosion and infill of buried Pleistocene tunnel valleys and associated seismic velocity effects. *Geological Society, London, Special Publications*, *368*(1), 159-172. https://doi.org/10.1144/SP368.15

Liu, X., & Flemings, P. B. (2006). Passing gas through the hydrate stability zone at southern Hydrate Ridge, offshore Oregon. *Earth and Planetary Science Letters*, *241*(1-2), 211-226. https://doi.org/10.1016/j.epsl.2005.10.026

Løseth, H., Wensaas, L., Arntsen, B., Hanken, N. M., Basire, C., & Graue, K. (2011). 1000 m long gas blow-out pipes. *Marine and Petroleum Geology*, *28*(5), 1047-1060. https://doi.org/10.1016/j.marpetgeo.2010.10.001

McCallum, M. E. (1985). Experimental evidence for fluidization processes in breccia pipe formation. *Economic Geology*, *80*(6), 1523-1543. https://doi.org/10.2113/gsecongeo.80.6.1523

Moss, J. L., & Cartwright, J. (2010a). 3D seismic expression of km-scale fluid escape pipes from offshore Namibia. *Basin Research*, *22*(4), 481-501. https://doi.org/10.1111/j.1365-2117.2010.00461.x

Moss, J. L., & Cartwright, J. (2010b). The spatial and temporal distribution of pipe formation, offshore Namibia. *Marine and Petroleum Geology*, *27*(6), 1216-1234. https://doi.org/10.1016/j.marpetgeo.2009.12.013

Nielsen, J. K., & Hanken, N. M. (2002). Late Permian carbonate concretions in the marine siliciclastic sediments of the Ravnefjeld Formation, East Greenland. *Geology of Greenland Survey Bulletin*, *191*, 126-132. https://doi.org/10.34194/ggub.v191.5140

Panieri, G., Bünz, S., Fornari, D. J., Escartin, J., Serov, P., Jansson, P., ... & Gracias, N. (2017). An integrated view of the methane system in the pockmarks at Vestnesa Ridge, 79 N. *Marine Geology*, *390*, 282-300. https://doi.org/10.1016/j.margeo.2017.06.006

Plaza-Faverola, A., Westbrook, G. K., Ker, S., Exley, R. J., Gailler, A., Minshull, T. A., & Broto, K. (2010). Evidence from three-dimensional seismic tomography for a substantial accumulation of gas hydrate in a fluid-escape chimney in the Nyegga pockmark field, offshore Norway. *Journal of Geophysical Research: Solid Earth*, *115*(B8). https://doi.org/10.1029/2009JB007078

Rensbergen, P. V., Rabaute, A., Colpaert, A., Ghislain, T. S., Mathijs, M., & Bruggeman, A. (2007). Fluid migration and fluid seepage in the Connemara Field, Porcupine Basin interpreted from industrial 3D seismic and well data combined with high-resolution site survey data. *International Journal of Earth Sciences*, *96*(1), 185-197.

Schramm, B., Berndt, C., Dannowski, A., Böttner, C., Karstens, J., & Elger, J. (2021). Seismic imaging of an active fluid conduit below Scanner Pockmark, Central North Sea. *Marine and Petroleum Geology*, *133*, 105302. https://doi.org/10.1016/j.marpetgeo.2021.105302

Schramm, B., Singhroha, S., Plaza-Faverola, A., Dannowski, A., Berndt, C., Bünz, S., (submitted). Characterization of an active gas chimney using seismic velocity analysis, west-Svalbard Margin. *Geophysical Research Letters.*

Whittaker, B. N., & Reddish, D. J. (1989). Subsidence: occurrence, prediction and control.

Woolsey, T. S., McCallum, M. E., & Schumm, S. A. (1975). Modeling of diatreme emplacement by fluidization. In *Physics and Chemistry of the Earth* (pp. 29-42). Pergamon. https://doi.org/10.1016/0079-1946(75)90004-X

9. Acknowledgements

First and foremost, I am very grateful for the supervision from Christian Berndt and Anke Dannowski. A special thank you to Christian Berndt for your mentoring, motivation and support throughout the last years. Thank you for always being generous with your time and your constructive input. I would like to thank Anke Dannowski for your continuous support throughout the entire time. Many thanks for proof-reading of this thesis. You are an excellent mentor for all my work with OBSs and modelling.

I would like to thank Christoph Böttner and Anouk Beniest, who shared the office with me. Thank you for all the nice conversations, the good working climate and many collaborative research cruises.

Special thanks to Michel Kühn for proof-reading this thesis and for your great support in general.

A special thanks to Gesa Franz for proof-reading this thesis, your motivation and support.

A big thank to Anne Völsch for your helpfulness and great support with all organizational matters.

Special thanks go to Florian Petersen, Felix Wolf, Peter Finger, Peter Haas, Rachel Barrett, Zahra Faghih and Konstantin Reek for spending this doctorate-time together.

Many thanks to Jasmin Mögeltönder, Julia Schätzel, Stefan Kontradowitz, Jens Karstens and Judith Elger for many lunches, research cruises and your support.

Many thanks to the entire GEOMAR geodynamics group for the nice atmosphere and support. Many thanks for the warm welcome to the team of BGR marine seismic and the supporting working climate.

I would like to thank the GEOMAR and STEMM-CCS project for financing my doctorate and enable me to visit various research conferences and cruises. Many thanks to ECORD for granting me financial support to visit the IODP Petrophysics summer school in Leicester, 2017. A special thanks to ISOS and Avan Antia for providing the Miniproposal framework and granting financial support to conduct fieldwork in Varna, Bulgaria. Many thanks to the captains and crews of all my research cruises for making this scientific work possible.

I would like to thank my family for always supporting me, no matter what I am doing. Thank you, Klaus, Astrid, Tine, Eva, Alex, Theo and Elise! I am grateful to know that I can always depend on you.

10. Curriculum Vitae

11. Publication list

Please find a digital list and access to all publications on OceanRep:

https://oceanrep.geomar.de/view/creators/1ee116c9-f1a1-4a74-a8c2-dea254fb5228.html

11.1. Articles in a Scientific Journal – peer-reviewed

Beniest, A., Dannowski, A., Schnabel, M., Kopp, H. and the SO267 Scientist Party (submittd). Tectonic quiescence in actively extending back-arc regions. Journal of Geophysical Research - Solid Earth.

Böttner, C., Berndt, C., Reinardy, B. T., Geersen, J., Karstens, J., Bull, J. M., ... & Haeckel, M. (2019). Pockmarks in the Witch Ground Basin, Central North Sea. Geochemistry, Geophysics, Geosystems, 20(4), 1698-1719. https://doi.org/10.1029/2018GC008068

Böttner, C., Callow, B. J., Schramm, B., Gross, F., Geersen, J., Schmidt, M., ... & Berndt, C. (2021). Focused methane migration formed pipe structures in permeable sandstones: Insights from uncrewed aerial vehicle-based digital outcrop analysis in Varna, Bulgaria. Sedimentology, *68*(6), 2765-2782. https://doi.org/10.1111/sed.12871

Connelly, D. P., Bull, J. M., Flohr, A., Schaap, A., Koopmans, D., Blackford, J. C., ... & Yakushev, E. (2022). Assuring the integrity of offshore carbon dioxide storage. Renewable and Sustainable Energy Reviews, *166*, 112670. https://doi.org/10.1016/j.rser.2022.112670

Karstens, J., Berndt, C., Urlaub, M., Watt, S. F., Micallef, A., Ray, M., ... & Brune, S. (2019). From gradual spreading to catastrophic collapse–Reconstruction of the 1888 Ritter Island volcanic sector collapse from high-resolution 3D seismic data. Earth and Planetary Science Letters, 517, 1-13. https://doi.org/10.1016/j.epsl.2019.04.009

Karstens, J., Schneider von Deimling, J., Berndt, C., Böttner, C., Kühn, M., Reinardy, B. T., ... & Bense, F. (2022). Formation of the Figge Maar Seafloor Crater During the 1964 B1 Blowout in the German North Sea. Earth Science, Systems and Society, *2*, 10053. https://doi.org/10.3389/esss.2022.10053

Robinson, A. H., Callow, B., Böttner, C., Yilo, N., Provenzano, G., Falcon-Suarez, I. H., ... & Reinardy, B. (2021). Multiscale characterisation of chimneys/pipes: Fluid escape structures within sedimentary basins. International Journal of Greenhouse Gas Control, 106, 103245. https://doi.org/10.1016/j.ijggc.2020.103245

Singhroha, S., Schramm, B., Plaza-Faverola, A., Domel, P., Bünz, S., Dannowski, A., Cooke, F., (2023, accepted). Stress constraints from shear-wave analysis in shallow sediments at an actively seeping pockmark on the W-Svalbard Margin. Earth and Space Science.

Schramm, B., Berndt, C., Dannowski, A., Böttner, C., Karstens, J., & Elger, J. (2021). Seismic imaging of an active fluid conduit below Scanner Pockmark, Central North Sea. Marine and Petroleum Geology, 133, 105302. https://doi.org/10.1016/j.marpetgeo.2021.105302

Schramm, B., Singhroha, Plaza-Faverola, A, Berndt, C., Dannowski, A., Bünz, S., (submitted). Characterization of an active gas chimney using seismic velocity analysis, Svalbard Margin. Geophysical Research Letters.

11.2. Presentations

Böttner, C., Schramm, B., Berndt, C., Karstens, J., Schmidt, M., Haeckel, M., Elger, J., Callow, B. J., Bull, J. M., Lichtschlag, A. and Reinhardy, B. (2018) Pockmark formation in the Witch Ground Basin, central North Sea. [Talk] In: EGU General Assembly 2018. , 08.-13.04.2018, Vienna, Austria.

Dannowski, A., Kopp, H., Grevemeyer, I., Lange, D., Thorwart, M., Crawford, W., Caielli, G., de Franco, R., Paul, A., Petersen, F., Wolf, F. N. and Schramm, B. and Cruise participants MSM71 (2018) Ligurian Ocean Bottom Seismology and Tectonics Research – LOBSTER. [Talk] In: AlpArray Science Meeting Zürich 2018. , 29.-30.08.2018, Zürich, Switzerland.

Dannowski, A., Kopp, H., Grevemeyer, I., Lange, D., Thorwart, M., Crawford, W., Caielli, G., de Franco, R., Paul, A., Petersen, F., Wolf, F. N. and Schramm, B. and MSM71 cruise participants, AlpArray Working Group (2019) Seismic investigations of the Ligurian Basin. [Talk] In: 79. Jahrestagung der Deutschen Geophysikalischen Gesellschaft (DGG)., 5.3. - 8.3.2019, Braunschweig, Germany.

Dannowski, A., Wolf, F. N., Kopp, H., Grevemeyer, I., Lange, D., Thorwart, M., Crawford, W., Caielli, G., de Franco, R., Paul, A., Petersen, F. and Schramm, B. and MSM71 cruise participants, AlpArray Working Group (2019) Investigations of the Ligurian Basin using refraction seismic data and the ambient noise technique. [Talk] In: EGU General Assembly 2019. , 08.-13.04.2019, Vienna, Austria.

Dannowski, A., Wolf, F. N., Kopp, H., Grevemeyer, I., Lange, D., Thorwart, M., Crawford, W., Caielli, G., de Franco, R., Paul, A., Petersen, F. and Schramm, B. and MSM71 Cruise participants, AlpArray Working Group (2019) LOBSTER - Ligurian Ocean Bottom Seismology and Tectonics. [Talk] In: 38. Convegno Nazionale del GNGTS 2019 (Gruppo Nazionale Geofisicadella Terra Solida). , 12.-14.11.2019, Rom, Italy.

Dannowski, A., Wolf, F. N., Kopp, H., Grevemeyer, I., Lange, D., Thorwart, M., Crawford, W., Caielli, G., de Franco, R., Paul, A., Petersen, F. and Schramm, B. and MSM71 Cruise participants, AlpArray Working Group (2019) Investigations of the crust and upper mantle in the Ligurian Basin using refraction seismic data and ambient noise – LOBSTER. [Invited talk] In: AlpArray & 4D MB Scientific Meeting. , 13.-15.11.2019, Frankfurt am Main, Germany.

11.3. Conference posters

Bayrakci, G., Minshull, T. A., Schramm, B., Bull, J. M., Henstock, T. J., Macdonald, C., Chapman, M., Dunn, R., Provenzano, G. and Callow, B. (2019) Characterization of azimuthal anisotropy in a natural fluid escape structure in the nothern North Sea vai wide-angle reflection-refraction travel-time tomography: Initial results. [Poster] In: EGU General Assembly 2019. , 08.-13.04.2019, Vienna, Austria.

Beniest, A., Dannowski, A., Schnabel, M., Schmid, F., Werner, R., Kopp, H., Riedel, M., Heyde, I., Barckhausen, U., Petersen, F., Schramm, B. and Hannington, M. D. (2021) Imaging the crustal structure of the southern plate boundary of the Niuafo'ou microplate, Lau Basin, southwest Pacific, with reflection and refractions seismic data. [Poster] In: 81. Jahrestagung der Deutschen Geophysikalischen Gesellschaft (DGG)., 01.03.-05.03.2021, Kiel (online).

Böttner, C., Schramm, B., Berndt, C., Karstens, J., Bull, J., Callow, B. and Gross, F. (2019) GRAPA – Quantifying fractures using drone imagery. [Poster] In: STEMM-CCS 3. Annual Meeting. , 27.2.-1.3.2019, Amsterdam, Netherlands.

Böttner, C., Callow, B. J., Schramm, B., Gross, F., Geersen, J., Schmidt, M., Vasilev, A., Petsinski, P. and Berndt, C. (2021) Focused methane migration formed pipe structures in permeable sandstones: Insights from UAV-based digital outcrop analysis in Varna, Bulgaria. [Poster] In: 81. Jahrestagung der Deutschen Geophysikalischen Gesellschaft (DGG)., 01.03.-05.03.2021, Kiel (online).

Bull, J. M., Berndt, C., Minshull, T. A., Henstock, T. J., Bayrakci, G., Gehrmann, R., Böttner, C., Schramm, B., Callow, B., Chapman, M., Yilo, N., Dewar, M., Chen, B., Saleem, U., Marin-Moreno, H., Provenzano, G., Lichtschlag, A., Falcon-Suarez, I., Roche, B., James, R., Connelly, D. P., Matter, J., Elger, J., Karstens, J. and Best, A. I. (2018) Constraining leakage pathways through the overburden above sub-seafloor CO2storage reservoirs. [Poster] In: International Conference on Greenhouse Gas Technology (GHGT-14)., 21.-26.10.2018, Melbourne, Australia.

Dannowski, A., Kopp, H., Grevemeyer, I., Lange, D., Thorwart, M., Crawford, W. C., Caielli, G., de Franco, R., Paul, A., Wolf, F. N., Petersen, F., Schramm, B. and Xia, Y. and AlpArray Working Group (2019) Extremely thinned continental crust underneath the Ligurian Basin?. [Poster] In: AGU Fall Meeting 2019. , 09.-13.12.2019, San Francisco, USA

Kopp, H., Dannowski, A., Grevemeyer, I., Lange, D., Thorwart, M., Caielli, G., Franco, R., Petersen, F., Wolf, F. N. and Schramm, B. (2020) Investigations of the Oligocene-Miocene opening of the Ligurian Basin using refraction seismic data. [Poster] In: EGU General Assembly 2020. , 04.05.-08.05.2020, Vienna, Austria. DOI 10.5194/egusphere-egu2020-6950.

Schmid, F., Dannowski, A., Kopp, H., Petersen, F., Schnabel, M., Barckhausen, U., Schramm, B., Beniest, A., Brandl, P., Weber, M. and Hannington, M. D. (2019) Formation and Rifting of backarc crust in the Lau Basin: First results of a recent seismic experiment. [Poster] In: 79. Jahrestagung der Deutschen Geophysikalischen Gesellschaft (DGG)., 5.3. - 8.3.2019, Braunschweig, Germany.

Schramm, B., Berndt, C., Dannowski, A., Bayrakci, G., Böttner, C. and Minshull, T. (2019) Imaging the 3D seismic velocity structure of the Scanner pockmark, central North Sea. [Poster] In: STEMM-CCS 3. Annual Meeting. , 27.2.-1.3.2019, Amsterdam, Netherlands.

Schramm, B., Berndt, C., Dannowski, A., Bayrakci, G., Minshull, T. and Böttner, C. (2019) Imaging the 3D seismic velocity structure of the Scanner pockmark, central North Sea. [Poster] In: 79. Jahrestagung der Deutschen Geophysikalischen Gesellschaft (DGG)., 5.3. - 8.3.2019, Braunschweig, Germany.

Schramm, B., Bayrakci, G., Dannowski, A., Böttner, C., Berndt, C., Henstock, T. J., Bull, J. and Minshull, T. (2019) Imaging the 3D seismic velocity structure of the Scanner pockmark, central North Sea. [Poster] In: AGU Fall Meeting 2019. , 09.-13.12.2019, San Francisco, USA.

Schramm, B., Singhroha, S., Dannowski, A., Vadakkepuliyambatta, S., Domel, P., Berndt, C. and Bünz, S. (2021) Characterization of the seismic velocities in a gas chimney blow the actively seeping Lunde pockmark, Vestnesa Ridge, Svalbard Margin: Preliminary results. [Poster] In: 81. Jahrestagung der Deutschen Geophysikalischen Gesellschaft (DGG)., 01.03.-05.03.2021, Kiel (online).

11.4. Reports – Cruise Reports

Berndt, C., Muff, S., Klaucke, I., Watt, S., Böttner, C., Schramm, B., ... & Roth, T. (2017). RV SONNE 252 Cruise Report/Fahrtbericht, Yokohama: 05.11. 2016-Nouméa: 18.12. 2016. SO252: RITTER ISLAND Tsunami potential of volcanic flank collapses. https://doi.org/10.3289/CR_SO252

Berndt, C., Elger, J., Böttner, C., Gehrmann, R., Karstens, J., Muff, S., ... & Völsch, A. (2017). RV MARIA S. MERIAN Fahrtbericht/Cruise Report MSM63-PERMO, Southampton–Southampton (UK) 29.04.-25.05. 2017. https://doi.org/10.3289/GEOMAR_REP_NS_37_2017

Berndt, C., Böttner, C., Elger, J., Kontradowitz, S., Kühn, M., Müller, S., ... & Stelzner, M. (2019). Sector collapse kinematics and tsunami implications-SEKT, Cruise No. M154/1, April 3-April 25, 2019, Mindelo (Cape Verde)-Point-á-Pitre (Guadeloupe). https://doi.org/10.2312/cr_m154_1

Berndt, C., Urlaub, M., Jegen, M., Faghih, Z., Reeck, K., Franz, G., ... & Diller, N. (2021). RV SONNE Fahrtbericht/Cruise Report SO277 OMAX: Offshore Malta Aquifer Exploration, Emden (Germany)–Emden (Germany), 14.08.–03.10. 2020. https://doi.org/10.3289/GEOMAR_REP_NS_57_20

Karstens, J., Schneider von Deimling, J., Böttner, C., Elger, J., Hilbert, H. S., Kühn, M., ... & Schramm, B. (2018). RV ALKOR Cruise Report 512 [AL512]-North Sea Blowouts, 15th July-26th July, 2018, Cuxhaven-Kiel (Germany). https://doi.org/10.3289/CR_AL512

Karstens, J., Böttner, C., Edwards, M., Falcon-Suarez, I., Flohr, A., James, R., ... & Wilson, M. (2019). RV MARIA S. MERIAN Fahrtbericht/Cruise Report MSM78-PERMO 2, Edinburgh–Edinburgh (UK), 16.10.–25.10. 2018. https://doi.org/10.3289/geomar_rep_ns_48_2019

Appendix